

**Synthesis and characterisation of silica  
adsorption platforms for use in  
environmental remediation**

**Khalid Mohammed Alotaibi**

**Dec 2014**

**Synthesis and characterisation of silica  
adsorption platforms for use in environmental  
remediation**

**Khalid Mohammed Alotaibi**

**Supervisor: Dr. Lorraine Gibson**

**Department of Pure and Applied Chemistry  
University of Strathclyde**

A thesis submitted to the Department of Pure and Applied Chemistry, University of Strathclyde, in part fulfilment of the regulations for the degree of Doctor of Philosophy (Ph.D).

**Dec 2014**

The copyright of this thesis belongs to the author under the terms of the United Kingdom Copyrights Acts as qualified by University of Strathclyde Regulation 3.51. Due acknowledgement must always be made of the use of any material contained in, or derived from, this thesis.

## Abstract

In this work a new method of production of MCM-41 was used which involved synthesis under mild conditions (room temperature) and shorter reaction times as well as reduced surfactant removal times (15 min) compared to the previously published methods that take approximately 10 h. This material was functionalised with an amine-based functional group to study the feasibility of separation of chromium (III) and chromium (VI) from aqueous solution. A maximum adsorption capacity calculated using Langmuir isotherms of  $111.1 \text{ mg g}^{-1}$  was achieved, which was higher than previously reported for competitive sorbents. Moreover, adsorbents containing silica nanoparticles with different porosity parameters were synthesized and evaluated for Cr (VI) uptake. The adsorption mechanism was defined by a two step adsorption mechanism for AP-MCM-41 while other sorbent exhibited a fast one step adsorption mechanism. The regeneration of MP-MCM-41 loaded with Hg (II) ions was also investigated with batch and dynamic methods using thiourea that was acidified using  $\text{HNO}_3$ ,  $\text{H}_2\text{SO}_4$ , or  $\text{HCl}$ ; with  $\text{HCl}$  being the most efficient with recovery efficiency of over 90 %.

A simple, rapid, bio-inspired green silica material was then developed producing a silica material with iron nanoparticles being incorporated into the framework (Fe-GN). The efficiency of Fe-GN material for the removal of arsenic ions from contaminated solution was evaluated. The material was found to be effective for the removal of arsenate ions with a maximum adsorption capacity of 69 mg/g of Fe-GN. Moreover, a method was developed to regenerate the Fe-GN allowing for full recovery and reuse of the adsorbent in subsequent extractions. Finally, the Fe-GNs material, along with other conventionally available materials, was assessed for the removal of naphthalene from aqueous solutions. The Fe-GN material was found to only have a slight affinity for the adsorption of naphthalene.

# Acknowledgments

I sincerely thank Allah, my God, the Most Gracious, and Most Merciful for giving me the health, ability, strength and blessing to complete this report.

First of all, I would like to express my sincere gratitude to my supervisor **Dr. Lorraine Gibson** for all of the help, knowledge, support and enthusiasm that she has been given to me during this study.

I would like to thank all **Dr. Christine Davidson, Dr. Alistair Wark, and Dr. Siddharth Patwardhan** for giving me the opportunity to use their instruments for MCM-41 synthesis or characterization.

I would also like to express my sincere gratitude to the analytical chemistry staff: **Prof. David Littlejohn and Dr. Alison Nordon** for their help during my first year study.

I would like to acknowledge **Mrs. Denise Gilmour** for her assistance in performing micro analysis, **Dr. Pamela Allan and Craig King** for their help and advice with the flame atomic absorption instrument, **Mr. Gavin Bain and Mr. Ian Airdrie** for their assistance of BET isotherms analysis, and to all people of the department of Pure and Applied Chemistry for their technical assistance throughout the project.

I would like also to thank **Dr. Peter Anderson and Dr. Tanya Peshkur** at Scottish Environmental Technology Network (SETN) for their assistance with ICP-OES.

Finally, it is pleasure to record my special thanks to **Dr. Salah Idris** for his friendship, encouragement, support, and advice during this study.

Last but not least I wish to avail myself of this opportunity, express a sense of gratitude and love to my beloved mother for her love, supplications, patience, and support.

# Table of Contents

<b>Chapter 1 : Introduction to porous materials</b> .....	<b>1</b>
<b>1.1. Definition and classification of porous materials:</b> .....	<b>2</b>
<b>1.2. A brief history of porous materials</b> .....	<b>5</b>
1.2.1. Development of zeolites and other porous adsorbents: .....	5
<b>1.3. Sol-Gel science based on mesoporous silica:</b> .....	<b>7</b>
<b>1.4. Mesoporous Silica Materials</b> .....	<b>8</b>
1.4.1. Methods of M41S material preparation:.....	12
1.4.1.1. The role of the surfactant in the synthesis mechanism: .....	12
1.4.1.2. Different sources of silica: .....	14
1.4.2. Template removal processes. ....	16
1.4.3. Functionalisation of mesoporous silica. ....	18
1.4.3.1. Silica functionalisation by PSG .....	18
1.4.3.2. Silica functionalisation by the co-condensation route .....	19
1.4.4. Mechanisms used to described the formation of M41S materials .....	20
<b>1.5. Silica mesopore properties and characterisation.</b> .....	<b>23</b>
<b>1.6. Applications of mesoporous silica materials.</b> .....	<b>26</b>
<b>1.7. Limitations of mesoporous silica materials:</b> .....	<b>27</b>
<b>1.8. Aim and objectives:</b> .....	<b>28</b>
<b>Chapter 2 : Instrumentation</b> .....	<b>30</b>
<b>2.1 Gas adsorption isotherms</b> .....	<b>31</b>
2.1.1 The BET surface area, pore volume and pore size distribution .....	34
<b>2.2 Fourier transform infrared spectroscopy (FTIR)</b> .....	<b>39</b>
2.2.1 Molecular vibrations .....	39
2.2.2 FTIR instrumentation .....	42
<b>2.3 CHN microanalysis [106,107]</b> .....	<b>45</b>
<b>2.4 Inductively Coupled Plasma Optical Emission Spectroscopy (ICP-OES)</b> .....	<b>46</b>
2.4.1 ICP-OES instrumentation .....	48
2.4.2 Sample introduction .....	49
2.4.3 The inductively coupled plasma torch .....	50
2.4.4 Detection of Emission .....	53
<b>2.5 Liquid chromatography (LC) [106,116-119]</b> .....	<b>54</b>
2.5.1 Mobile phase in LC.....	56

2.5.2 Sample Introduction for HPLC .....	57
2.5.3 HPLC Column.....	58
2.5.4 Spectrophotometric Detectors .....	61
<b>Chapter 3 : Experimental and Safety.....</b>	<b>64</b>
<b>3.1 Preparation of mesoporous materials .....</b>	<b>65</b>
3.1.1 MCM-41 .....	65
3.1.2 SBA-15.....	65
3.1.3 Bio-inspired silica materials .....	66
3.1.4 Surface modification of materials.....	66
<b>3.2 Characterisation of mesoporous silica material .....</b>	<b>67</b>
3.2.1 Measurement of Brunauer-Emmett-Teller (BET) isotherms .....	67
3.2.2 Fourier transform infrared spectroscopy (FTIR) .....	67
3.2.3 Scanning electron microscopy (SEM) measurements .....	67
3.2.4 Nanosight system.....	68
<b>3.3 The extraction and regeneration procedures for removal and recovery of potentially toxic metals .....</b>	<b>69</b>
3.3.1. The adsorption isotherms (Langmuir and Freundlich models).....	69
3.3.1.1 The Langmuir model.....	69
3.3.1.2 Freundlich model .....	70
3.3.1.3 Evaluation of maximum adsorption capacity. ....	71
3.3.2 The sorbent extraction efficiencies for metal ions mixed with real water samples .....	71
3.3.3. Examination of sorbent performance in dynamic mode.....	72
3.3.4. Determination of metal ion concentrations in aqueous solution using ICP-OES. ....	73
<b>3.4 Safety .....</b>	<b>73</b>
<b>Chapter 4 : Synthesis of microwave digested MCM-41 (MWD-MCM-41) .....</b>	<b>75</b>
<b>4.1 Introduction .....</b>	<b>76</b>
<b>4.2 Experimental.....</b>	<b>78</b>
4.2.1 Materials and reagent .....	78
4.2.2 Synthesis of MWD-MCM-41 .....	78
4.2.3 Synthesis of resol reagent.....	78
4.2.4 Synthesis of resol-MCM-41.....	79
<b>4.3 Results and discussion .....</b>	<b>80</b>
4.3.1 Nitrogen adsorption-desorption analysis .....	80

4.3.2 The particle size distribution (PSD) of MWD-MCM-41.....	81
4.3.3 Examination of MWD-MCM-41 using a Scanning Electron Microscope. ....	82
4.3.4 Examination of MWD-MCM-41 with Transmission electron microscopy (TEM)...	84
4.3.5 Fourier transform infrared spectroscopy (FTIR) and elemental analysis of MCM-41 materials. ....	86
4.3.6 New methods of MCM-41 preparation .....	87
4.3.7 Incorporation of Resol into the silica framework: .....	91
<b>4.4 Conclusion.....</b>	<b>91</b>
<b>Chapter 5 : Adsorption of chromium species from water samples.....</b>	<b>93</b>
<b>5.1 Introduction:.....</b>	<b>94</b>
<b>5.2 Experimental.....</b>	<b>96</b>
5.2.1 Determination of Cr (VI) in water samples using a colourimetric method .....	96
5.2.2 Determination of total chromium Cr <sub>Total</sub> in water samples using inductively coupled plasma- optical emission spectrometry (ICP-OES): .....	97
5.2.3 Extraction and recovery of chromium ions .....	101
5.2.4 Analysis of real water samples .....	102
5.2.5 Adsorption kinetics study .....	102
5.2.5.1 The pseudo first-order equation: .....	103
5.2.5.2 The pseudo second-order equation: .....	103
5.2.5.3 The intraparticle diffusion model:.....	103
5.3 Results and discussion .....	104
5.3.1 Exclusive removal of Cr (VI) in the presence of Cr (III) .....	104
5.3.2 Characterisation of pre- and post-modified MWD-MCM-41 using FTIR and elemental analysis. ....	106
5.3.3 Determination of adsorption isotherms for Cr (VI) onto AP-MWD-MCM-41 and calculation of adsorption capacity.....	109
5.3.3.1 Example calculation for determination of the Langmuir or Freundlich isotherm equations.....	109
5.3.3.2 Resultant adsorption isotherm models for the removal of Cr (VI) from aqueous solutions. ....	110
5.3.4 Removal of Cr (VI) from contaminated, multi-element, solutions. ....	111
5.3.5 Pre-concentration of Cr (VI) from water samples. ....	114
5.3.6 Examination of sorbent performance in packed-bed under continuous flow systems: .....	115
5.3.7 Kinetic study of chromium (VI) adsorption onto AP-MWD-MCM-41.....	116



5.3.8 The effect of pore size distribution of mesoporous silicate on the extraction kinetics of chromium (VI).....	122
5.3.8.1 FTIR characterisation.....	122
5.3.8.2 Materials characterisation by N <sub>2</sub> adsorption. ....	124
5.3.8.3 Elemental analysis. ....	127
5.3.8.4 Adsorption isotherms.....	128
5.3.8.5. Kinetic study of chromium (VI) adsorption onto AP- loaded MWD-MCM-41, Cal-MCM-41 and SBA-15. ....	130
5.3.9 Conclusion:.....	133

**Chapter 6 : Regeneration of mercapto- loaded MWD-MCM-41 using acidified thiourea.....134**

<b>6.1 Introduction .....</b>	<b>135</b>
<b>6.2 Experimental.....</b>	<b>137</b>
6.2.1 Batch method .....	137
6.2.2 Examination of sorbent performance in dynamic mode.....	137
<b>6.3 Results and discussion .....</b>	<b>138</b>
6.3.1 Regeneration of MP-MCM-41 adsorbents of mercury using acidified thiourea. ....	138
6.3.1.1 Regeneration of MP-MCM-41 using a batch method. ....	138
6.3.1.2 Extraction and recovery of Hg (II) using MP-MCM-41 loaded solid phase extraction (SPE) cartridges. ....	141
6.3.2 Preconcentration of Hg (II) using MP-MCM-41 loaded solid phase extraction (SPE) cartridges. ....	142
<b>6.4 Conclusion .....</b>	<b>143</b>

**Chapter 7 : Synthesis of iron supported on bioinspired green silica for the removal of arsenic ions from water .....144**

<b>7.1 Introduction .....</b>	<b>145</b>
<b>7.2 Experimental.....</b>	<b>150</b>
7.2.1 Material and reagent .....	150
7.2.2 Synthesis of Fe-GN.....	151
7.2.3 Reduction of GN:.....	152
7.2.4 Synthesis of iron loaded MCM-41. ....	152
7.2.6 The efficiencies of sorbents in real water samples .....	152
7.2.7 Adsorption isotherms for the maximum adsorption capacity evaluation.....	153
7.2.8 Characterisation and analysis .....	154

<b>7.3 Results and discussion .....</b>	<b>155</b>
7.3.1 Materials characterisation.....	155
7.3.1.1 Iron loading efficiency and nitrogen adsorption isotherms analysis: .....	155
7.3.1.2 Elemental (CHN) analysis.....	158
7.3.1.3 X-ray Photoelectron Spectroscopy (XPS).....	159
7.3.1.4 Mössbauer Spectroscopy .....	161
7.3.1.5 Attenuated Total Reflectance Fourier Transform Infrared spectroscopy (ATR-FTIR)	163
7.3.2. CASE STUDY: The adsorption of arsenic using different silica platforms. ....	166
7.3.2.1 Effect of solvents on the signal intensity of ICP-OES.....	166
7.3.2.2 Effect of pH.....	167
7.3.2.3 Adsorption isotherms for As(V) on as made-Fe-GN .....	170
7.3.2.4 Assessment of Fe-GN performance in real samples.....	173
7.3.2.5 Examination of sorbent performance in packed-bed under continuous flow systems	
.....	174
<b>7.4 Conclusion .....</b>	<b>175</b>
<b>Chapter 8 : Case study: Comparison of Polycyclic aromatic hydrocarbon removal</b>	
<b>from water for silica and carbon supports .....</b>	<b>177</b>
<b>8.1 Introduction: .....</b>	<b>178</b>
<b>8.2 Experimental.....</b>	<b>182</b>
8.2.1 materials and reagents .....	182
8.2.1 Synthesis of adsorbents .....	182
8.2.2 Adsorption of naphthalene using carbon and silica based materials.....	182
8.2.3 Determination of naphthalene's concentration using high performance liquid	
chromatography with fluorescence detectors (HPLC/FLD) .....	182
<b>8.3 Results and discussion .....</b>	<b>184</b>
8.3.1 Materials characterization.....	184
8.3.2 Extraction efficiency of naphthalene using carbon and silica based materials...	186
<b>8.4 Conclusion .....</b>	<b>188</b>
<b>Chapter 9 : Conclusions and future work .....</b>	<b>189</b>
<b>9.1 The removal of potentially toxic elements from aqueous solutions using MWD-</b>	
<b>MCM-41 .....</b>	<b>190</b>
<b>9.2 Synthesis of iron supported on bioinspired green silica for the removal of arsenic</b>	
<b>ions from aqueous solution .....</b>	<b>192</b>
<b>9.3 Challenges of using nanomaterials for <i>in situ</i> groundwater remediation: .....</b>	<b>193</b>

<b>9.4 Future work .....</b>	<b>195</b>
<b>Reference .....</b>	<b>196</b>

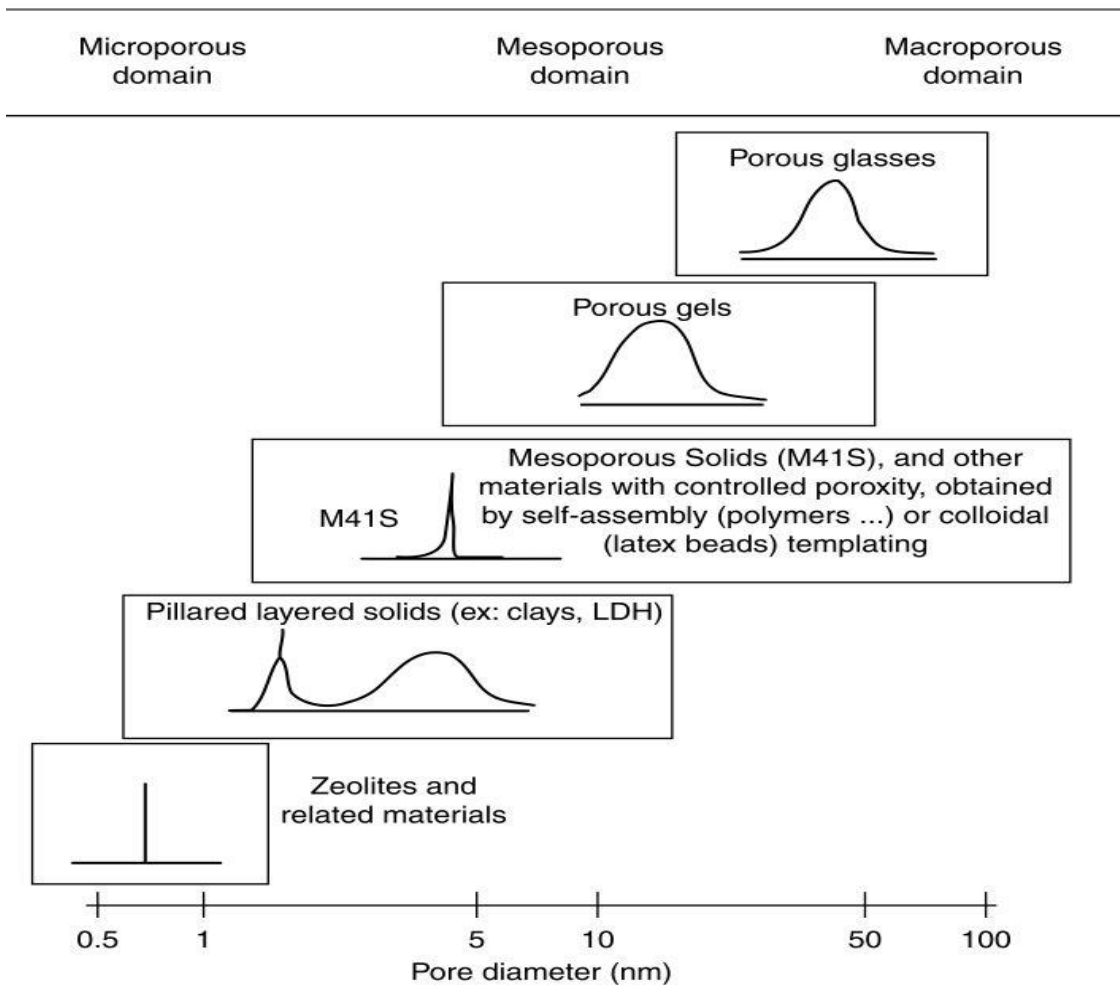
## **Chapter 1 : Introduction to porous materials**

## 1.1. Definition and classification of porous materials:

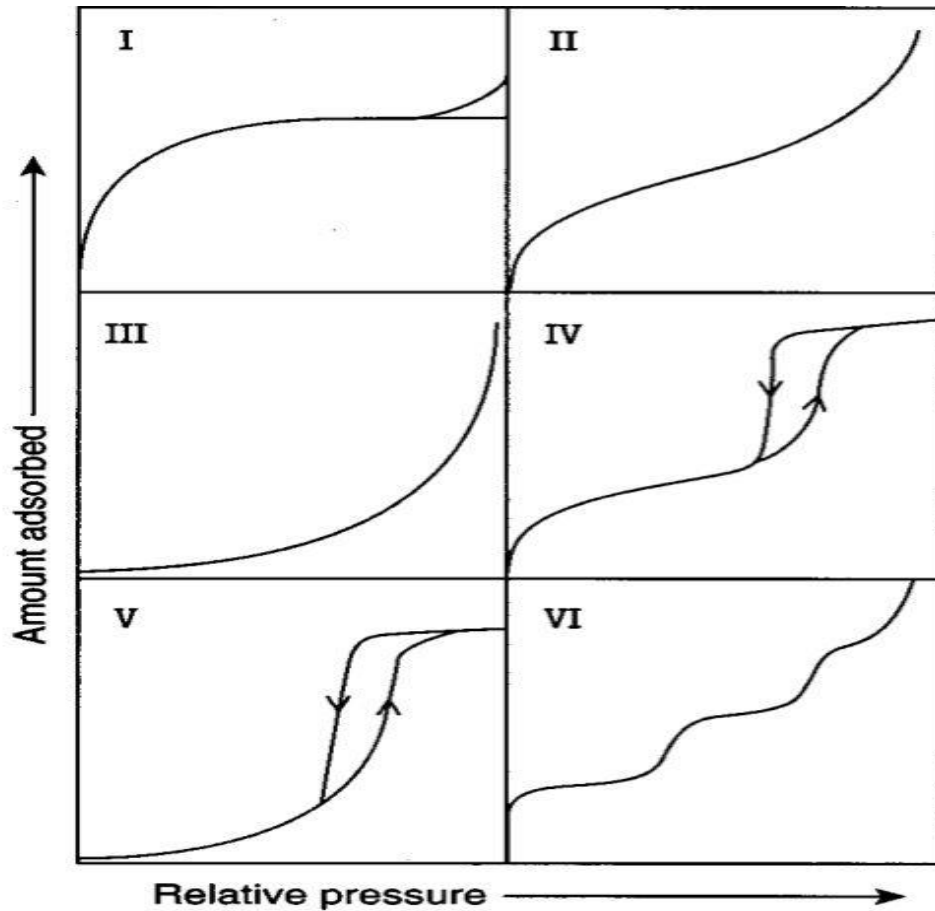
Porous materials are solids that consist of empty pores dispersed within their framework. There are two types of pores: closed pores (which are isolated from the outside of the material and may contain fluid) and open pores (which are connected to the surface of the material). Open porous materials are required for industrial applications, e.g. filters and gas distribution, whereas closed pores can be used for sonic and thermal isolation. Porosity can change a material's properties mainly by increasing its specific surface area and by decreasing density. These changes can provide the materials with useful features, such as fluid permeability, which are not observed in dense materials [1]. Porous materials are classified according to many different criteria, e.g. pore shape, pore size and production methods. In terms of pore size, the porous solid materials are classified by the International Union of Pure and Applied Chemistry (IUPAC), Fig 1-1 as:

- Microporous material ( $X < 2$  nm).
- Mesoporous material ( $2 \text{ nm} < X < 50$  nm).
- Macroporous material ( $X > 50$  nm).

Porous materials can also be classified according to their adsorption properties. The term adsorption refers to the condensation or attachment of particles (e.g. gas molecules) to a porous surface. The adsorption of gases, such as  $N_2$  can be expressed quantitatively with an adsorption isotherm (the amount of gas adsorbed by the material at constant temperature as function of pressure). Porous materials can be characterised in terms of pore diameter as based on the obtained gas adsorption data. As a consequence, the IUPAC conventions are available detailing the classifications for both pore size and gas adsorption isotherms in conjunction with associated hysteresis loops [2,3]. The IUPAC classification of adsorption isotherms is shown in Fig 1-2:



**Fig 1-1: Shows an example of some porous materials and their pore size distribution [2].**



**Fig 1-2: IUPAC classification of adsorption isotherms [4].**

These isotherms are characteristic of adsorbents that are microporous (type I), macroporous or non-porous (types II, III, and VI), and mesoporous (types IV and V). This classification can provide useful information about the adsorption and pore filling mechanisms. The shape of the isotherm provides direct information about the fluid – solid interactions, pore structure (shape and size), monolayer–multilayer adsorption, and filling/emptying of pores. In particular, the adsorption process in mesopores is controlled by capillary condensation and multilayer adsorption. In contrast, the filling of micropores is dominated by stronger interaction between the adsorbate molecules and the pore walls. The differences between types II and III isotherms and between types IV and V isotherms are derived from the fluid interaction strength: types III and V are associated with weaker fluid–solid interactions, and types II and IV are associated with stronger fluid–solid interactions [2,3].

In general porous materials have attracted a great deal of attention in research and industry because of their potential use in a wide range of practical applications, e.g. adsorption, separation, catalysis and sensing systems. The main challenges that scientists working on porous materials have to face are how to design, synthesis and modify the materials, tailoring them to suit specific applications. Therefore, several synthesis mechanisms have recently been reported on the production of nanoporous materials [5,6].

## **1.2. A brief history of porous materials**

Most porous materials are ubiquitous in nature, except ceramics and metals that are fired at high temperatures (this process known as sintering which involves heating the metal clay to a point where the metal particles stick to each other, consequently, it will contain a tiny holes between the metal particles and hence the materials are somewhat porous). As with the use of many other materials of practical importance, the applications of wood, hides, clays, and other porous materials do not have any well-documented beginnings and are believed to date back to prehistoric times. These porous solids were commonly used by humans in their natural form; occasionally following some form of heat treatment or other minor alterations. One example of this is charcoal, which was used both as a drawing material and also by the Ancient Egyptians around 1500 B.C. in water filtration systems [7].

### **1.2.1. Development of zeolites and other porous adsorbents:**

Zeolites are crystalline aluminosilicate-based materials which were discovered in 1756 by Swedish mineralogist Cronstedt, who noticed that when the unidentified mineral was subject to a flame, a frothy mass of bubbles formed. Based on this observation, he named the material 'Zeolite', from the Greek zeo "to boil" and lithos "stone". During the nineteenth century, zeolite minerals began to be well documented with scientific interest starting in the early nineteenth century. The term 'molecular sieves' was given by McBain [8] in 1931, when he found that chabazite (a tectosilicate mineral of the zeolite



group) rapidly sorbed the vapours of small molecules (H<sub>2</sub>O, ethanol, methanol, and formic acid), whereas larger molecules were largely excluded (benzene, acetone and ether) [8]. A decade later, Barrer *et al.* [9] studied the sorptive properties of chabazite and analcite, and stated that the separation of N<sub>2</sub> and O<sub>2</sub> could be achieved using a zeolite that had been treated under certain conditions to produce the necessary shape selectivity to discriminate between molecular dimensions of N<sub>2</sub> and O<sub>2</sub>. A few years later, zeolites began to be synthesised on a large scale for the production of O<sub>2</sub> from air [7]. In the years between 1949 and 1954, a number of new zeolites (types A, X, and Y) were synthesised by Milton and colleagues [10]. The new zeolite materials were commercialised in 1954 by Union Carbide Corporation, as new methods were developed for the separation and purification of small molecules. In 1955, the structure of syntactic zeolite type A was reported by D. Breck and colleagues [11]. Since then, extensive research has been performed in this field, which has led to the development of a new family of silicoaluminophosphates and aluminophosphates [12-14].

Zeolite materials, particularly those with a small pore size (e.g. 0.4 nm in A-type zeolites), first attracted commercial interest as they provided the opportunity for selective adsorption according to the differences in the size of the separated gas molecules. In addition, Jules Rabo, who was working at Union Carbide Research Centre, reported that a certain type of zeolite had shown catalytic activity for cracking hydrocarbons. Initially the oil industry did not accept the idea because it was felt that the pore size was not big enough for cracking activity. In 1983, Plank and his colleagues reported that rare earth containing zeolite X was capable of acting as a cracking catalyst. Therefore, a few years later, the amorphous silica-alumina catalysts were replaced by the zeolite cracking catalysts [7].

Major efforts were made to enlarge the pore size of the zeolite type materials from the micropore region ( $\leq 2$  nm width) to the mesopore region ( $2 \text{ nm} \leq X \leq 50 \text{ nm}$ ), due to increasing demand for mesoporous materials. Examples of applications of mesoporous materials include the separation and synthesis of large molecules (e.g. proteins and the extraction of large organic molecules from waste water) and the treatment of heavy feeds

(e.g. the processing of oil sand from high distillates of crude oils to valuable low boiling products) [14]. Preparation of zeolite-type materials with larger pore diameters was accomplished by Wilson and colleagues,[13] who synthesised a material, identified as an ultra-large pore molecular sieve (ALPO4-8), by changing the composition of the synthesis gel. This zeotype material contained 14-membered rings, whereas the traditional zeolites contained 12 rings. By 1990, more than 25 different structures, and at least 15 elements, were incorporated into the framework of the ALPOs. This discovery altered the traditional viewpoint that the organic templates used to synthesise zeolites could not be constructed with more than 12 rings, and also led to the synthesis of other ultra-large pore molecular sieves (e.g. VPI-5, JDF-20, and cloverite). However, due to poor stability or weak acidity of these materials, they have not had significant success in applications. As a result, they remain to be inferior when compared to pillared, layered clays.

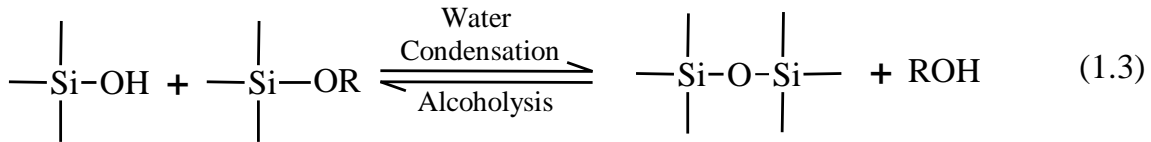
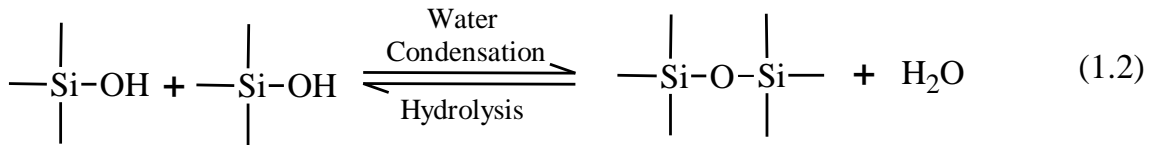
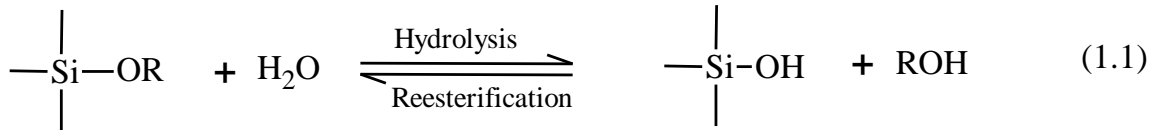
### **1.3. Sol-Gel science based on mesoporous silica:**

Sol-gel chemistry has been studied extensively since the mid-1970s, when sol-gel reactions were first reported to produce different inorganic networks that are obtained from a metal alkoxide solution. Accordingly, homogenous, high-purity inorganic oxide glasses can be obtained at room temperature, compared to the conventional approaches that require high temperatures. Sol gel procedures have been used to create a range of porous materials (e.g. spun fibers, molecular cages, moulded gels and Xerogels) that have been used in applications such as gas separation, coatings and laminates [15].

The term “sol-gel” is derived from the process whereby a solution becomes a gel [16]. Sol-gel processing precursors are composed of metals or metalloids that are bound to various reactive ligands. Metal alkoxides, e.g. zirconates, aluminates and titanates, are the most popular precursors used due to their ease of hydrolysis in the presence of water. Alkoxy silanes, such as tetraethyl orthosilicate (TEOS) and tetramethoxysilane (TMOS), are the most commonly used precursors for the production of silica gels.

The sol-gel process involves a series of hydrolysis and condensation reactions of alkoxides, as illustrated in Fig 1-3. The hydrolysis step, (Equation 1.1) is initiated via the

addition of water to the alkoxy silane solution under neutral, acidic, or basic conditions, resulting in the generation of a silanol group. Depending on the water/alkoxide ratio and the quantity and nature of the catalyst, hydrolysis may or may not go to completion. The hydrolysis step is followed by the condensation of the silanol group with either an alkoxide or another silanol group (Equations 1.3 and 1.2 respectively) [17,18].



**Fig 1-3: Sol-gel general reaction scheme.**

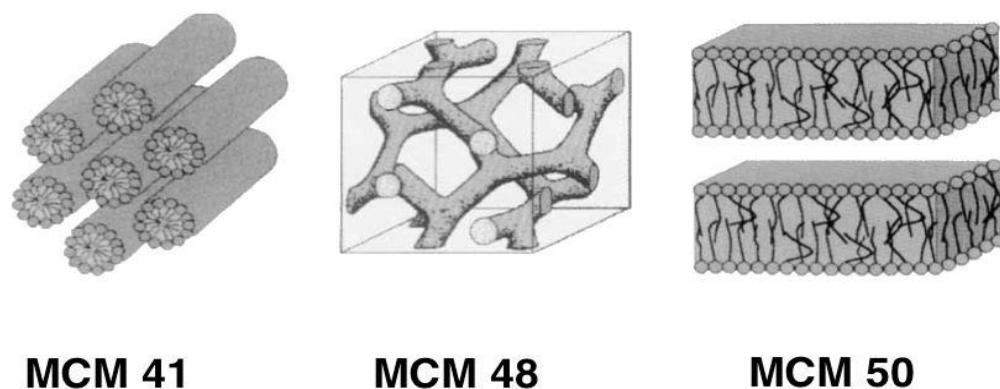
It is noteworthy that the hydrolysis and condensation reactions occur simultaneously when the hydrolysis reaction is initiated. Moreover, the low molecular weight by-products that are generated from the hydrolysis and condensation reactions, such as water and alcohol, must be removed from the system, and such a removal yields a vitrified, dense glass network[18].

## 1.4. Mesoporous Silica Materials

Mesoporous materials, as classified by the IUPAC, are those having a pore diameter that ranges from 2 nm to 50 nm. Most silicate materials are included under this description,

such as sol-gels (aerogels and xerogels), controlled pore or vycor glasses and surfactant template mesoporous materials [20]. The walls of all such silica materials are amorphous. As described above Xerogels and Aerogels are obtained by a gelation process of silica solutions, whereas controlled-pore glasses are produced from a borosilicate-based material which is subjected to heat; these have a relatively large pore size distribution which limits their use in applications which require a uniform pore size system, e.g. size-selection catalysis or optical waveguides.

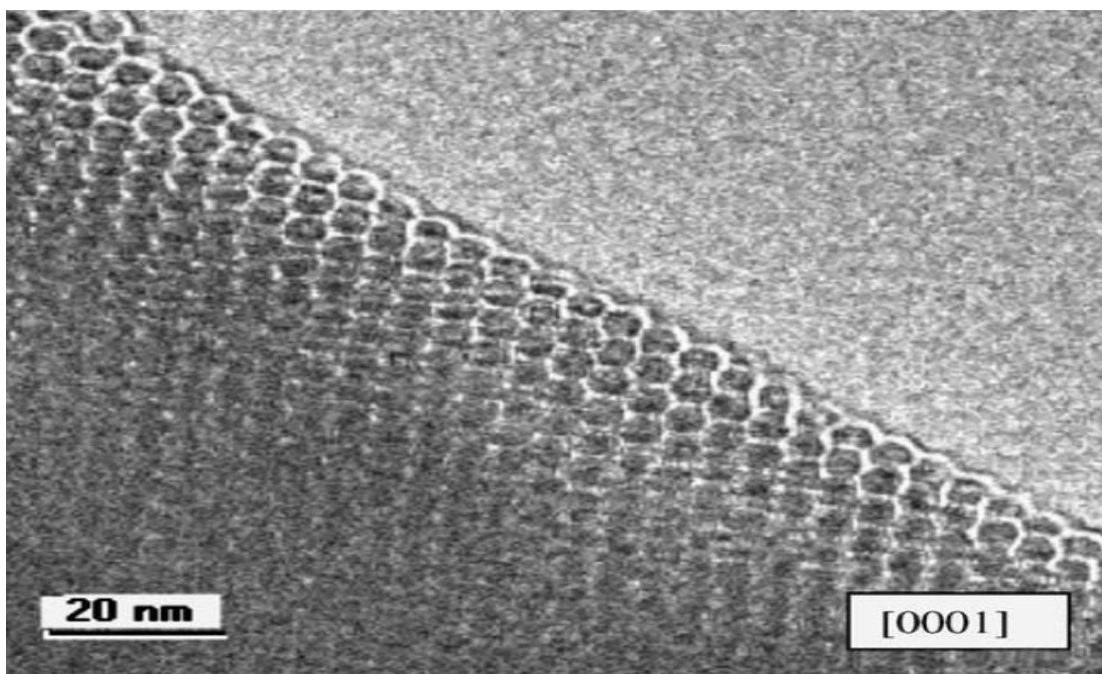
In 1990 Yanagisawa and colleagues [21] were the first to report the preparation of mesoporous material through the interaction of alkyltrimethylammonium chloride into a layered polysilicate Kanemite. The organic species was then removed by calcination, which resulted in three-dimensional SiO<sub>2</sub> networks with mesoporous properties (2-4 nm in diameter). However, because of the lack of characterisation data provided, the Yanagisawa results were largely ignored by the scientific community. Two years later Beck *et al.*, [6] at the Mobile Research and Development Corporation, reported the synthesis of a new family of ordered mesoporous molecular sieves through the use of a liquid crystal template, and named it M41S. These materials have a high surface area, large pore dimension and specific pore volume. The organic template used was no longer a single, solvated organic molecule or metal ion, but rather a self-assembled molecular array of surfactants [6,14]. M41S materials have been classified according to the order of pores, i.e. MCM-41 refers to material that has a hexagonal phase, MCM-48 refers to material that has a cubic phase and MCM-50 refers to material that has a meso-lamellar phase (see schematic illustrations in Fig 1-4). These surfactant-templated mesoporous silicate materials have drawn much attention in both scientific research and practical applications since the Beck publication [6,22]. To date, more than 9000 papers have been published on the synthesis and application of M41S based materials. Most of these applications have been focused on catalysis, but recently the application of these materials has been expanded into other areas, such as drug delivery, optical guides and low k dielectric layers in microelectronics [23].



**Fig 1-4: Phase structure of (a) MCM-41, (b) MCM-48, and(c) MCM-50 [7].**

MCM-41 exhibits a long-range ordered framework with uniform mesopores. However, it should be noted that the long-range order is in the pore structure and not in the solid itself, which could be virtually amorphous. The pores of these materials are nearly as regular as in zeolite materials, thus offering new opportunities for applications in adsorption media [24-26], chemical separation [27,28] and catalysis [29,30]. Accordingly, MCM-41 has attracted more attention than the other members of this family, which are either thermodynamically less stable or are more difficult to synthesise [31].

Ordered mesoporous molecular sieves, based on MCM-41, are silicates produced by a templating mechanism [6]. Such materials exhibit several remarkable features, e.g. well-defined pore sizes and shapes (tubular channels with tunable pore diameters in the range of 25-150 Å, that are ordered to some degree to obtain arrays of non-intersecting hexagonal channels, identifiable by means of X-ray powder diffraction (XRD) and transmission electron microscopy (TEM), as shown in Fig 1-5.



**Fig 1-5: Transmission electron micrograph of the hexagonal phase of calcined MCM-41 [5].**

These materials show a high surface area of about  $1000 \text{ m}^2 \text{ g}^{-1}$  and a high porosity of up to 80 % of the total volume. The walls of MCM-41 channels consist of amorphous  $\text{SiO}_2$  which has a structured framework with high thermal and hydrolytic stabilities [32]. The synthesis procedure of MCM-41 involves the use of neutral, cationic or anionic surfactants. Furthermore, changing the reaction parameters (e.g. pH, temperature, aging time and composition), the silica source (e.g. tetraethylorthosilicate (TEOS), fused silica and colloidal silica), the surfactants (e.g. cetyl trimethyl ammonium bromide (CTAB) and myristyl trimethyl ammonium bromide) [33,34] or adding auxiliary organic chemicals (e.g. 1,3,5- trimethylbenzene) [20,35] will lead to the production of materials with different wall thicknesses, pore sizes and pore volumes, and can also affect the thermal, mechanical, and hydrolytic stabilities of the mesoporous materials [6,32].

Functionalisation of mesoporous silica, with organic or inorganic functional groups, provides opportunities to adjust the chemical and physical properties of the resulting mesoporous material. These modified materials offer promising possibilities for numerous applications, including catalysis, separation, adsorption and drug delivery

[36,37]. The rest of this section will focus on the synthesis, functionalisation and application of M41S materials.

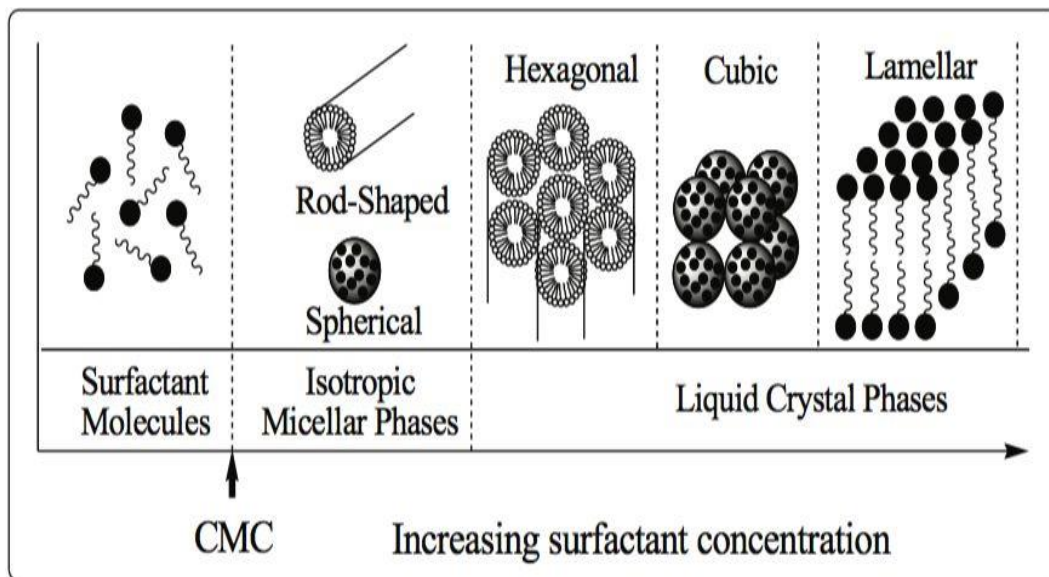
#### **1.4.1. Methods of M41S material preparation:**

The synthesis of templated mesoporous materials is in principle straightforward, requiring a silica source (e.g. TEOS or sodium silicate), a catalyst for the polymerisation of silica, the template (cetyl trimethylammonium bromide), and solvent (usually water). The behaviour of the surfactant in the aqueous synthesis solution can be affected by the presence of co-solvents, which results in changes to the characteristics of product [38,39]. An example is the addition of ethanol into the aqueous synthesis solution, which has been shown to favour particles with spherical and cubic phase structures from synthesis, where otherwise hexagonal structures (MCM-41) would be formed [40].

##### ***1.4.1.1. The role of the surfactant in the synthesis mechanism:***

The term “surfactant” is an abbreviation of “surface active agent”, which refers to its ability to lower the interfacial tension between water and a less polar phase [7]. Therefore, the structure of the inorganic materials framework produced mainly relies on the size and shape of micelles used during the preparation. In terms of MCM-41 production the surfactants are typically added at a concentration which permits the creation of micelles; these micelles then act as the structural directing agent for the silica material. The surfactants aggregate in water due to their amphiphilic character, as the head of a surfactant molecule is hydrophilic and the tail (long hydrocarbon chain) is hydrophobic. Accordingly, the surfactant micelles arrange themselves so that the hydrocarbon tail (hydrophobic) is removed from the water, leading to the formation of aggregates in the bulk solution above a certain concentration level known as the critical micellar concentration (CMC) [23]. Zhao and colleagues [14] described the behaviour of surfactant molecules in solution in terms of their concentration, as shown in Fig 1-6. At concentrations below the CMC, surfactant molecules are present in solution as monomeric units. When the concentration of surfactant increases, the monoatomic molecules aggregate to form isotropic micelles to reduce the system’s entropy. As the concentration process continues, hexagonal close-packed arrays of cylinders appear [41]. The next step in the process is the coalescence of the adjacent, mutually parallel cylinders

to produce the lamellar bilayer structures. Additionally, the cubic phase can also appear prior to the lamellar phase [14,41,42] and according to Fromhers [43], the cubic phase is believed to be composed of complex, interwoven networks of rod-like aggregates [14].



**Fig 1-6: Phase sequence of surfactant-water binary system [14].**

The particular phase of an amphiphilic material, present at a given concentration, depends not only on the concentration but also on other factors, such as the molecular structure (e.g. the hydrophobic carbon chain length, the hydrophilic head group and the counterion) and the environmental parameters (e.g. temperature, ionic strength of the aqueous phase, pH, and presence of additives). Generally, an increase in the chain length of the surfactant, the ionic strength and the valence of the counterions of the solution, will result in a decrease in the critical micellar concentration. On the other hand, the CMC increases with increasing pH, temperature, and counterion radius [14,41].

The pore size of a silica material depends on the length of the hydrophobic tail of the surfactant molecules used to produce the material. For example, cetyltrimethylammonium bromide (CTAB) was found to produce materials with a pore diameter in the range of 20–30 Å, which can be controlled in steps of 2-3 Å by altering the length of the hydrophobic tail of the surfactant. Interaction of the surfactant micelles



with swelling agents, such as mesitylene [44], trimethylbenzene [6,45] and alkanes[46], can also result in the formation of larger pores. Furthermore, surfactants with two or more alkyl tails on one charged head group have been synthesised, but they are not popular as the large tail volume can lead to the formation of lamellar phases which collapse after the removal of the surfactant [23].

#### **1.4.1.2. Different sources of silica:**

Condensation reactions of silica can be performed under alkaline, acidic, or neutral conditions (see Fig 1-7); all of which have been used to synthesise mesoporous silica materials. In the case of neutral conditions, the surfactant itself acts as a catalyst for the condensation of silica, since the formation of the templated materials occurs significantly faster than precipitation or gel formation in silica only solutions at the same pH [23]. Therefore precipitation occurs immediately after the addition of the silica source to the surfactant solution. When the solution is known to be indefinitely stable sodium fluoride has been used as a catalyst to promote the reaction under neutral conditions [47].

Under alkaline conditions, in the pH range 9.5-12.5, the templating reaction occurs rapidly and immediate precipitation is observed when the silica source is added into the surfactant solution. The polymerisation and cross-linkage mechanisms are reversible under alkaline conditions, therefore silica sources that can be utilised for the synthesis of mesoporous materials are diverse and include colloidal sols, silica gels, sodium silicates, silica aerogels or TEOS, which all readily dissolve in alkaline solutions [48]. Ammonia, potassium hydroxide, tetramethylammonium hydroxide, tetraethylammonium hydroxide and sodium hydroxide can be used as a base. Sometimes disordered mesoporous silica materials are obtained when ammonia is used, due to its weak alkalinity.



Under acidic conditions, below but near to the isoelectric point (IEP) of silica ( $\text{pH} \approx 2$ ), the induction times could be longer, up to several hours, depending on the pH and surfactant type used [23]. Acidic conditions favour the formation of mesoporous silicates with diverse morphologies, such as spheres, hollow spheres, thin films and fibres, [49], as the hydrolysis produces linear silicate oligomers that favour various regular morphologies. The polymerisation and cross-linkage mechanisms are irreversible, which means that it is difficult to change the structure of the material once the gel forms, compared to synthesis under basic conditions where the structure of the materials can be changed by simply adjusting temperature, concentration, etc. [48].

Efforts have been made to find cheaper silica sources, with coal fly ash [50,51], geothermal silica [52], and rice husk ash [53,54] being used to produce mesoporous materials. However, as these silica sources require dissolution of  $\text{SiO}_2$ , a formation of complex oligomeric silica species in the solution has been observed, which results in the interaction of these species with the surfactant during the formation of mesoporous materials [23]. Hence these sources, although cheaper, produce inferior materials to those using e.g., TEOS.

#### **1.4.2. Template removal processes.**

Removal of the surfactant template from the as-synthesised inorganic-organic composites is required to obtain the pores and various methods have been proposed. Calcination is one of the most common approaches used, due to the ease of operation and complete template elimination. In this process the surfactant is burned out at elevated temperatures in an ashing furnace. The process can be performed in atmospheric air [55], flowing nitrogen or nitrogen followed by oxygen [23]. The temperature normally used is  $500\text{ }^\circ\text{C}$  for a period of 5 h, with a temperature ramping rate of  $1\text{-}2\text{ }^\circ\text{Cmin}^{-1}$ . Bagshaw and colleagues suggested that rapid heating rates could be possible for some porous materials to fine-tune the porosity in the structure [56]. Several studies have been carried out to understand the mechanism of the thermal process for both polymeric templates and ionic surfactant templates. It was established that the surfactant is removed in several steps, most of it at temperatures below  $200\text{ }^\circ\text{C}$ , producing several volatile organic compounds (VOCs) [57-59]. Keene and colleagues proposed that the surfactant degradation is in



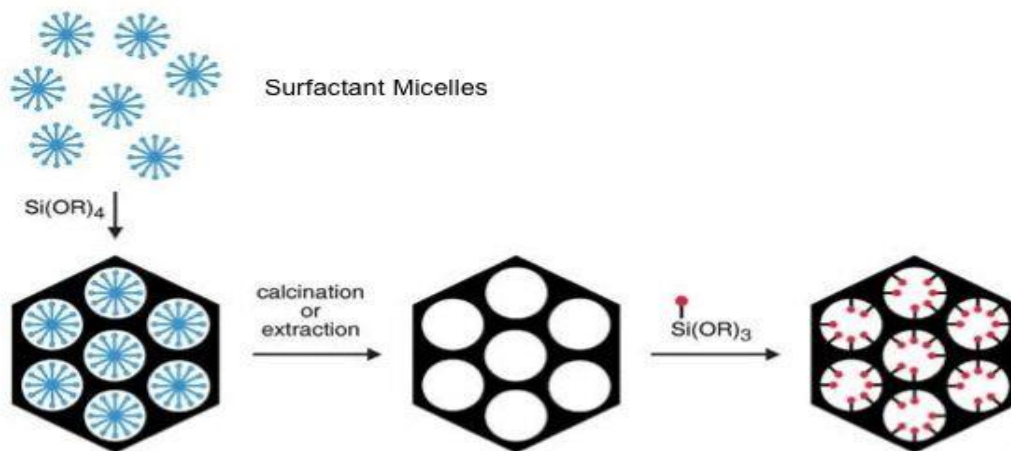
pore volume and pore size, and higher silanol group availability compared with those obtained from the previously described conventional template removal methods.

### 1.4.3. Functionalisation of mesoporous silica.

Modification of the silica wall takes advantage of the large surface area and high stability of the mesoporous materials. The strategy to link organic groups onto the silanol groups is critical for specific functions such as adsorption [66]. Generally, chemical surface modification is obtained by covalently bonding the organic group onto the silanol by either post-synthesis grafting (PSG) [6,66] or co-condensation [67,68] methods.

#### 1.4.3.1. Silica functionalisation by PSG

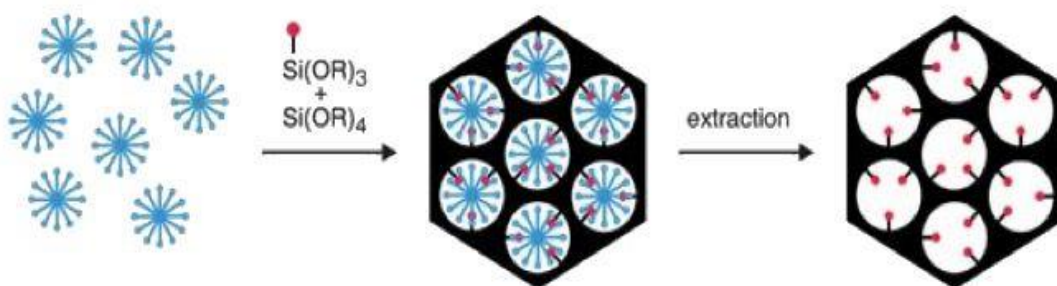
The PSG process involves reacting an organosilane reagent with the silica surface, normally in an inert organic solvent (e.g. toluene) under reflux conditions and in the presence of silane coupling agents, such as alkoxy-silanes or chlorosilanes [37,69]. This reaction must be performed under wet conditions as increasing the density of hydroxyl groups on the silica surface leads to self-condensation of the organosilane species away from the pore walls [70]. The modified products are washed, filtered, and dried [66]. A schematic diagram illustrating the procedure is given in Fig 1-8.



**Fig 1-8: Schematic diagram for grafting method applied to produce organically functionalised mesoporous silica. A trialkoxysilane molecule bearing a functional moiety (red) is shown as an example of a precursor.**

### 1.4.3.2. Silica functionalisation by the co-condensation route

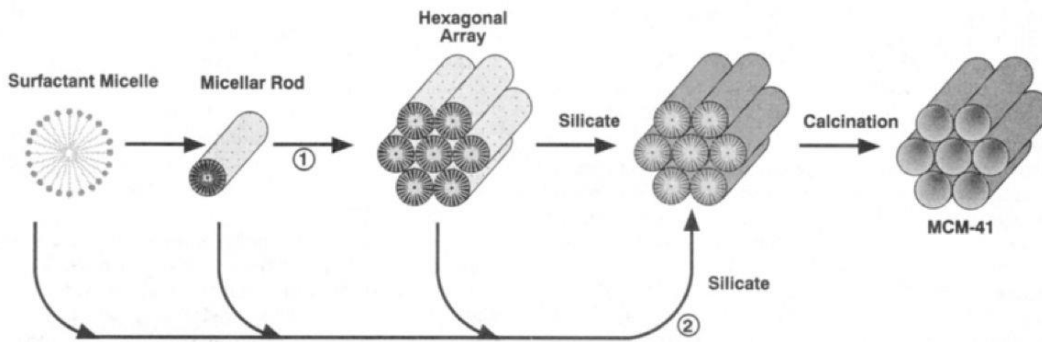
Co-condensation of tetraalkoxysilane, and organoalkoxysilane precursors, via sol-gel chemistry to produce functionalised mesoporous silica has been extensively investigated [18,70]. During the co-condensation (also called one-pot synthesis) process the organic moieties are incorporated into the silica framework while the mesoporous materials are being prepared (see Fig 1-9). Macquarrie [71] and Burkett et.al [67] were the first researchers to combine this method with the super molecular templating technique to produce, in one step, mesoporous silica-based materials with covalently linked organic functional groups protruding from the inorganic walls into the pore channel [70,72]. Lim *et. al.* [73] compared vinyl-functionalisation of MCM-41 by PSG and co-condensation methods concluding that the vinyl groups were homogeneously distributed throughout the mesoporous materials when the latter method was used, whilst the functional groups occurred near the channel openings when PSG was used. There are a number of disadvantages associated with the co-condensation method; in general, increasing the concentration of organosilane (i.e. to more than 20 %) in the reaction mixture will result in a significant decrease in the level of mesoporous ordering in the final product. Furthermore, a purely methodological disadvantage of the co-condensation method is that attention must be paid to the compatibility of the organic functional group with the synthesis conditions to avoid any destruction of organic functionality [69].



**Fig 1-9: Schematic diagram for co-condensation method applied to produce organically functionalized mesoporous silica. A trialkoxysilane molecule bearing a functional moiety (red) is shown as an example of a precursor.**

#### 1.4.4. Mechanisms used to described the formation of M41S materials

Experimental factors that are most influential in terms of governing synthesis mechanisms are the surfactant properties and concentrations, and the presence of additional ions. Initially, Beck *et al.* [6,22] proposed that there was a “liquid crystal templating” (LCT) mechanism, see Fig 1-10, that described the formation of the M41S materials. They concluded this after observing similarities between mesostructured materials and the liquid crystalline surfactants phases. Their hypothesis suggests that the organisation of surfactant molecules into liquid crystalline phases defines the structure of the templates used to build M41S structures. As shown in Fig 1-10, in this example, the inorganic silicate species occupy the space that occurs at the pre-formed hexagonal lyotropic crystal phase; deposits are made on the micellar rods present in the liquid crystal phase (pathway 1).



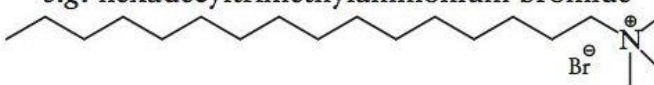
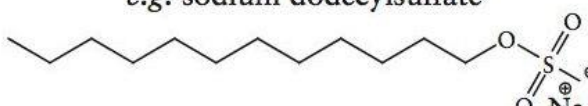

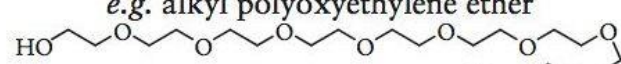
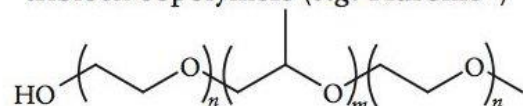
**Fig 1-10: schematic diagram shows the possible mechanism pathway for the formation of MCM-41, liquid crystal phase initiated (1) and silicate anion initiated (2) [6].**

Due to the fact that liquid crystal structures can be very sensitive to the components of the solution in which they are formed, it was proposed that addition of the silica source was required to initiate ordering of the surfactants into the specific framework (pathway 2). The potential for these two possible pathways stems from an extensive variation of surfactant properties, which depends significantly on both the presence, and concentration, of electrolytes [74]. In both pathways there is electrostatic interaction

between the inorganic species and the charged surfactant head group. This then condenses to produce a continuous framework such as that comprising a hexagonal array of surfactant micellar rods that are embedded in an inorganic matrix. Following pathway 2, Davis *et al.* [75] suggested a replacement approach to the formation mechanism of MCM-41. Their work had shown that liquid crystalline phases are not present in the synthesis medium during the formation of MCM-41. They suggested a process occurred where two or three monolayers of silicate are deposited onto the isolated surfactant micellar rods that are known to occur at the levels of surfactant concentration being studied. Silicate-surfactant rods are in the first instance randomly orientated; they eventually become packed into a hexagonal mesostructure as condensation progresses, ordered by self-organisation. Monnier *et al.* [32] studied how MCM-41 formed at concentration levels (1% g/g) where only spherical micelles were present leading to the proposal of a silicate-initiated mechanism. They also developed a “charge density matching” model, which was based on the cooperative organization into three-dimensional structures of both organic and inorganic molecular species. The model detailed three steps as follows: 1) multidentate binding of silicate oligomers to the cationic surfactant through electrostatic interactions resulting in a surfactant-silica interface, 2) preferential silicate polymerization in the surfactant-silicate interface 3) charge density matching between both the surfactant and the silicate. Prior to the addition of the silicate, it was suggested that the surfactant molecules experienced a dynamic equilibrium balancing the spherical or cylindrical micelles and single molecules. When a silicon source was added displacement occurred; the silicate species are multicharged and do displace the surfactant counteranions, thus forming organic-inorganic ion pairs that are then reorganized. First through silicatropic mesophases and then via silica cross-linking. As a consequence the resulting mesophase could then be managed through the multidentate interaction, via the interface packing density. A subsequent general cooperative mechanism for formation has been described by Huo *et al.* [76,77] founded on the knowledge of the specific electrostatic interactions linking the inorganic precursor (I) and the surfactant head group (S), Fig 1-11 To obtain mesoporous materials there are various strategies that can be employed; either using  $S^-I^+$ , or a reverse charge matching  $S^+I^-$ . In addition, synthesis routes leading to the interactions of surfactants and inorganic



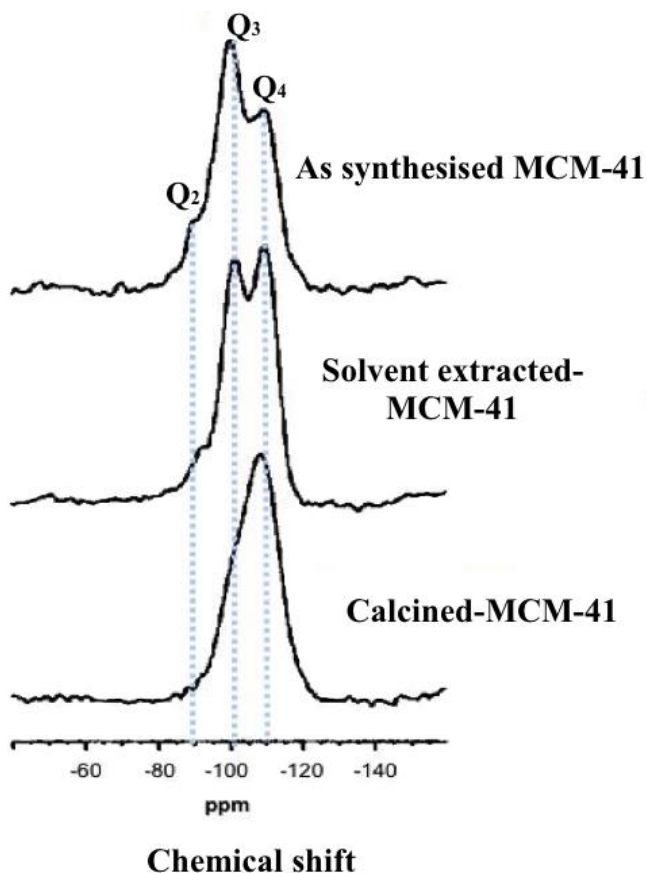
ions of similar charges can occur through the mediation of ions with an opposite charge counterions ( $S^+X^-I^+$ ,  $X^- = \text{halides}$  or  $S^-M^+I$ ,  $M^+ = \text{alkali metal ion}$ ). Further, the liquid crystal templating methods have been extended using neutral ( $S^0$ ) [78] or non-ionic surfactants ( $N^0$ ) [79]. In the approaches denoted, ( $S^0I^0$ ) and ( $N^0I^0$ ), hydrogen-bonding is mainly considered to be the driving force of mesophase formation.

Surfactant	Templating conditions	Interaction
<p>Cationic</p> <p><i>e.g.</i> hexadecyltrimethylammonium bromide</p> 	Alkaline	$S^+I^-$
	Acidic	$S^+X^-I^+$
<p>Anionic</p> <p><i>e.g.</i> sodium dodecylsulfate</p> 	Alkaline	$S^-X^+I^-$
	Acidic	$S^-I^+$
<p>Neutral</p> <p><i>e.g.</i> dodecylamine</p> 	Neutral	$S^0I^0$
<p>Nonionic</p> <p><i>e.g.</i> alkyl polyoxyethylene ether</p>  <p>triblock copolymers (<i>e.g.</i> Pluronic®)</p> 	Acidic	$S^0H^+X^-I^+$
	Neutral	$S^0I^0$

**Fig 1-11: Surfactants Utilized for templating, conditions under which mesoporous silicas were formed, and the interaction between surfactant and inorganic species [23].**

## 1.5. Silica mesopore properties and characterisation.

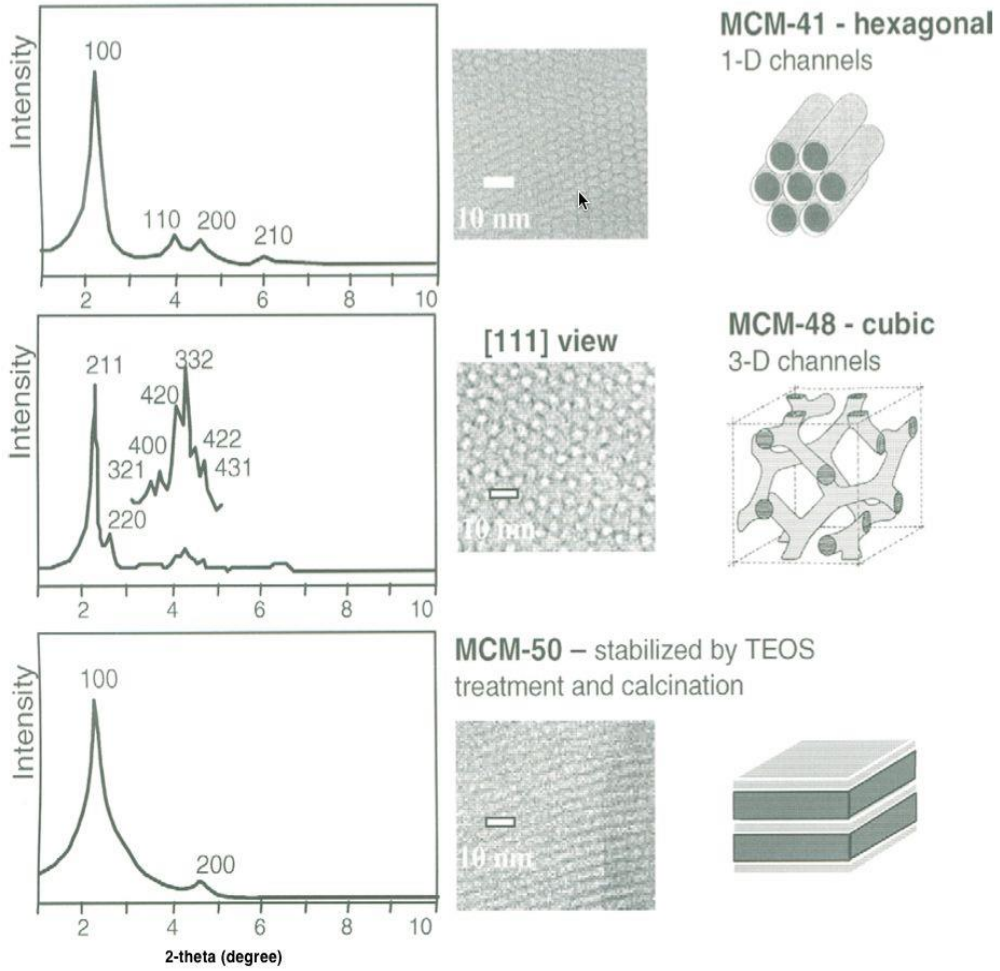
Mesoporous silica materials have yielded their important properties from their porosity; their most attractive features being the highly uniform, controllable pore shape, pore size, and high surface area. Characterisation of mesoporous silica can be performed using different techniques, such as solid state  $^{29}\text{Si}$  MAS NMR, small-angle XRD and gas adsorption (BET). Solid state NMR is used to quantify the degree of silica condensation as illustrated in Fig 1-12.



**Fig 1-12:**  $^{29}\text{Si}$  MAS NMR spectra of MCM-41 samples adapted from ref [75].

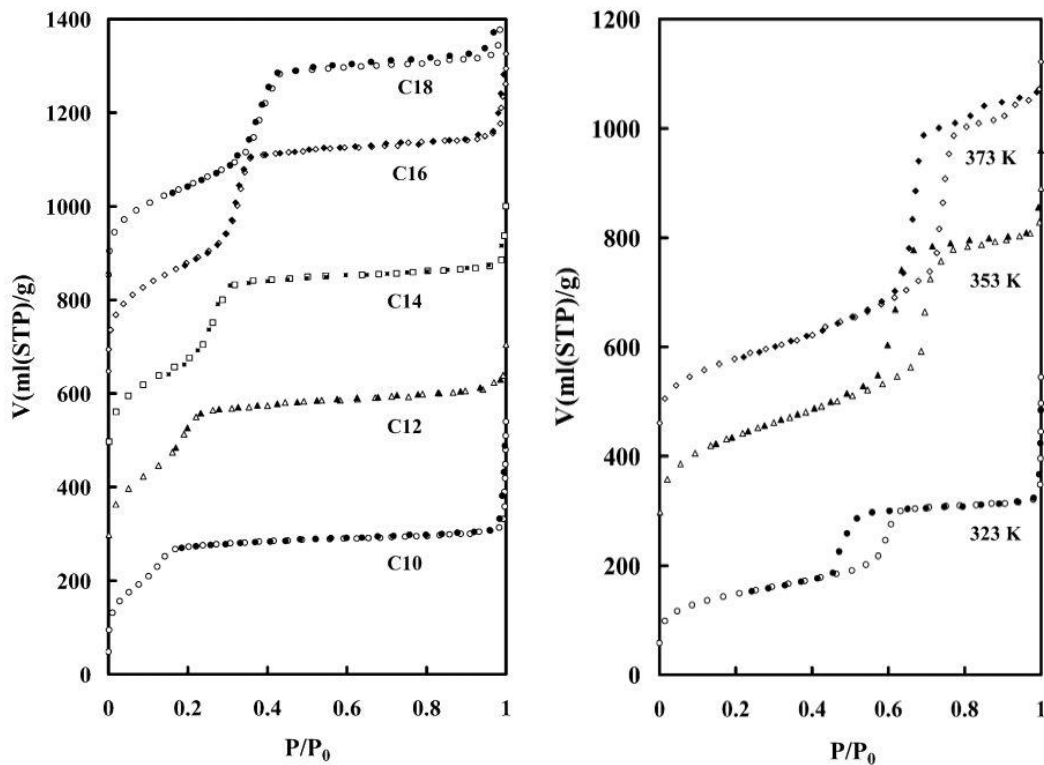
The signal from a central silicon atom is referred to as  $Q_n$ , depending on the degree of condensation in a purely inorganic  $\text{SiO}_x$  environment. Materials with more intense peaks in the  $Q_4$  (at about -110.3 ppm) environment than in the  $Q_3$  (at about -100.7 ppm) or  $Q_2$  (at about -90 ppm) environments have more strongly cross-linked silica walls, and are therefore considered to be more hydrothermally stable [23,75]. Small-angle XRD and

transmission electron microscopy techniques are generally used to assign the pore geometry in surfactant templated silicas. Based on unique and indexable XRD patterns, various surfactant-silica mesophases can be identified (Fig 1-13) [80].



**Fig 1-13: M41S family of ordered mesoporous materials - X-ray powder diffraction patterns, representative TEM images and proposed structures [80].**

Gas adsorption techniques such as BET can provide information about the surface and structure properties of porous materials. The characterisation of amorphous materials such as MCM-41 is usually performed using nitrogen adsorption isotherms at 77 K to obtain the surface area, pore volume and pore size distributions. According to the IUPAC classifications, the isotherm types IV and V are characteristic of the mesotype materials (see Fig 1-2, p 4). However, the shape of the isotherm can be affected by changing the pore size of the materials, either by using swelling agents or increasing the temperature, or by increasing the hydrocarbon chain lengths, which results in shifting the adsorption hysteresis to higher relative pressures (Fig 1-14).



**Fig 1-14: Typical nitrogen adsorption–desorption isotherms at 77 K ( $C_n$ ,  $n$ =number of carbon’s atoms, and  $mK$ ,  $m$ = aging temperatures) [81].**

## **1.6. Applications of mesoporous silica materials.**

Originally, mesoporous silica was synthesised in the hope of yielding larger pores compared to zeolitic materials for catalyst applications. The applications now being pursued include optical applications, drug delivery, adsorption, and separation. However, as the area of interest of the author is the removal of potentially toxic elements (PTEs) from contaminated water, this section of the report will be dedicated to the use of mesoporous silica-based materials as effective adsorbents in water and wastewater treatment.

PTE water contamination derives from numerous sources, some have a natural origin, whilst others are a result of industrial activity. Problems are also geographically specific, in Bangladesh [82-84] and North America arsenic contaminates the water supply. The Environmental Protection Agency (EPA) has issued a guidelines defining the regulations to limit the presence of arsenic in drinking water supplies [85,86], with a high level of priority. Contaminants from industrialized sources include mercury and lead (particularly from lead-based paints and leaded gasoline). Consequently the blood lead concentrations for US children are of significance and so of concern. Further, nuclear activity (such as weapons testing over ground and accidents at nuclear plants) has spread radioactive actinides and radiocesium at low levels across the globe [87].

When seeking to remove PTEs from a water supply (for example mercury, lead, or cadmium ions), traditional sorbent materials can be employed; one such material is alumina. However alumina binds non-specifically to metal ions and so the material can become saturated by other less harmless compounds (for example zinc, calcium and magnesium ions) which are present in addition to the target PTEs. An additional problem identified with traditional sorbent materials relates to the equilibrium process itself, as the metal ion is bonded to a ceramic oxide surface which can later be desorbed back into the water supply. Alternatively, flocculation or precipitation can be used to remove metal ions from aqueous solution, but such methods are generally only fully effective with high contaminant concentrations, commonly failing to perform successfully in cases of lower metal ion concentrations. This is a problem in the case of drinking water, where lower metal concentrations are found.

Due to the vast volume of water consumed daily, any solution requires that metal ion sorption occurs quickly to support the continual demand for removal. Thus, an adsorbent capable of performing in this area must achieve several points. First the material must have a high binding capacity with the target metal ion and second that a sensitive analytical method exists, or can be developed, to detect contamination effectively to support the lowering of acceptable contamination limits. There have been many recent developments in the use of modified mesoporous silica as efficient materials for the selective pre-concentration of trace metal ions from aqueous systems [88].

Chemical modification of the silica surface with organosilanes via heterogeneous reaction has produced materials that exhibit high selectivity towards specific metal ions. For instance, modifying the silica with amine ligands such as aminopropyl and propyl diethylenetriamine was found to be effective in the extraction of  $\text{Cu}^{2+}$ ,  $\text{Ni}^{2+}$  and  $\text{Cd}^{2+}$ , whereas thiol ligands such as mercapto-propyl were found to be highly effective for  $\text{Hg}^{2+}$  and  $\text{Ag}^+$  uptake [89-92]. By adjusting the pH of the solution, a variety of metal ions can be selectively extracted, even when high concentrations of alkaline earth metal ions are present in the medium. These features make these materials preferable for the analysis of trace metals in natural waters where high concentrations of alkaline earth metals could be present [93].

### **1.7. Limitations of mesoporous silica materials:**

Prolonged exposure of mesoporous silica materials to aqueous solutions has been observed to cause a loss of pore shape uniformity as well as a significant decrease in pore size [94]. On solution contact, the basic solution (at pH 7.8-8.9) in particular causes a major decrease in crystallinity, average pore diameter and pore volume. In contrast, little change has been observed in the structure properties for materials exposed to acidic or neutral solutions [95]. The impact of water immersion on the structure of mesoporous silica materials has been found to increase with increasing treatment time, as well as when the temperature of the solution is increased in the range 25–100 °C [95,96]. This poor stability restricts the life of mesoporous silica materials in aqueous systems above room temperature [97]. Furthermore, Gusev and colleagues [98] studied the effects of

compression on the properties of mesoporous silica materials and found that the materials can be considerably affected at pressures as low as 86 MPa, and destroyed at 224 MPa, which is lower than that of crystalline structures such as zeolites [98,99].

### **1.8. Aim and objectives:**

The objective of this work was to develop novel, cost-effective, chelate-based adsorbents specifically designed for the removal of potentially toxic elements (PTEs) or polycyclic aromatic hydrocarbons (PAHs) from contaminated water solution. Therefore, our target was to synthesis an adsorbent with satisfactory adsorption capacity which can be achieved by enhancing the material physical properties such as the pore size and the density of the silanol group on the surface of the material. Furthermore, the material should exhibit a high selectivity toward the targeted analytes and that can be achieved using a suitable functional group.

This thesis is consists of 9 chapters, chapter one provide an overall study of the synthesis, modification, characterisation, formation mechanisms and applications of mesoporous silica materials. Chapter 2 and 3 provide an overview of the instrumental and experimental methods used in this work. In order to understand the physical properties of the microwave digested MCM-41, chapter 4 will be dedicated for studying the physical properties of the material using different techniques including nitrogen adsorption-desorption analysis (BET), scanning electron microscopy (SEM), transmission electron microscope (TEM), fourier transform infrared spectroscopy (FTIR), and elemental analysis. Chapter 5 will study the feasibility of speciation and separation of chromium (III) and chromium (VI) from aqueous solution using microwave digested MCM-41 that was initially functionalized with two different functional groups (i.e. aminopropyl and diethylenetriamine). The parameters that influence the sorption process such as contacting time, the concentration of Cr ions, the present of other ions and pH were investigated. Moreover, adsorbents containing silica nanoparticles with different porosity parameters were synthesised, amino- functionalized and used to evaluate Cr (VI) uptake. The linearised Langmuir and Freundlich equations were used to fit the equilibrium isotherms. Kinetic data were analysed by pseudo-first, pseudo-second and intra-particle diffusion models to obtain the kinetic constants, establish the rate limiting step of Cr (VI)

removal and postulate the mechanism of Cr (VI) removal by porous materials. Chapter 6 will study the possibility of regenerating mercapto loaded MWD-MCM-41 material that was initially loaded with Hg (II) ions using thiourea solution that was acidified using three different acids (i.e. hydrochloric acid, sulphuric acid and nitric acid). Chapter 7 will provide information about the synthesis of new porous silica materials encapsulated with iron which was synthesised using bio-inspired route drawing the inspiration from bio-silicification process and the new materials were examined for the removal of arsenic ions from aqueous solution. Chapter 8 will investigate the possibility of using the new materials as an adsorbent for polycyclic hydrocarbons (PAHs). Finally, chapter 9 presents the thesis conclusions and future work.

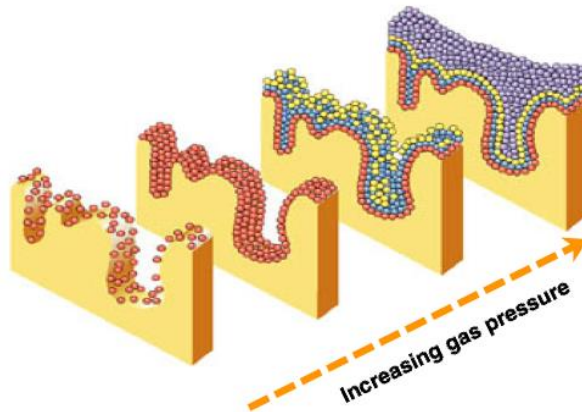


## **Chapter 2 : Instrumentation**

## 2.1 Gas adsorption isotherms [2,4,100-102]

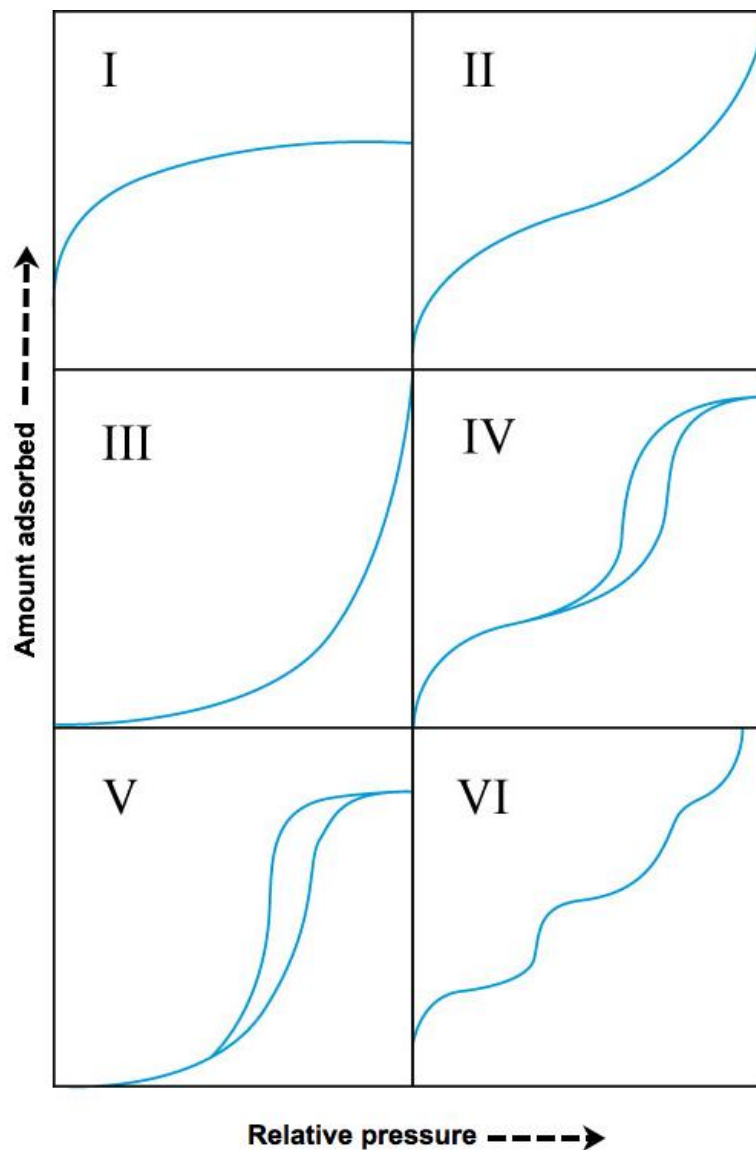
Physical adsorption is a technique that is widely used to characterize the surface, and pore features, (textural properties) of solids. The physical adsorption analytical technique involves exposing a carefully prepared sample to an inert gas. Sample preparation is often referred to as degassing which is the process of cleaning a sample using either evacuation or an inert gas purge while heating to remove weakly adsorbed molecules. The analysis is typically performed at the liquefaction temperature of the gas, when the gas molecule is attracted to the surface of the solid by the intrinsic surface energy of the sample. The gas molecule may become bonded, at least momentarily, to the surface of the solid. As the pressure increases, the number of molecules, per unit time, striking the surface increases and correspondingly the quantity of gas adsorbed increases, meaning that the number of molecules adsorbed in any instant increases as a function of increasing pressure. Further increases in the pressure will result in the formation of multiple layers of molecules on the free surface and on pore walls (see Fig 2-1). Ultimately the surface becomes completely covered and all the pores are filled. The energy involved in physical adsorption does not exceed 40 to 50 kJ mol<sup>-1</sup>, thus the adsorbed molecules can be easily be removed, or desorbed, by decreasing the pressure over the sample or by increasing the temperature.

However, rather than using the absolute pressure, a relative pressure is normally used which is the ratio of absolute pressure to the saturation pressure (the saturation pressure being the vapor pressure of the pure liquid). During adsorption analysis the absolute pressure approaches the saturation pressure which for the most commonly used gases such as nitrogen and argon is close to atmospheric pressure, at this point adsorption is maximized and its pressure is systematically reduced and desorption occurs. The quantities of molecules adsorbed or desorbed as a function of the relative pressure is known as the adsorption and desorption isotherms, respectively. The shape of the adsorption isotherm is the fingerprint of the texture of the solid.



**Fig 2-1: Gas adsorption by porous materials using physical adsorption technique.**

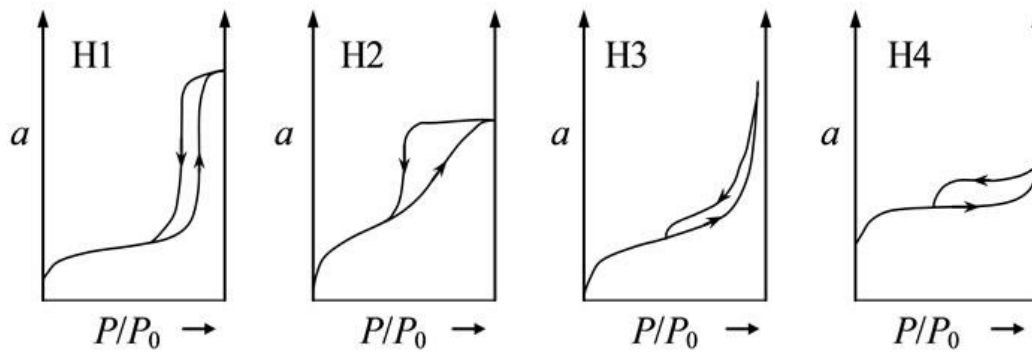
According to the International Union of Pure and Applied Chemistry (IUPAC) classification there are six types of adsorption isotherms; each relating to different textural properties of a solid, see Fig 2-2. Isotherm type I is characterized by a plateau which is nearly horizontal, intersects the relative pressure axis sharply and does not exhibit hysteresis in the desorption curve. The plateau on the adsorption isotherm exist because the pores in the solid are so narrow that they fill at low pressure (below 0.01 relative pressure). Once the pores are filled the remaining adsorption is on the exterior of the porous material. Therefore this isotherm shape is associated with microporous solids in which pores do not exceed 2 nm in diameter. Isotherms type II and type IV are very similar in shape with the difference being that type IV exhibits hysteresis between the adsorption and desorption branches of the isotherm (hysteresis is commonly observed for porous materials and is observed when the shape of the pores causes the adsorption and desorption portions of the isotherm to have a different path termed hysteresis) this type of isotherm corresponds to mesoporous materials with pore width ranging between 2 and 50 nm .The type II isotherm does not show any hysteresis and saturation takes place at much higher relative pressure, these adsorption characteristics correspond to nonporous or macropores solids.



**Fig 2-2: IUPAC classification of adsorption isotherms.**

Types III and V adsorption isotherms are also very similar in shape but are quite different from the previous isotherms since they do not have a plateau indicating a completion of the monolayer. This effect is due to weaker fluid–solid interactions. The type V isotherm exhibits hysteresis and capillary condensation takes place at intermediate relative pressure and is corresponds to mesoporous materials while the type III isotherm corresponds to solids having large pores. Finally, the type VI adsorption isotherm corresponds to a non-porous adsorbent with a completely uniform surface.

Hysteresis loops, which appear in the multilayer range of physisorption isotherms, are generally associated with capillary condensation. There are four major types of hysteresis loops that have been classified by the IUPAC, as illustrated in Fig 2-3. The characteristic features of some types of loop are associated with certain well-defined pore structures. Hence, type H1 loops are associated with adsorbents that have a narrow and uniform pore size distribution such as MCM-41 and SBA-15 type materials. Type H2 loops are normally associated with inorganic oxide gels which have a complex pore structure and tend to be made up of interconnected networks of pores of different shape and size. Type H3 loops are often obtained by the aggregates of platy particles. Finally, H4 loops are given by activated carbon and other adsorbent that have slit-shaped pores, mainly in the micropore range.



**Fig 2-3: The IUPAC classification of hysteresis loops.**

### 2.1.1 The BET surface area, pore volume and pore size distribution

A typical  $N_2$  gas adsorption and desorption isotherm for a mesoporous material is indicated in Fig 2-4. Generally, adsorption begins with a relatively few molecules adsorbed on the surface as pressure begins to increase. At about 0.05  $p/p_0$  the filling of the first layer on the solid is being established which is indicated by the first point A. The linear region of the isotherm B is attributed to the multilayered adsorption on the surface, the BET models can be used here to assess the monolayer capacity and then estimate the specific surface area.

The BET equation and its linear form are shown in Eq. 2-1

$$\frac{1}{V_a[(P_o/P) - 1]} = \frac{1}{V_m C} + \frac{C - 1}{V_m C} \left(\frac{P}{P_o}\right) \quad \text{Eq. 2-1}$$

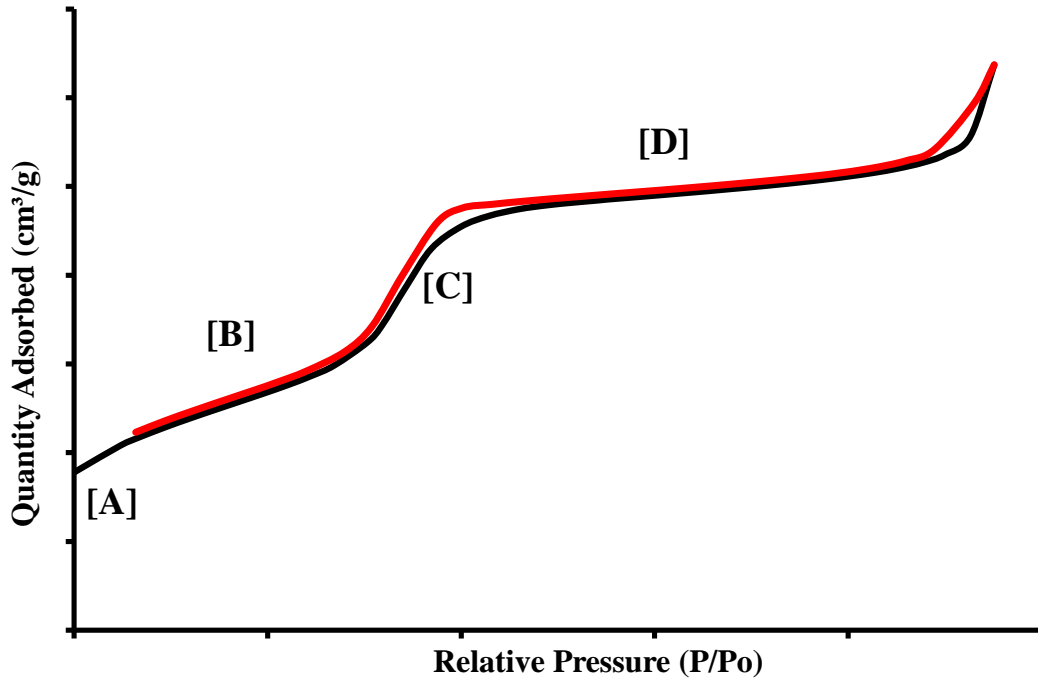
Where  $V_a$  is the quantity of gas adsorbed at a specific pressure,  $P/P_o$  is the relative pressure of adsorbate,  $V_m$  is the quantity of gas required to produce a monolayer and  $C$  is BET constant associated with the adsorption energy. According to the BET equation and its linear form are shown in Eq. 2-1, the BET plot of  $\left(\frac{1}{V_a[(P_o/P)-1]}\right)$  versus  $(P^o/P)$  should be a straight line with slope  $s = \left(\frac{C-1}{V_m C}\right)$  and intercept  $i = \left(\frac{1}{V_m C}\right)$ . By solving these two simultaneous equations, the following is obtained:

$$V_m = 1/(S + i) \quad \text{Eq. 2-2}$$

The specific surface area of a solid is then calculated as follows:

$$\text{Specific surface area (s)} = (V_m \cdot \sigma \cdot N_a)/(m \times 22400) \quad \text{Eq. 2-3}$$

Where  $V_m$  is the monolayer capacity expressed (ml),  $\sigma$  is effective cross-sectional area of one adsorbate molecule, ( $m^2$ ) (0.162  $nm^2$  for nitrogen),  $N_a$  is Avogadro constant ( $6.022 \times 10^{23} \text{ mol}^{-1}$ ),  $m$  is the mass of sample used in the test (g), and 22400 corresponds to volume occupied by 1 mole of the adsorbate gas at STP.



**Fig 2-4: N<sub>2</sub> gas adsorption and desorption isotherm for a porous solid.**

Subsequent studies have revealed that BET plots for nitrogen at 77 K generally exhibit a somewhat shorter linear region, so that  $p/p_0$  (0.05–0.30). On the other hand for the determination of porosity a full adsorption isotherm, and often desorption isotherm, is measured. However it needs to be realised that any micropores in the sample material are filled long before the monolayer is formed and therefore at higher pressures mesopores and macropores are being filled. As the relative pressure continues to increase beyond that required to form a monolayer [point C], adsorption takes place in multilayers for materials with mesopores as pressure is increased a capillary condensation may occur and the mesopores are filled with liquid nitrogen. At this stage, the pore size can be estimated using the Kelvin equation Eq. 2-4:

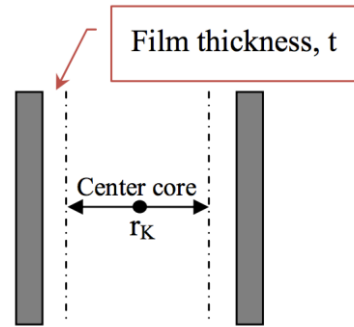
$$\ln[P/P^o] = -\frac{2\gamma v'}{RT r_k} \quad \text{Eq. 2-4}$$

Where  $\gamma$  is the surface tension of liquid,  $v'$  is the molar volume of liquid,  $r_k$  (known as the 'Kelvin radius') represents the radius of curvature of the meniscus of the liquid condensate in the filled pore which permits calculation of the radius of the pore,  $R$  is the

ideal gas constant and  $T$  is the analysis temperature. Using nitrogen as adsorptive gas at its boiling temperature (77 K). The Kelvin equation can be written as:

$$r_k = \frac{4.15}{\log[P/P^o]}$$

Eq. 2-5



The only variables in the equation are  $p$  and  $r_k$  thus for any value of pressure and therefore relative pressure, pores of size  $r_k$  will fill. In addition to capillary condensation for any unfilled pore as pressure is increasing towards its critical filling pressure, the walls of the pores are being coated with layers of adsorbed molecules and the thickness of this layer of film is a function of pressure.

Thickness at in any pressure can be determined using one of several thickness equations derived for specific adsorbent and adsorbate combinations such as Halsey equation. Halsey equation for  $N_2$  adsorption on a planar surface to predict  $t$ . is given by:

$$t = 3.54 \left[ \frac{5}{2.303 \log(P^o/P)} \right]^{1/3}$$

Eq. 2-6

Therefore the pore being filled is the remaining open core of the actual pore in the sample material. The radius of the pore  $r$  is the sum of the radius calculated by the Kelvin equation  $r_k$  and the thickness  $t$  of the adsorb layer on the internal wall of the pore ( $r = r_k + t$ ).

At the end of the adsorption isotherm as the relative pressure approaches unity [point D], all pores up to approximately 200 to 300 nm will be completely filled with liquid and the total pore volume of the solid can be determined by taking the cumulative volume from the Y axis of the adsorption isotherm and applying the Gurvitch rule which converts the quantity of gas adsorbed into its volume in liquid.



At saturation ( $p/p^0 \approx 1$ ) the liquid volume of different adsorbate, when measured on porous adsorbents, is essentially constant and is independent of adsorbate. Thus, the pore volume,  $V_p$ , is given by:

$$v_p = \frac{w_a}{\rho} \quad \text{Eq. 2-7}$$

Where  $w_a$  is the amount of gas adsorbed (g), and  $\rho$  is the liquid density at saturation. With an implicit assumption that no surface other than the inner walls of the pores exists, the average pore radius ( $\bar{r}$ ) can be calculated as follows:

$$\bar{r} = \frac{2v_p}{S_{BET}} \quad \text{Eq. 2-8}$$

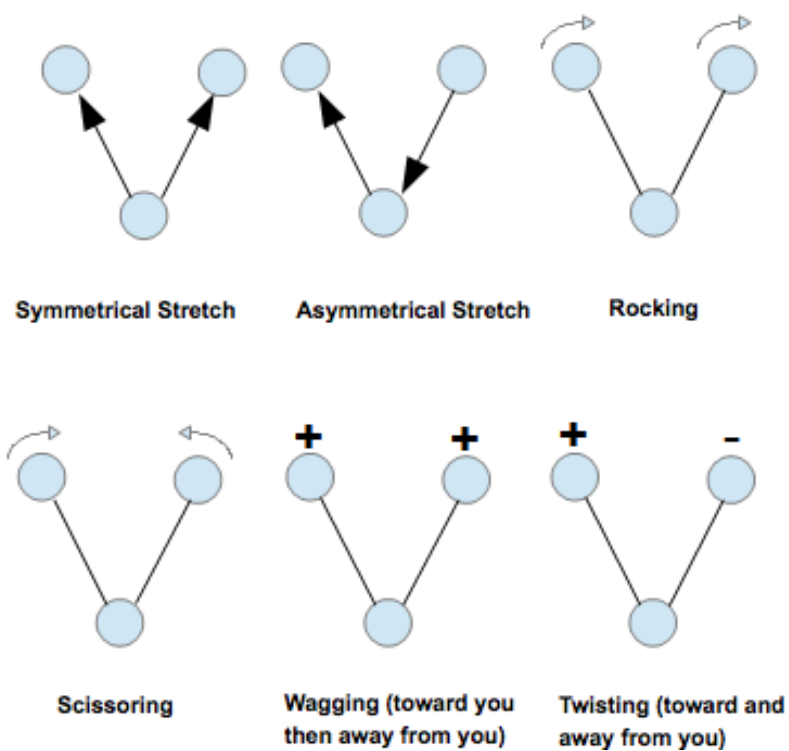
Where  $S_{BET}$  is the total surface area.

## 2.2 Fourier transform infrared spectroscopy (FTIR) [103-106]

Infrared spectroscopy (IR) is one of the most useful and most widely used techniques employed in the elucidation of the structure as well as the qualitative and quantitative analysis of organic molecules. It is based upon the vibrations of atoms of a molecule. The spectrum of infrared is obtained by passing a beam of IR radiation through the studied sample and determining what fraction of the incident radiation is absorbed at a particular energy. The energy at which any peak in an absorption spectrum appears corresponds to the frequency of a vibration of part of a sample molecule. For a molecule to show infrared absorptions it must possess a specific feature, i.e. an electric dipole moment, which must change during the vibration. An example of an 'infrared-active' molecule would be a heteronuclear diatomic molecule. The dipole moment of such a molecule changes as the bond expands and contracts. By comparison, an example of an 'infrared-inactive' molecule would be a homonuclear diatomic molecule such as  $N_2$ ,  $O_2$ , or  $H_2$ , because its dipole moment remains zero no matter how long the bond is.

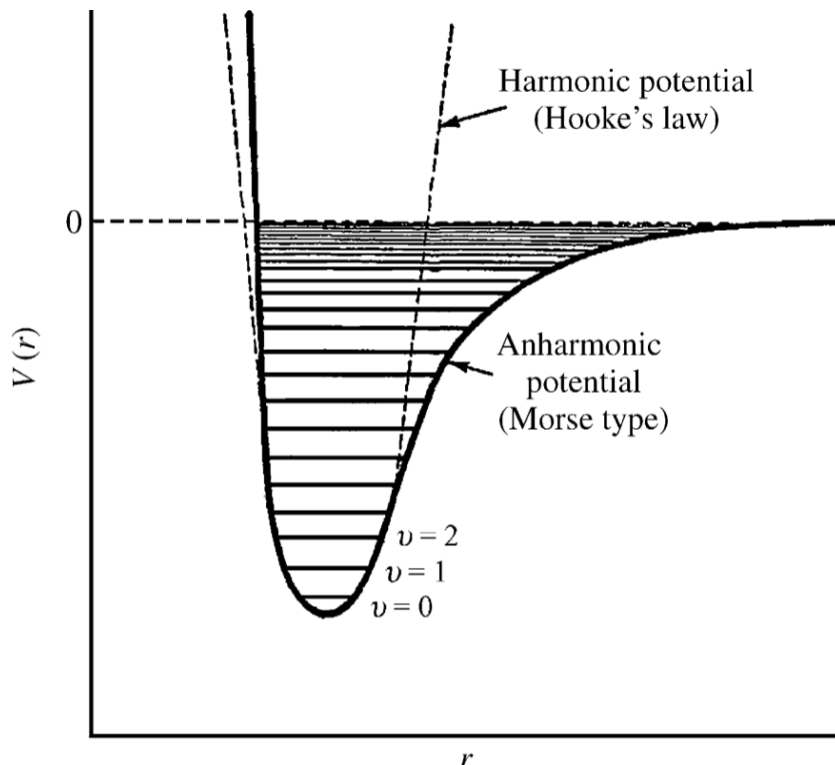
### 2.2.1 Molecular vibrations

The common molecular vibrations that are excited by infrared radiation are bending and stretching vibrations; known as vibration modes. Bending is the result of a change in the angle of the bond or in the position of a group of atoms with respect to the rest of the molecule, whereas, stretching is the results of a change in bond length (i.e. a change in interatomic distance). Fig 2-5 shows some of the more common stretching and bending motions in a molecule. Among these motions the symmetric stretching vibration is considered to be infrared-inactive as it does not change the dipole moment of the molecule. For molecules containing  $N$  atoms, the number of coordinates required to specify the nuclei position in space is  $3N$ . This number is known as the total number of degrees of freedom possessed by the molecule. The atoms are combined so they do not move independently and three coordinates are needed to specify the centre of mass position and describe the rotational motion of molecule around its centre of mass. Therefore, for non-linear molecules, the number of possible of vibrational mode is  $(3N-6)$ , while linear molecules can have  $(3N-5)$  possible variations.



**Fig 2-5: Types of Molecular Vibrations.**

Each vibrational mode shows approximately harmonic displacements of the atoms from their equilibrium positions; for each mode ( $i$ ), all the atoms vibrate at a particular characteristic frequency ( $\nu_i$ ). The potential energy  $V(r)$ , of a harmonic oscillator is shown as a dashed line in Fig 2-6.



**Fig 2-6: Potential energy of a diatomic molecule as a function of the atomic displacement during a vibration.[103]**

A simple model of vibration in diatomic molecule can be made by considering a chemical bond as spring with a mass on each end of the spring. From a simple statement of Hooke's law we can express the fundamental vibrational frequency of a molecular ensemble according to Eq. 2-9:

$$v = \frac{1}{2\pi} \sqrt{\frac{k}{\mu}} \quad \text{Eq. 2-9}$$

Where  $v$  is the fundamental vibration frequency,  $k$  is the force constant (measure of the stiffness of the spring), and  $\mu$  is the reduced mass and can be calculated as follows:

$$\mu = \frac{m_1 m_2}{m_1 + m_2} \quad \text{Eq. 2-10}$$

Where  $m_1$  and  $m_2$  are the component masses for the chemical bond under consideration. From Eq. 2-9, it can be seen that the natural oscillation frequency of a mechanical oscillator depends on mass of the object (atoms) and the force constant of the spring (bond), but is independent of the amount of energy imparted to the spring. Therefore, the actual variation of the potential energy as a function of the displacement of the atoms from their equilibrium positions is shown as a solid line in Fig 2-6. From this curve it can be seen that Eq. 2-9 is valid only for low values of the vibrational quantum number and is not valid when  $v_i$  is large. In practice,  $v_i$  must be described using an anharmonic potential function. Therefore, the frequency of vibration can be predicted with a modified Hooke's Law:

$$\bar{\nu} = \frac{1}{2\pi c} \sqrt{\frac{k}{\mu}} \quad \text{Eq. 2-11}$$

Where  $\bar{\nu}$  is the frequency of vibration ( $\text{cm}^{-1}$ ) and  $c$  is the velocity of light ( $\text{cm/s}$ ). The term  $k$  is proportional to the bond order (i.e. triple bond between two atoms is three times as strong as single bond) and relies upon the electronegativity of the vibrating atoms as well as the distance between them. Table 2-1 shows the average value of  $k$  for single, double and triple bonds.

**Table 2-1: Values of the force constant**

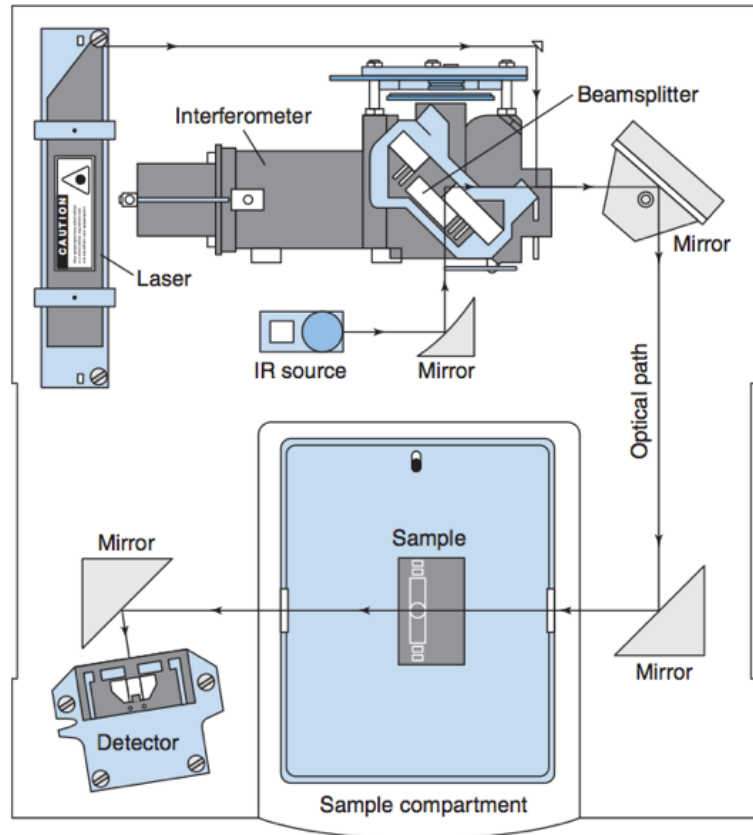
Bond order	Average force constant $k$ (N/m)
Single bond	500
Double bond	1000
Triple bond	1500

### 2.2.2 FTIR instrumentation

An overview of a FTIR spectrometer is shown in Fig 2-7 A. The IR radiation which is emitted from the source is first passed through an interferometer where the "spectral encoding" takes place. The most widely used interferometer in FTIR is the "Michelson

interferometer”, see Fig 2-7 B. A Michelson interferometer consists of two mutually perpendicular plane mirrors, one of which can be moved along an axis perpendicular to its plane. A beamsplitter is located in between the two mirrors, which reflects some the input beam of radiation into the fixed mirror and some to the moving mirror. The two beams are then reflected by the mirrors and travel back to the beamsplitter where they recombine and interfere. Half of the beam that was reflected from the fixed mirror is transmitted through the beamsplitter to the detector while the other half heads back to the source. The variation in the intensity of the beams seen by the detector is a function of the path difference and a plot of this intensity is known as an interferogram. The collected interferogram signal is then converted into the conventional FTIR spectrum using the Fourier transform algorithm.

[A]



[B]

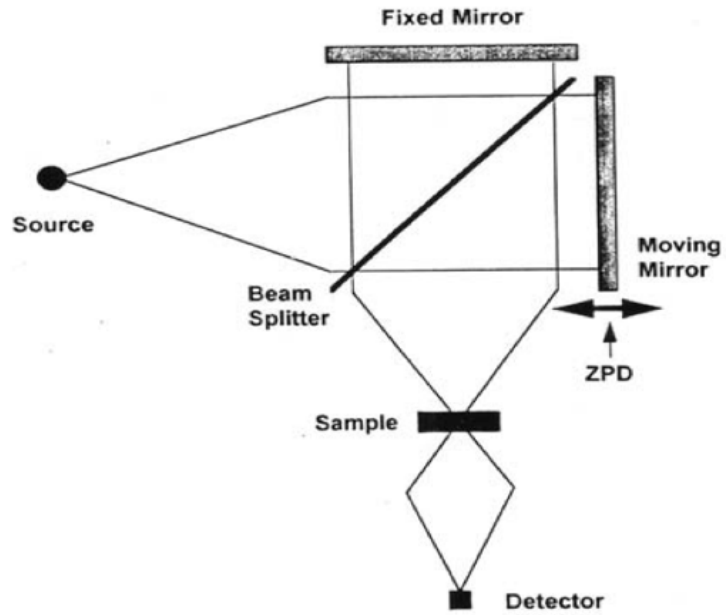
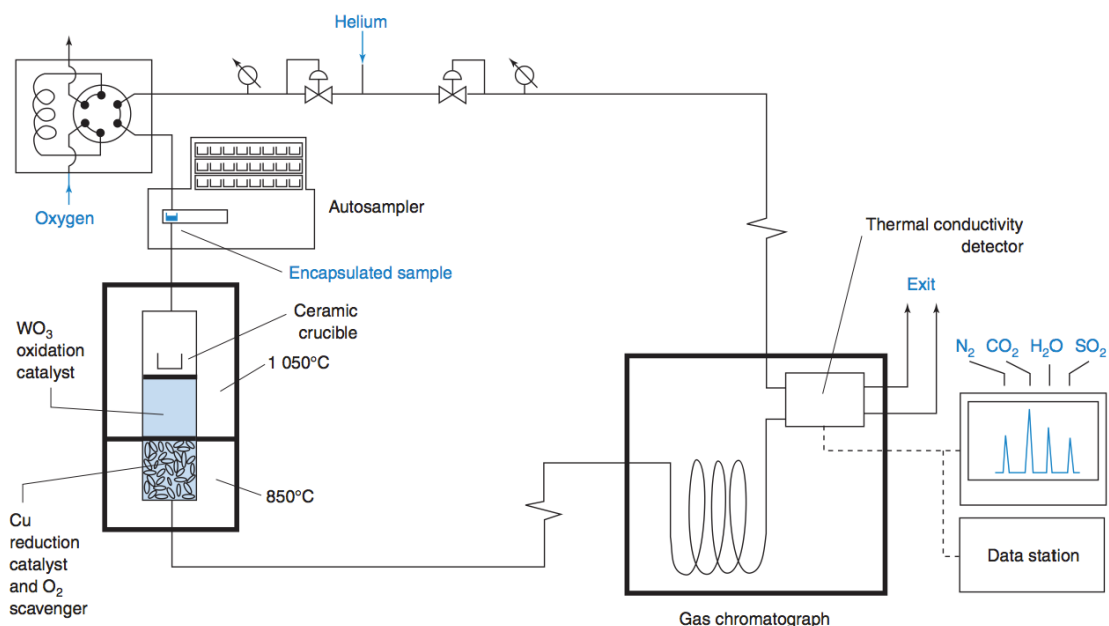


Fig 2-7: A) a simple commercial FTIR spectrometer layout B) a schematic diagram of a Michelson interferometer.[106]

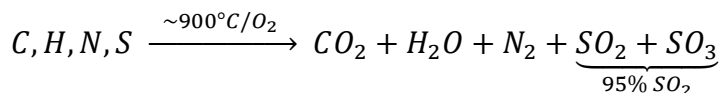
## 2.3 CHN microanalysis [106,107]

The use of several molecular compounds that contain carbon (C), hydrogen (H), nitrogen (N) and sulfur (S) have lead to the necessity to develop a technique that is capable to measure these elements for a wide range of industrial, research and academic applications. Fig 2-8 shows the instrument used to measure the C,H,N and S elements in a single operation.



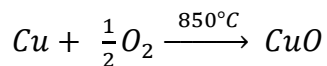
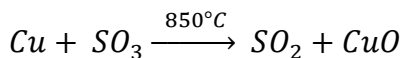
**Fig 2-8: Microanalysis apparatus with gas chromatographic separation and thermal conductivity detection.[106]**

An accurate mass of the sample is first weighted and sealed in a silver or tin capsule. Then helium gas flows through the analyser to remove any traces of CO<sub>2</sub>, H<sub>2</sub>O and O<sub>2</sub>. The sample is pyrolysed at approximately 900 °C in the reactor chamber in the presence of an excess amount of oxygen.





The He carrier gas pushes the combustion gases through a hot tungsten trioxide catalyst to complete the combustion of carbon to CO<sub>2</sub>. The product gas mixture flows through a metallic copper at 850 °C where excess oxygen is removed and SO<sub>3</sub> gas is converted into SO<sub>2</sub>.



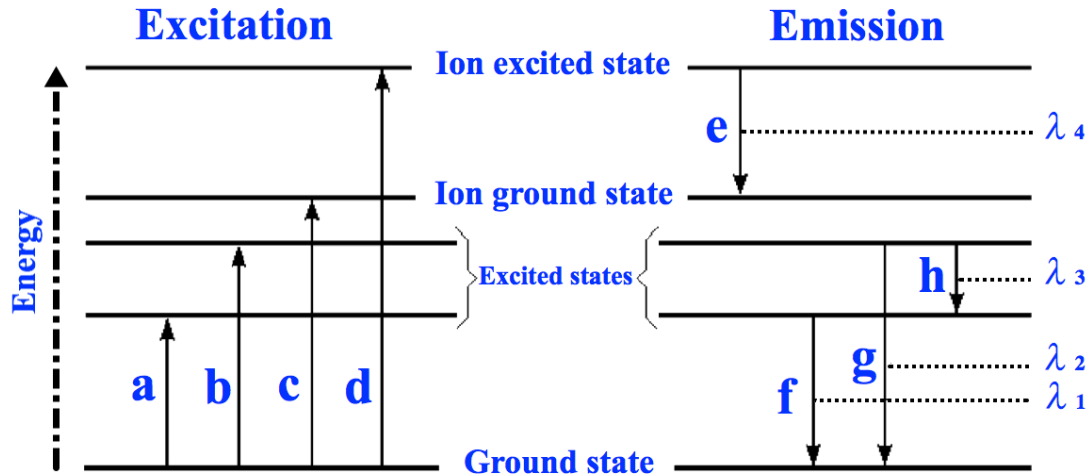
The mixture of N<sub>2</sub>, CO<sub>2</sub>, SO<sub>2</sub> and O<sub>2</sub> is separated using a packed GC column and detected and quantified using a thermal conductivity detector.

## **2.4 Inductively Coupled Plasma Optical Emission Spectroscopy (ICP-OES).** [108-110]

In atomic spectroscopy techniques, metal ions in solution are atomised by means of a flame, plasma or furnace that operates between 1930 to 11000 K.[111] These techniques use absorption or emission spectrometry to assess the concentration of analyte in solutions or in solid samples. Atomic emission spectroscopy is a widely used technique, and it begins by adding energy to the atom caused via absorption of electromagnetic radiation, or through a collision with another particle (molecule, ion, atom, or electron). The two most common phenomenon that take place are the energy to be used to increase the velocity of the atom (i.e. increasing the kinetic energy of the atom) or for the atom to become excited by absorbing the energy (this process known as excitation). The excitation process will lead to the promotion of that atom to its excited electronic state and as the atom is less stable in its excited state, it will return to its lower energy state by emitting photons.

The absorption of high energy by the atom will results in the complete dissociation of an electron from the atom, leaving an ion with a net positive charge. This process is known as “ionisation” and the energy required to reach this atomic state is known as the ionisation potential and is different for each element. Fig 2-9, shows a schematic diagram

of excitation, ionisation and emission processes. The energy difference between the upper and lower energy levels of a radiative transition defines the wavelength of the radiation that is involved in that transition.



**Fig 2-9: A diagram showing transitions of electrons between energy levels in an atom, where (a and b) represent excitation process, c is ionization, d is ionization/excitation, e is ion emission, and f, g and h are atom emission.**

The energy of a photon, in joules, is related to wavelength by Planck's equation, Eq. 2-12:

$$E = h\nu \quad \text{Eq. 2-12}$$

Where  $h$  is Planck's constant ( $6.626 \times 10^{-34} \text{ J}\cdot\text{s}$ ) and  $\nu$  is the frequency of the radiation.

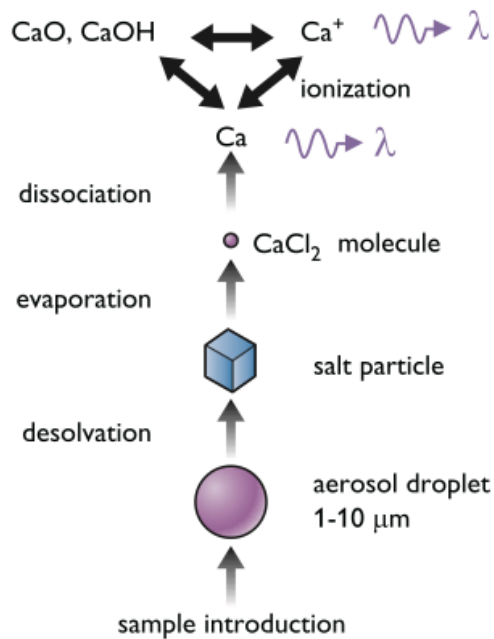
The relationship between the energy of photon and the wavelength can be written as:

$$E = h \frac{c}{\lambda} \quad \text{Eq. 2-13}$$

Where  $c$  is the speed of light and  $\lambda$  is wavelength. Every element has its own characteristic set of energy levels and therefore the wavelength of the photons can be utilised to identify the elements from which they originated. On the other hand, the intensity of the photons is directly proportional to the concentration of the originating element in the sample analysed.

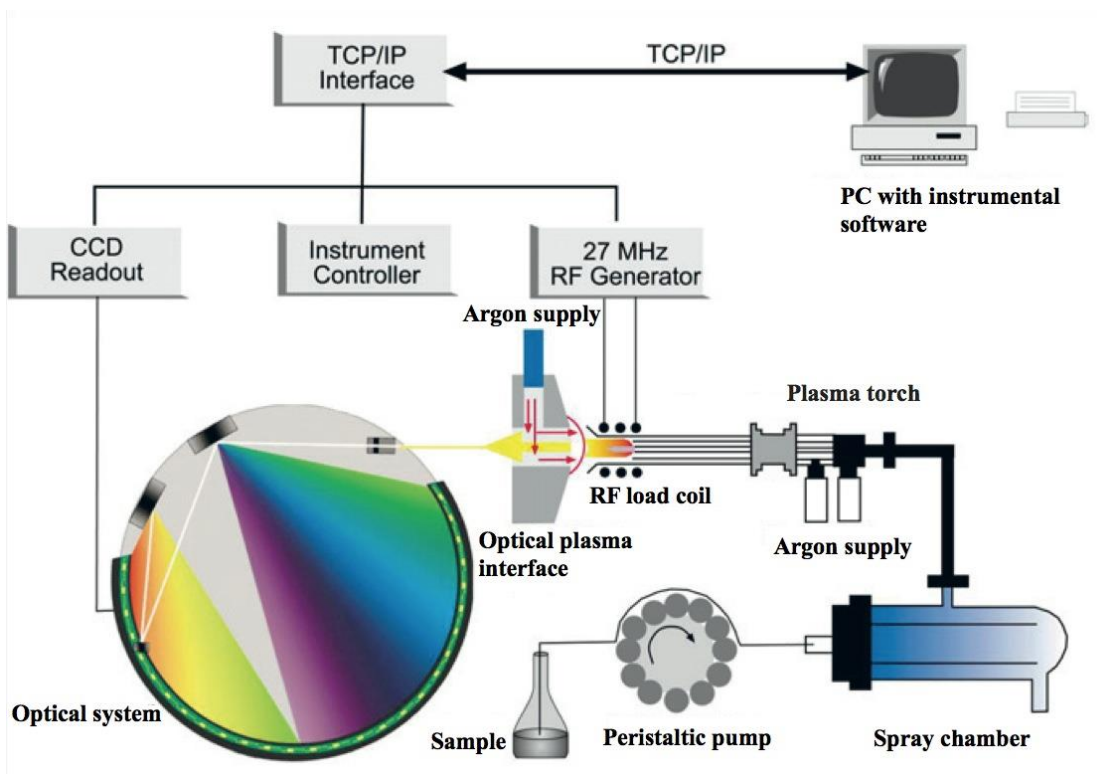
### 2.4.1 ICP-OES instrumentation

In the inductively coupled plasma-optical emission spectrometer, the sample is usually introduced into the system as a stream of liquid sample. Inside the instrument, the solution is transformed into fine aerosol particles via a process known as nebulisation. The aerosol particles (less than 10  $\mu\text{m}$ ) are then transferred by an argon flow into the argon plasma. In the hot area of the plasma the aerosol droplets are converted into particles by desolvation. These particles are then split into individual molecules that will subsequently fall apart to form ions and atoms (Fig 2-10).



**Fig 2-10: processes that take place in an ICP.**

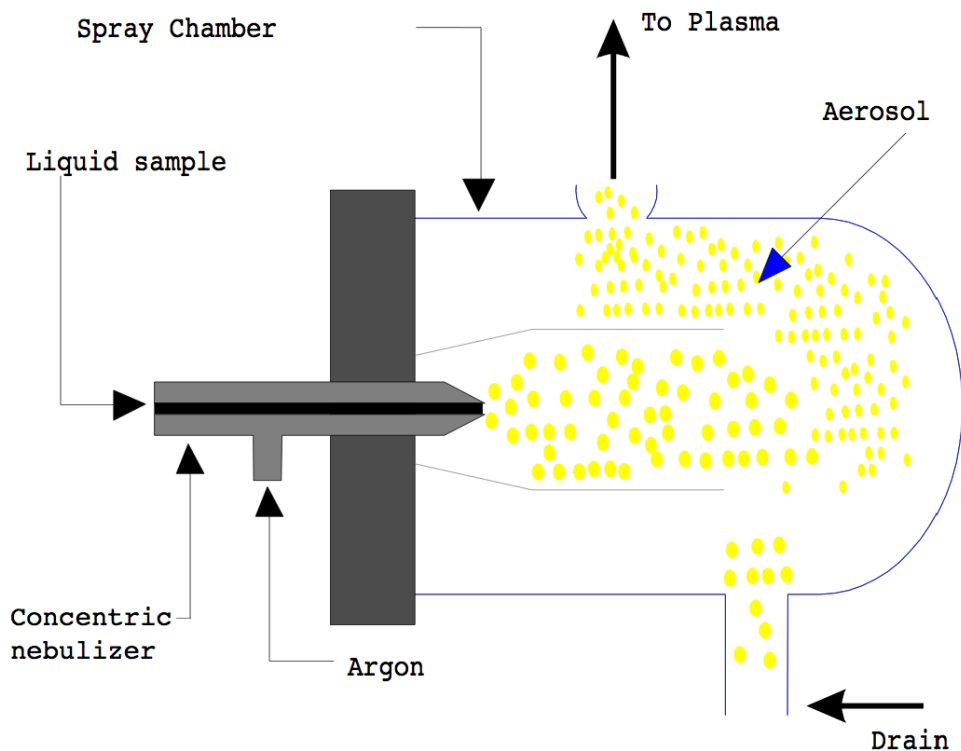
The excited atoms and ions emit their electromagnetic radiation at wavelengths characteristic of a particular element. Fig 2-11 shows an overview of the main component of ICP-OES instrument.



**Fig 2-11: Overview of inductively coupled plasma-optical emission spectroscopy (ICP-OES), adapted from [108].**

### 2.4.2 Sample introduction

The common way of sample introduction is through the generation of an aerosol using a nebuliser system. A nebulizer is a device that is used to convert the sample solution into fine aerosol particles. This process is considered to be one of the critical steps in the inductively coupled plasma. Therefore, the utility of the nebuliser used in the ICP-OES can be determined by its ability to produce small droplets for a wide variety of samples. The typical nebuliser as used in an ICP-OES is the concentric nebuliser shown in Fig 2-12. The sample solution is passed through a nebuliser by the flow of a nebulising gas that creates a fine mist of liquid particles known as aerosol. The aerosol droplets are then separated in the spray chamber according to their size with the larger droplets (>10  $\mu\text{m}$ ) being removed through the drain while the smaller droplets are transferred by the argon flow into the argon plasma.

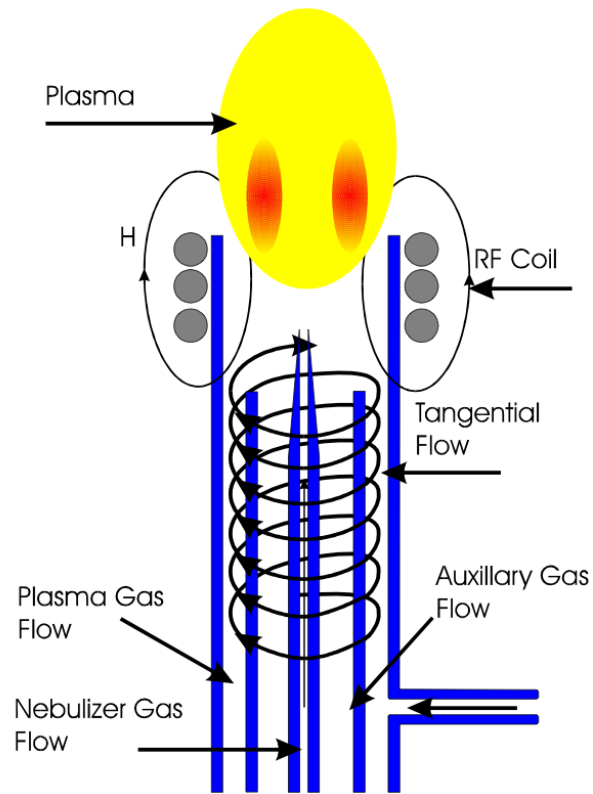


**Fig 2-12: Diagram of concentric nebulizer and the spray chamber used in the ICP-OES system. [112]**

### **2.4.3 The inductively coupled plasma torch**

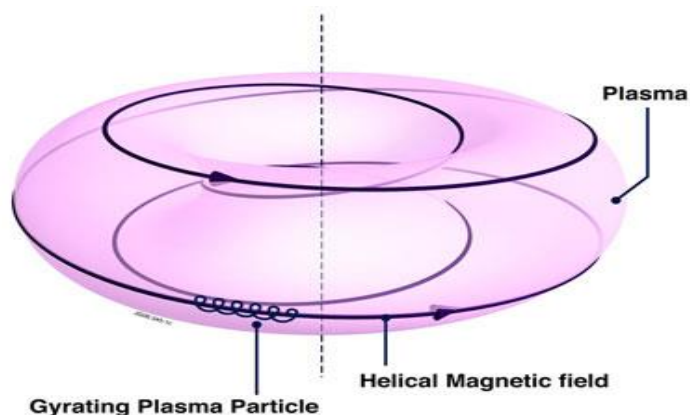
The ICP torch is used to generate and sustain a plasma, Fig 2-13. The ICP is formed by passing argon gas into a specially constructed quartz glass “torch” that comprises three concentric cylinders. A water-cooled copper coil is placed around the top of the torch. The coil is connected to a radio frequency (rf) generator operated at a fixed frequency in the range of 27-50 MHz. Typically, 40 MHz is used, and the power applied is 1–2 kW. With the gas flowing and the rf generator switched on, some seed electrons are created at the top of the torch using an electrical spark. The passage of radio frequency energy through the copper coil creates magnetic fields, which cause the electrons to move in circular paths. Electrons are accelerated in a magnetic field; they collide with the argon atoms, causing the ionisation of some, leading to the creation of more electrons. When high energy electrons collide with the argon ions they recombine, producing heat and radiation as a result of the excess energy produced; this appears as a very bright highly energised plasma. However, it is hot enough to efficiently atomise sample solutions,

introduced as a spray of droplets via a nebuliser and spray chamber, and to atomise and ionise the elements to different degrees.



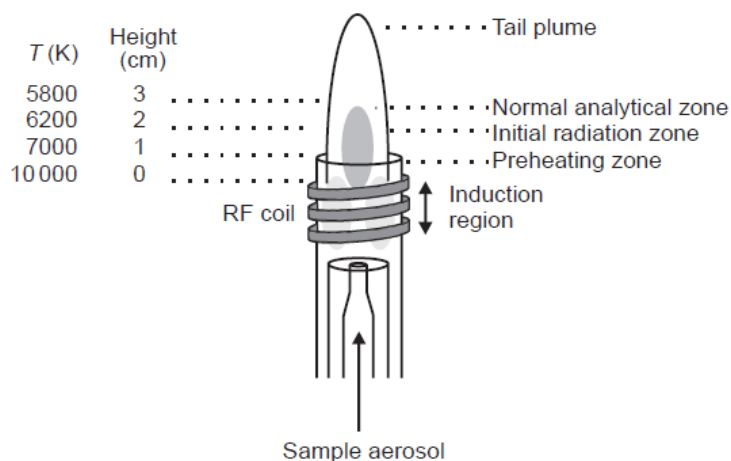
**Fig 2-13: Schematic diagram of ICP torch. [112]**

The plasma has a certain radius (skin depth), which varies with the frequency of the rf generator (smaller at higher frequencies). If the torch is designed with the optimum outer tube diameter, it is possible to create a ring plasma with a central hole, as illustrated in Fig 2-14.



**Fig 2-14: Schematic diagram of the plasma doughnut shape [113].**

This is a convenient channel through which to direct the aerosol spray from the nebuliser and spray chamber. Without the central hole in the “doughnut”, it would be difficult for the aerosol to penetrate the plasma. As the aerosol passes through the core of the plasma, electrons, Ar meta-stable species and  $\text{Ar}^+$  are diffused into the central channel to cause excitation and ionization of the analyte species. Fig 2-15 shows the temperature gradient within the ICP as well as classification of the different zones that present in the plasma.



**Fig 2-15: Schematic diagram of the temperature gradient within the ICP.[114]**

When the aerosol carried by the argon gas into the centre of the plasma, it undergoes three processes as described in Fig 2-10. The first step is known as desolvation or the removal of solvent molecule from the droplets, usually leaving the sample as microscopic solid particulates, or a dry aerosol. This process is followed by the vaporisation or the

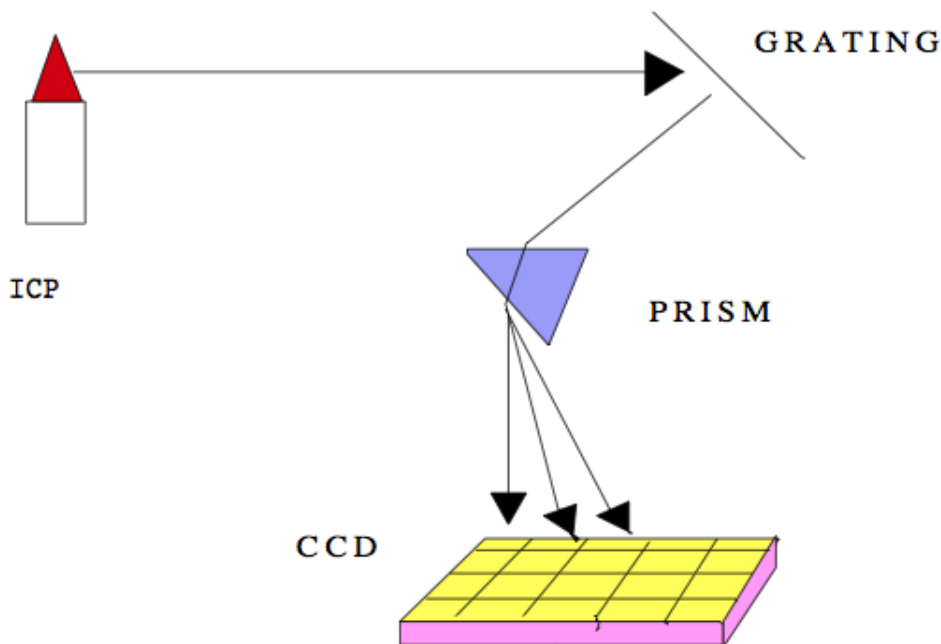
decomposition of the solid particles into its gaseous state followed by the dissociation of the gaseous species into atoms (atomisation). These steps take place mostly in the preheating zone. The final step is the excitation and ionisation of the atoms, followed by the emission of radiation from these excited species. The excitation and ionisation processes take place mostly in the initial radiation zone while the normal analytical zone is the region from which the analytical emission is usually collected and measured.

#### **2.4.4 Detection of Emission**

In order to obtain information about the analysed sample in the ICP-OES, the light emitted by the excited atoms and ions in the plasma is measured. However, since the excited species in the plasma emit light at different wavelengths, the emission from the plasma is polychromatic. Therefore, the resulted polychromatic radiation must be separated into individual wavelengths in order for the emission of each excited species to be identified along with the measurement of its intensity without interfering with other wavelengths. This is achieved using a spectrometer which is used to separate, isolate and measure light according to the wavelength. In ICP-OES, two types of spectrometers are used, sequential (monochromator) and simultaneous (polychromator).

There are three basic types of detector systems: photo diode arrays (PDAs), photomultiplier tubes (PMTs), and charge coupled devices (CCDs). Most often a CCD detector is used (Fig 2-16), which provides the advantages of having high resolution and simultaneous detection. The CCD detector is divided up into a large number of light-sensitive small areas (known as pixels) which can be used to build up an image of the scene of interest. A photon of light which falls within the area defined by one of the pixels will be converted into one (or more) electrons and the number of electrons collected will be directly proportional to the intensity of the scene at each pixel [115] .

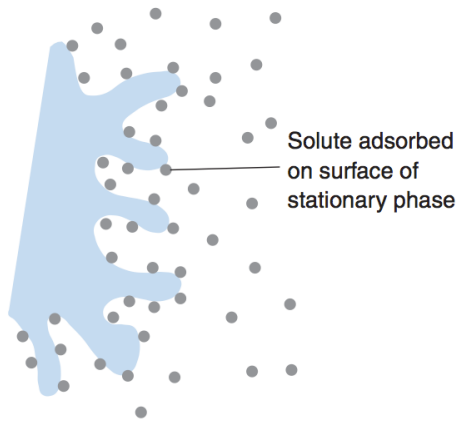




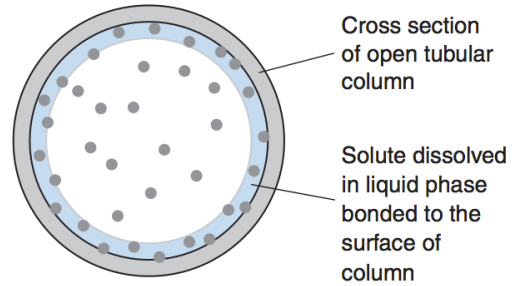
**Fig 2-16: Two-dimensional dispersion and detection of radiation using a charge-coupled device [112].**

## **2.5 Liquid chromatography (LC) [106,116-119]**

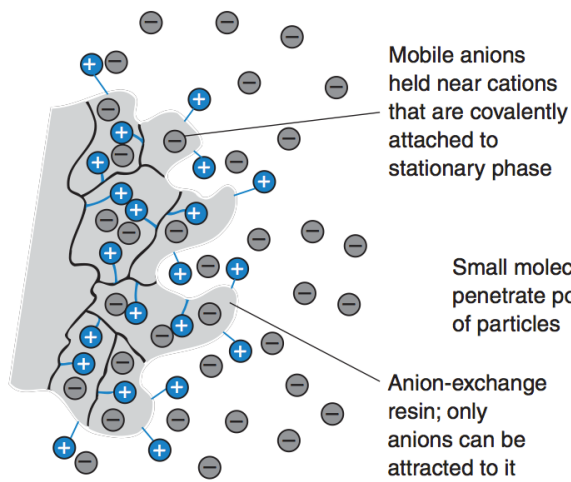
Chromatography is an analytical technique used for the separation of a mixture of compounds in order to identify, quantify or purify the individual components of a mixture. Generally, chromatography is a process in which a sample is allowed to pass through the system over a stationary phase (column). The different affinities and interactions of the sample with the stationary phase will result in the separation of molecules. The different compounds present in the sample can be separated from each other as they move through the column in which the component of the sample that exhibit stronger interaction with the column will elute later than the components with weaker interactions. Chromatography can be classified according to the mechanism of interaction of the solute with the stationary phase into adsorption, partition, ion exchange, molecular exclusion, and affinity chromatography, as shown in Fig 2-17.



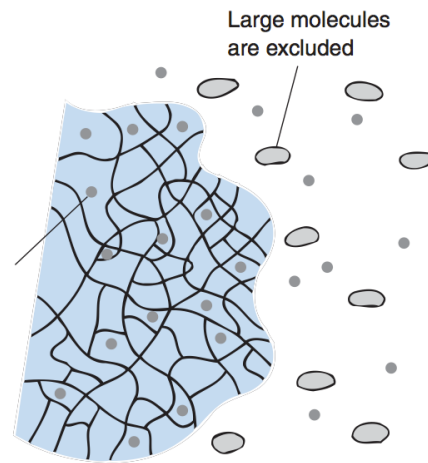
Adsorption chromatography



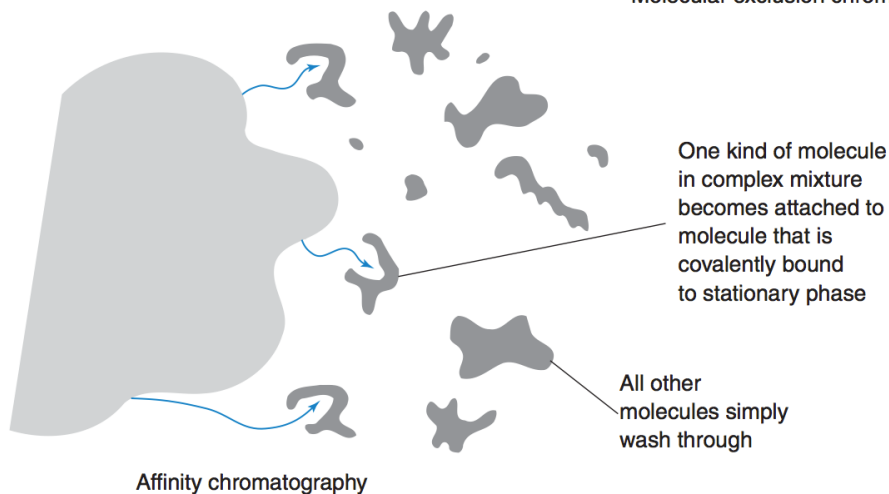
Partition chromatography



Ion-exchange chromatography



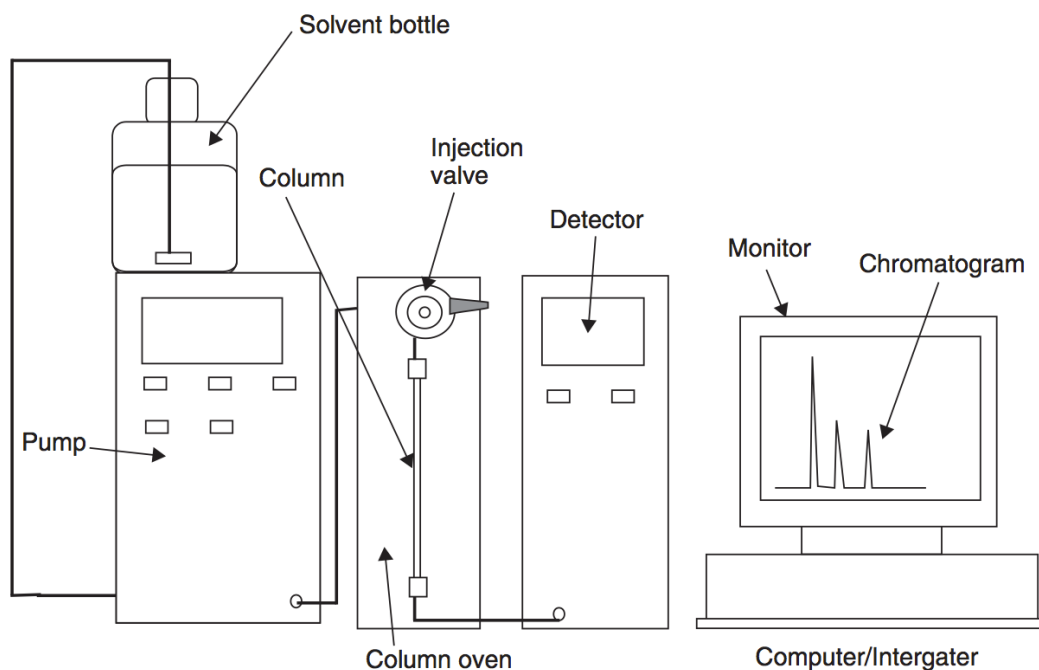
Molecular exclusion chromatography



Affinity chromatography

**Fig 2-17: Types of chromatography.[106]**

High-performance liquid chromatography can be classified under partitioning type chromatography. HPLC uses high pressure to force solvent through packed columns containing very fine particles that provide high-resolution separations. Fig 2-18 shows the main component of the HPLC system. These components and the factors that affect the quality of a chromatographic separation will be discussed in this section.



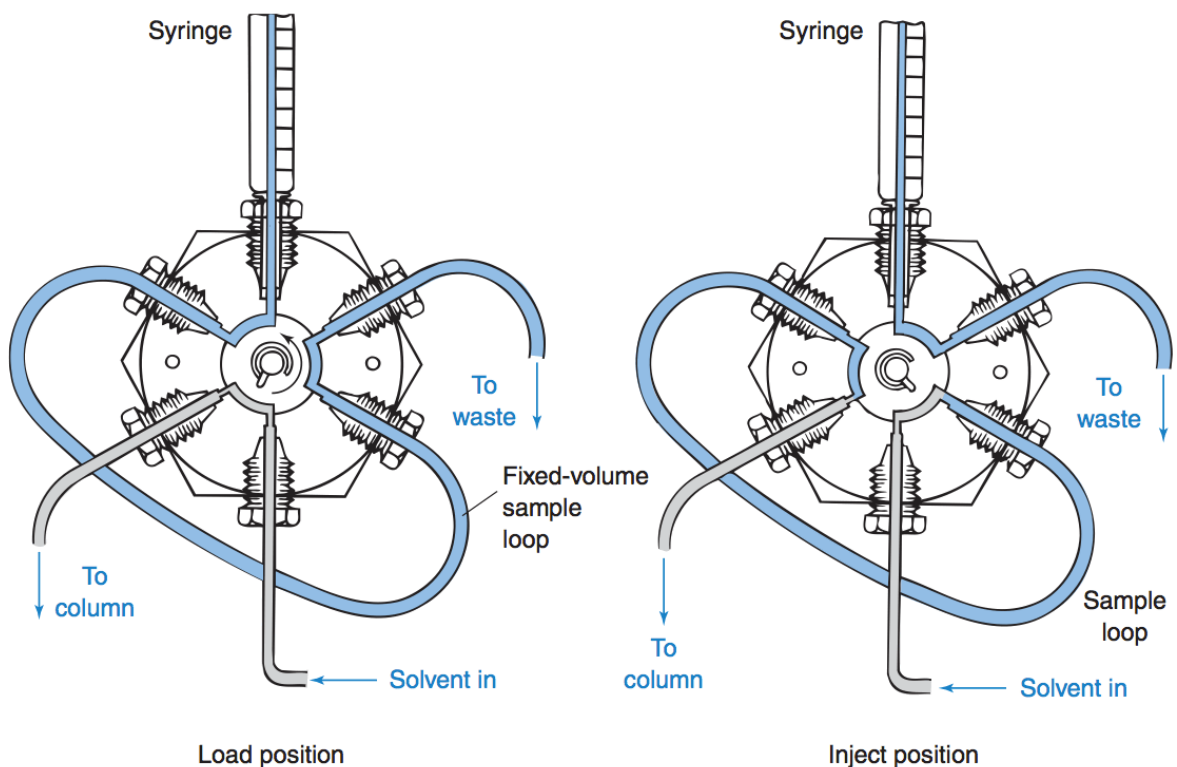
**Fig 2-18: Schematic diagram of high performance liquid chromatography. [107]**

### **2.5.1 Mobile phase in LC**

The HPLC the mobile phase consists of an organic solvent (typically acetonitrile or methanol) and water (or buffer solution). In order to remove particulates and air bubbles from the mobile phase, the used solvents are normally filtered and degassed prior to being pumped to the column. The pumping system can be operated using one mode (isocratic elution) or two modes (gradient elution). In the isocratic mode a single solvent or constant solvent mixture is used throughout the analysis while in the gradient elution mode the solvent composition of the mobile phase is changed to increase eluent strength using a microprocessor-controlled gradient programmer. The gradient mode is normally used with the complex organic compound mixtures that can not be achieved under isocratic conditions.

## 2.5.2 Sample Introduction for HPLC

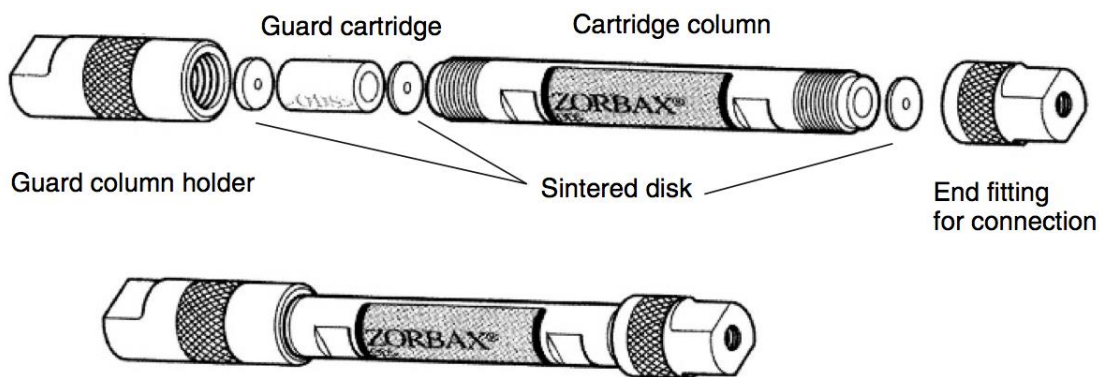
The sample is normally introduced into the column using a rotary 6-port injection valve, Fig 2-19. The sample, or standard, solution can be injected either manually or through a computer-controlled autosampler. The rotary 6-port injection valve has an interchangeable sample loop which can hold a fixed volume (2 to 1000  $\mu\text{l}$ ). In the load position, the pump is connected directly to the column inlet. The syringe is used to load the loop with fresh sample at atmospheric pressure; and from the loop excess sample goes to waste. High-pressure flow from the pump to the column passes through the segment of valve at the lower left. The content of the sample loop can be injected into the column at high pressure by rotating the valve a 60° counterclockwise.



**Fig 2-19: Schematic diagram of a typical injection valve used for HPLC.[106]**

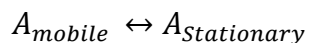
### 2.5.3 HPLC Column

The column in HPLC consists of a stainless steel tube that fit with appropriate end fittings that allow coupling to connecting tubes, Fig 2-20. The length of column varies from 1 and 25 cm with an internal diameter of 1- 4.6 mm. The stationary phase is chemically bonded to the silica particles. The properties of a stationary phase are determined by the nature of the functional group attached to the silica particles. If functional group is a polar, then the mobile phase is a nonpolar or moderately polar solvent. The combination of a polar stationary phase and a nonpolar mobile phase is called normal-phase chromatography. Examples of polar stationary phases include silica with cyano ( $-\text{C}_2\text{H}_4\text{CN}$ ) or amino ( $-\text{C}_3\text{H}_6\text{NH}_2$ ) functional groups. On the other hand the reversed-phase chromatography, which is the most commonly used in HPLC, the stationary phase is nonpolar and the mobile phase is polar. Examples of nonpolar stationary phases are octadecylsilane (ODS) also known as  $\text{C}_{18}$  or octyl  $\text{C}_8$ .



**Fig 2-20: Standard HPLC column [107].**

In partition chromatography, separation is based on a difference in the equilibrium partitioning of analytes between the liquid stationary phase and the mobile phase. For analyte Species A, the equilibrium involved can be described by the following equation



The equilibrium constant, K, for this reaction is known as the partition coefficient; and is defined as

$$K = \frac{C_s}{C_M} \quad \text{Eq. 2-14}$$

Where  $C_s$  is the molar concentration of an analyte in the stationary phase and  $C_m$  is its analytical concentration in the mobile phase. The retention time,  $t_R$ , for each component is the time required for the sample to reach the detector after sample injection. The dead time  $t_M$  provides the measure of the average rate of the migration of the mobile phase and is an important parameter in the identification of the analyte peaks. Often the mobile phase or the sample will contain the species that is not retained by the stationary phase. The average linear range of the migration of analyte through the column is given by

$$\bar{v} = \frac{L}{t_R} \quad \text{Eq. 2-15}$$

Where  $L$  is the length of the column packing. Another important experimental parameter is the capacity factor  $K'_A$  or the retention factor which is widely used in describing the migration rates of the analyte on column and is given by

$$K'_A = \frac{t_R - t_M}{t_M} \quad \text{Eq. 2-16}$$

When the capacity factor is larger than 20, elution times will become long. The ideal separation can be achieved when  $K'_A$  for the analytes in a mixture lie in the range of (1-5). The selectivity factor  $\alpha$  is also another term used to provide a measure of how well is the column in separating analyte A and B and is defined as

$$\alpha = \frac{K_B}{K_A} \quad \text{Eq. 2-17}$$

Where  $K_B$  is the partition coefficient for the more strongly retained species B while  $K_A$  is the partition coefficient for the more rapidly eluted species A. This equation can be rearranged to provide a relationship between the selectivity factor and the capacity factor

$$\alpha = \frac{(t_R)_B - t_M}{(t_R)_A - t_M} \quad \text{Eq. 2-18}$$

## Column efficiency

There two terms used widely as a measure of the efficiency of the column; number of theoretical plates  $N$  and the plates height  $H$  (the height equivalent to a theoretical plate). The model of the theoretical plates assumes that the column consists of a large number of separate layers known as theoretical plates in which equilibrium between the concentrations of the analyte compound in the mobile phase and the stationary phase is established under the given conditions.

The number of the theoretical plates can be calculated using the following equation

$$N = 16 \left( \frac{t_R}{W} \right)^2 = 5.55 \left( \frac{t_R}{W_{1/2}} \right)^2 \quad \text{Eq. 2-19}$$

Where  $W$  and  $W_{1/2}$  is the peak width at the base of the peak, or at half peak height. Columns with high plate numbers are considered to be more efficient than columns with a low plate count. The relationship between the height equivalent to a theoretical plate and the number of the theoretical plates can be written as follows

$$H = \frac{L}{N} \quad \text{Eq. 2-20}$$

Where  $L$  is the length of the column. The shorter plate heights the higher column efficiency.

## Column resolution

The resolution  $R_s$  of the column is widely used as a quantitative measure of the ability of the column to separate two analytes and is defined as

$$R_s = \frac{2 [(t_R)_B - (t_R)_A]}{W_A + W_B} \quad \text{Eq. 2-21}$$

Resolution number higher than 1.50 indicates that there is baseline between the peaks and number less than 1.50 indicates that there is some degree of co-elution.

## 2.5.4 Spectrophotometric Detectors

A broad range of HPLC detectors are available to meet different sample requirements. Specific detectors respond to a particular compound only and the response is independent of mobile phase composition. On the other hand the response of bulk property detectors is dependent on collective changes in composition of sample and mobile phase. The most common HPLC detectors are listed in Table 2-2. Each detector will have different sensitivity and linear range.

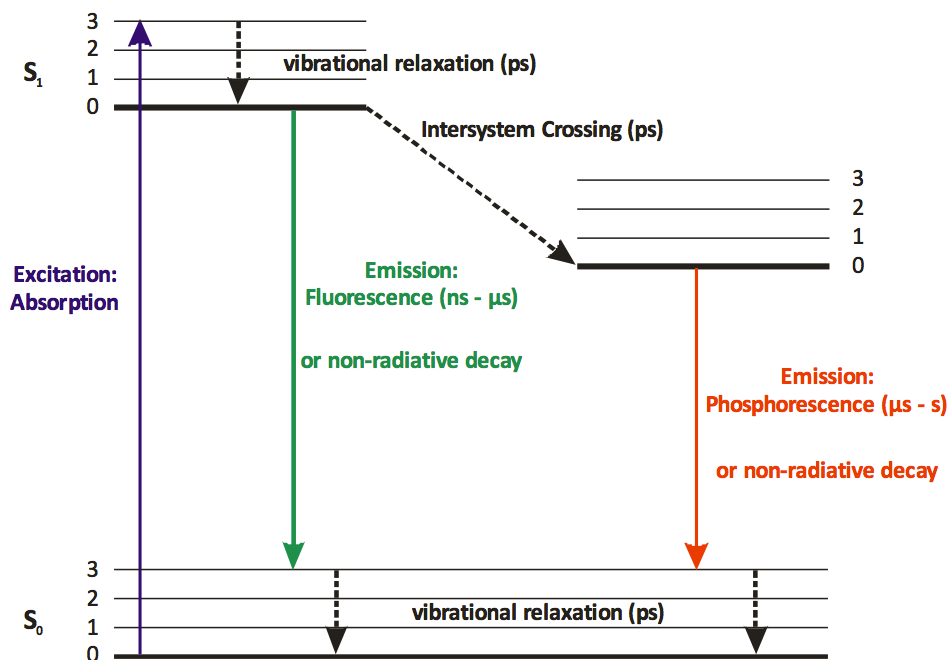
**Table 2-2: High performance liquid chromatography detectors**

Detection method	Selectivity	Characteristics
UV-VIS absorption	Variable, wavelength-dependent	Common for organic solutes, full spectra possible with array detector
Fluorescence	Fluorescent solutes, wavelength-dependent	Can be very sensitive
Mass Spectrometer	Universal or highly selective	Can provide structural confirmation
Refractive Index	Universal	Less sensitive
Electrochemical	Redox active solutes	Redox active
Conductivity	Ion only	Ions



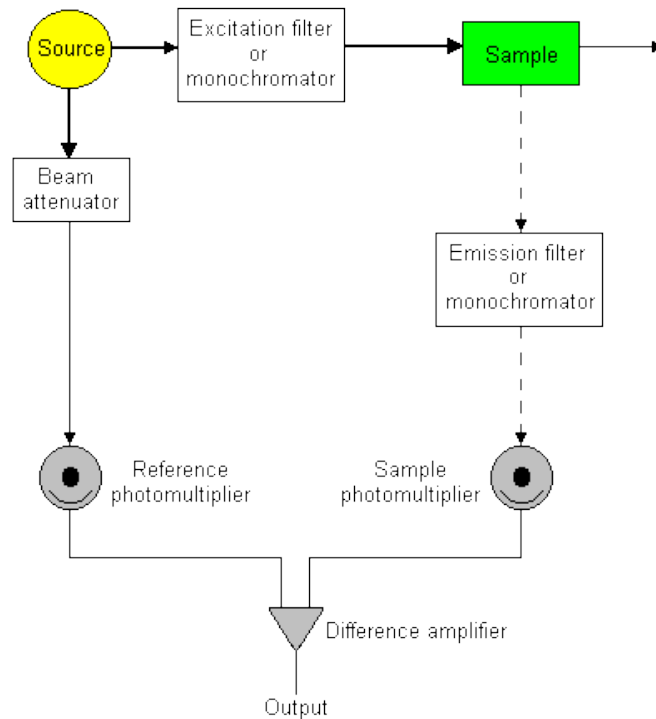
## Fluorescence Detector

Fluorescence detection provides a greater sensitivity compared to UV-VIS detector. However, the number of naturally fluorescent compounds is smaller in comparison to light absorbing compounds. This limitation is overcome by post column derivatization. Fig 2-21 is a schematic diagram, known as Jablonski diagram that illustrates the processes associated with the absorption and emission of light. Atoms, molecules, or solids that are excited to higher levels can relax to lower levels giving up their excess energy as photons. For atoms that have been excited by a high temperature energy source such as plasma, this radiation is known as atomic or optical emission. Light emission from molecules can be divided into two categories, fluorescence and phosphorescence. Fluorescence describes the transition between states of the same spin while phosphorescence if the transition occurs between the states of different spin.



**Fig 2-21: Jablonski diagram that shows the electronic (—) and vibrational energy levels (0, 1, 2, 3).  $S_0$  is the ground state,  $S_1$  the first excited state. For each electronic state additional vibrational levels are displayed. Absorption (—), Fluorescence (—), Phosphorescence (—) and vibrational relaxation processes (- - -) are indicated.**

Molecular fluorescence is usually measured by exciting the sample at the absorption wavelength, also called the excitation wavelength, and measuring the emission at a longer wavelength called the emission or fluorescence wavelength. Fig 2-22 illustrates a typical configuration of the fluorometer components. In order to compensate for the fluctuation in the power of the source, the fluorometer is usually designed with a double beam. The radiation from an excitation source passes through a primary filter or primary monochromator and strikes the sample. The sample will then absorb some of the incident light causing some of the molecules in the sample to fluoresce. Fluorescence radiation is propagated from the sample in all directions. Some of this fluorescent light will reach the photoelectric detector after passing through a second filter or monochromator, which isolates a fluorescence peak for measurement. The second filter or monochromator is normally placed at 90° to the incident light beam to minimize the risk of transmitted or reflected incident light reaching the detector. A reference beam will pass through an attenuator to reduce its power to approximately that of the fluorescence radiation. The reference beam will pass through an attenuator to reduce its power to approximately that of the fluorescence radiation.



**Fig 2-22: Schematic diagram of the configuration for fluorescence measurements.**

## **Chapter 3 : Experimental and Safety**

## 3.1 Preparation of mesoporous materials

### 3.1.1 MCM-41

MCM-41 was prepared according to the method reported by Idris *et. al.* [65]. Briefly; 8.8 g of CTAB was dissolved in a mixture of 208 cm<sup>3</sup> of distilled water and 96 cm<sup>3</sup> of aqueous ammonia solution under slight warming (35 °C). Then, 40 cm<sup>3</sup> of TEOS was slowly added under stirring. After further stirring for 3 h, the gel was aged at room temperature for 24 h in a closed container. The product was obtained by filtration, washed with distilled H<sub>2</sub>O, and dried in air at room temperature. The organic template was removed using a microwave digestion method [65]. approximately 0.3 g of as-synthesised samples of MCM-41 were added to multiple Teflon vessels to which 5 cm<sup>3</sup> of HNO<sub>3</sub> and 2 cm<sup>3</sup> of H<sub>2</sub>O<sub>2</sub> were added. The Teflon vessels were then inserted into a MARS 5 microwave, CEM Corporation, Buckingham, UK. The operating conditions used included a power output of approximately 1600 W, a pressure and temperature lower than 1.3 MPa and 200 °C and a working frequency of 2450 MHz and 220 V for 15 min. The product was filtered, washed with copious amounts of distilled water and dried in oven at 100 °C for 2 h. This product will be referred to as ‘MWD-MCM-41’. A second batch of MCM-41 was produced where template removal was performed using a conventional calcination rig by heating in air at 550 °C for 8 h. This material will be referred to as ‘Calcined-MCM-41’.

### 3.1.2 SBA-15

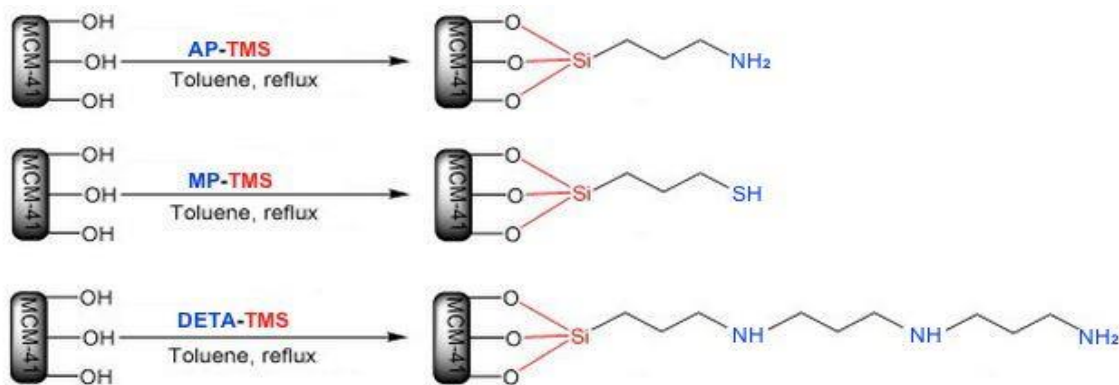
SBA-15 was prepared by modifying the original method reported by Zhao *et al* [4]. A surfactant tri-block copolymer solution of 4 g Pluronic P123, PEO<sub>20</sub>PPO<sub>70</sub>PEO<sub>20</sub> (BASF Corporation, 3000 Continental Drive), was dissolved in 120 cm<sup>3</sup> of 2 M hydrochloric acid (HCl, 37%, Sigma Aldrich) and 60 cm<sup>3</sup> of distilled water in a glass bottle at room temperature, and the mixture was magnetically stirred at 330 rpm. The surfactant solution was then heated to 40 °C and 11.3 g of tetraethoxysilane (TEOS) was added and left for 24 h at 40 °C. The mixture was then placed in an oven for 5 days at 60 °C before calcination at 550 °C for 24 h. The resulting product had a ratio of SiO<sub>2</sub>: 0.0032 P123: 4.4 HCl:144 H<sub>2</sub>O.

### 3.1.3 Bio-inspired silica materials

The bioinspired green nanoparticle (GN) silica was synthesized using a method reported by Ewlad-Ahmed *et.al.* [120]. A solution of sodium metasilicate in deionized water was acidified using 1 M HCl and mixed with a solution of PEHA and, if required, the final solution pH adjusted with 1M HCl to  $7.0\pm 0.1$ . The final concentration of silicate and amine were 30mM. Rapid precipitation of silica was visible within 1-2 min. The resultant as-synthesized precipitate was collected after 15 min by filtration, washing three times with deionized water, and drying in air at room temperature (hereafter referred to as “as made GN”) before calcination at 550 °C for 5 h, to produce GN.

### 3.1.4 Surface modification of materials

Surface modification of MCM-41 was carried out by condensation using the organosilane of choice with MCM-41, (Fig 3-1). Briefly, approximately 5 g of MCM-41 was pre-treated at 140 °C for 2 h before being immersed in 50 cm<sup>3</sup> of toluene and 10 cm<sup>3</sup> of AP-TMS, MP-TMS or DETA-TMS, in a 250 cm<sup>3</sup> flask. The mixture was refluxed for 4 h and the solid produced was filtered, washed with 100 cm<sup>3</sup> ethanol, and oven-dried at 80 °C for 2 h to produce an amino-functionalised (AP-MCM-41), mercapto- functionalised (MP-MCM-41), or diethylenetriamine-functionalised (DETA-MCM-41) MCM-41 sorbent, respectively.



**Fig 3-1: Modification of activated silica using 3-aminopropyltrimethoxy-silane, 3-mercaptopropyltrimethoxy silane, and N-(3-trimethoxysilylpropyl) diethylenetriamine.**

## **3.2 Characterisation of mesoporous silica material**

### **3.2.1 Measurement of Brunauer-Emmett-Teller (BET) isotherms**

Nitrogen adsorption–desorption isotherms were collected using a Micromeritics ASAP 2420 surface area and porosity analyser. A mass of approximately 0.3 g of each sample was accurately weighed and transferred to a gas adsorption sampling tube. The weight of the sample tube was recorded before and after the addition of the sample. The sample tube was then attached to the degas port of a gas adsorption instrument and degassed for 6 h at 200 °C prior to analysis. The Brunauer–Emmett–Teller (BET) surface areas were calculated using experimental points at a relative pressure ( $P/P_0$ ) of 0.05–0.25. The total pore volume was calculated from the  $N_2$  amount adsorbed at the  $P/P_0$  of 0.99, and the average pore size distribution of the materials was calculated using the Barret–Joyner–Halenda (BJH) model from a 28-point BET surface area plot. Desorption isotherms were used to calculate the pore diameters.

### **3.2.2 Fourier transform infrared spectroscopy (FTIR)**

FTIR transmission spectra in the range 4000 to 400  $cm^{-1}$  were recorded, at 64 scans per spectrum at 4  $cm^{-1}$  resolution, using an ATI Mattson FTIR spectrophotometer. Samples were dispersed in KBr and compressed into pellets. The IR disc sample was prepared by mixing approximately 0.2 g of dried KBr powder (Fisher Scientific, U.K.) with about 0.05 g of the solid sample. The mixture was then placed into a circular die with a diameter of 13mm and pressed into a disk using press machine with a pressure of about 5 KN. The disk was then placed on the disk sample holder and put into a closed infrared room (sample chamber) for analysis.

### **3.2.3 Scanning electron microscopy (SEM) measurements**

SEM measurements were obtained using an FEI Sirion 20 ultra-high resolution Schottky field emission scanning electron microscope with FEI software. Si wafer substrates (5 x 5 mm; Ted Pella Inc.) were first rinsed sequentially with methanol and distilled water and dried in a stream of  $N_2$ . Next, the Si wafers were treated in an  $O_2$  plasma cleaner for approximately 60 s and then immediately covered with approximately 10  $mg\ cm^{-3}$  solution of PDDAC in 1 mM NaCl for 30 min to create a positively charged surface. Each wafer was washed with distilled water and dried under a stream of  $N_2$  before

approximately 40  $\mu\text{l}$  of the sample (suspended in Millipore water) was dropped onto the wafer and stored in a humidity chamber for a further 30 min, to prevent the droplet drying, before rinsing with water and  $\text{N}_2$  drying. The deposition methodology was designed to ensure that the sample distribution was representative of the bulk solution. It was noted that if dropets of the sample suspension were simply air-dried on the substrate wafer (the method of drying-induced aggregation) the analysis was less successful.

### 3.2.4 Nanosight system

A Nanosight instrument consists of a microscope, scientific camera and a sample viewing unit LM20 (NanoSight Ltd., Amesbury, United Kingdom) and is used in conjunction with a computer control unit that runs the Nanoparticle Tracking Analysis (NTA) software (v. 2.1), as illustrated in Fig 3-2. The sample viewing unit uses a 638 nm red laser diode to illuminate particles in liquid suspension, which are held within the unit. NTA is used to analyze videos captured using the instrument, giving a particle size distribution and particle count.



**Fig 3-2: NanoSight LM20 system [121].**

The sample suspension was further diluted in water to a level that enabled around 10-50 nanoparticles to be tracked in the instrument field of view simultaneously.

### 3.3 The extraction and regeneration procedures for removal and recovery of potentially toxic metals

Adsorption experiments were carried out by suspending given amounts of sorbent in aqueous solutions (typically 25 cm<sup>3</sup>) containing initially the desired metal ion at the required pH value. After equilibration under constant stirring for 2 h, sorbents were filtered off and the remaining metal ion concentration in the supernatant was determined quantitatively by ICP-OES.

#### 3.3.1. The adsorption isotherms (Langmuir and Freundlich models)

Adsorption isotherm models were used to model the interaction of the adsorbate (metal ions) with the adsorbent and also to evaluate the maximum adsorption capacity of the potentially toxic elements adsorbed by the sorbent. Collected data were fitted to either the Langmuir or the Freundlich isotherm models. The Langmuir isotherm model suggests the formation of an adsorbed solute monolayer with no side interactions occurring between the adsorbed molecules. In addition, this model assumes that each active site can adsorb only one ion, and that a homogeneous energetic distribution of active sites [122]. The Freundlich isotherm model assumes that the adsorption surface is heterogeneous; with interactions between the adsorbed ions. It considers the occurrence of multilayered adsorption mechanism. The mathematical descriptions of these models are given below.

##### 3.3.1.1 The Langmuir model

The Langmuir model is mathematically expressed as shown in (Eq. 3-1):

$$\frac{C_e}{q_e} = \left(\frac{1}{q_m b}\right) + \left(\frac{1}{q_m}\right) C_e \quad \text{Eq. 3-1}$$

Where  $q_e$  and  $C_e$  are the equilibrium concentrations of the metal ions in the adsorbed (mg g<sup>-1</sup>) and liquid phases (mg dm<sup>-3</sup>), respectively.  $q_m$  (mg g<sup>-1</sup>) and  $b$  (dm<sup>3</sup> mg<sup>-1</sup>) are the Langmuir constants of the system denoting maximum monolayer capacity and the affinity binding sites, respectively. The  $q_m$  value can be calculated from the slope of the Langmuir model and the  $b$  value is calculated from the intercept. The amount of metal ions extracted at equilibrium  $q_e$ , can be calculated as (Eq. 3-2):



$$q_e = \frac{C_0 - C_e}{W} V \quad \text{Eq. 3-2}$$

Where  $C_0$  or  $C_e$  ( $\text{mg dm}^{-3}$ ) are the liquid phase initial or equilibrium metal ion concentrations,  $V$  is the volume of the solution ( $\text{dm}^3$ ), and  $W$  is the mass of sorbent (g) used. For predicting the favourability of an adsorption system, the Langmuir equation can also be expressed in terms of a dimensionless separation factor ( $R_L$ ) by using the Langmuir constant  $b$  and the initial concentrations of the metal ion, (Eq. 3-3).

$$R_L = \frac{1}{1 + C_0 b} \quad \text{Eq. 3-3}$$

When,  $R_L > 1$ ,  $R_L = 1$ ,  $0 < R_L < 1$  and  $R_L = 0$ , indicates unfavourable, linear, favourable and irreversible, adsorption isotherms, respectively [123,124].

### 3.3.1.2 Freundlich model

The Freundlich model is mathematically expressed as shown in Eq. 3-4:

$$\ln q_e = \ln K_f + \left(\frac{1}{n}\right) \ln C_e \quad \text{Eq. 3-4}$$

Where  $K_f$  ( $\text{mg g}^{-1}$ ) and  $n$  ( $\text{dm}^3 \text{mg}^{-1}$ ) are the Freundlich constants which are related to the sorption capacity (calculated from the intercept) and intensity (calculated from the slope), respectively. Larger value of  $n$  (smaller value of  $1/n$ ) implies stronger interaction between the sorbent and the metal ions while  $1/n$  equal to 1 indicates the linear adsorption leading to identical adsorption energies for all sites.[125,126]

### **3.3.1.3 Evaluation of maximum adsorption capacity.**

To study the maximum adsorption capacity of the metal ions on the studied sorbent, the Langmuir and Freundlich models were applied. Various initial concentrations of metal ion solutions (10- 200  $\mu\text{g m}^{-3}$ ), were prepared. The conditions used for each experiment were a stirring speed of 250 rpm, a temperature of 20 ° C, stirring time of 120 min, sorbent weight of 0.05 g and the pH value was chosen according to the studied metal ion.

### **3.3.2 The sorbent extraction efficiencies for metal ions mixed with real water samples**

To demonstrate the potential environmental performance of the sorbents they were used to extract metal ions from a river water sample collected from the Bothlin River in Glasgow. The sampling method followed BS 6068-6.4:1987. Briefly the samples were collected from a point that was approximately 2 m from the river bank using plastic container and then stored in a sealed container at 4 °C together with a tap water sample that had been taken from a building in the Drygate campus in Glasgow. Note that the tap water was left running for 15 min prior to sampling [127]. The tap water sample was also stored in a glass container of size 100  $\text{cm}^3$  with teflon lined screw caps at 4 °C. Prior to addition of sorbents, the river water and tap water samples were analysed to determine the concentration of the metal ions in solution, the results are given in Table 3-1. As the two case studies focus on extraction of chromium or arsenic ions from water, both solutions were spiked with those metal ions individually to produce solutions containing each metal ion at a known concentration. After the spiked water samples were prepared, 0.025 g of each sorbent was added to the solutions which were stirred for 2 h. 5  $\text{cm}^3$  aliquots were removed and filtered (Fisherbrand QL100) prior to analysis by ICP-AES.

**Table 3-1: : ICP/MS concentration data recorded for heavy metals in river and tap water samples.**

Heavy Metal	River Water (ppb) <sup>b</sup>	Tap water (ppb) <sup>b</sup>
Cr	4	14
As	1	3
Cd	6	13
Ca <sup>a</sup>	43,600	11,500
Fe	60	250
Mn	3	10
Mg <sup>a</sup>	6000	8500
Pb	3	55
Ni	12	50
Zn	3	354
Cu	12	60

<sup>a</sup> Measured by FAAS.

<sup>b</sup> Reported values are based on an average result of three experiments.

### 3.3.3. Examination of sorbent performance in dynamic mode

An accurate mass, 0.1g, of the studied sorbent was mixed with 2 g of glass beads (1.5 mm) and packed in a self-made polypropylene column (6 cm<sup>3</sup>) plugged with modified filter paper at both ends to give a final sorbent bed height of approximately 2 cm. In order to equilibrate, clean and neutralize the column before use, diluted solutions of nitric acid and doubly distilled water were passed over the sorbent bed. Then sample solutions containing the analyte of interest were prepared with a pH value being adjusted to 3 using 1 M HCl and 1 M ammonia solutions. Each solution was allowed to pass through the column at flow rate of 1, 2, 3, 5, 7, or 9 cm<sup>3</sup> min<sup>-1</sup>, controlled by a peristaltic pump. The eluates were collected prior to analysis by ICP-OES.

### 3.3.4. Determination of metal ion concentrations in aqueous solution using ICP-OES.

Metals ions were measured in water samples using a Perkin Elmer Optima 5300DV instrument (Perkin Elmer, UK) at an RF power of 1300 W, plasma, auxiliary and nebuliser argon gas flows of 15, 0.2 or 0.75 dm<sup>3</sup> min<sup>-1</sup>, respectively, and a pump flow rate of 1.5 cm<sup>3</sup> min<sup>-1</sup>. Multi-element calibration standards in the concentration range 0.02 - 1 µg cm<sup>-3</sup> were used and the emission intensity measured at appropriate wavelengths. For all elements, analytical precision (RSD) was typically 1-5 % for individual aliquots (n=3). Table 3-2 summarises the wavelengths used in the analysis of metal ions studied in this research.

**Table 3-2: The wavelength used in the measurement of elements using ICP-OES.**

Analyte	Cr	Hg	As	Cd	Co
Wavelength (nm)	267.7	194.2	193.7	226.5	230.8
Analyte	Ca	Mg	Fe	Mn	Cu
Wavelength (nm)	317.9	279	239.6	257.6	324.6
Analyte	Ni	Pb	Zn		
Wavelength (nm)	231.6	220.4	213.9		

### 3.4 Safety

All work involving apparatus and chemical substances were performed in a safe and controlled manner in accordance with experimental risk assessments. In this work several substances are used (Table 3-3) which are classified as hazardous to health's regulation. Due to their hazardous chemical properties, lab coat and safety glasses were worn while in the laboratory, even while performing non-laboratory work and substances were handled with gloves in a fume cupboard and were sealed and stored when not used in appropriate cupboards.

**Table 3-3: Hazardous substances associated with experimental methods.**

Substance	Very Toxic	Toxic	Carcinogenic	Mutagenic	Harmful	Flammable	Corrosive	Irritant
Toluene					✓	✓		
Tetraethylorthosilicate (TEOS)					✓	✓		✓
Cetyltrimethylammonium Hydroxide		✓						✓
Hydrochloric Acid								
Ethanol							✓	
Methanol		✓					✓	
Potassium dichromate		✓	✓				✓	
Chromium (III)					✓			
Mercury (II)		✓	✓					
1,5-diphenylcarbazide					✓			✓
Ammonia		✓			✓	✓		
Hydrogen peroxide		✓			✓			✓
3-aminopropyltrimethoxysilane								✓
3-mercaptopropyltrimethoxy silane		✓			✓			
Diethylenetriamine (DETA)					✓		✓	
Thiourea		✓	✓		✓			
Sodium metasilicate							✓	✓
Pentaethylenehexamine (PEHA)					✓			
Iron nitrate								✓
Borohydride solution		✓			✓		✓	
Sodium arsenate dibasic heptahydrate		✓	✓					
Sodium (meta) arsenite		✓	✓					
Naphthalene	✓		✓		✓	✓		
Acetonitrile		✓			✓	✓		✓

**Chapter 4 : Synthesis of microwave digested MCM-41  
(MWD-MCM-41)**

## 4.1 Introduction

Mesoporous silica materials have attracted a great deal of attention in research and industry because of their potential use in a wide range of practical applications, e.g. adsorption, separation, catalysis and sensing systems. [128] Several methods have been proposed for the synthesis of mesoporous silica materials. [129,130] Among these materials, MCM-41 type materials were the most extensively studied, probably due to their high surface area, thermal stability, large pore size and pore volumes. Initially MCM-41 was synthesised using cationic alkyltrimethylammonium as the surfactant and tetraethoxysilane (TEOS) as the silica source in a medium of tetramethylammonium hydroxide (TMAOH) as a base source at 150 °C for 48 hours. Since then extensive effort has been made to enhance the physical properties of MCM-41 materials. For example, Zhang *et al* [131] reported the synthesis of MCM-41 materials in an autoclave under high-pressured conditions. The synthesised materials were shown to have thicker pore walls, and shorter Si-O bond, leading to the enhancement of its thermal and hydrothermal stability. Wenyong *et al* [132] reported the synthesis of MCM-41 in the presence of various base sources, such as diethylamine, dimethylamine, ethylamine, and methylamine instead of TMAOH which resulted in the formation of a material with a high quality MCM-41 structure. Furthermore, Ryoo *et al* [60] observed that the silica source used can also affect the pH value of the reaction mixture which influences the quality of the material material produced. When sodium silicate was used as the silica source the pH value of the reaction mixture increased and acid had to be added to the synthesis medium in order to adjust the pH to its original value. This adjustment was not required when the TEOS was used since the pH value can be maintained without any pH adjustment.[132] However, these methods suffer the problems of high temperature processing (90-150 °C), long preparation time (24-96 h), and the production of small quantities of MCM-41.

Therefore, a method that allows the preparation of larger quantities of high-quality MCM-41, in a short period of time at room temperature, is a topic of great interest. Brühwiler [133] successfully prepared MCM-41 materials with a well-defined morphology using TEOS as the silica source, CTAB as the surfactant in the presence of ammonia (NH<sub>4</sub>OH) as a base source at room temperature. A scale-up friendly room

temperature procedure was proposed by Ritter [134] for the synthesis of MCM-41 using TEOS, CTAB, and  $\text{NH}_4\text{OH}$  as a silica source, surfactant, and catalyst, respectively.

Elimination of the template, after MCM-41 synthesis, is a necessary process in order to generate a porous structure providing adequate adsorbent properties. Conventionally MCM-41 material were synthesized using a method that employs removal of surfactant micelles by calcination.[6] This method of production has been favoured over the years as it produces a well-ordered material with long-range ordering of the mesopores. However there are some disadvantages to the method which include long times (5 – 6 h) to remove the surfactant as well as the fact that burning out the organic templates may lead to the structure shrinkage, or collapse, of the silica framework as well as the production of less silanol groups on the surface of the materials; which are all factors of vital importance for surface functionalization. [135-138] Hence, a number of alternative approaches have been proposed for the removal of the template, including solvent extraction [75,135] or supercritical fluid extraction [139,140]. However, the templates cannot be removed completely by these methods, and a calcination step is still necessary after the extraction. Yang *et. al* [138] studied the removal of the organic template of SBA-15 materials by treating them with an oxidizing agent ( $\text{H}_2\text{O}_2$ ) at 100 °C for 24 h. The results showed that complete removal of the polymer template was achieved and the resulting material exhibited higher specific surface areas, larger pore volumes, more uniform particle sizes and a higher density of silanol groups on the pore wall than those obtained by conventional methods. One of the fastest methods used to remove the template from mesoporous silica is perhaps by microwave digestion. When MCM-41 [65], or SBA-15 [64], was mixed with  $\text{H}_2\text{O}_2$  and  $\text{HNO}_3$  and exposed to microwave radiation for a short period of time, the organic templates were completely removed. The resulting samples also contained a high silanol group density, no structural shrinkage (which yield higher surface area), larger pore volume and pore size.

In this work a new method of production of MCM-41 was used [65] which involved the synthesis under mild conditions (room temperature) and shorter reaction times as well as reduced surfactant removal times (15 min) compared to the previously published methods that take approximately 10 h. The physical properties of the material was studied using



different techniques including nitrogen adsorption-desorption analysis, a scanning electron microscope (SEM), a transmission electron microscopy (TEM), a Fourier transform infrared spectroscopy (FTIR), and elemental analysis.

## 4.2 Experimental

### 4.2.1 Materials and reagent

Tetraethoxysilane (TEOS) 98%, aqueous ammonia (30% NH<sub>3</sub>), and hydrogen peroxide solution (30 wt.%) were purchased from Sigma–Aldrich. Cetyltrimethylammonium bromide (CTAB) was supplied by BDH. Nitric acid (65 wt.%) was provided by Fisher Scientific. Glassware was soaked in 5% HNO<sub>3</sub> overnight and cleaned with deionised water before use. All products were used as supplied and deionised water was used throughout this work.

### 4.2.2 Synthesis of MWD-MCM-41

The synthesis method was outline in section 3.1.1. Briefly, 8.8 g of CTAB was dissolved in a mixture of 208 cm<sup>3</sup> of distilled H<sub>2</sub>O and 96 cm<sup>3</sup> of aqueous NH<sub>3</sub> under slight warming (35 °C). Then, 40 cm<sup>3</sup> of TEOS was slowly added under stirring. After further stirring for 3 h, the gel was aged at room temperature for 24 h in a closed container. The product was obtained by filtration, washed with distilled H<sub>2</sub>O, and dried in air at room temperature. The organic template was removed using a microwave digestion method.[65] The functionalisation was performed as outlined in section 3.1.4, Briefly, approximately 5 g of MWD-MCM-41 was pre-treated at 140 °C for 2 h before being immersed in 50 cm<sup>3</sup> of toluene and 10 cm<sup>3</sup> of the desired functional group, in a 250 cm<sup>3</sup> flask. The mixture was refluxed for 4 h and the solid produced was filtered, washed with 100 cm<sup>3</sup> ethanol, and oven-dried at 80 °C for 2 h.

### 4.2.3 Synthesis of resol reagent

Resol precursors were prepared by modifying the original method reported by Gu *et al.*[141] Briefly; 0.61 g of phenol was melted at approximately 40 °C in a conical flask and mixed with 0.13 g of 20 wt % NaOH aqueous solution under stirring. After 10 min, 1.05 g of 37 wt % formaldehyde was added dropwise below 50 °C, under further stirring

for 1 h at 75–80 °C, the mixture was then cooled to room temperature. The pH value was adjusted with 1M HCl solution until it reached a pH value between 6–7, and water was removed by vacuum evaporation below 50 °C. The resulting product was dissolved in ethanol as the concentration of phenol was adjusted to 12.1 wt %. The final product had a ratio of phenol/formaldehyde/NaOH 1:2:0.1.

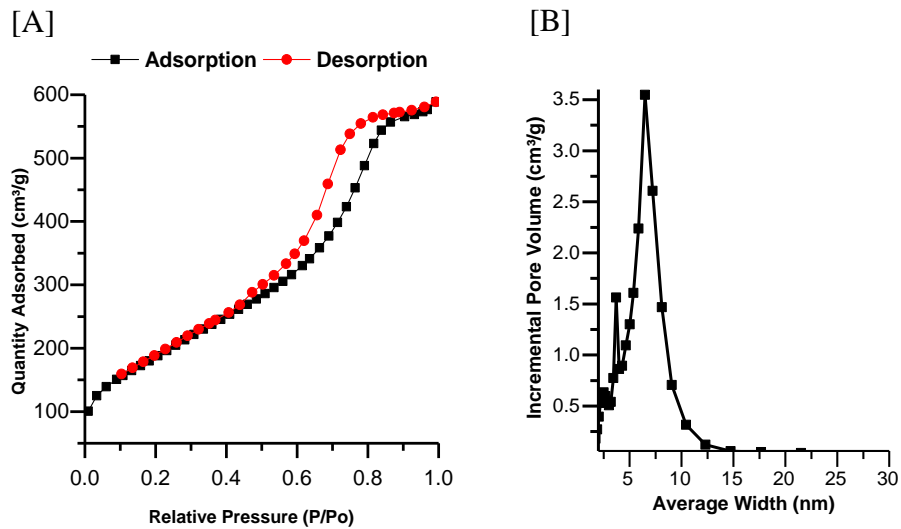
#### **4.2.4 Synthesis of resol-MCM-41**

Resol-MCM-41 was prepared by modifying the original method reported in section 3.1.1. Briefly; 4.4 g of CTAB was dissolved in a mixture of 104 cm<sup>3</sup> of distilled H<sub>2</sub>O and 48 cm<sup>3</sup> of aqueous NH<sub>3</sub> under slight warming (35 °C). Then, 20 cm<sup>3</sup> of TEOS was slowly added under stirring. After further stirring for 3 h, the gel was aged at room temperature for 24 h in a closed container. The product was obtained by filtration, washed with distilled H<sub>2</sub>O, and dried in air at room temperature (the color of the material was light brown) and 7 h at 100 °C in an oven for the thermo-polymerization. The organic template was removed using a microwave digestion method [65]. approximately 0.3 g of as-synthesised samples of Resol-MCM-41 were added to multiple Teflon vessels to which 5 cm<sup>3</sup> of HNO<sub>3</sub> and 1.5 cm<sup>3</sup> of H<sub>2</sub>O<sub>2</sub> were added using MARS 5 microwave, CEM Corporation, Buckingham, UK. The operating conditions used included a power output of approximately 1600 W, a pressure and temperature lower than 1.3 MPa and 200 °C, respectively and a working frequency of 2450 MHz and 220 V for 15 min. The product was filtered, washed with copious amounts of distilled water and dried in oven at 100 °C for 2 h.

## 4.3 Results and discussion

### 4.3.1 Nitrogen adsorption-desorption analysis

The porous properties of MWD-MCM-41 materials were investigated using nitrogen sorption analyses and revealed that MWD-MCM-41 exhibited a type IV isotherm confirming their mesoporous nature, Fig 4-1 A, a high surface area  $760 \text{ m}^2\text{g}^{-1}$  and pore volume  $0.99 \text{ cm}^3\text{g}^{-1}$  was obtained, Fig 4-1 B. Remarkably, a high pore size of 6.74 nm was achieved, which was almost three times higher than the conventional used method of template removal (e.g. calcination and solvent extraction). This was attributed to joining of 2 or 3 pores together after pore wall teardown.

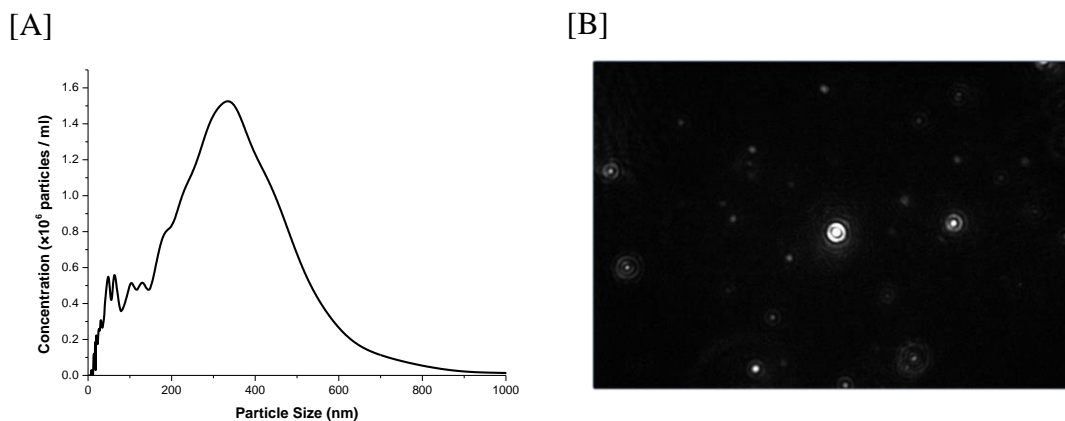


**Fig 4-1: Nitrogen adsorption isotherms of MWD-MCM-41 (A) and their relative pore size distribution (B).**

### 4.3.2 The particle size distribution (PSD) of MWD-MCM-41.

Particle size distribution of sorbent materials used in environmental remediation is an important property to consider in contaminated water treatment practice for 2 reasons. First, the particle size of the sorbent used has a major influence on the backpressure when the sorbent is used in dynamic mode (e.g. if the material is packed into a solid phase extraction column); increasing the particle size results in lower backpressures, consequently allowing faster flow rates. Second, it has been shown that the concentration of adsorbed metal ions is related to the particle size of the materials used to remove them from contaminated solution [142]; materials with smaller particle size had higher metal ion uptake than those with a larger particle size because of their larger surface area.

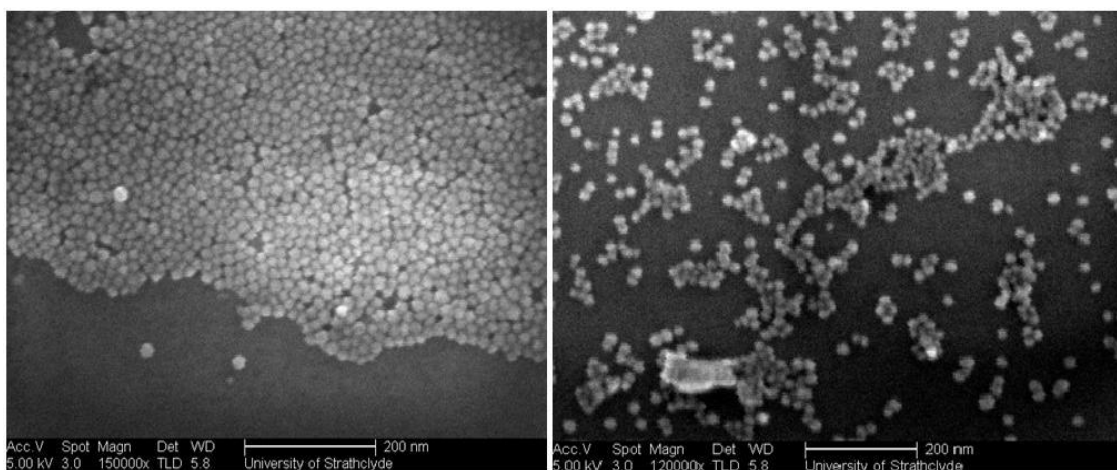
A sample of MWD-MCM-41 was prepared as discussed in Section 3.2. A pre-weighed subsample (0.1 mg) was removed and prepared for analysis using the Nanosight instrument as outlined in Section 3.6, using the instrumental operating conditions given in Section 3.6.2. The particle size distribution of MWD-MCM-41 is illustrated in Fig 4-2. The data collected indicated that most of the particles were in the range of 200 to 500 nm.



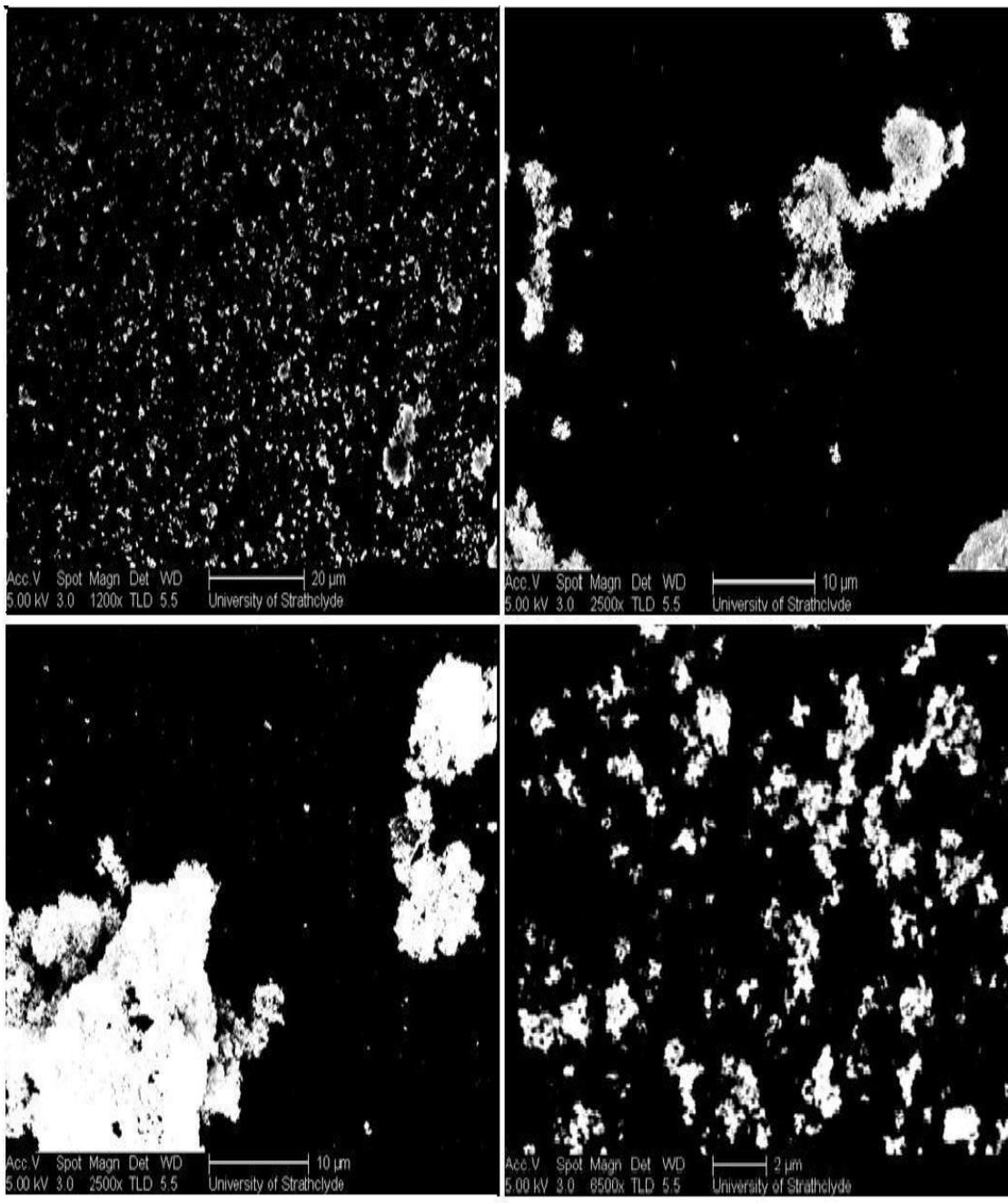
**Fig 4-2: A) represent the particle size distribution of MWD-MCM 41 and B) a frame of the video used to determine the particle size measured, the positions of individual particles are clearly identified as point like objects on the frame.**

### 4.3.3 Examination of MWD-MCM-41 using a Scanning Electron Microscope.

The MWD-MCM-41 material was also examined, together with a sample functionalized with (mercaptopropyl), using scanning electron microscopy. The scanning electron micrograph images are shown in Fig 4-3 and Fig 4-4. The image of MWD-MCM-41 shows that the material was non-uniform and dispersed evenly over the stub (see top RHS image with magnification of 1200x). At higher resolution (2500x and 6500x) the material was shown to clump together forming larger particles of various different size. In contrast, after the materials were functionalized by derivatisation in toluene, the recovered materials had an entirely different morphology (see Fig 4-3). Immersion in the solvent system altered the morphology with the result that the final materials had a uniform spherical shape with an approximate diameter of 20-40 nm. Such morphology would be ideal for a sorbent that would be used in dynamic mode to remediated contaminated water. The production of smaller particle sizes can be attributed to the phenomenon that have been described by the DLVO (named after Derjaguin, Landau, Verwey and Overbeek) theory [143]. When the silica particles are immersed in a solvent, a charge surface will be produced that will lead to competition between van der Waals forces, which tries to aggregate particles, and the repulsion produced by the surface charges of each particle. When the functional group was covalently bonded to the silica nanoparticle surface, an electrostatic repulsion between the particles were created, caused by the increase in the surface activity.



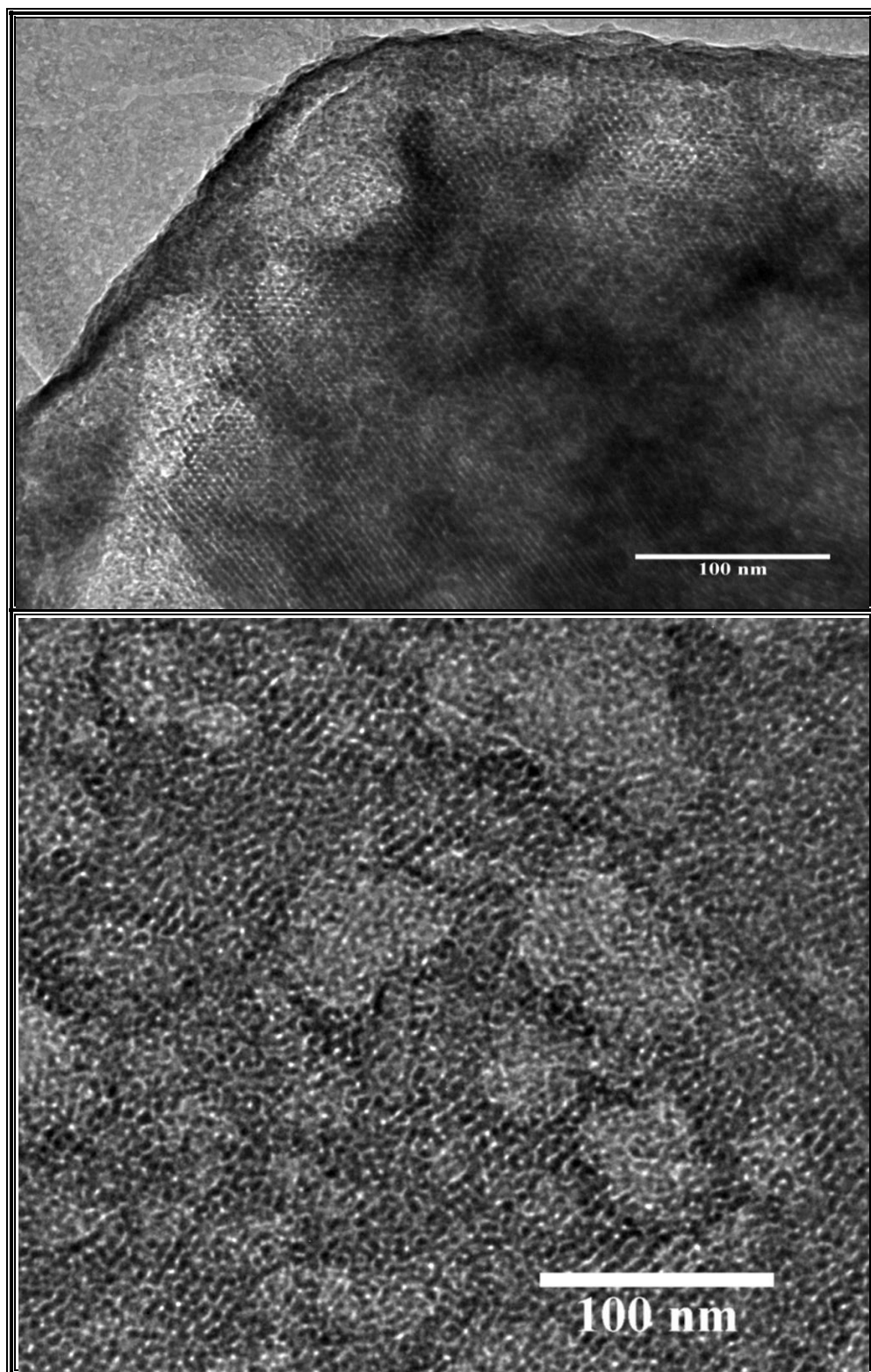
**Fig 4-3 : SEM image of functionalised-MWD-MCM-41**



**Fig 4-4: SEM image of MWD-MCM-41.**

#### **4.3.4 Examination of MWD-MCM-41 with Transmission electron microscopy (TEM)**

The TEM images of MWD-MCM-41, shown in Fig 4-5, confirm that MWD-MCM-41 had ordered hexagonal pore arrangements. Furthermore, other interesting morphological features were also revealed, such as some of the walls between the pore channels were broken down (known as porewall teardown) leading to the formation of larger mesotunnels. The porewall teardown would be the reason why the average pore size was higher than normally found in calcined MCM-41 materials. The mesotunnels that were created were thought to be advantageous and facilitate transport and diffusion of adsorbate molecules through the sorbent channels. The pore diameters of the channels were found to vary between 2.84 and 9.35 nm. These values are in good agreement with the B.J.H pore size distribution calculated from the BET analysis (see Fig 4-1). In order to calculate the wall thickness of the channels, two pore channels that were connected to each other (not subjected to porewall teardown) were selected and the distance from channel centre to channel centre was measured. An average wall thickness of 2.08 nm was measured.



**Fig 4-5: TEM image of MWD-MCM-41**



### 4.3.5 Fourier transform infrared spectroscopy (FTIR) and elemental analysis of MCM-41 materials.

The FTIR spectra for the MCM-41 materials, before and after the removal of organic template, are shown in Fig 4-7 (A). The spectra showed absorbance bands at 1030–1240  $\text{cm}^{-1}$  which were assigned to Si–O–Si stretching. The water bending mode was observed at around 1650  $\text{cm}^{-1}$ . A large broad band was observed at 3300–3500  $\text{cm}^{-1}$  which was assign to the O-H stretching mode of the H-bonded water as well as the surface silanol groups.[144]Furthermore, The spectrum of the as made MCM-41 showed absorption bands at 2850 and 2930  $\text{cm}^{-1}$  which were assigned to ( $\text{C}_{\text{sp}^3}$ -H) stretching, and the band observed around 1490  $\text{cm}^{-1}$  was identified as the C-N stretching mode.[144] After organic template these bands disappeared confirming the success of organic template removal. The elemental analysis Fig 4-7 (B) confirmed that the MWD-MCM-41 sample had no carbon and nitrogen present further confirming template removal success.

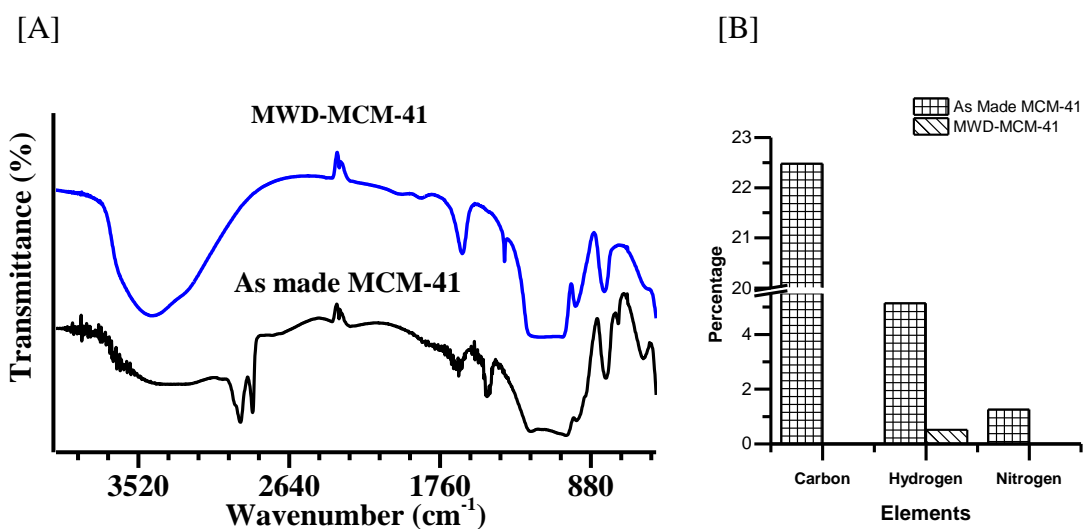


Fig 4-6: show FTIR Spectra (A) and elemental analysis (B) of as made MCM-41 and MWD-MCM-41

### 4.3.6 New methods of MCM-41 preparation

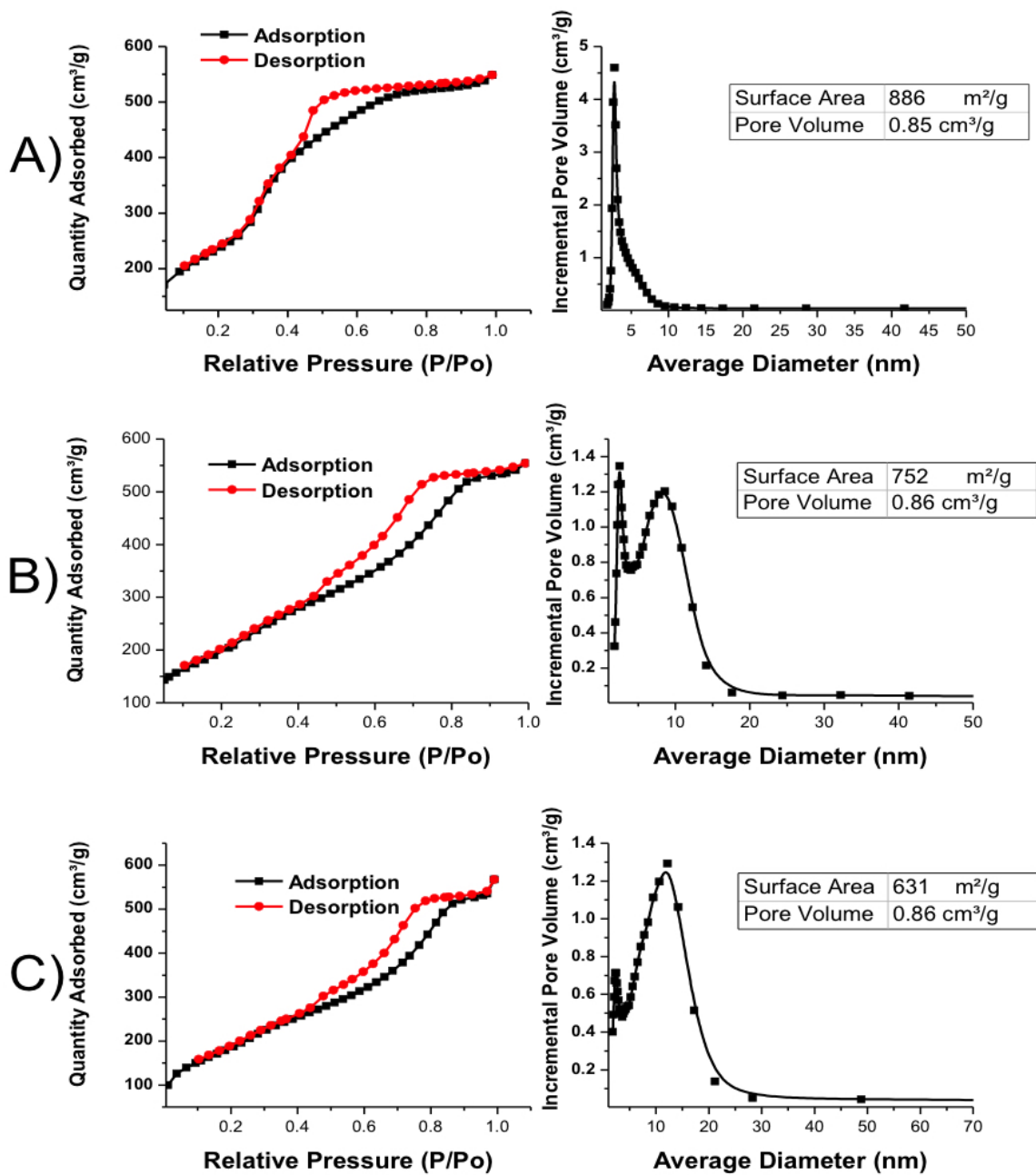
The use of microwave digestion as a mean of complete removal of the organic templates from mesoporous materials has shown many advantages over the conventional used methods (i.e. calcination, solvent extraction etc.) such as lower structural shrinkage, extreme rapidness, larger surface areas and pore volumes, and retention of a higher density of silanol groups.[65] However, during the course of the work, and with the continued use of the modified preparation method, it became apparent that the use of hydrogen peroxide and nitric acid as oxidising agents caused damage to the Teflon microwave vessels. The damage observed included distortion of the vessel and in some cases puncture holes being observed in the vessel. Despite confirming the solvents and volumes used in the digestion vessels with the CEM Microwave engineer it was obvious that the solvents used (specifically the volume of solvents used which was 5 cm<sup>3</sup> nitric acid and 2 cm<sup>3</sup> hydrogen peroxide) were too aggressive. On heating hydrogen peroxide (H<sub>2</sub>O<sub>2</sub>) expands considerably and a 2 cm<sup>3</sup> aliquot of this solution in the microwave digestion vessel caused significant increases in the digestion vessel leading to the damage observed. Therefore an attempt was made to modify the used method in order to obtain milder conditions either by reducing the digestion time or by reducing the amount of H<sub>2</sub>O<sub>2</sub>. Furthermore, a new method was proposed for the synthesis of MCM-41 using resol reagents. Samples of MCM-41 were prepared as discussed in section 3.2 but the microwave digestion procedures were altered as indicated in

Table 4-1.

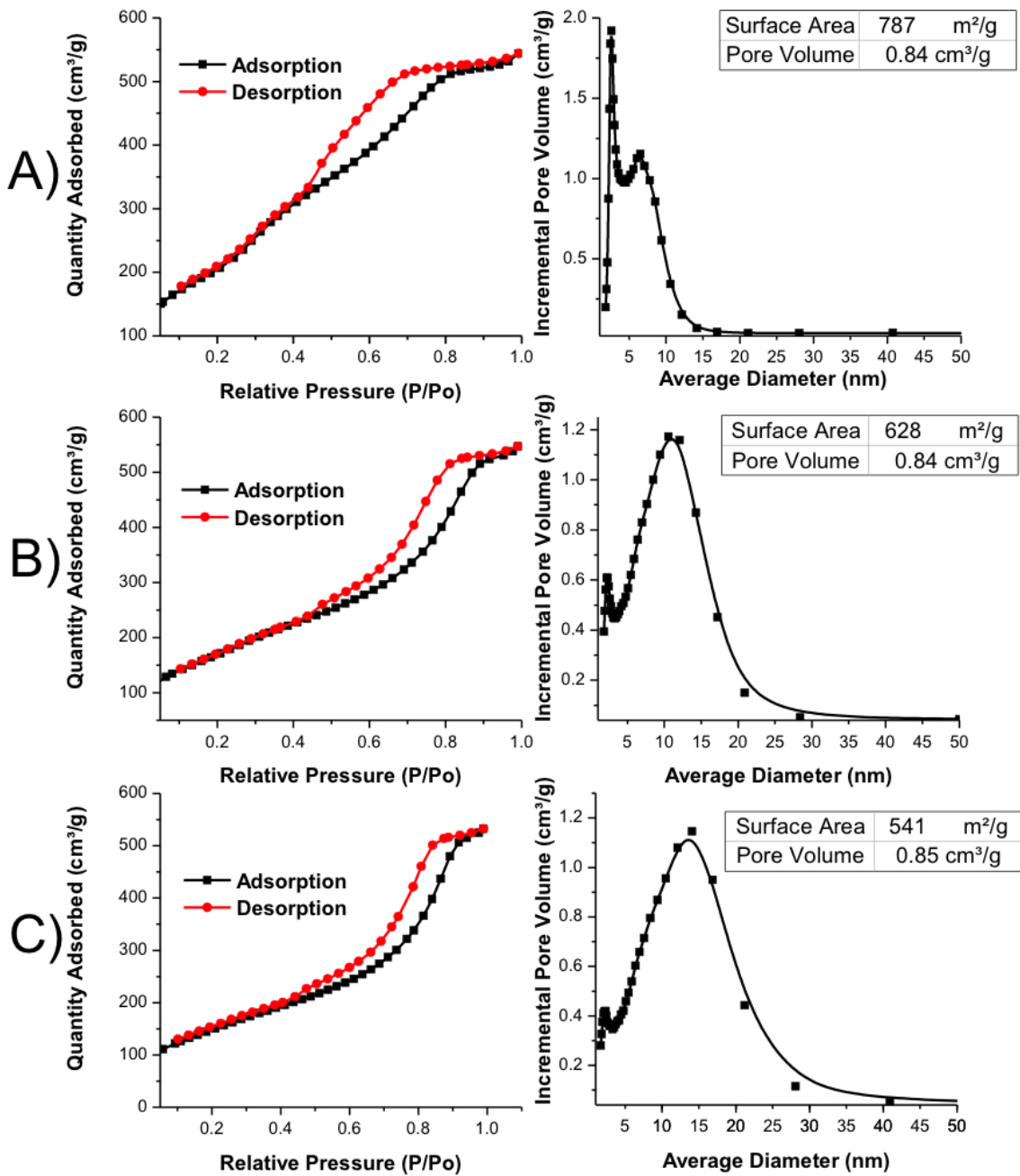
**Table 4-1: Operation conditions used for the microwave digestion of as made-MCM-41:**

Digesting time (min)	Nitric acid volume (cm <sup>3</sup> )	Hydrogen peroxide volume (cm <sup>3</sup> )	Temperature (°C)	Mass of As-made MCM-41 (g)
5	5	0.5	180	0.3
10	5	0.5	180	0.3
15	5	0.5	180	0.3
5	5	2	180	0.3
10	5	2	180	0.3
15	5	2	180	0.3

Samples (300 mg) were added to Teflon vessels using a digestion solution containing 5 cm<sup>3</sup> of nitric acid and 0.5 cm<sup>3</sup> H<sub>2</sub>O<sub>2</sub>, using digestion times of 5, 10 or 15 min. The samples were recovered from the microwave (filtered and dried at 100 °C for 2 h), before they were analysed by BET analysis (see Section 3.2.1.) The BET results illustrated in Fig 4-8 and Fig 4-8 indicated a linear relationship between microwave digestion time and the material's average pore size. As the digestion time increased from 5 to 10 then 15 min, the average pore size of the MCM-41 material increased from 2.75, 8.6 to 12 nm, respectively. This significant result indicated that the material produced could be tuned to provide mesoporous materials with different average pore size simply by alteration of the microwave digestion procedure. Previously, tuning mesopores was performed by use of different surfactants, with longer hydrophobic tails producing larger pores, or by the addition of swelling agents.[23,44,46] The results obtained here provide the first evidence that mesoporous materials can be easily tuned by alteration of the microwave digestion time. Furthermore, when the volume of H<sub>2</sub>O<sub>2</sub> is altered from 0.5 to 2 cm<sup>3</sup> and different digestion times are used the effect obtained on the average pore size was more significant with times of 5, 10 or 15 min producing materials with average pore sizes of 7, 12 and 14 nm, respectively. However, until a more robust microwave digestion vessel can be used in this procedure the volume of H<sub>2</sub>O<sub>2</sub> will remain at 0.5 cm<sup>3</sup> to protect the Teflon vessels used. Note that in each case as the pore size increases the material's surface areas decrease accordingly. However even in the case of the material with the smallest surface area, it was still greater than 500 m<sup>2</sup> g<sup>-1</sup> which is higher than most commercial sorbents.



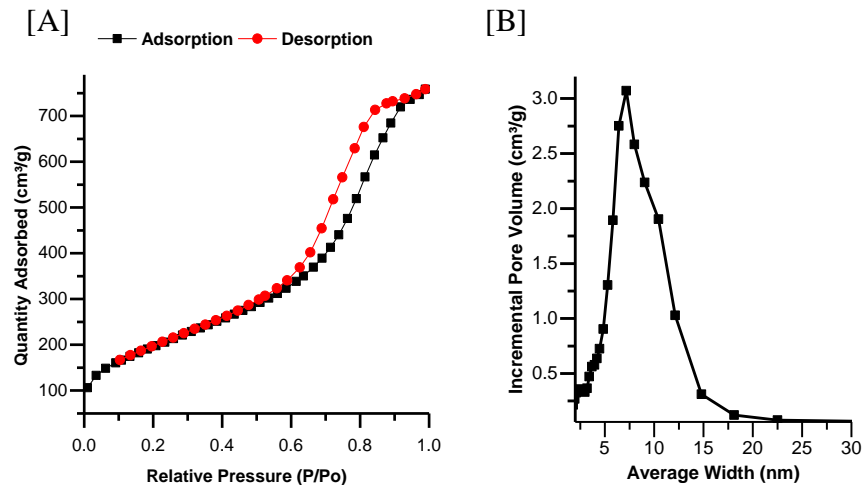
**Fig 4-7: Nitrogen sorption isotherms and pore size distributions of MWD-MCM-41 prepared using 0.5 ml H<sub>2</sub>O<sub>2</sub> and the exposure time was A) 5 min, B) 10 min, and C) 15 min.**



**Fig 4-8: Nitrogen sorption isotherms and pore size distributions of MWD-MCM-41 prepared using 2 ml H<sub>2</sub>O<sub>2</sub> and the exposure time was A) 5 min, B) 10 min, and C) 15 min.**

### 4.3.7 Incorporation of Resol into the silica framework:

To assess the ease at which MCM-41 can be prepared with large pores (and smaller volumes of  $\text{H}_2\text{O}_2$ ) a swelling agent was added to produce a mesostructured-MCM 41 nano composite. The experiment described Section 4.2.4 involved the use of a triconstituent co-assembly of preformed resol (phenol-aldehyde), TEOS and CTAB. Previous results obtained by Liu *et.al.*[145] indicated that the addition of resol to the synthesis regime enhanced the thermal and mechanical stability of the silica framework. The as-synthesised material (300 mg) was added to a Teflon vessel and the surfactant and resol removed by microwave digestion using the operating parameters described in Section 3.1.1. The final material was filtered and dried prior to analysis by BET. Despite using a smaller volume of  $\text{H}_2\text{O}_2$  ( $1.5 \text{ cm}^3$ ) the material exhibited a higher surface area of  $711 \text{ m}^2 \text{ g}^{-1}$ , a significantly larger pore volume ( $1.17 \text{ cm}^3 \text{ g}^{-1}$ ) and a larger average pore size (12 nm) compared to the previous material which was digested using  $2 \text{ cm}^3$  of  $\text{H}_2\text{O}_2$  and the same microwave digestion procedure; the results are shown in Fig 4-10. However, as the quantity used to prepare the resol reagent was very low it was found to be hard to control the preparation conditions. Therefore, another experiment was conducted by increasing the amount of starting materials to 4 g instead of the 1 g while keeping the same molar ratio. The obtained final product after mixing the resol reagent with the MCM-41 materials shown to form a pink color in the surface of the materials after the filtration step which indicated that the phenol was not converted into resol.



**Fig 4-9: Nitrogen sorption isotherms and pore size distribution of Resol-MWD-MCM-41.**

## 4.4 Conclusion

The incorporation of a microwave digestion step into the synthesis of MCM-41 allowed the preparation of materials over faster time periods whilst the highly ordered framework was retained. The data collected using the Nanosight system indicated that most of the particles were in the range of 200 to 500 nm. Furthermore, the results obtained from BET and TEM analysis show that the material has an average pore diameter of 6.74 nm and pore thickness of 2.08 nm. The use of high volume of hydrogen peroxide and nitric acid has resulted in the damage of the microwave vessels. Therefore, an attempt was made to optimize the operation conditions in order to see the effect of the time and the acid volume on the mesoporous silica materials. The results indicated that both time and acids volume added have significant effects on the textural properties of the resultant material. When the volume of H<sub>2</sub>O<sub>2</sub> is altered from 0.5 to 2 cm<sup>3</sup>, and different digestion times were used, the effect obtained on the average pore size was more significant with times of 5, 10 or 15 min producing materials with average pore sizes of 7, 12 and 14 nm, respectively. A new material was also prepared using resol as swelling agent that was incorporated into the framework of MCM-41 materials. The material exhibited a higher surface area of 711 m<sup>2</sup> g<sup>-1</sup>, a significantly larger pore volume (1.17 cm<sup>3</sup> g<sup>-1</sup>) and a larger average pore size (12 nm) compared to the previous studied material. However, the materials production method needs to be altered to extend vessel lifetime. Therefore, further work is required to assess the ability of using longer digestion times with lower volumes for both MCM-41 and Resol-MCM-41 materials

## **Chapter 5 : Adsorption of chromium species from water samples**



## 5.1 Introduction:

Chromium has been used widely in the chemical industry for different applications such as stainless steel, metal plating, pigments, and leather tanning as well as in chemical production (e.g. chemical synthesis and as catalysts). As a consequence, significant amounts of chromium species are released into the surrounding environment.[146-148] Chromium can exist in different oxidation states from 0 to VI. However, only two stable oxidation states are present in the environment; namely, Cr (III) and Cr (VI). Chromium (III) is recognized as an essential nutrient in the human diet and is generally used as a nutritional supplement for both humans and animals.[149,150] Nevertheless, it has also been demonstrated that a small concentration of Cr (III) is capable of causing eczema and genetic damage in cell-culture systems. [150-152] Hexavalent chromium (Cr VI) is estimated to be 100 times more toxic than Cr (III) for both acute and chronic exposure and has been classified as a human carcinogen by the EPA and as a class I human carcinogen by the International Agency for Research on Cancer (IARC).[153-155] The behaviour of Cr (VI) and Cr (III) in aqueous media is largely dependent on the pH and redox potential.[146] Under acidic medium, Cr (III) species exist as hexa-aquachromium (3+)  $[\text{Cr}(\text{H}_2\text{O})_6^{3+}]$  whereas under alkaline conditions Cr (III) ions exist in as hydroxylated forms [e.g.  $\text{Cr}(\text{OH})_2^+$  and  $\text{Cr}(\text{OH})_2^{2+}$  ] [146]. Cr (VI) is significantly different to Cr (III) as it exists as oxyanions whereas, as shown above, Cr (III) is present in the solution as Cr (III) ions. Depending on medium pH and total concentration of Cr, several Cr (VI) species can be formed. From low to intermediate pH values the chemical species of Cr (VI) ranges from hydrogen chromate ( $\text{HCrO}_4^-$ ) and dichromate ( $\text{Cr}_2\text{O}_7^{2-}$ ) whereas from slightly to highly alkaline conditions chromate ( $\text{CrO}_4^{2-}$ ) is the predominant form of Cr (VI).[146]

A number of treatment methods have been reported for the removal of chromium ions from aqueous solution including the reduction of Cr (VI) to Cr (III) by the addition of reducing agents (e.g.  $\text{FeSO}_4$ ,  $\text{NaHSO}_3$  or  $\text{SO}_2$ ) followed by precipitation of Cr (III) using a precipitating agent [149]. Cr species are also removed from solution by solvent extraction [151,156-160], ion exchange [153,155,161-165] and membrane separation [147,150,152,166]. However, these methods require high levels of expertise, they often result in the formation of toxic by-products, have low efficiencies, involve high-energy requirements and high maintenance costs.[167-169]

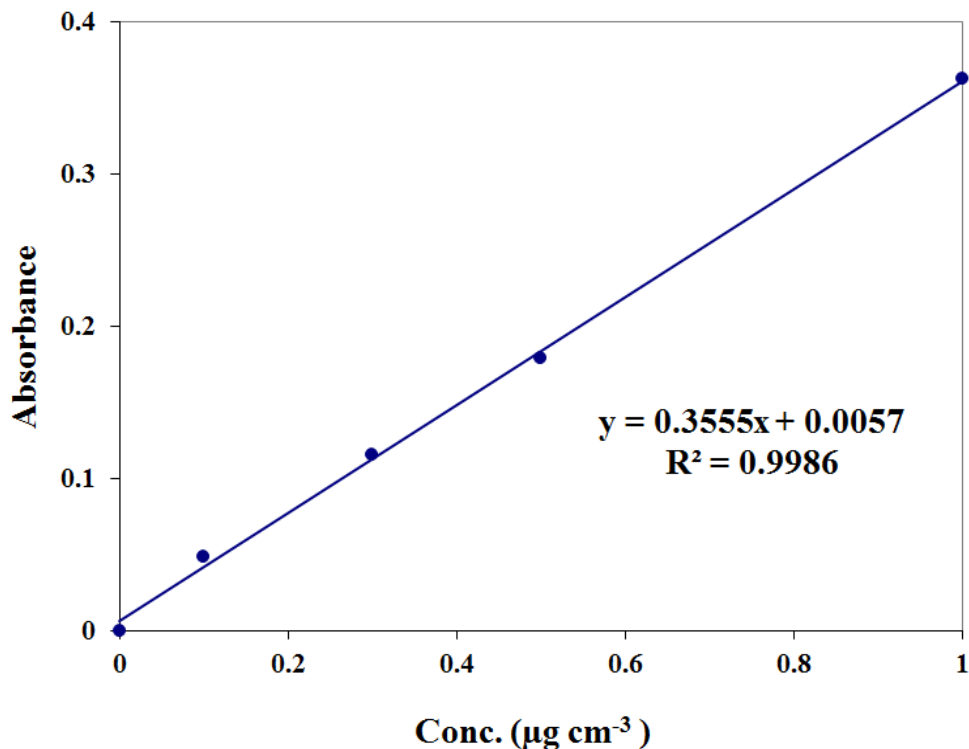
Adsorption is a widely used technique used to remove potentially toxic elements from industrial wastewaters due to a low-operating cost, easy recovery of metal ions and the possibility to reuse the adsorbent. Hence, rising attention has been given to the development of good adsorbents. Among the different adsorbents mesoporous silica materials, especially silica immobilized with various organic ligands with metal chelating ability, have received great attention.[127,156-160] Amino-functionalised mesosilica is perhaps the most studied adsorbent for chromium and has exhibited high affinity towards chromium ions.[161-165] However, many of these adsorbents have low loading capacity of chromium ions and slow process dynamics. Therefore, it is important to develop novel adsorbents with high capacity and fast kinetics for the removal of Cr (VI) from water.

The objective of this chapter was to study the feasibility of speciation and separation of chromium (III) and chromium (VI) from aqueous using MWD-MCM-41 that was initially functionalized with an amine-based functional group. The parameters that influence the sorption process such as contacting time, the concentration of Cr ions, the present of other ions and pH were investigated. Moreover, adsorbents containing silica nanoparticles with different porosity parameters were synthesized, amino-functionalized and used to evaluate Cr (VI) uptake. The linearised Langmuir and Freundlich equations were used to fit the equilibrium isotherms. Kinetic data were analysed by pseudo-first, pseudo-second and intra-particle diffusion models to obtain the kinetic constants, establish the rate limiting step of Cr (VI) removal and postulate the mechanism of Cr (VI) removal by porous materials.

## 5.2 Experimental

### 5.2.1 Determination of Cr (VI) in water samples using a colourimetric method

The method of determination for Cr (III) or Cr (VI) in aqueous solution was a slight modification of a previously reported method. [167,169] A stock solution of  $1000 \mu\text{g cm}^{-3}$  of Cr (VI) was prepared in distilled water (0.2828g of potassium dichromate [ $\text{K}_2\text{Cr}_2\text{O}_7$ ] was dissolved in  $100 \text{ cm}^3$  of distilled water). Five different calibration standards, including a reagent blank as the first calibrant, were prepared with a concentration range from  $0.1 \mu\text{g cm}^{-3}$  to  $1.0 \mu\text{g cm}^{-3}$ . A  $1 \text{ cm}^3$  aliquot of diphenylcarbazide (DPC) solution (250 mg of DPC was dissolved in  $50 \text{ cm}^3$  acetone and stored in brown bottle) was added to  $1 \text{ cm}^3$  of the calibrants, and unknown water samples, and the solution pH was adjusted to the desired value (between 1 and 2) by the addition of  $0.2 \text{ cm}^3$  1 M HCl and allowed to stand 15 min for full colour development. An appropriate portion of each solution was transferred to a 1 cm absorption cell and measured at an absorbance of 540 nm using a solution without added Cr (VI) as a reference. The solutions were analysed using a SI Photonics (M-420) CCD Array UV-Vis spectrophotometer. The calibration curve indicated a correlation between concentration and absorbance with a correlation co-efficient of 0.9986 as shown in Fig 5-1.



**Fig 5-1: Calibration graph for chromium (VI) as determined by the colorimetric method.**

### **5.2.2 Determination of total chromium $Cr_{Total}$ in water samples using inductively coupled plasma- optical emission spectrometry (ICP-OES):**

A Thermo Scientific iCAP 6200 ICP-OES instrument was used to determine the concentration of total Cr ions in solution. Calibration standards were prepared in 5 %  $\text{HNO}_3$  at the following concentrations: 0.1, 0.5, 1, 5, or 10  $\mu\text{g cm}^{-3}$ . A quality control (QC) check solution was prepared at 1  $\mu\text{g cm}^{-3}$  to check the recovery values and test the stability of the method. The QC check solution was repeatedly analysed after every set of 20 samples. Instrumental operating conditions are summarised in Table 5-1.

Prior to determination of the total chromium concentration in water samples, it was necessary to study the differences between the calibration curves obtained for Cr(III) or Cr(VI) standard solutions. Therefore, three standard solution sets were prepared, each containing final chromium concentrations of 0.1-1  $\mu\text{g cm}^{-3}$ . In the first set of solutions only Cr (III) ions were present, in the second only Cr (VI) ions were present

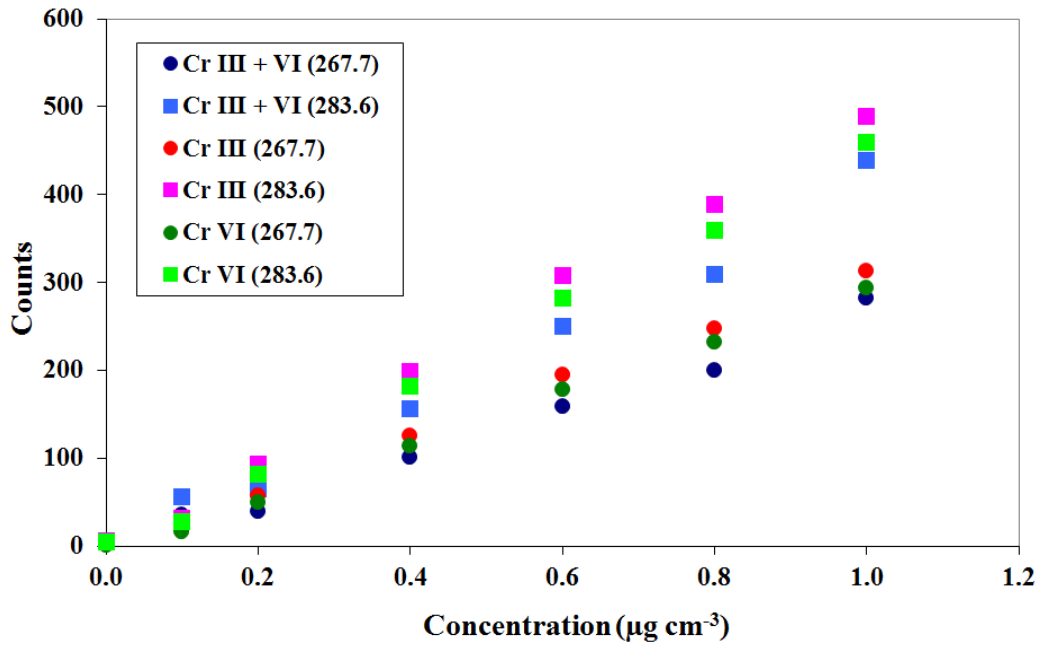
and in the final set of solutions both Cr (III) and Cr (VI) ions were present (each at half the concentration in the single ion solutions).

**Table 5-1: ICP-OES instrumental parameters employed for chromium determination.**

RF Power	1150 W
Auxiliary gas flow	0.5 L/min
Nebuliser argon gas flows	0.5 L/min
Nebulizer	Glass concentric
Spray chamber	Glass cyclonic
Coolant gas flow	12 L/min
Flush pump rate	100 rpm
Analysis pump rate	50 rpm
Pump Stabilisation	5 s
Pump tubing	Sample tygon orange/white; Drain tygon
Sample repeats	3
Sample Flush time	30 s
Analysis maximum	Radial 15 s
Integration times	Radial 5 s
Wavelength rang	Low

In order to determine the most sensitive wavelength for the detection of chromium, two different wavelengths (283.6 or 267.7 nm) were selected for measurement of the three calibration solution sets. The obtained regression lines were analysed to determine whether the slopes were significantly different, hence confirming the need to standardise the instrument using three different calibration solutions during every analysis. Using the three regression lines, a sample concentration of  $0.50 \mu\text{g cm}^{-3}$  was measured according to the three calibration curves obtained (Fig 5-1). Highest sensitivity was obtained using a detection wavelength of 283.6 nm and so this wavelength was used to measure Cr ions in all subsequent solutions. An ANOVA test was applied to assess the validity of utilising one calibration curve for all samples (See Table 5-2). The ANOVA test showed that the results were not statistically significant when the Cr (III) regression line was used to calculate the sample concentration, whereas, a significant difference was observed when Cr (VI) calibration curves were used to determine the concentration of Cr in solution; although the F-test failed by a small difference ( $F_{\text{calculated}}=3.58$  and  $F_{\text{critical}}= 3.10$ ) in

the mixed chromium (III+VI). By examination of all regression lines shown in Fig 5-2, a decision was made to use chromium (VI) calibration solutions for future calibrations. This regression line of chromium (VI) lies between the chromium (III) and mixed chromium (III+VI) calibration curves, therefore it will give a minimum error if used to the calibration curve of both chromium species.



**Fig 5-2: A graph of concentration ( $\mu\text{g cm}^{-3}$ ) versus counts for the Cr (III), (VI) or mixed Cr(III) + (VI) standard solutions using ICP-OES.**

**Table 5-2: The Anova-test for three different chromium standard solutions.**

0.5 ppm of Chromium sample	Concentration found (ppm) according to different calibration curves						F-test		
	Cr III + VI (267.7)	Cr III + VI (283.6)	Cr III (267.7)	Cr III (283.6)	Cr VI (267.7)	Cr VI (283.6)	F <sub>calc</sub>	F <sub>crit</sub>	Result
Cr (III) Replicate 1	0.5529	0.5565	0.5368	0.5529	0.5242	0.5285	1.3906	3.1059	Pass
Cr (III) Replicate 2	0.5476	0.548	0.5394	0.5346	0.5474	0.5501			
Cr (III) Replicate 3	0.5517	0.5463	0.5422	0.5384	0.5431	0.541			
Cr (III) Average	0.5508	0.5503	0.5395	0.542	0.5382	0.5399			
Cr (VI) Replicate 1	0.5096	0.5177	0.4962	0.493	0.4949	0.5004	11.2029	3.1059	Failed
Cr (VI) Replicate 2	0.5074	0.5146	0.5005	0.4945	0.4965	0.5079			
Cr (VI) Replicate 3	0.5114	0.5138	0.4969	0.5041	0.5019	0.4978			
Cr (VI) Average	0.5094	0.5154	0.4979	0.4972	0.4978	0.502			
Cr (III) +(VI) Replicate 1	0.4752	0.4897	0.4797	0.4761	0.4776	0.4773	3.582	3.1059	Failed
Cr (III) +(VI) Replicate 2	0.4843	0.4831	0.477	0.4762	0.4783	0.4816			
Cr (III) +(VI) Replicate 3	0.4786	0.4926	0.4838	0.4598	0.4809	0.4844			
Cr (III) +(VI) Average	0.4794	0.4885	0.4802	0.4707	0.4789	0.4811			

The obtained statistical results show that either detection wavelength could be applied for the determination of chromium ions in solution; with a slightly higher sensitivity using wavelengths of 283.6 nm. The method detection limits (MDL) were  $0.003 \mu\text{g cm}^{-3}$  or  $0.004 \mu\text{g cm}^{-3}$  using wavelengths of 283.6 or 267.7 nm.

The ICP-OES was used to determine the total concentration of chromium in solution. The colorimetric method is then used to determine the concentration of chromium (VI) in solution. Hence, the chromium (III) concentration was obtained by subtraction:  $\text{Cr}_{(\text{III})} = \text{Cr}_{\text{Total}} - \text{Cr}_{(\text{VI})}$ .

### 5.2.3 Extraction and recovery of chromium ions

The general procedures for extraction of Cr (III), or Cr (VI), can be summarised as follows. Approximately 25 mg samples of AP-MCM-41 or DETA-MCM-41 were suspended in  $25 \text{ cm}^3$  solutions containing  $100 \mu\text{g cm}^{-3}$  Cr (III), or Cr (VI), at various pH values (between 1 and 11) and the solution was stirred (250 rpm) for approximately 2 h. After this time the solution was filtered (Fisherbrand QL100) and the filtrate was analysed using ICP-OES. Removal of captured ions and regeneration of the sorbent was carried out by passing  $25 \text{ cm}^3$  of water solution at pH 3 for recovery of Cr(III) or pH 9 for recovery of Cr(VI); water pH was adjusted by using 1M HCl or 1M  $\text{NH}_4\text{OH}$ .

Solutions containing Cr (VI) ions were trapped onto modified sorbents and then recovered using extraction solutions to assess the use of modified silica in pre-concentration experiments. The experiments used  $20 \text{ cm}^3$  solutions of Cr (VI) at 3 different concentrations ( $0.01$ ,  $0.1$  or  $1 \mu\text{g cm}^{-3}$ ), or  $100 \text{ cm}^3$  at  $0.01 \mu\text{g cm}^{-3}$  with 25 mg of functionalised silica. Solutions were stirred with the sorbent for 2 h then the solutions were filtered and eluates were analysed by ICP-OES. The sorbent material that remained in the filter paper was washed with  $10 \text{ cm}^3$  water at pH 9 and the extracted solutions were analysed by ICP-OES after filtration.



#### **5.2.4 Analysis of real water samples**

Water samples were collected from the Bothlin river in Glasgow and a tap water sample was collected from a building in the Drygate campus in Glasgow. In the case of the river sample, the samples were collected from a point that was approximately 2 m from the river bank using plastic container and then stored in a sealed container at 4 °C [127]. Whereas, in case of the tap water sample, the tap water was left running for 15 min prior to sampling and then the sample bottle was clearly labelled and stored in a sealed container at 4 °C.

Both samples were analysed by ICP-OES to determine the concentration of Cr (VI) in solution, however both solutions contained Cr (VI) at concentrations lower than the detection limit. Solutions were then spiked with Cr (VI) to produce solution concentrations of 25  $\mu\text{g cm}^{-3}$ . To each spiked solution, an accurate weight of approximately 25 mg of AP-MCM-41 was added and solutions were stirred (250 rpm) for approximately 2 h. After this time the concentration of Cr (VI) in solution was determined by ICP-OES. After confirmation that sorbents removed Cr (VI) from solutions, the recovery of ions was assessed to regenerate sorbent materials. To regenerate the sorbent it was immersed in a 25  $\text{cm}^3$  volume of water adjusted to solution pH of 3.

#### **5.2.5 Adsorption kinetics study**

A kinetic study was undertaken to determine the rate of Cr (VI) removal from water samples using functionalised mesoporous sorbents. Solutions (25  $\text{cm}^3$ ) containing the same initial concentration of 10  $\mu\text{g cm}^{-3}$  Cr (VI) were stirred in the presence of 50 mg adsorbent at 25 °C for different selected times ranging from 1, 5, 10, 20, 30 or 40 min. After each time, solutions were filtered and analysed by ICP-OES to determine the concentration of Cr (VI) left in solution. The data collected allowed the kinetics of Cr(VI) adsorption onto the surface of mesoporous sorbents to be analysed using pseudo first-order [146,154,170], pseudo second-order [171], or intraparticle diffusion [172,173] kinetic models. The conformity between experimental data and the model predicted values was expressed by the correlation coefficients ( $r^2$ , values close or equal to 1). A

relatively high  $r^2$  value indicating that the model successfully describes the kinetics of Cr (VI) adsorption.

#### **5.2.5.1 The pseudo first-order equation:**

The pseudo first-order equation is generally presented as follows, (Eq. 5-1):

$$\log(q_e - q_t) = \log(q_e) - \frac{k_1}{2.303} t \quad \text{Eq. 5-1}$$

Where  $q_e$  and  $q_t$  are the adsorption capacity at equilibrium and at time  $t$ , respectively ( $\text{mg g}^{-1}$ ),  $k_1$  is the rate constant of pseudo first-order adsorption ( $\text{L min}^{-1}$ ). The plot of  $\log(q_e - q_t)$  vs.  $t$  should give a linear relationship from which  $k_1$  and  $q_e$  can be determined from the slope and intercept of the plot, respectively.

#### **5.2.5.2 The pseudo second-order equation:**

The pseudo second-order adsorption kinetic rate equation is expressed as, (Eq. 5-2):

$$\log(q_e - q_t) = \log(q_e) - \frac{k_2}{2.303} t \quad \text{Eq. 5-2}$$

where  $k_2$  is the rate constant of pseudo second-order adsorption ( $\text{g mg}^{-1} \text{min}^{-1}$ ). The plot of  $(t/q_t)$  and  $t$ , should give a linear relationship from which  $q_e$  and  $k_2$  can be determined from the slope and intercept of the plot, respectively.

#### **5.2.5.3 The intraparticle diffusion model:**

To study the mechanism of the particle diffusion the Morris–Weber equation was applied (Eq. 5-3):

$$q_t = k_{id} \sqrt{t} \quad \text{Eq. 5-3}$$

Where  $q_t$  is the amount of metal ion sorbed ( $\text{mg L}^{-1}$ ) at time  $t$  and  $k_{id}$  is the intraparticle diffusion rate constant ( $\text{mg L}^{-1} \text{min}^{-1/2}$ ).

## 5.3 Results and discussion

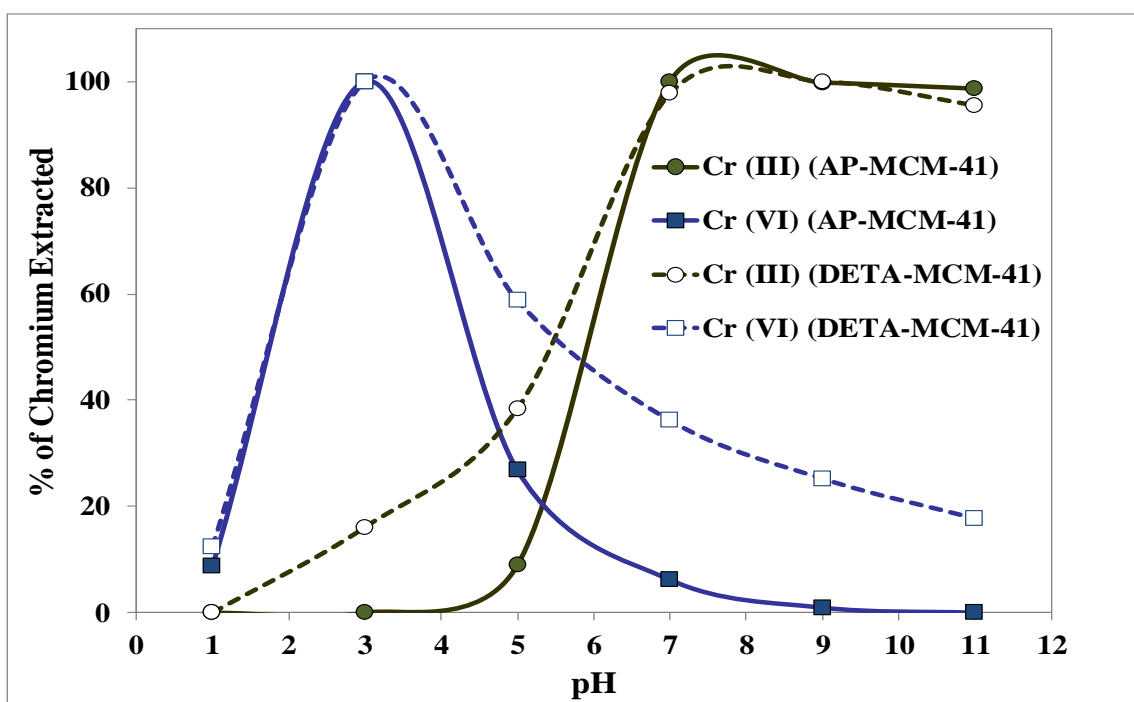
### 5.3.1 Exclusive removal of Cr (VI) in the presence of Cr (III)

To determine which sorbents would be suitable to remove Cr ions from water, two different chelates were chosen; both containing amino groups. Sorbents samples of AP-MWD-MCM-41 or DETA-MWD-MCM-41 were used to extract Cr (VI) or Cr (III) from spiked water samples at various pH values. The extraction efficiencies were determined by measuring the residual concentration of Cr ions in solution after stirring for 2 h with each sorbent. A colourimetric method of analysis was used to determine the concentration of Cr (VI) in solution. All solutions were also analysed by ICP-OES to determine the total concentration of Cr ions and so the concentration of Cr (III) in solution was calculated by subtraction. The results are shown in Fig 5-3 and Table 5-3 .

Using AP-MWD-MCM-41, complete and selective removal of Cr (VI) was achieved at pH 3 and the Cr (III) ions remained in solution. The opposite situation was observed when the solution pH was adjusted to 9; Cr (III) was selectively removed from solution. Therefore, either Cr (III) or Cr (VI) could be selectively and efficiently extracted from aqueous solutions by simply adjusting the pH of the solution, (see Fig 5-3). Sorbent materials functionalized with DETA were also studied to compare their extraction efficiencies for both Cr (III) or Cr (VI). Despite the complete removal of both Cr species at their respective optimum pH values, it was not possible to extract Cr (VI) selectively. In conclusion it was shown that to extract Cr ions from water could be controlled by adjustment of solution pH either to pH 3 (for removal of Cr (VI) or pH 9 for the removal of Cr (III)) using AP-MWD-MCM-41.

In addition to the examination of extraction efficiencies, the loaded sorbents were also washed to assess whether it was possible to recover Cr ions from loaded sorbents and regenerate the sorbent for repeated use. The materials were washed with water at pH 9 when loaded with Cr (VI) or at pH 3 when loaded with Cr (III).

The concentration of Cr ions in wash solutions were determined as outlined in Section 5.2.3. The results demonstrated that the ions could be fully recovered from loaded sorbents, see Table 5-3. This allowed reuse of the functionalised materials making them more economically possible. It should be noted that the recovery values for Cr (III) and Cr (VI) were slightly lower when removed from DETA-MWD-MCM-41 sorbent with recovery values of less than 85 %, compared to AP-MWD-MCM-41, which had recovery values of more than 99.9 %. This makes AP-MCM-41 an ideal sorbent for the selective removal and recovery of Cr (VI) from contaminated aqueous systems and this sorbent will therefore be used in all future Cr (VI) experiments.



**Fig 5-3: The effect of pH on the removal of Cr (III) and Cr (VI) ions.**

**Table 5-3: Efficiency of adsorbents to extract 2500 µg of Cr(III) or Cr(VI) from water.**

pH	Mass (µg) of Cr (III) extracted		Mass (µg) of Cr (VI) extracted	
	3	9	3	9
	AP-MCM-41	trace/nil	2461.5	995.3
DETA-MCM-41	400.24	2487.5	1754	311.33

### 5.3.2 Characterisation of pre- and post-modified MWD-MCM-41 using FTIR and elemental analysis.

Elemental analysis (EA) was carried out using an Exeter Analytical CE440 elemental function which was used to estimate the amount of molecules ( $L_o$ ) attached to functionalised samples (AP- or DETA-MCM41) from the percentage of nitrogen, in the functionalised mesoporous silica, using Eq. 5-4; as an example for nitrogen [174]

$$L_o = \frac{\%N}{\text{nitrogen atomic weight}} \times 100 \quad \text{Eq. 5-4}$$

The calculated  $L_o$  values are listed in Table 5-4. A higher degree of functionalisation was achieved using DETA.

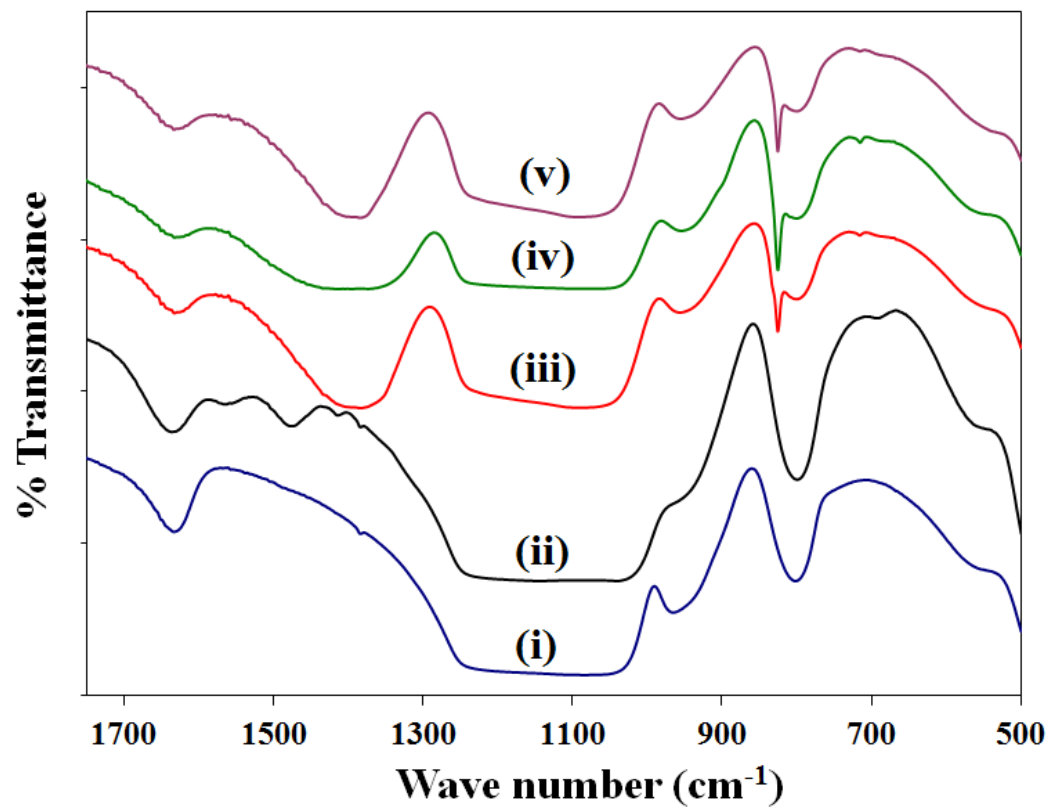
**Table 5-4: Elemental analysis data recorded for the MCM-41 samples.**

Silica	%C	%H	%N	%S	Lo (mmol/g) <sup>a</sup>
As made MCM-41	22.5	5.1	1.3	0	
MCM-41	Trace/nil	0.5	Trace/nil	0	
AP-MCM-41	8.2	2.3	2.8	0	2
DETA-MCM-41	17.1	4.2	10.1	0	7.2

<sup>a</sup> Functionalisation degree (Lo = millimoles of ligand per gram of functionalised silica).

The FTIR spectra of as-made MCM-41 and AP-MCM-41 (before and after the extraction of Cr ions) are illustrated in Fig 5-4. An absorption band observed in the range 1030 – 1240 cm<sup>-1</sup> was interpreted as stretching vibrations due to the presence of Si-O-Si bridges, while the 806 cm<sup>-1</sup> band was thought to result from the symmetric stretching vibration of Si-O. The peak at 1630 cm<sup>-1</sup> was assigned to the bending vibration of adsorbed water. After modification the surface of the MWD-MCM-41 material with amino groups, absorption bands appeared at 1470 and 693 cm<sup>-1</sup> corresponding to a symmetric stretching vibration and bending vibration of the N-H bond, respectively; thus demonstrating successful functionalization of the MCM-41 material.

After loading the sorbent with Cr (III) ions (spectrum iv) and Cr (VI) ions (spectrum iii), the N-H stretching band at 1470 cm<sup>-1</sup> disappeared and a broad peak appeared at a lower wavenumber range of 1340-1400 cm<sup>-1</sup>; this vibration was attributed to secondary C-N stretching [175,176]. Additionally, the Si-OH stretch band at 970cm<sup>-1</sup> was also shifted to 950 cm<sup>-1</sup>; indicating the influence of the associated anion with the chelate. After loading the AP-MWD-MCM-41 samples with Cr ions a sharp peak appeared at 823 cm<sup>-1</sup>, providing evidence of success Cr loading as previous work reported that the broad band at 1340-1400 cm<sup>-1</sup> was assigned to a Cr-N stretch and the sharp peak at 823 cm<sup>-1</sup> was assigned to a Cr-O vibration [177,178]. Thus, the appearance of both bands in loaded samples only confirmed that Cr ions co-ordinated with active sites on the surface of the sorbent.



**Fig 5-4: FTIR spectra of (i) MCM-41, (ii) AP-MCM-41, (iii) Cr(III)-AP-MCM-41, (iv) Cr(VI)-AP-MCM-41 and (v) Cr(III)+Cr(VI)-MCM-41.**

**5.3.3 Determination of adsorption isotherms for Cr (VI) onto AP-MWD-MCM-41 and calculation of adsorption capacity.**

In order to compare the maximum adsorption capacity of Cr (VI) onto AP-MWD-MCM-41 with other materials reported in the literature, its adsorption isotherm was calculated. Experiments were conducted as described in Section 5.2.3 and in summary are described below. Extraction experiments used 25 cm<sup>3</sup> spiked (10, 50, 100 or 200 µg cm<sup>-3</sup>) solutions of Cr (VI) and 50 mg of sorbent. The solutions were then stirred for 2 hrs. Examples of the calculations are given for the solution with starting concentration of 10 µg cm<sup>-3</sup>.

**5.3.3.1 Example calculation for determination of the Langmuir or Freundlich isotherm equations.**

The parameters used for plotting Langmuir, or Freundlich, adsorption isotherms are listed in Table 5-5. The adsorption capacity at equilibrium  $q_e$  was calculated from the initial concentrations ( $C_0$ ) and equilibrium concentration ( $C_e$ ) of Cr (VI) in the water samples and were applied to the values in (Eq. 3-2) in section 3.3.1.

**Table 5-5: Chromium (VI), parameters for plotting Langmuir or Freundlich adsorption isotherms**

$C_0$ (mg/L)	$C_e$ (mg/L)	W (g)	V (L)	$q_e$ (mg/g)	$\ln q_e$	$\ln C_e$	$C_e/q_e$ (g/L)
10	0.05	0.05	0.025	4.98	1.6	-3	0.01
50	0.4	0.05	0.025	24.8	3.21	-0.92	0.02
100	1	0.05	0.025	49.5	3.9	0	0.02
200	8	0.05	0.025	96	4.56	2.08	0.08

The values of  $q_e$  (mg g<sup>-1</sup>) and  $C_e$  were then applied into the relations expressed in (Eq.3-1) for the Langmuir isotherm and (Eq. 3-4) for Freundlich isotherm then the conformity between experimental data and the model predicted values were expressed by the correlation coefficients ( $r^2$ , values being close or equal to 1). A relatively high  $r^2$  value indicates that the isotherm model successfully describes the adsorption.



### 5.3.3.2 Resultant adsorption isotherm models for the removal of Cr (VI) from aqueous solutions.

As demonstrated by the isotherm plots given in Fig 5-5, the interaction between Cr (VI) and AP-MWD-MCM-41 had a best fit with the Langmuir isotherm model as the regression coefficient for this model was higher than Freundlich isotherm model. This indicated that 1:1 adsorption mechanism process occurred between Cr (VI) and AP-MWD-MCM-41, which describes a mono layer adsorption theory. Using experimental data, the maximum adsorption capacity  $q_m$  of Cr (VI) can be obtained from the slope of the Langmuir model as  $q_m = 1/\text{slope}$  (0.009) giving a maximum adsorption capacity of  $111.1 \text{ mg g}^{-1}$ . This result was higher than previously reported data associated with other materials that have been designed to extract Cr (VI) from aqueous systems, see Table 5-6. The calculated  $R_L$  value was 0.11 which suggested favourable adsorption properties for Cr (VI) species onto AP-MWD-MCM-41.

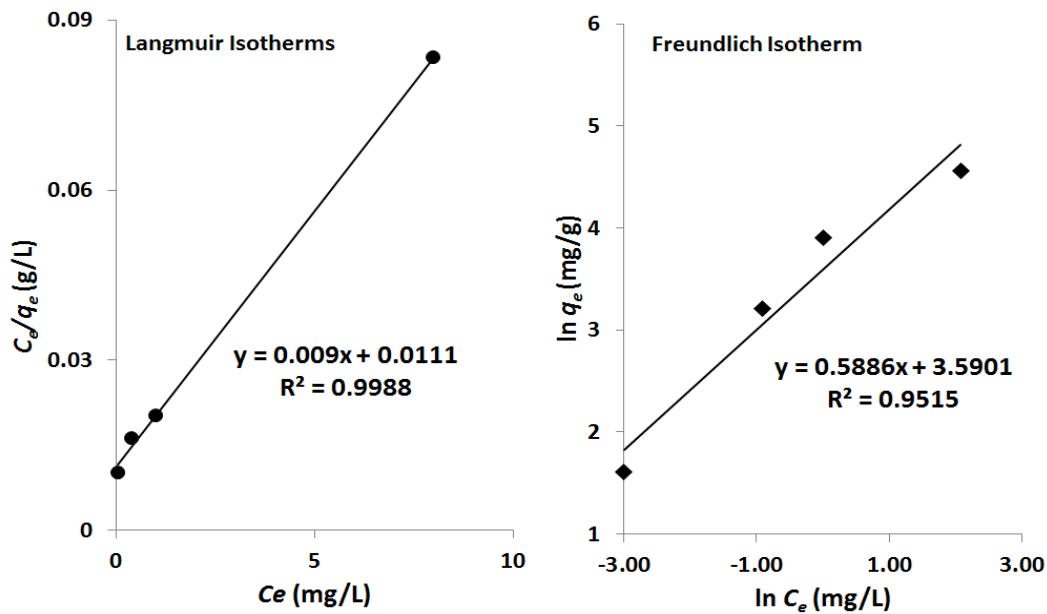


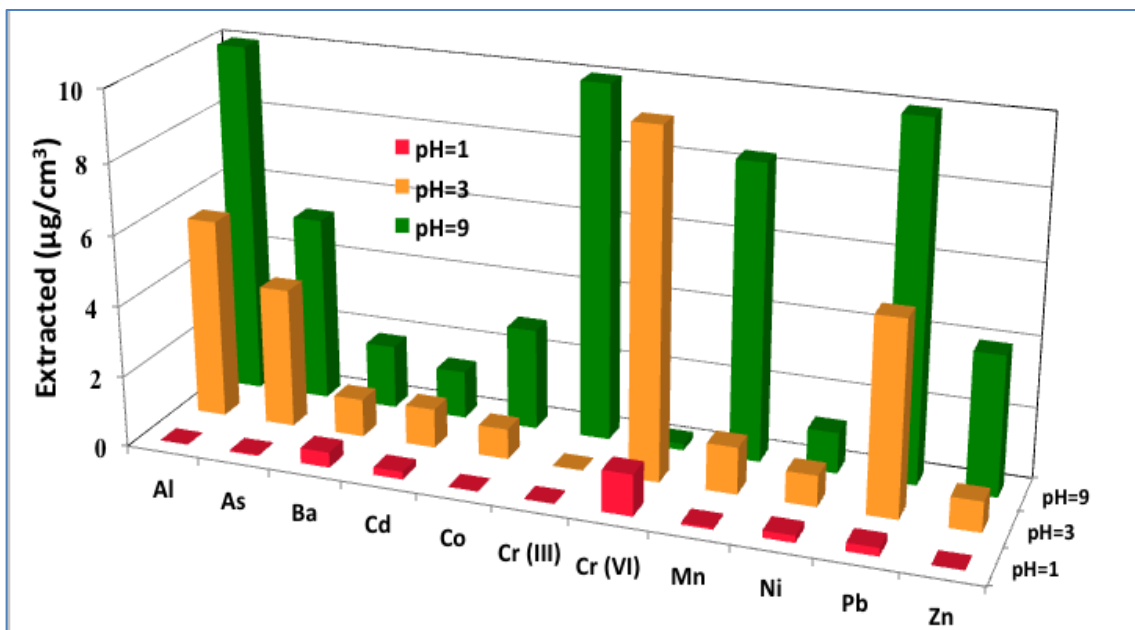
Fig 5-5: Langmuir and Freundlich isotherms for Cr (VI) adsorption onto AP-MCM-41

**Table 5-6: Adsorption capacities of AP-MCM-41 compared to other adsorbents.**

Sample	BET Surface area (m <sup>2</sup> g <sup>-1</sup> )	Maximum loading (mg/g)	Ref
Clinoptilolite	641	30	[179]
ZSM-5 zeolites	215	11	[179]
ACF	1565	22	[180]
NN-MCM-41	586	41	[181]
NN-SBA-1	606	80	[181]
AP-MCM-41	760	111	This work

### 5.3.4 Removal of Cr (VI) from contaminated, multi-element, solutions.

AP-MWD-MCM-41 has shown potential to selectively remove Cr (VI) from aqueous solution when in the presence of Cr (III) ions by adjusting the solution pH to 3, and demonstrated higher adsorption capacity values than previously reported in the literature. However if the sorbent is to be used in environmental applications its utility needs to be examined when the contaminated solution contains many other metal ions, as would be expected in the case of a river water or effluent sample. AP-MWD-MCM-41 (50 mg) was added to a 250 cm<sup>3</sup> solution containing a range of metal ions (Mn, Co, Cd, Ni, Pb, Zn, Cr (VI), Cr (III), Ba, As and Al) at a concentration of 10 µg cm<sup>-3</sup>. Three solutions were prepared at different pH value of 1, 3 or 9 and each was stirred for 2 h and the concentration of metal ions present before and after sorbent addition was determined by ICP-OES. The results obtained are illustrated in Fig 5-6.



**Fig 5-6: Effect of pH for extraction of potentially toxic metals from water using AP-MCM-41.**

When the solution pH was adjusted to 1, very little metal ions were removed by AP-MWD-MCM-41, presumably because of the a competition between protons and metal ions on the surface of the sorbent [182]. When the solution pH was adjusted to 3, the sorbent removed more than 97 % of Cr (VI) and this extraction percentage was higher for Cr (VI) than for any other metal ion present. This result was significant as it demonstrated the efficacy of AP-MWD-MCM-41 for Cr (VI) removal even when it was present in water with many other metal ions. Should the sorbent be required to remove other metal ions from contaminated solution, then the pH can be adjusted to 9 where Al, Cr (III), Mn and Pb are all removed with high efficiency which can be attributed to the fact that amino propyl is consider to be a hard ligand which co-ordinates with hard metal ion. After the AP-MWD-MCM-41 sorbent was exposed to the metal ion solution at pH 3, loading it with Cr (VI), it was washed with distilled water at pH 9. This permitted full recovery of Cr (VI) with a recovery value of 98.2 %, allowing the sorbent to be reused with a second contaminated solution. Extraction of Cr (VI) using the regenerated sorbent was again 100 %.

The ability of AP-MCM-41 to remove Cr (VI) from a spiked river water sample and a spiked tap water sample was also examined. Experimental details were given in Section 3.3.2. All samples were first analysed by ICP- OES to determine the concentration of metal ions in solution. The results are given in Table 3-1 section 3.3.2. As can be seen from the results in Table 3-1, several metal ions in the environmental water samples contained metal ions, such as Ca or Mg, at high concentration. However Cr (VI) was not measured at the limits of detection available, hence solutions were spiked with Cr (VI) to achieve a spiked solution concentration of 1  $\mu\text{gcm}^{-3}$ . After spiking, the samples were stirred with sorbent and the residual Cr (VI) ion concentrations were measured by ICP-OES. Further the loaded sorbents were then washed with water at pH 9 and the amount of Cr (VI) recovered from loaded sorbents was determined. The Cr (VI) concentrations are given in Table 5-7.

**Table 5-7: Concentration ( $\mu\text{g cm}^{-3}$ ) of Cr (VI) in filtered solutions; as measured by ICP-OES.**

<b>Sample</b>	<b>Prior to sorbent addition.</b>	<b>After sorbent addition</b>	<b>Cr (VI) recovered from loaded sorbent</b>	<b>% Recovery</b>
Tap Water	1.011	0.008	0.99	99
River water	1.005	0.011	0.97	97
Distilled Water	1.001	0.005	0.99	99

Despite the present of other metal ions with considerably higher concentrations than Cr (VI), the extraction efficiency of more than 99.9% was achieved for extraction of Cr (VI) from both solutions. This indicates that the interaction between Cr ions and the amino group was not appreciably hindered by the presence of other coordinating ions at high concentrations. These results provide further evidence for the high performance, and selectivity, of AP-MCM-41 toward Cr (VI) ions. After the removal of Cr (VI) from the water samples, the sorbents were washed with water at pH 9. The recovery efficiency of Cr (VI) was greater than 97%.

### 5.3.5 Pre-concentration of Cr (VI) from water samples.

A batch experiment was performed to assess the ability of AP-MWD-MCM-41 sorbent to pre-concentrate Cr (VI) ions from water samples, see Table 5-8. Water samples (100 cm<sup>3</sup> or 1000 cm<sup>3</sup>) were spiked with different concentrations of Cr (VI) ions (0.01, 0.1 or 1 µg cm<sup>-3</sup>) and the pH of the solution was adjusted to 3. AP-MWD-MCM-41 sorbent (25mg) was dispensed into all sample solutions and the solutions were stirred for approximately 2 h. Loaded sorbents were collected by filtration and washed with 10 cm<sup>3</sup> of 0.1 M NH<sub>4</sub>OH to remove the loaded Cr (VI) ions. The aliquots were collected and analysed by ICP-OES.

**Table 5-8: Preconcentration of Cr(VI) from water samples.**

Sample (volume used)	Cr conc. (µg ml <sup>-1</sup> )	Washed 0.1M NH <sub>4</sub> OH (10 ml)	Enrichment factor	% Recovery
Distilled Water (100 cm <sup>3</sup> )	0.011	0.112	10	111
Distilled Water (100 cm <sup>3</sup> )	0.107	1.089	10	108
Distilled Water (100 cm <sup>3</sup> )	1.002	9.703	10	97
Distilled Water (1000 cm <sup>3</sup> )	0.013	0.771	100	77

Enrichment factors of 10 and 100 were achieved with this simple pre-concentration process, permitting the sorbent to be utilised in solid phase extraction experiments (for removal or pre-concentration of Cr (VI)). This would offer the advantage that the presence of trace concentration of Cr (VI) (<0.004 µg cm<sup>-3</sup>) in solutions can be measured using by ICP-OES.

### 5.3.6 Examination of sorbent performance in packed-bed under continuous flow systems:

Although the batch extraction results provide the fundamental information related to sorbent behaviour and metal sorption performance, a continuous mode of operation would be preferred in large scale water treatment applications with perceived advantages including high yields, simple operation, easy regeneration of packed bed, and ease of scale up from a laboratory to industrial or environmental application. Hence, the extraction of Cr (VI) was also studied in continuous flow at different flow rate from 1 to 9  $\text{cm}^3 \text{min}^{-1}$ . Experimental details were given in section 3.3.3. The results shown in Fig 5-7 indicate that more than 90% extraction efficiencies, and above 80% recovery efficiencies, were achieved over the flow rate range studied.

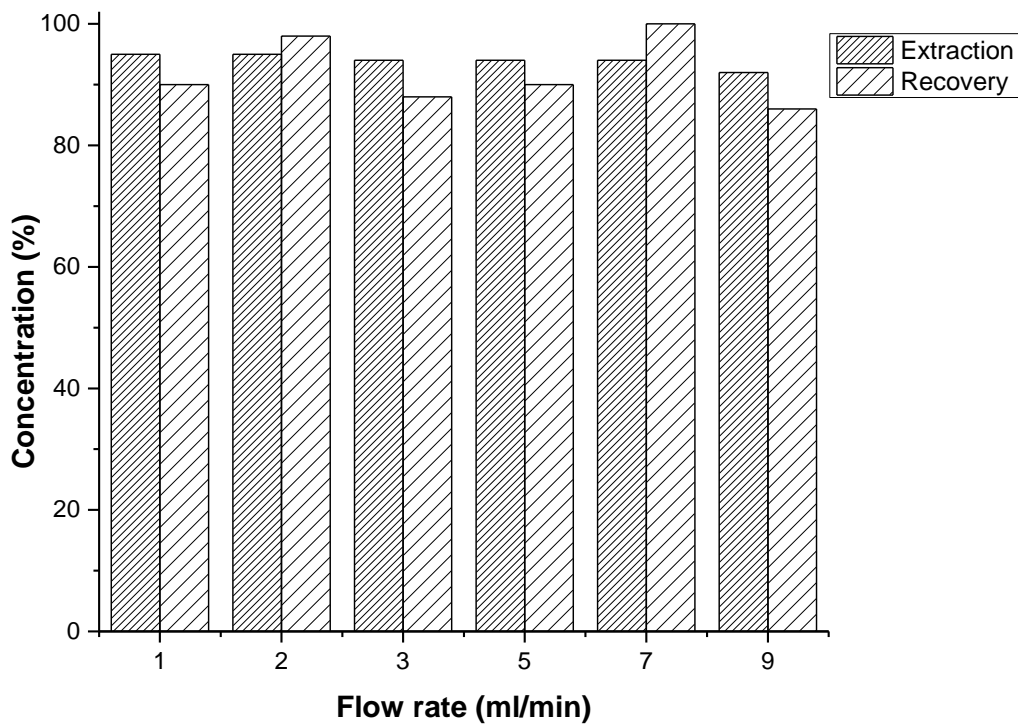


Fig 5-7: the extraction of Cr (VI) ions under different flow rate.

### 5.3.7 Kinetic study of chromium (VI) adsorption onto AP-MWD-MCM-41.

To examine the rate of removal of Cr (VI) ions from water using AP-MCM-41, six experiments were set up where 50 mg of sorbent was stirred at room temperature in a 25 cm<sup>3</sup> solution containing 1, 5, 10, 20, 30 or 40 µg cm<sup>-3</sup> of Cr (VI) ions. These initial concentrations are referred to as C<sub>o</sub>. The solutions were stirred for 10, 50, 100 or 200 min when the concentration of Cr (VI) remaining in solution (C<sub>e</sub>) were determined by ICP-OES. The measured concentrations of Cr (VI) at equilibrium (C<sub>e</sub>) at time t are shown in Table 5-9.

**Table 5-9: shows the initial concentrations (C<sub>o</sub>) and equilibrium concentrations (C<sub>e</sub>) of chromium in water.**

C <sub>o</sub> (µg cm <sup>-3</sup> )	C <sub>e</sub> (µg cm <sup>-3</sup> )					
	Time (min)	1	5	10	20	30
10	5.2	2.1	0.08	0.07	0.06	0.05
50	26	1.2	0.55	0.53	0.47	0.4
100	71	42	19	7	1.1	1
200	139	85	43	11	8.1	8

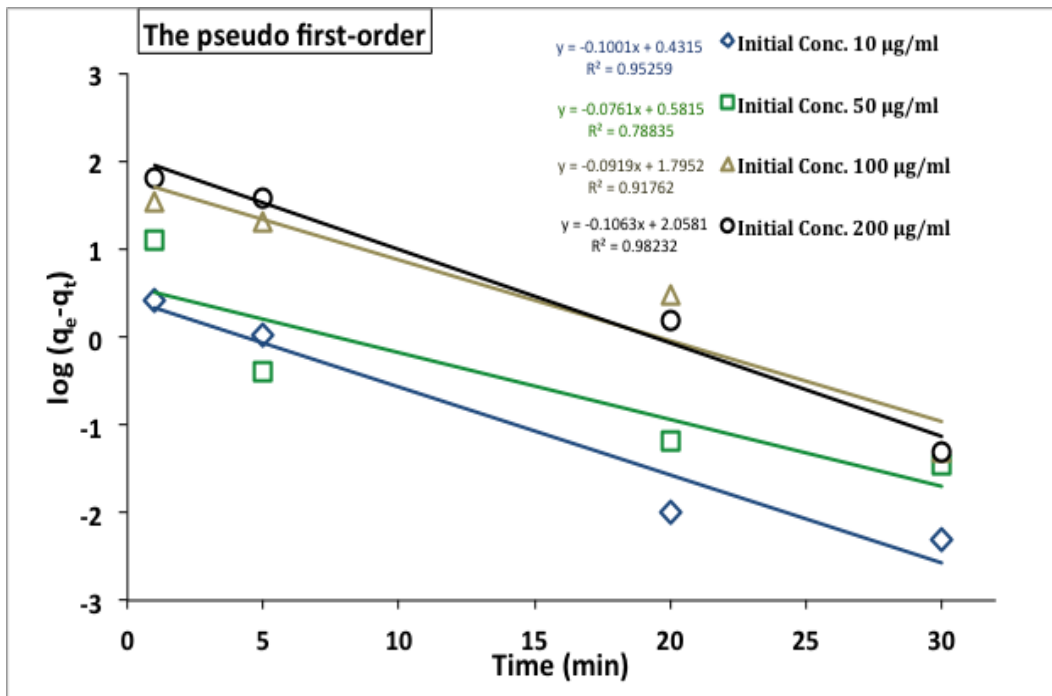
Based on the measured values of C<sub>e</sub> in Table 5-9, the adsorption capacity at equilibrium (q<sub>e</sub>) and at time t (q<sub>t</sub>) were calculated by apply those values in equation 3-2. The adsorption capacities q<sub>e</sub> and q<sub>t</sub> (mg g<sup>-1</sup>) results are given in Table 5-10:

The pseudo first-order, and pseudo second order, models were applied to the experimental data to study the adsorption rate of chromium. In the first order model the time is plotted against log (q<sub>e</sub> – q<sub>t</sub>) values, whereas in the second order model the time is plotted against t/q<sub>t</sub>. The resultant plots are given in Fig 5-8 and Fig 5-9, along with the regression curves and correlation coefficients (r<sup>2</sup>). The r<sup>2</sup> values suggested that the experimental data had a better fit to the pseudo second-order model confirming that the adsorption process of chromium (VI) onto AP-MCM-41 was more complicated than

could be explained by the pseudo first-order model, despite what has been previously reported in the literature [183].

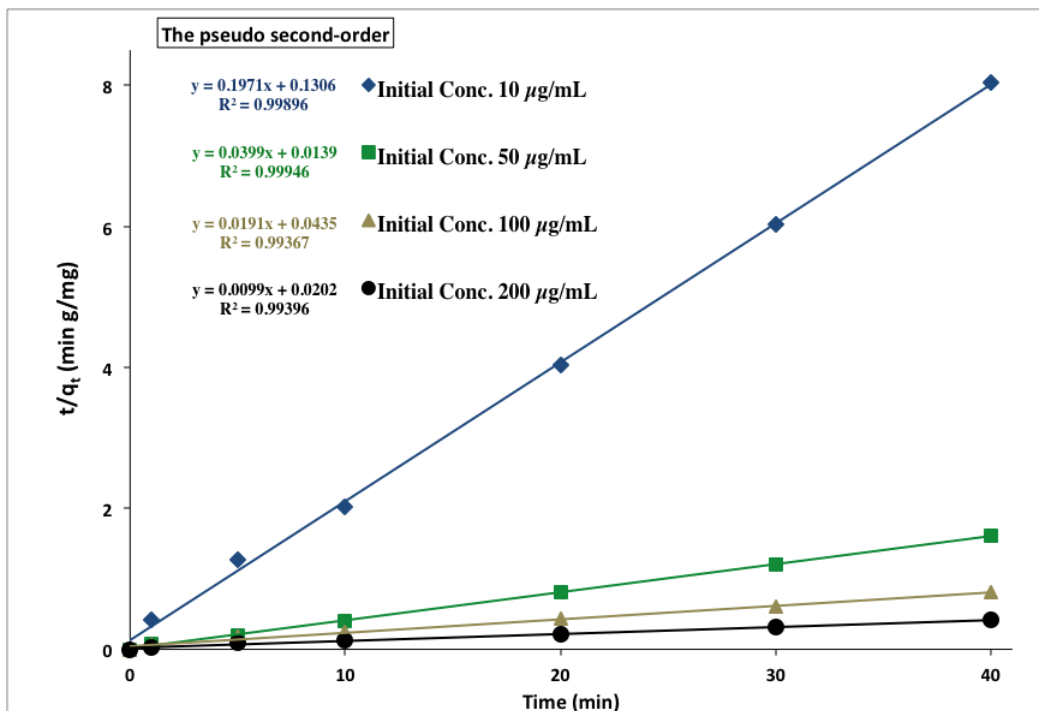
**Table 5-10: The adsorption capacity at equilibrium ( $q_e$ ) and at time  $t$  ( $q_t$ ).**

$q_t$ at 1 min	$q_t$ at 5 min	$q_t$ at 10 min	$q_t$ at 20 min	$q_t$ at 30 min	$q_e$ at 40 min
2.4	3.95	4.96	4.9	4.97	4.98
12	24.4	24.73	24.73	24.77	24.8
14.5	29	40.5	46.5	49.45	49.5
30.5	57.5	78.5	94.5	95.95	96



**Fig 5-8: Pseudo-first order kinetics models of chromium (VI) onto AP-MCM-41.**





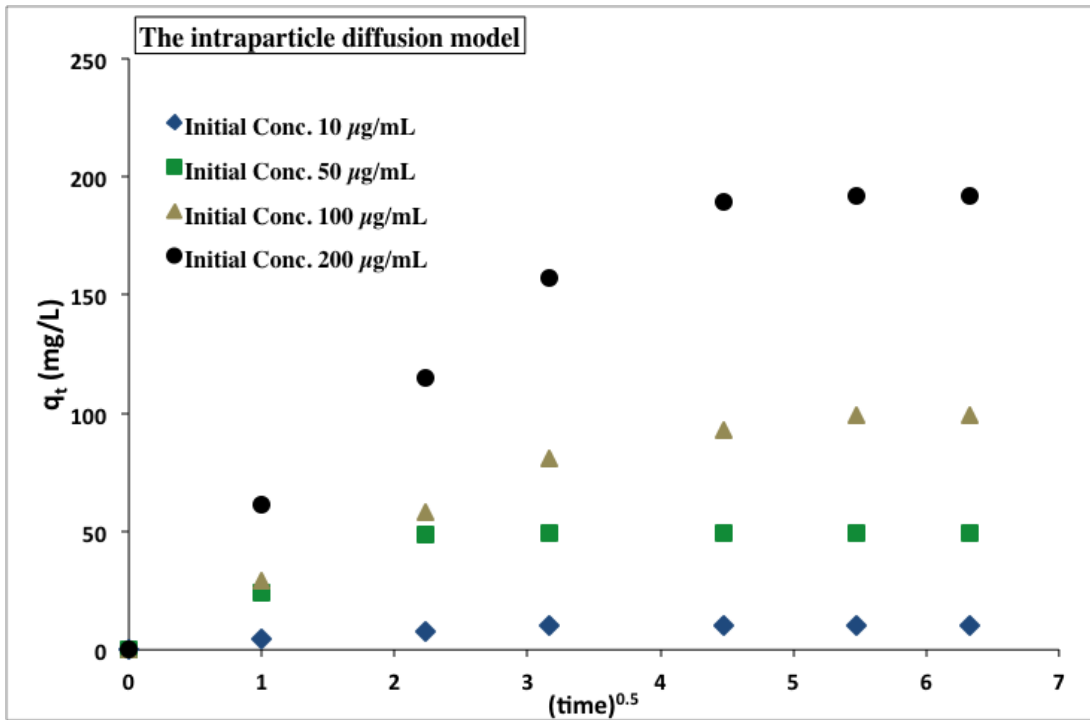
**Fig 5-9: Pseudo-second kinetic model of chromium (VI) onto AP-MCM-41.**

The first order kinetic processes indicates reversible interactions with an equilibrium being established between liquid and solid phases.[184] Whereas the second order kinetic model assumes that the rate-limiting step is most likely to involve chemical interactions resulting in binding of the ions to the surface by bonding as strong as covalent bonding. These two models have been widely tested by various workers and conformity to either of the models or both have been reported in the literature.[173]

In addition to the pseudo-first and pseudo-second order models the adsorption behaviour of Cr (VI) onto AP-MWD-MCM-41 was also examined by fitting the experimental data to the intra-particle diffusion model. In this model, time is plotted against  $q_t$ , and the results are shown in Fig 5-10. The resultant curve demonstrated two kinetic effects for the interaction between Cr (VI) and the AP-sorbent. An initial linear rate curve ( $t=0$  to  $t=10$  min) was observed and attributed to a mass transfer effect (slope= $K_{id(1)}$ ) while a second linear rate curve was thought to indicate intraparticle diffusion (slope  $K_{id(2)}$ ). This result

revealed, for the first time, two types of adsorption processes occurred between Cr (VI) and AP-MWD-MCM-41.

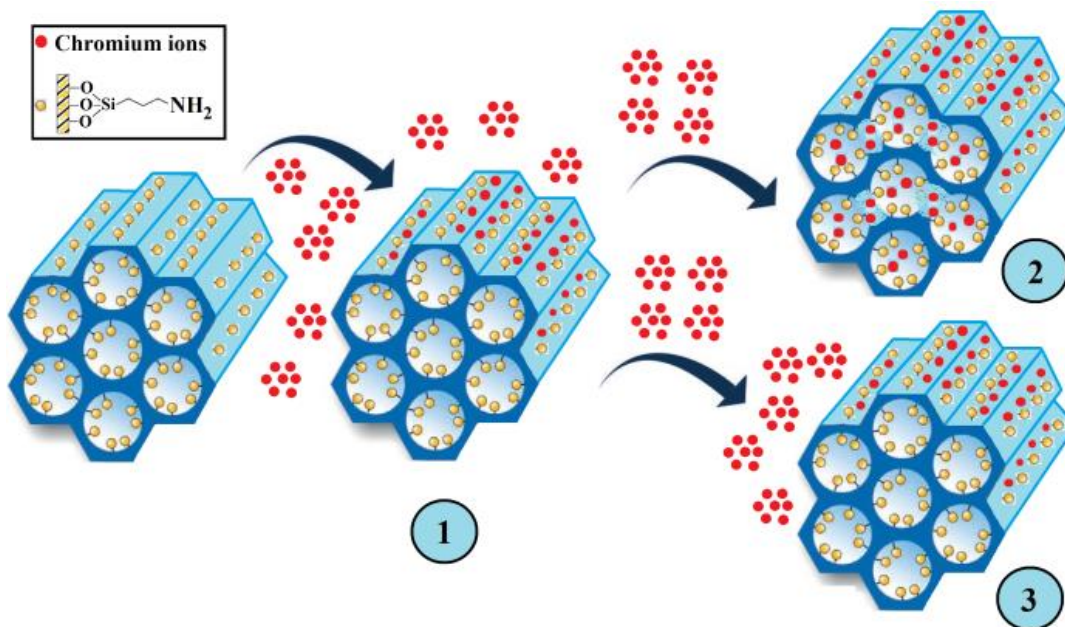
The mechanism of Cr (VI) adsorption onto AP-MWD-MCM-41 sorbent was therefore shown to be complex and involved both surface and intra-particle adsorption; both reactions mechanisms contributing to the rate determining step of adsorption kinetics.



**Fig 5-10: Intraparticle diffusion sorption kinetic model of chromium (VI) onto AP-MCM-41.**

In other words the adsorption mechanism of Cr (VI) onto AP-MWD-MCM-41 as shown to follow two steps: film diffusion at the earlier stages of the adsorption process followed by intra-particle diffusion (pore diffusion). By examination of the slopes it would appear that the rate-determining step in the adsorption process was diffusion of ions through the sorbent pores.

These results are in contrast to previously published results which reported that Cr (VI) adsorption onto functionalised silica followed the pseudo first-order reaction mechanism. Clearly this was not the case here as the measured data demonstrated. It was postulated that the different adsorption behaviour given by this material was influenced by the method utilised for the removal of the surfactant from the silica pores. There are two key proposed advantages to surfactant removal using microwave digestion: (i) the product exhibits a higher degree of functionalisation owing to the production of more silanol groups on the surface of the material and (ii) larger pores are created and functionalisation take place inside the pores channel as well as on the surface of the material. The result being that rates of adsorption were demonstrated by both surface adsorption (the faster initial rate of reaction) and chelation of metal ions in the larger pores (the second slower rate of reaction). A schematic diagram of the two different adsorption processes is illustrated in Fig 5-11 (steps 1 and 2), with the conventional adsorption process illustrated in step 3. The calculated diffusion rate parameters  $K_{id(1)}$  and  $K_{id(2)}$  are shown in Table 5-11. The value of  $K_{id(1)}$  suggested that the intra-particle diffusion process occurred at high Cr (VI) concentrations, whereas at low concentration, Cr (VI) ions were removed by amine groups on the external surface of the material. The diffusion rate parameters indicated that intra-particle diffusion controlled the adsorption rate; which was the slowest step. The results obtained by these kinetic models implied that the reaction of Cr (VI) with AP-MWD-MCM-41 was defined by a sequence of processes that contributed towards the overall adsorption rate: mass transfer of ions through the liquid surrounding the surface of sorbent particle and diffusion of ions through the particle pores. The slowest step was considered to be diffusion of ions through the sorbent pores which was observed at high concentration of Cr (VI).



**Fig 5-11:** shows three different adsorption processes: the first is film diffusion which is the initial adsorption process, the second is intraparticle transport (pore diffusion) which occurs only when the pores of MCM-41 are large enough to allow Cr (VI) to be bound to the inner surface. The third adsorption process would occur for most other MCM-41 material with smaller pores (and pseudo first order kinetic would occur).

**Table 5-11:** Rate constants of the pseudo-first order pseudo second-order and the intraparticle diffusion kinetic models.

Conc. (ppm)	The pseudo first-order		The pseudo second-order		The intra-particle diffusion model		
	$k_1$	$R^2$	$k_2$	$R^2$	$k_{id(1)}$	$k_{id(2)}$	$R^2$
10	0.23	0.9526	0.30	0.9990	3.06	---	0.9662
50	0.18	0.7884	0.11	0.9995	16.30	---	0.9182
100	0.21	0.9176	0.08	0.9937	25.34	3.32	0.9980
200	0.24	0.9823	0.05	0.9440	48.91	1.66	0.9940

### **5.3.8 The effect of pore size distribution of mesoporous silicate on the extraction kinetics of chromium (VI).**

The rates at which adsorbate (analyte ions) are transferred from the bulk solution toward the adsorbent surface where they are accumulated, determines the kinetics of adsorption and therefore, the efficiency of the adsorption process. Studying the kinetics of a chemical reaction provides a better understanding of the possible mechanism of adsorption along with the reaction pathways. The residence time of the adsorbate on the surface of the adsorbent is an important factor that determines whether or not the process will go to completion as well as to estimate the total uptake. These parameters play a significant role in designing an appropriate sorbent for the removal of different contaminants from aqueous systems.[173]

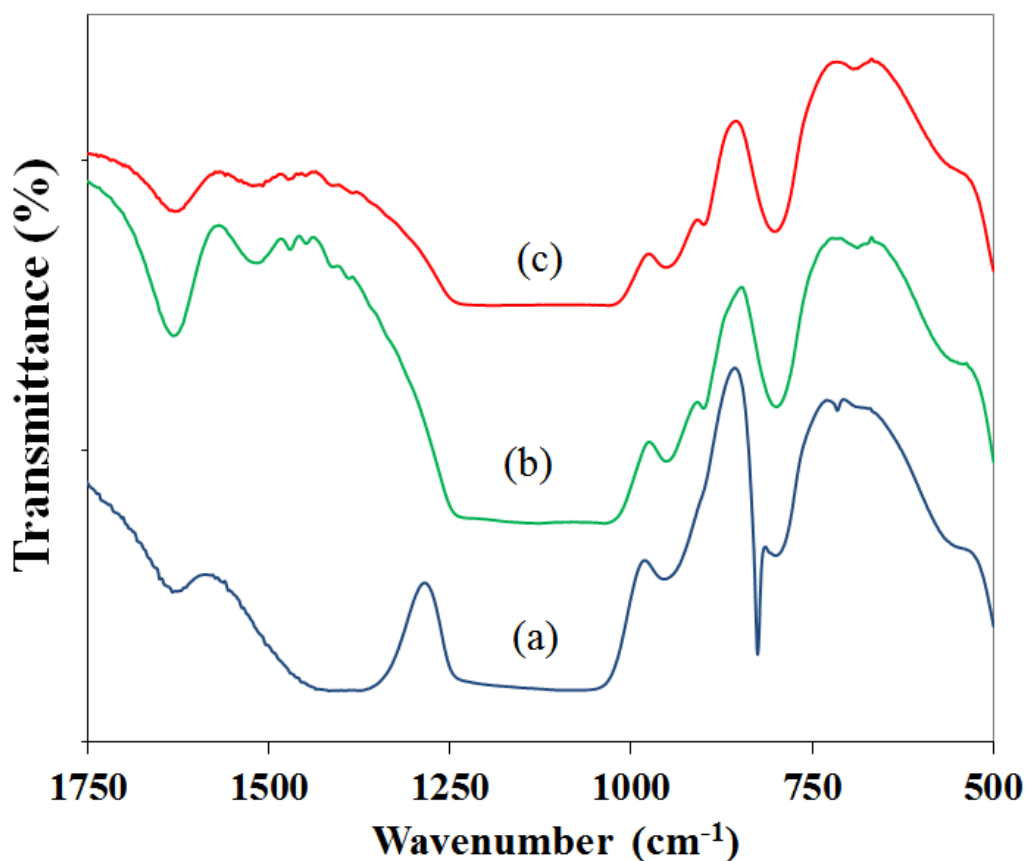
On porous adsorbents, the pore size and shape is also likely to play an important role in the rate at which the metal ions diffuse into the porous channels. Therefore, the effect of the pore size distribution on Cr (VI) ion uptake was assessed; three different types of mesoporous silica materials with different porosity and pore geometry were synthesized (SBA-15, calcined-MCM-41, and MWD-MCM-41) and functionalised with an amino propyl functional group. The sorbents were prepared as described in Section 3.2. and functionalized in Section 3.5. The kinetics of Cr (VI) adsorption on all adsorbents were analysed using pseudo-first order, pseudo-second order, and intraparticle diffusion models.

Kinetic experiments were performed as described in Section 5.2.4. In summary, A series of Cr solutions (each with a volume of 25 cm<sup>3</sup>) with concentration of 10 µg cm<sup>-3</sup> were stirred at 25 ° C in the presence of 50 mg of each adsorbent (i.e. AP-MWD-MCM-41, AP-Calcined-MCM-41, and AP-SBA-15) for 1, 5, 10, 20, 30 or 40 min. After the appropriate stirring time, solutions were filtered and Cr concentrations were measured by ICP-AES.

#### **5.3.8.1 FTIR characterisation.**

The FTIR spectra of all sorbents that were loaded with Cr (VI) are illustrated in Fig 5-12. The N-H stretch at 1470 cm<sup>-1</sup> disappeared from the spectrum of AP-MWD-MCM-41 loaded with Cr (VI) and a broad band appeared in the range 1340- 1400 cm<sup>-1</sup>; which

could attributed to a secondary C-N stretch.[176] Interestingly the N-H stretch at  $1470\text{ cm}^{-1}$  was still evident in both spectra of Cr loaded AP-Calcined-MCM-41 and AP-SBA-15. This indicted that some of the aminopropyl functional groups were not involved in the adsorption process. It was postulated that these NH- groups were present in the pores of the material. As the pores were smaller they could not accommodation Cr species and thus remained uncoordinated. A sharp peak at  $823\text{ cm}^{-1}$  was observed in the AP-MWD-MCM-41 spectrum alone. This was assigned to a Cr-O vibration. A weak band appeared with AP-Calcined-MCM-41 and AP-SBA-15 at  $893\text{ cm}^{-1}$  which can be assigned to an N-O vibration. The appearance of these peaks with AP-MWD-MCM-41 provided evidence of Cr loading with different co-ordination geometries.



**Fig 5-12: FTIR spectra of chromium loaded (a) AP-MWD-MCM-41, (b) AP-Calcined-MCM-41 and (c) AP-SBA-15.**

### 5.3.8.2 Materials characterisation by N<sub>2</sub> adsorption.

The characteristic data of the surface area, the pore volume, and the average pore diameter are summarized in Table 5-12. It was shown that the total surface area of the MWD-MCM-41 was slightly lower than the calcined-MCM-41 and that result from the small, well defined pores of the calcined-MCM-41. However, the average pore size diameter of the MWD-MCM-41 was almost three times higher than that of calcined-MCM-41 which is attributed to the joining of two or three pores together after the teardown of the pore wall. This characteristic is not normally found in MCM-41 type materials, which typically has a pore size in the range of 2.5 to 4.5nm. On the other hand, SBA-15 exhibited larger surface area as well as larger average pore size and almost had the same pore volume as MWD-MCM-41.

**Table 5-12: Physiochemical data recorded for the MWD-MCM-41, Calcined-MCM-41 and SBA-15 samples.**

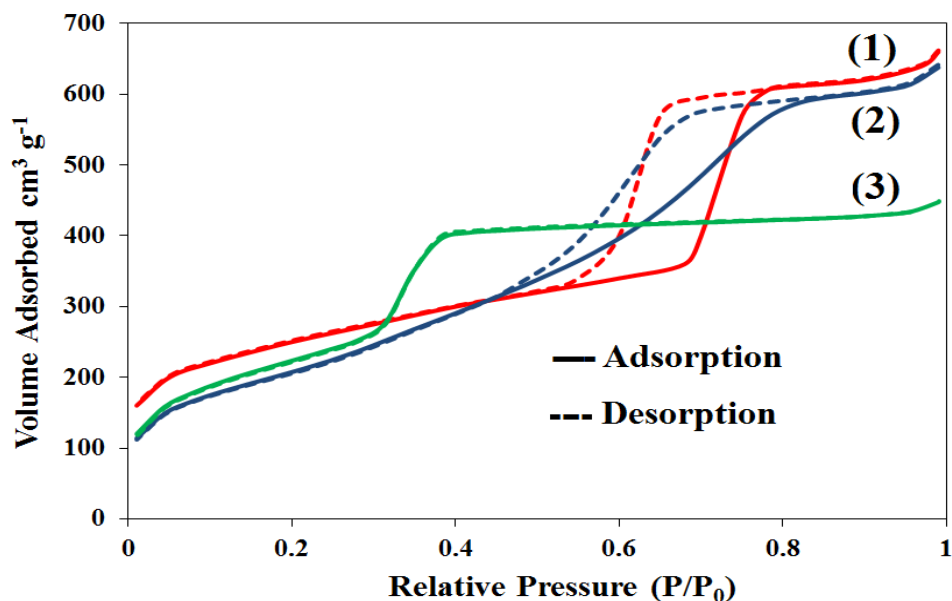
Sample Name	BET Surface Area (m <sup>2</sup> g <sup>-1</sup> ) <sup>a</sup>	Pore Size(nm) <sup>b</sup>	Pore Volume (cm <sup>3</sup> g <sup>-1</sup> ) <sup>c</sup>
MWD-MCM-41	760	6.74	0.99
Calcined-MCM-41	813	2.53	0.69
SBA-15	850	7.18	1.01

*a* Calculated by the BJH model from sorption data in a relative pressure range from 0.05–0.25.

*b* Calculated by the BJH model from the adsorption branches of isotherms.

*c* Calculated from N<sub>2</sub> amount adsorbed at a relative pressure P/P<sub>0</sub> of 0.99.

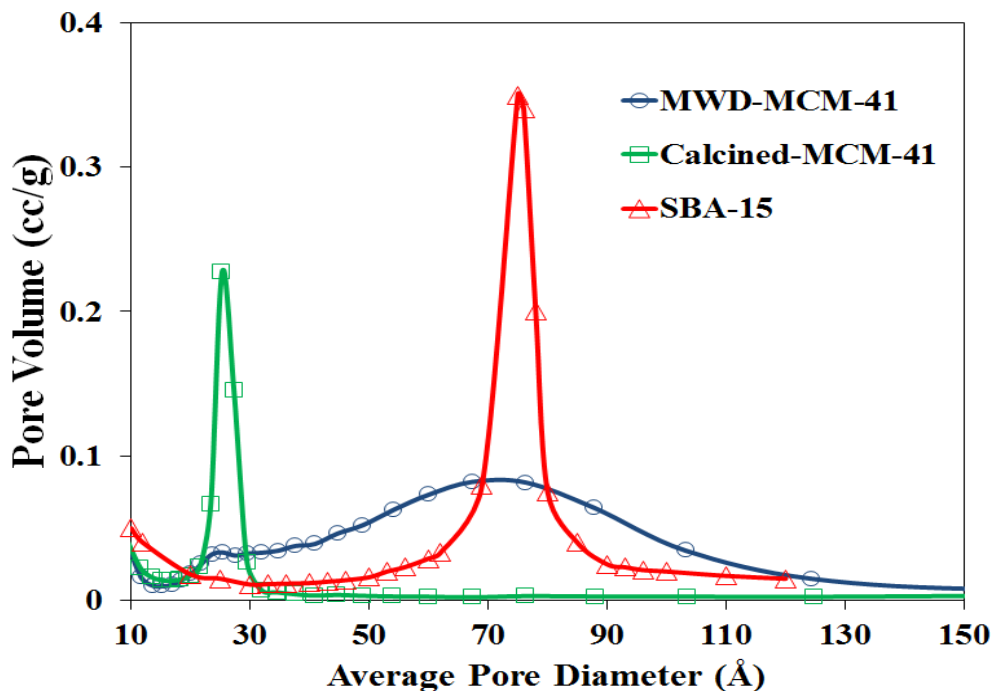
Fig 5-13 shows the nitrogen adsorption–desorption isotherms for all 3 mesoporous silica samples. All samples (SBA-15, MWD-MCM-41, and calcined-MCM-41) exhibited a type IV isotherm, according to the IUPAC classification, and had a H1 hysteresis loop that was characteristic of mesoporous materials. However, a slight difference in the capillary condensation steps were observed at higher relative pressure for MWD-MCM-41 and SBA-15 compared to calcined-MCM-41, which suggested that MWD-MCM-41 and SBA-15 exhibited larger pore size.



**Fig 5-13: : Nitrogen adsorption isotherms and mesoporous silica sorbents SBA-15 (1), MWD-MCM-41 (2) and Calcined-MCM-41 (3).**

The hysteresis loop was boarder for MWD-MCM-41 and SBA-15 indicating that these materials contained pores of different shape compare to calcined-MCM-41. This phenomenon is normally observed for SBA-15 type materials as it has both micro- and meso-pores on the surface but this feature is not commonly observed with MCM-41 type materials. It was postulated that the larger average pore size and pore size distribution found for MWD-MCM-41 was due to pore wall teardown which occurs during the intense temperature and pressures created during the microwave digestion procedure.





**Fig 5-14: BET pore size distribution patterns of the SBA-15, MWD-MCM-41 and Calcined-MCM-41.**

The pore size distribution (PSDs) of the studied samples are shown in Fig 5-14. This results provided further evidence for the hypothesis mentioned above. The MWD-MCM-41 sample showed a broader pore-size distribution (from 20 to 120 Å) than SBA-15 and calcined-MCM-41. It is postulated that the differences in the porosity geometries were, in part, responsible for the excellent behaviour of functionalised MWD-MCM-41 shown in this research when used as an adsorbent for metal ions. In addition the use of nitric acid/hydrogen peroxide was thought to induce a higher degree of silanol groups on the surface of the silica. In combination this implied that MWD-MCM-41 had 3 key features which made it suitable as an adsorbent: (i) larger pores due to pore wall teardown which make the pores more accessible to functionalization and amenable to co-ordinating metal ions and (ii) the larger pore size distribution allowing easier co-ordination and (iii) a higher degree of silanol groups which permit a higher degree of functionalization.

### 5.3.8.3 Elemental analysis.

To assess the degree of functionalization of each sample, elemental analysis was performed to evaluate the amount of molecules ( $L_o$ ) attached to functionalised samples from the percentage of nitrogen, in the functionalised mesoporous silica using (Eq. 5-4):

The calculated  $L_o$  (Table 5-13) value for AP-MWD-MCM-41 was significantly higher than those for AP-SBA-15 and AP-calcined-MCM-41 which indicated that the use of microwave digestion to remove the organic template does allow a higher degree of hydroxyl groups in the surface and then a higher ability of the material to be functionalised.

**Table 5-13: Elemental analysis data recorded for the functionalised mesoporous silica.**

Silica	% Carbon	% Hydrogen	% Nitrogen	$L_o$ (mmol/g) <sup>a</sup>
AP-Calcined-MCM-41	5.81	1.97	1.81	1.29
AP-MWD-MCM-41	8.20	2.32	2.79	1.99
AP-SBA-15	6.90	1.66	2.21	1.58

<sup>a</sup> Functionalisation degree ( $L_o$  = millimoles of ligand per gram of functionalized silica)

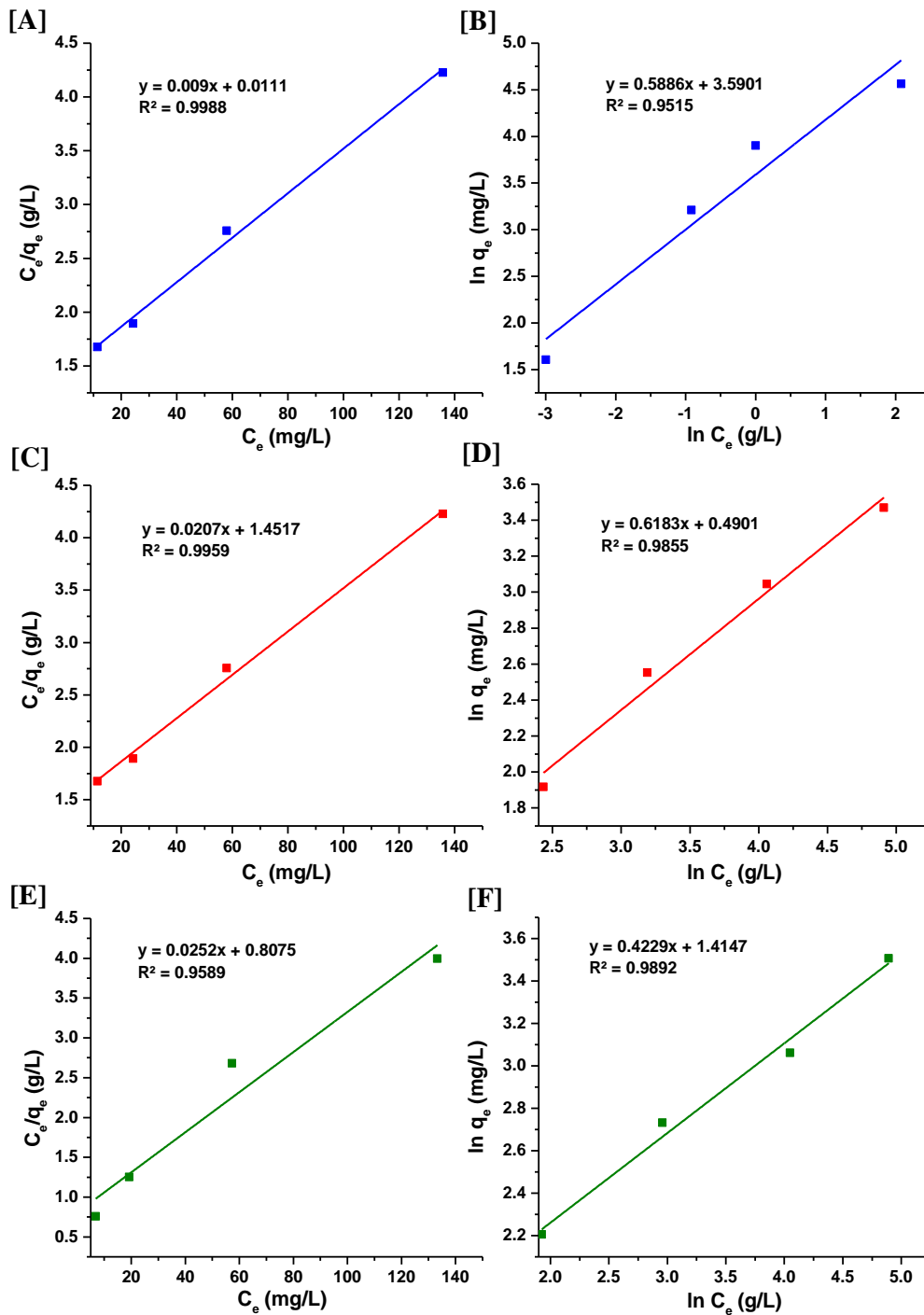
#### 5.3.8.4 Adsorption isotherms.

Kinetic experiments, as described in Section 5.3.3.2 for AP-MWD-MCM-41 were performed for AP-calcined-MCM-41 and AP-SBA-15. The same experimental procedure and calculations were performed. The experimental data were applied to the Langmuir and Freundlich isotherm models as given in Fig 5-15. Note that the results for AP-MWD-MCM-41 are given again here to aid data comparison. The calculated maximum adsorption capacities are given in Table 5-14.

**Table 5-14: Isotherm parameters for Cr(VI) sorption on functionalised mesoporous silica.**

Sample	Langmuir			Freundlich	
	$q_m$ (mg/g)	$b$ (L/mg)	$R_L$	$K_f$ (mg/g)	$n$ (L/mg)
AP-MWD-MCM-41	111.1	0.811	0.110	36.24	1.70
AP-Calcined-MCM-41	39.68	0.031	0.763	4.115	2.36
AP-SBA-15	48.31	0.014	0.877	1.632	1.62

According to the Langmuir model, the maximum adsorption capacity value obtained for AP-MWD-MCM-41 was significantly higher than the values obtained by AP-calcined-MCM-41 or AP-SBA-15. Moreover, the constant  $b$  was higher when using AP-MWD-MCM-41 which indicated that Cr (VI) has a higher affinity towards this material than the other 2 sorbents. The interaction between Cr (VI) and the surface of AP-MWD-MCM-41 and AP-SBA-15 was best explained via the Langmuir isotherm as the regression coefficients of the Langmuir isotherm plot was higher than that of the Freundlich isotherm model suggesting that the Cr (VI) was adsorbed via a 1:1 mechanism (mono layer sorption). The calculated  $R_L$  values were in the range of 0 and 1, suggesting favourable adsorption for chromium species onto all studied sorbents.



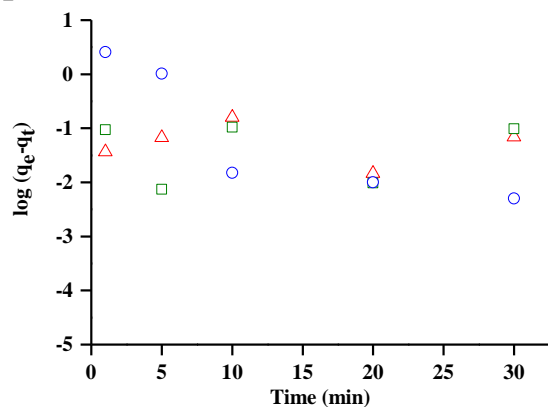
**Fig 5-15:** A, C and E show the Langmuir isotherms of AP-MWD-MCM-41, AP-SBA-15, and AP-Calcined-MCM-41 materials, respectively. Whereas figures B, D, and F show the Freundlich isotherms of AP-MWD-MCM-41, AP-SBA-15, and AP-Calcined-MCM-41 materials, respectively.

#### **5.3.8.5. Kinetic study of chromium (VI) adsorption onto AP- loaded MWD-MCM-41, Cal-MCM-41 and SBA-15.**

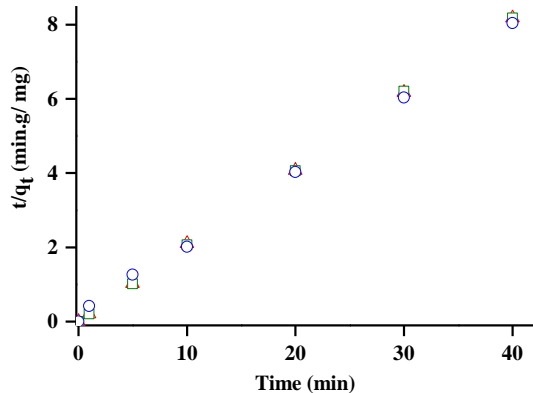
The adsorption kinetics of chromium (VI) were studied using three different models, pseudo-first-order, pseudo-second-order and intraparticle diffusion kinetic models. The results obtained from the kinetic studies are illustrated in Fig 5-16. Based on the linear regression values, the kinetics of Cr (VI) adsorption onto all sorbents reported here did not fit well with pseudo first-order model. However, more information was obtained when applying the intra-particle diffusion model Fig 5-16 C. The adsorption of chromium (VI) onto AP-SBA-15 or AP-calcined-MCM-41 involved one fast kinetic process ( $9.7$  and  $9.2 \text{ mg L}^{-1} \text{ min}^{-1/2}$ ), which suggested that the adsorption process occurred in one step until equilibrium was reached. On the other hand, two distinct kinetic regions were observed from the AP-MWD-MCM-41 plot. A faster adsorption process ( $4.8 \text{ mg L}^{-1} \text{ min}^{-1/2}$ ) took place within the first minute after adding the sorbent into the chromium (VI) solution, followed by a slower adsorption step ( $2.52 \text{ mg L}^{-1} \text{ min}^{-1/2}$ ) until equilibrium is reached.

These findings indicated that the AP-MWD-MCM-41 contained pores that were large enough to allow functionalisation and coordination with chromate ions inside the pore channel. If the intra-particle diffusion plots are examined in more detail, it was noted that the adsorption rate decreased with increasing the adsorption time when using AP-MWD-MCM-41 as an adsorbent. This phenomenon was not observed with the other two sorbents. The diffusion rate parameters suggested that, in case of AP-MWD-MCM-41, the intra-particle diffusion best described the sorption rate; where the slowest adsorption step was diffusion of the ions into the pores. But it was not the rate-controlling step for AP-SBA-15 or AP-Calcined-MCM-41 which contained smaller pore size distribution.

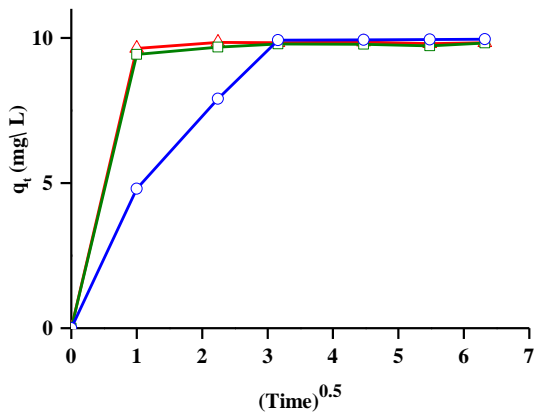
[A] △ AP-SBA-15 □ AP-Calcined-MCM-41 ○ AP-MWD-MCM-41



[B] △ AP-SBA-15 □ AP-Calcined-MCM-41 ○ AP-MWD-MCM-41

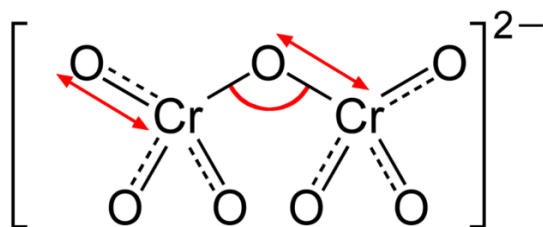


[C] △ AP-SBA-15 □ AP-Calcined-MCM-41 ○ AP-MWD-MCM-41



**Fig 5-16: Pseudo-first order (a), Pseudo-second order (b) and Intraparticle diffusion (c) kinetics models of Cr (VI) onto AP-Mesoporous sorbents**

The complicated adsorption process for the removal of Cr (VI) from the liquid phase was expected since its behaviour is poorly understood. Cr (VI) ions can form complexes which are up to 7-coordinate in solution. Dichromate dianion ( $\text{Cr}_2\text{O}_7^{2-}$ ) is considered to be the most abundant species in solutions where the pH values are in the range of 2 to 6.[185] In some cases the dichromate dianion may be found in the form of a trimer, as found, e.g. in rubidium tri-chromate or even a tetramer as found in  $\text{K}_2\text{Cr}_4\text{O}_{13}$ .[186] In addition to the various chromium species found in solution, the dimensions of the dichromate dianion were also reported to vary because of the varieties of bonds length and angles possible in this species [186] (see Fig 5-17). The geometrical parameters that chromium species have (e.g. their presence in larger molecules size as well as their ability to stretch), suggesting that AP-MWD-MCM-41 might be the only sorbent that is capable to adsorb the analyte ions both on the surface of the material, and within the pore channels. This resulted in a significantly higher adsorption capacity and enhanced performance towards chromium (VI) compared to sorbents that exhibit narrower pore size distributions.



**Fig 5-17: The theoretical structure of dichromate dianion: The Cr–O–Cr angle varies between 116.2° and 162.1°. The range for the Cr–O(terminal) bond lengths is between 1.469 and 1.777 Å. The range for the Cr–O(bridging) is 1.622–1.956 Å.[186]**

### 5.3.9 Conclusion:

AP-MCM-41 was evaluated for the removal of chromium (VI) from aqueous solution. Removal involved monolayer interaction with the chelate on the silica surface and the functionalisation, and loading, could be tracked using FTIR spectroscopy. The adsorption capacity was extremely high when AP-MCM-41 produced using a MWD method was used (compared to a production method which used calcinations) or even compared to SBA-15. Almost exclusive removal of Cr (VI) was achieved at pH 3 and moreover, the sorbent could be used to extract a wide range of other metal ions from water if its pH was modified above 7. No reduction in performance was observed even when removing Cr (VI) from water which contained other metal ions (e.g.  $\text{Ca}^{2+}$  and  $\text{Mg}^{2+}$ ) at significantly higher concentration. The ease, at which AP-MCM-41 was synthesised, tuned and regenerated all combined well to suggest that this sorbent could be used for environmental remediation, recovery of Cr (VI) from contaminated water, solid phase extraction or pre-concentration processes. Examination of the effect of pore size distribution on adsorption provided evidence that the material's extremely high adsorption capacity was due to the larger pores and surface activation. With the Cr (VI) concentration range studied here, within 10 min more than 99 % of Cr (VI) was removed from solution. The microwave digestion method provide a material with (i) higher degree of functionalisation due to the production of more silanol groups on the surface of the material and (ii) larger pores compared to the materials reported in the literature.



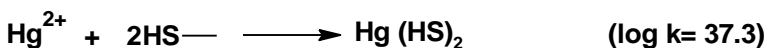
**Chapter 6 : Regeneration of mercapto- loaded MWD-  
MCM-41 using acidified thiourea**

## 6.1 Introduction

Mercury is classified as one of the most toxic and carcinogenic chemical elements and has been designated as priority pollutants by the US Environmental Protection Agency (EPA) [187]. Mercury can damage the central nervous system by entering into the human body from the food cycle.[188] It is widely dispersed throughout the environment, and can therefore destroy the functions of natural metabolism and incretion, leading to maladjustment in hormone secretion. Therefore, the determination of trace level of mercury concentration in the environment is of great interest in pollution monitoring.

Several methods have been applied for the removal of mercury from water sources, including ion exchange [189-191], flotation [192], chemical co-precipitation [193], extraction chromatography [194], electrochemical deposition [195], and adsorbents [160,174,196-199]. Of all these methods, the use of mesoporous silica materials as an adsorbent is the most widely used approach. However, without modification of the MCM-41 surface, the material cannot adsorb Hg (II) ions selectively and quantitatively at trace levels, resulting in poor Hg (II) ion removal and high interference from other coordinating ions will be encountered.

The introduction of sulfur-containing functional groups, that have strong affinities for mercury, into the mesoporous materials seems to be promising and sulfur-modified adsorbents have been explored by several workers [158,159,200-203]. However, the regeneration of the mercury-loaded thiol functionalised silica is not easily achieved due to the high equilibrium constant of the system.



Idris *et.al* [91] proposed a method for the recovery of mercury from loaded mercaptopropyl-MCM-41 using microwave digestion, with recovery values of approximately 97 % of Hg (II) from loaded sorbents. This was achieved using low-energy microwave radiation and the sorbent was anticipated to be used for up to four times. However, an alternative method of regeneration is required if the sorbent is to be regenerated in the field. Removal of Hg (II) from propylthiol-functionalised silica

material has been reported [200] using chemical treatment with 12 M HCl; this was shown to be an effective method recovering more than 90 % of Hg (II). However, the concentrated acid caused partial damage to the silica mesostructure. Moreover, the mercury ion uptake capacity dropped to about 60 % of the original value after regeneration.[204-206] Arencibia *et.al* [207] studied the regeneration of thiol-functionalized SBA-15 adsorbents of mercury using complexing agents (e.g. KBr, KSCN, CS(NH<sub>2</sub>)<sub>2</sub>, and HBr). They all demonstrated partial regeneration of the mercury-loaded adsorbent, with 1 M hydrobromic acid yielding the best result with a recovery of 65 % of loaded mercury. Zhang *et.al* [159] developed a new sorbent for trace Hg(II) removal by grafting 1-(3 carboxyphenyl)-2-thiourea (CPTU) onto SBA-15 mesoporous silica. A maximum adsorption capacity of Hg(II) 64.5 mg g<sup>-1</sup> was achieved. The regeneration experiments were conducted using different concentrations of HCl in 5% thiourea. The recovery of Hg(II) dramatically increased from 42 % to 97 % when the concentration of HCl increased from 0.1 M to 1 M.

There are currently no simple, field recovery methods that exist for the efficient removal of Hg (II) from mercapto-modified MCM-41 (MP-MCM-41). It is well known that thiourea [CS(NH<sub>2</sub>)<sub>2</sub>], and its derivatives, form aqueous complexes with Hg(II) that are more stable than other complexing agents such as chloride anions (through S bonding).[208] In this work, the removal and recovery of Hg (II) ions was conducted in both batch method and under dynamic mode using mercapto loaded MWD-MCM-41 and the sorbent was regenerated using acidified thiourea solution.

## 6.2 Experimental

### 6.2.1 Batch method

A general procedure for the extraction of Hg (II) from solution using the batch method can be summarised as follows. Approximately, 25 mg of a sample of MP-MCM-41 was suspended in 25 cm<sup>3</sup> solutions containing known concentrations of Hg (II) at a pH value of 3. Solutions were stirred (250 rpm) for approximately 2 h then filtered (Fisherbrand QL100) and the filtrate was analysed using ICP/OES. Experiments were then conducted to determine whether the Hg (II) ions could be successfully removed from the loaded sorbent. In this experiment, a 25 mg sample of Hg (II) loaded sorbent was mixed with 25 cm<sup>3</sup> of different regenerating solutions and stirred for 2h. The solutions were then filtered and the aqueous mercury concentration was analyzed by ICP-OES. The regeneration effectiveness was calculated according to equation reported by Arencibia *et al.*[207]

$$\%Regeneration = \frac{\text{Initial concentration of Hg}}{\text{Concentration of Hg at equilibrium}} \times 100$$

Samples of MP-MCM-41 were first loaded with 500 µg of Hg (II) ions and the analysis of the residual solutions (after stirring with MP- MCM-41) confirmed removal of Hg (II) by the sorbent. Samples were then known to contain 500 µg of Hg (II).

### 6.2.2 Examination of sorbent performance in dynamic mode.

A 100 mg sample of MP-MCM-41 was loaded into an empty SPE column (6 cm<sup>3</sup>) equipped with two porous frits at the top or bottom. In order to equilibrate, clean and condition the column before use, 5 % v/v HNO<sub>3</sub> solution and doubly distilled water were passed over the sorbent bed. To determine the efficacy of the modified sorbent for Hg (II) ion removal in dynamic mode, a solution containing a known concentration of Hg (II) was passed over the sorbent, the eluates were then collected in a glass tubes and the concentration of Hg (II) determined by ICP-OES. After the sorbents had removed Hg (II) ions the possibility of regenerating the sorbent and recovering Hg (II) from loaded sorbents was assessed. As the 0.1 M HCl / 5 % thiourea solution approved to be the best reagent in the recovery of Hg (II) ions using the batch method, it was chosen to assess

the recovery of Hg (II) in the dynamic mode experiments. Solutions of 0.1 M HCl / 5 % thiourea were passed through the loaded sorbents held in the SPE column. The eluates were then collected to determine the concentration of Hg (II) recovered from the sorbent.

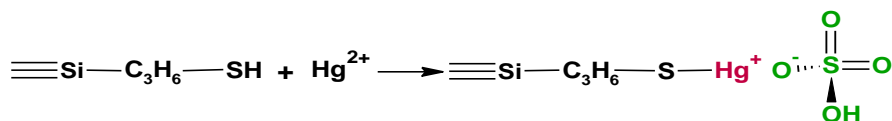
## 6.3 Results and discussion

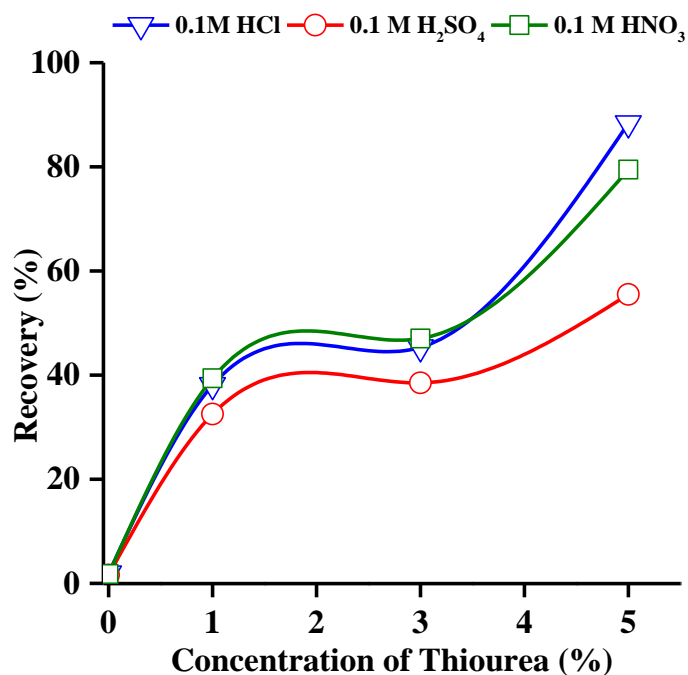
### 6.3.1 Regeneration of MP-MCM-41 adsorbents of mercury using acidified thiourea.

#### 6.3.1.1 Regeneration of MP-MCM-41 using a batch method.

Solutions of varying concentrations of thiourea prepared in different acidic media (i.e. 0.1 M of hydrochloric acid, nitric acid, or sulfuric acid) were used to examine the potential recovery of mercury ions. As shown in Fig 6-1, the use of acids alone was not able to remove Hg (II) from the mercapto- ligand, with only 1 % recovery being measured. The addition of thiourea into the acidic solutions significantly increased the recovery efficiencies, with highest recovery values of 90 % being measured for 0.1 M HCl. The effectiveness of the acidic thiourea solution in recovering Hg (II) was attributed to a double-effect: the acidic hydrogen ions competing for adsorption sites on MP-MCM-41, whilst the nitrogen and sulfur atoms of CS(NH<sub>2</sub>)<sub>2</sub> interacted with the adsorbed mercury ions. As a consequence, the coordination linkage of (Hg-MP) was easily disrupted causing the Hg(II) ions to be released into the aqueous solution [159].

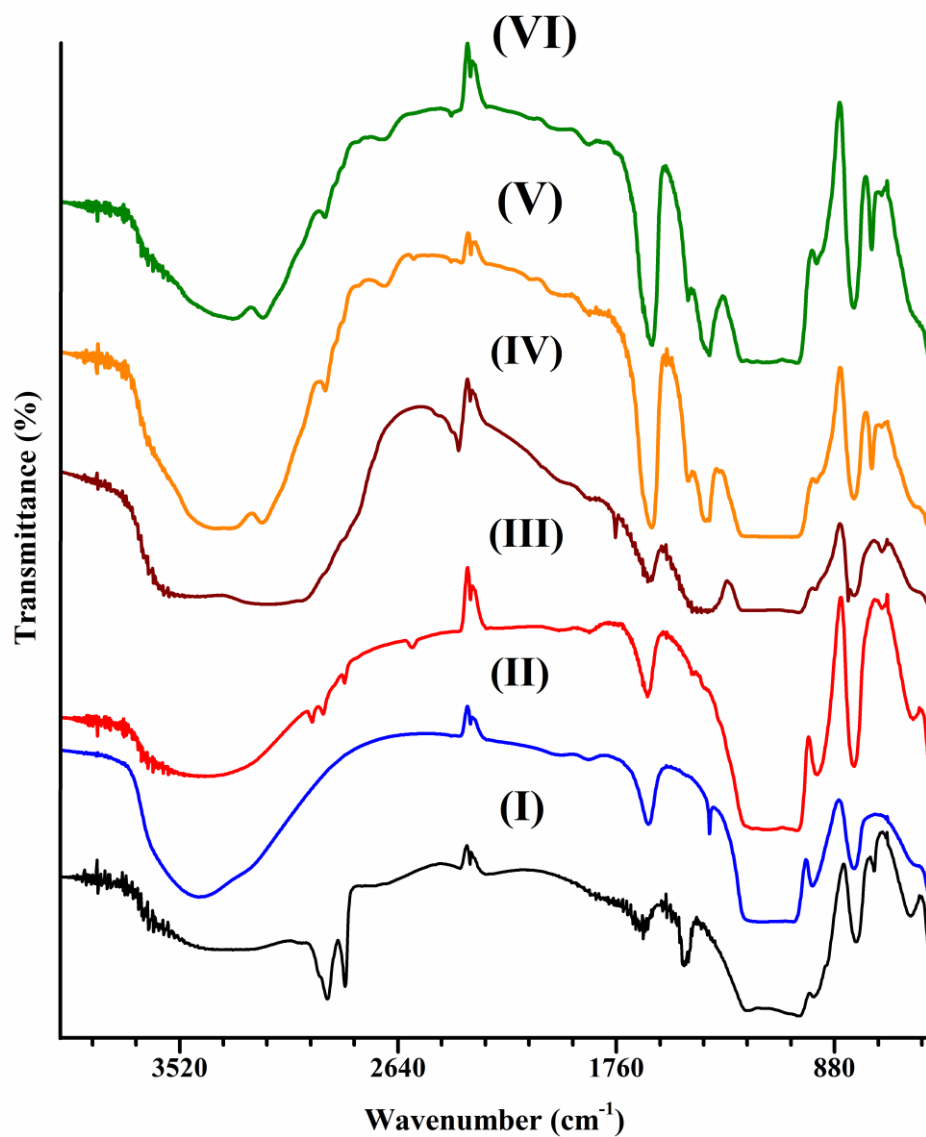
Furthermore, the recovery efficacy of mercury in the different acids medium was improved in the following order HCl > H<sub>2</sub>SO<sub>4</sub> > HNO<sub>3</sub> being HCl the most efficient with recovery efficiency of almost 90%. As indicated, the use of H<sub>2</sub>SO<sub>4</sub>/TU exhibited slightly lower regeneration efficiency than both HCl and HNO<sub>3</sub> and that may be attributed to the partial dissociation of H<sub>2</sub>SO<sub>4</sub> into the bisulfate anion (*HSO*<sub>4</sub><sup>-</sup>). Hence, as the complexation of mercury to thiol group results in the formation of a positive charge, stabilized by production of the bisulfate anion is possible as shown below.





**Fig 6-1: Regeneration of MP-MCM-41 using various concentration of thiourea in 0.1M of HCl, H<sub>2</sub>SO<sub>4</sub>, and HNO<sub>3</sub>**

In the absence of a suitable solid state NMR instrument to examine adsorbent-adsorbate interaction, all materials used in the Hg (II) regeneration work were examined by FTIR. The FTIR spectra of all samples before and after regeneration are shown in Fig 6-2. Absorbance bands at 1030–1240 cm<sup>-1</sup> were observed for Si–O–Si stretching. The O–H bond stretching bands of the silanol groups of MCM-41 were observed at 3200 – 3500 cm<sup>-1</sup>. After functionalisation the peak intensity of the -OH stretching band of the silanol group decreased. In addition, the FTIR spectrum of MP-MCM-41 had bands at 2841 and 2934 cm<sup>-1</sup> that were assigned to the C–H stretching mode, and a weak band at 2550-2600 cm<sup>-1</sup> which was assigned to the S–H stretching mode. After the modified sorbents were loaded with Hg (II) the S–H stretching mode confirming the co-ordination between S and Hg. The FTIR spectrum of the regenerated MP-MCM-41 had additional peaks that may have resulted from oxidation (autodecomposition) of thiourea over time to produce elemental sulfur.[209]



**Fig 6-2: FT-IR spectra of (I) as made MCM-41, (II) MCM-41, (III) MP-MCM-41, (IV) Hg-MP- MCM-41, (V) Re-HCl/TU-MCM-41, and (VI) Re-H<sub>2</sub>SO<sub>4</sub>/TU- MCM-41.**

### 6.3.1.2 Extraction and recovery of Hg (II) using MP-MCM-41 loaded solid phase extraction (SPE) cartridges.

To further evaluate the extraction and recovery performance of MP-MCM-41, the adsorption-desorption experiments were carried out using a SPE column. The extraction of Hg (II) was studied in continuous flow at a maximum flow rate of  $9 \text{ cm}^3 \text{ min}^{-1}$  (the flow limits of the system used). The dynamic mode experiments were conducted using only the extracting solution that provided the highest level of Hg (II) removal in the batch experiment (i.e. 5% thiourea in 0.1 M HCl). The results shown in Fig 6-3 indicate that almost 100 % extraction efficiencies, and 100 % recovery efficiencies, were achieved over the full flow rate range studied. More importantly this system involved reuse and clean-up of the same sample cartridge which (as shown in Fig 6-3 ) has been used 6 times without any detrimental effects on either extraction or Hg (II) recovery values. The high performance of this material may be due to the high affinity of mercury ions for the mercapto functional group as well as the ability of microwave digested MCM-41 to load a higher number of functional group [65].

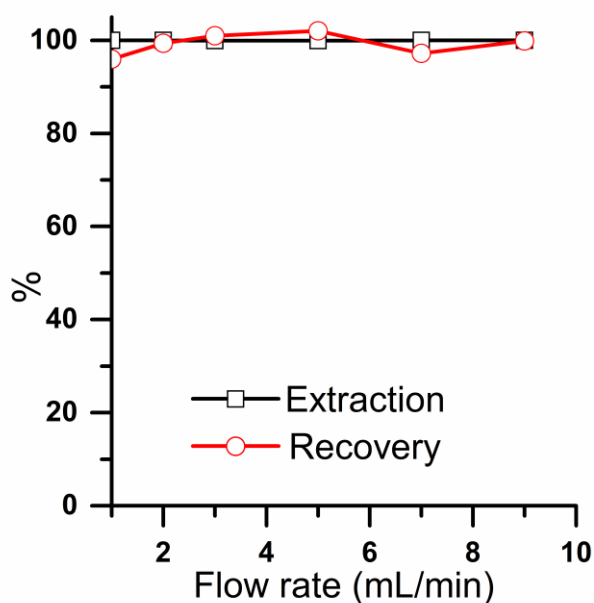


Fig 6-3: The extraction of mercury ions under different flow rate.



### 6.3.2 Preconcentration of Hg (II) using MP-MCM-41 loaded solid phase extraction (SPE) cartridges.

As the concentration of mercury in environmental water samples is usually lower than the detection limit of analytical instruments, it is generally necessary to enrich target analytes from large volume of water samples. To explore the possibility of concentrating low concentrations of mercury from large volumes of solution, four solutions containing 100 cm<sup>3</sup> of water were spiked with different concentrations of Hg (II) (from 0.01 to 1 µg cm<sup>-3</sup>) and the solution pH was adjusted to 3. Solutions that contain Hg were passed over the sorbent in the SPE column. To assess the performance of the sorbent, eluates were collected in a glass tubes and the concentration of Hg (II) determined by ICP-OES. Then, recovery of Hg (II) was examined using 10 cm<sup>3</sup> of the recovery solution (0.1 M HCl / 5 % thiourea). As shown in Table 6-1, an enrichment factor of 10 was easily achieved with this simple process indicating that the method may be of use to pre-concentrate trace amounts of Hg (II) in water samples.

**Table 6-1: Preconcentration of Hg (II) from water samples using SPE column.**

Sample	Hg concentration found (µgml <sup>-1</sup> )	Eluted with 10 cm <sup>3</sup> of 0.1M HCl/5% TU (µgml <sup>-1</sup> )	Enrichment factor	Recovery (%)
0.01ppm Hg (II)	BDL*	0.09	10	94
0.05ppm Hg (II)	BDL*	0.53		106
0.1ppm Hg (II)	BDL*	0.97		97
1 ppm Hg (II)	BDL*	10.30		102

\*BDL – below detection limit.

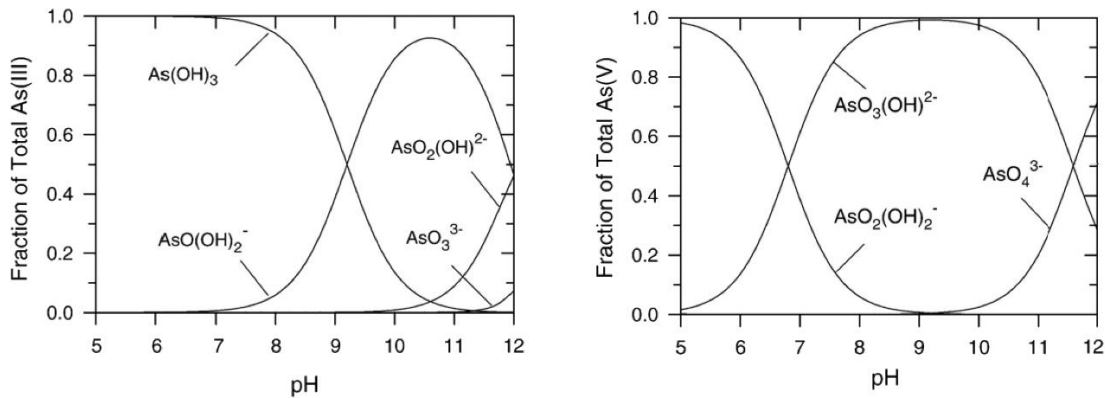
## 6.4 Conclusion

The regeneration of MP-MCM-41 loaded with Hg (II) ions was investigated with batch and dynamic methods using thiourea that was acidified using different acidic solutions (i.e. HNO<sub>3</sub>, H<sub>2</sub>SO<sub>4</sub>, and HCl); with HCl being the most efficient with recovery efficiency of almost 90 %. The dynamic method regeneration experiments were conducted using HCl / thiourea. The results indicated that a high elution efficiencies, of almost 100 % could be achieved; the high elution efficiency was attributed to the fact that the loaded sorbent was in contact continuously with acidified thiourea. Furthermore, the results indicated that it was possible to pre-concentrate Hg (II) from a large sample volume using this dynamic recovery method. In addition, the preparation of the SPE column is relatively easy and rapid. Therefore, this new developed method could be used for trace mercury analysis in environmental samples with satisfactory results.

**Chapter 7 : Synthesis of iron supported on bioinspired green silica for the removal of arsenic ions from water**

## 7.1 Introduction

The contamination of water by heavy metal ions, such as arsenic, has posed severe health problems in many countries such as Bangladesh, Canada, Cambodia, China, Hungary, India, and the USA. [210-213] Arsenic has been classified as group 1 carcinogen and chronic exposure to low arsenic levels has been linked to health complications, including cancer of the lung, kidney, skin, and bladder, as well as other potential effects include neurologic impairment.[214,215] Inorganic and organic arsenic species are found in the environment as naturally occurring substances, with inorganic forms being more abundant.[216] In natural waters, two forms of arsenic are common: arsenite and arsenate referred to As (III) and As (V), respectively. Several forms of arsenic undergo acid–base equilibria, therefore different minor and major species will be present as function of pH, as shown in Fig 7-1.



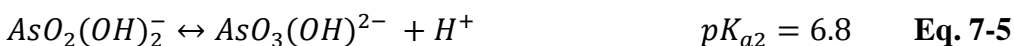
**Fig 7-1: Distribution of As (III) and As (V) hydroxide species as a function of pH at 25 °C.[217]**

The sequential dissociation of As (OH)<sub>3</sub> in water will be according to the following equations (Eq. 7-1 - Eq. 7-3)



According to Fig 7-1, at neutral pH As (OH)<sub>3</sub> is the dominant species while As (OH)<sub>2</sub>O<sup>-</sup> is present as small fraction (< 1%).

As (V) is triprotic acid (Eq. 7-4 - Eq. 7-6)



At neutral pH, almost equal concentration of  $AsO_3(OH)^{2-}$  and  $AsO_2(OH)_2^-$  will be present, Fig 7-1. Whereas at low pH value (pH < 2) As (V) will be present as H<sub>3</sub>AsO<sub>4</sub>. [217]

As (III) is usually more mobile and toxic than As (V) due to its high affinity for the sulfhydryl groups of biomolecules such as glutathione-S-transferases (GST) and lipoic acid-containing enzymes. [217,218] As (III) is difficult to remove from water using techniques such as ion exchange, coagulation/precipitation, or reverse osmosis.[219] Therefore, the removal of As (III) is usually carried out by first oxidizing it to As (V) and then As (V) can be removed using various adsorption techniques using adsorbents including iron oxides, activated alumina, activated carbon and polymer resins.[220,221] The air oxidation of As (III) was found to be a very slow process taking weeks for full oxidation to take place.[222] Hence, the reaction of As (III) oxidation should be catalysed, in order to convert As (III) to As (V) within the time scale of few minutes. Kin and co-workers,[223] investigated the oxidation of As (III) in ground water using oxygen and ozone. The results showed that when iron was present, the reaction occurred very quickly. This was due to iron and oxygen at neutral pH producing H<sub>2</sub>O<sub>2</sub>, which rapidly oxidised As (III) to As (V).[215,223]

One of the common methods used for the removal of arsenic species is by adsorption onto amine- or thiol- surface modified silica materials. [224-227]. Yoshitake *et al.*[181] studied the influence of amine group density on the extraction of arsenate ions via exposing arsenate solution into mono-, di-, tri amino functionalized silica materials, the

results show that increasing the number of amine group resulted in improvements in the adsorbent performance.

The use of iron loaded mesoporous materials have also been shown to be a potential sorbent for the removal of arsenic species from contaminated aqueous solutions.[228] Jeon *et.al* [229] studied the adsorption of arsenate ions using iron-coated zeolite (ICZ) as adsorbent. The results obtained indicated that As (V) was completely removed within 30 min (at a concentration of  $2 \mu\text{gcm}^{-3}$ ). Zhu *et.al* [230] synthesised nanoscale zero-valent iron supported onto activated carbon and it was evaluated for the adsorption of As (III) and As (V), a maximum adsorption capacity of 18.2 or 12.0 mg/g was achieved for As (III) or As (V).

Previous sections of this thesis have demonstrated similar successful removal of metal ions from water using surface modified mesoporous materials (such as MCM-41 or SBA-15). However, it was thought that, although the adsorbents performed very well in extraction experiments, the use of conventional syntheses methods might lead to further environmental problems. For example, the unused initial reactants that remain in discarded solutions, (including the silica, organic templates, and the corrosive solutions) will contribute to severe health and environmental impacts.[231,232] Furthermore, care needs to be given to the use of alkoxysilanes which can cause acute toxicity. Finally, after months of experience working with mesosilica materials it became apparent that the synthesis procedures were lengthy (11 – 72 h), involved various steps, required high temperatures and extremes of pH (80-120°C and pH~1). Thus, faster, cheaper and greener synthesis routes, taking into consideration the whole life-cycle of mesoporous silica materials from extraction of the raw material to disposal at the end of their life, were explored to provide alternative cost effective, reusable silica adsorption platforms for removal of As from water.

The new methods explored were based on the production of silica using bioinspired *green* routes which mimic the biosilicification process.[233,234] since bioinspired synthesis routes have been shown to be simpler to perform and use milder conditions.[235] The biomolecules involved in biosilica formation have been used to establish synthetic “additives” which are effective for producing silica on a laboratory scale.[236] Additives

can significantly affect the process of silica production and often act as catalysts, hence allowing the process to be carried out rapidly, and under milder conditions.[237] Furthermore, bioinspired methods allow a better control over chemical and physical properties of the products and offers the possibility of one-pot green synthesis of hybrid materials such as optical and catalytic materials.[238]

In this work bioinspired silica will be prepared with and without inclusion of iron ions. There has been increased interest in the use of iron as a reductive agent to decontaminate a wide range of pollutants including polyaromatic hydrocarbons (PAHs), chlorinated aliphatic hydrocarbons (CAH), nitroaromatic compounds (NAC), inorganic ions (nitrates and phosphates), organic dyes and pesticides and heavy metal ions.[239-243] The use of nano-iron particales has also received a great attention due to its large active surface area and high arsenic adsorption capacity.[228] When used in a nanoparticle form, the small particles size (1-100 nm) of iron contributes to high surface area and hence better decontamination. Moreover, iron has been reported to be flexible in both *in situ* and *ex situ* remediation systems.[244] However, the problem of aggregation of iron was observed which leads to the declined in iron reactivity.[245] In addition, this material usually appears as fine powders, hence cannot be applied in water treatment system because of the fast loss of the iron particles in drinking water.[230] Therefore, it is necessary to load the iron nanoparticles onto materials with high surface area such as zeolite, activated carbon, and mesoporous silica.[229,230,246] Various studies showed that the aggregation of iron was reduced by introducing support materials such as clay mineral, polymers, ceramics and porous carbon which increased the surface area of iron in addition to rendering improved stability and better dispersion of iron and hence increased the efficiency for catalytic decontamination.[247-251]

These supported catalysts are typically prepared in a two-step process: synthesis of the support followed by catalyst (iron) loading on the support, usually via adsorption or co-precipitation.[250] In the one-step procedure, the supported catalyst is produced in a single step, whereby the iron nanoparticles and the silica gel are produced simultaneously. This has been accomplished by a variety of methods, such as arc-discharge,[252] sol-gel,[253] micro-emulation,[254-256] reactors,[257] or low pressure

flames.[258] Among these methods, a sol-gel technique followed by processing at elevated temperatures was the most widely used. Typically, the iron precursor was first mixed with a silica source (tetraethylorthosilicate) in ethanol and gelation was allowed to occur over several days before the filtration step. The materials was then heated to the desired temperature to obtained the desired iron oxide phase (  $\alpha$ - ,  $\gamma$ - , or  $\epsilon$ -Fe<sub>2</sub>O<sub>3</sub>-SiO<sub>2</sub>).[259-262] In the two-step procedure, both silica gel and iron nanoparticles were produced first and the encapsulation process was performed later.[263-266] Although the one-step procedure is the most widely used compare to the two-step procedure, the one-step procedure suffers from a major disadvantages, including the use of surfactants, reactors, or stabilizer to improve the dispersion process. It is well known that these chemicals are not easily removed, hence it was not suitable for some uses such as in biomedical applications.[255]

In summary, in this chapter a simple, fast, and green synthetic route of porous silica materials encapsulated with iron was assessed. The iron supported by silica was synthesised using a bio-inspired route drawing the inspiration from the bio-silicification process. Furthermore, the Fe-GN material was reduced using a reducing agent in order to obtain zero-valent iron as several studies reveal that zero-valent iron has shown high affinity toward the removal of organic and inorganic contaminants that present in the aqueous solutions. [267-271] Although the preparation of nanoparticles encapsulated in silica using bioinspired routes has been demonstrated for quantum dots, iron oxide particles and gold particles,[272-275] iron supported on silica – hereafter referred to as (Fe-GN) has not been reported before, let alone for applications in environmental remediation. The novel iron supported on the green silica nano particles (Fe-GN) were characterised in order to determine their chemical, textural and surface properties, to aid refinement of synthesis conditions. The new materials were examined, for the first time for As removal, together with determination of the adsorption capacity, effect of extraction pH, regeneration of the sorbent and applicability for clean-up of environmental samples. The effectiveness of these GN were also assessed in a packed-bed column under continuous flow of As contaminated water. Finally, the potential of GN in treating real polluted water samples were examined.



## 7.2 Experimental

In order to evaluate the difference between the synthesis regimes of conventional mesoporous silica with bioinspired green nanoparticles (GN) the reaction conditions are compared in Table 7-1. Before evaluating the performance of GN for water treatment and arsenic removal, the material's physical and chemical properties were investigated

**Table 7-1: Comparison between the synthetic conditions for Fe-MS and Fe-GN.**

	Conditions	Fe-MS	Fe-GN
Step 1	<i>Chemicals</i>	Alkoxysilane, surfactant, ethanol	Sodium silicate, additive, iron precursor, water
	<i>T, t, pH</i>	60-100°C, 2-5 days, pH2 or 10	20°C, 15 min, pH7
Step 2	<i>Chemicals</i>	Iron precursor, acetone or ethanol	n/a
	<i>t</i>	5-24h	n/a

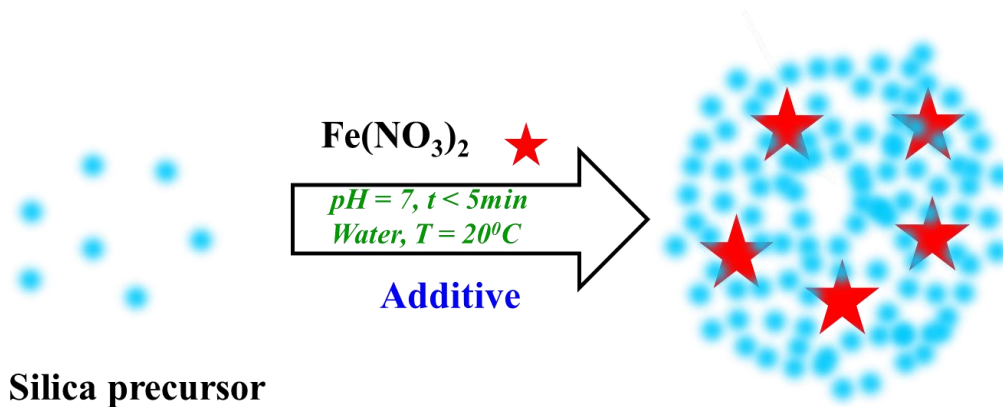
### 7.2.1 Material and reagent

Sodium metasilicate ( $\text{Na}_2\text{SiO}_3 \cdot 5\text{H}_2\text{O}$ , Fisher Scientific), pentaethylenhexamine (PEHA,  $\text{C}_{10}\text{H}_{28}\text{N}_6$  Sigma Aldrich), iron nitrate (Sigma Aldrich), hydrochloric acid (HCl, 36 wt.%, Fisher Scientific), borohydride solution ( $\text{NaBH}_4$  Sigma Aldrich), sodium arsenate dibasic heptahydrate (99.995%, Sigma Aldrich), nitric acid ( $\text{HNO}_3$ , 65 wt.%, Fisher Scientific) and ethanol absolute (Sigma Aldrich) were used as supplied. Glassware was soaked in 5%  $\text{HNO}_3$  overnight and cleaned with deionised water before use. Deionised water was used throughout this work.

### 7.2.2 Synthesis of Fe-GN

The synthesis of bioinspired silica, GN, was performed as outlined in section 3.1.3. Briefly, a solution of sodium metasilicate in deionized water was acidified using 1 M HCl and mixed with a solution of PEHA and, if required, the final solution pH adjusted with 1M HCl to  $7.0 \pm 0.1$ . The final concentration of silicate and amine were 30mM. The resultant as-synthesized precipitate was collected after 15 min by filtration, washing three times with deionized water, and drying in air at room temperature.

In order to synthesise iron containing GN, approximately 6 g of iron nitrate was dissolved in water than was added to the silicate-PEHA mixture immediately before the pH was set to 7 to obtain 1:2 Fe:Si ratio (50% Fe/Si). After mixing the solution pH was adjusted to  $7.0 \pm 0.1$  as above. The solution was left for approximately 15 min producing as-synthesized iron-silica precipitate which was collected by filtration, washing three times with deionized water, and drying in air at room temperature (hereafter referred to as “as made Fe-GN”) before calcination at  $550\text{ }^{\circ}\text{C}$  for 5 h, to produce Fe-GN. Another set of samples of different iron to silica ratio were prepared by dissolving an amount of 0, 0.6, 1.2, 2.44 and 3 g of iron nitrate in water prior to the addition to the silicate-PEHA mixture to obtain 0, 5, 10, 20, 25% of Fe/Si samples, respectively. A schematic diagram which illustrates the material is given in Fig 7-2.



**Fig 7-2: A schematic diagram of the synthesis of Fe-GN sorbent.**

### **7.2.3 Reduction of GN:**

0.5 M of sodium borohydride solution was added in excess to Fe-GN and the solution was left to react for 1 h. Since the reduction reaction will produce hydrogen gas, the cap of vial was removed frequently to avoid pressure build up. The solution was centrifuged for 15 min at 8000 rpm and the supernatant was disposed. The reduced Fe-GN were then washed with ethanol and centrifuged. This method was repeated twice and the particles were dried in oven at 85 °C for 2 h to produce R-Fe-GN.

### **7.2.4 Synthesis of iron loaded MCM-41.**

Iron loaded MCM-41 was synthesised for the sake of comparing its performance with the new Fe-GN material and it was synthesised as follow, approximately 8.8 g of CTAB was dissolved under slight warming (35 °C) in a mixture of 208 cm<sup>3</sup> of distilled H<sub>2</sub>O and 96 cm<sup>3</sup> of aqueous NH<sub>3</sub>. To this clear solution, 40 cm<sup>3</sup> of TEOS (approximately 0.2 moles of Si) was slowly added under stirring followed by the addition of 25 cm<sup>3</sup> of 20 % w/w iron nitrate (0.012 moles of Fe), to give a Si/Fe ratio of approximately 16%. [276] After further stirring for 4 h, the gel was aged at room temperature for 24 h in a closed container. The product was obtained by filtration, washed with 600 cm<sup>3</sup> of distilled H<sub>2</sub>O, and dried in air at room temperature the sample was then calcined at 550 °C (hereafter referred to as Fe-MCM-41). Reduction of Fe-MCM-41 was done using the method described in section 8.2.4 and the obtained material was dried in oven at 85 °C for 2 h to produce Fe-MCM-41-R. The surface of MCM-41 was also functionalised with and without iron using mercapto using the method described in section 3.1.4 to produce MP-Fe-MCM-41 and MP-MCM-41.

### **7.2.6 The efficiencies of sorbents in real water samples**

To evaluate the environmental performance of sorbents with real samples, a river water sample and a tap water sample were analysed as outlined in section 3.2.2. The river and tap water samples were known to contain high concentrations of metal ions, but not arsenic and so they were spiked to produce solutions containing 1 µg cm<sup>-3</sup> of As (V). In each experiment 25 mg of Fe-GN was added to solutions which were stirred for 2 h. Then the solutions were filtered and the aliquots were analysed by ICP-OES to examine the extraction efficiency. Then the material was washed with 0.1 M sodium hydroxide to

examine the possibility to recover metals ions from the sorbent after extraction.

### 7.2.7 Adsorption isotherms for the maximum adsorption capacity evaluation

To study the maximum adsorption capacity of arsenic on the prepared GN, the Langmuir and Freundlich isotherm models were applied to experimental data. Extraction experiments used 25 cm<sup>3</sup> spiked solutions (40, 60,80 or 100 µg cm<sup>-3</sup>) of As (V) and 50 mg of each GN adsorbent. Solutions were held at 20 ° C, pH 3 and stirred at 250 rpm for 120 min. The amount of As (V) extracted at equilibrium;  $q_e$  (mg/g) was calculated according to the following equation:

$$q_e = \frac{C_0 - C_e}{W} V \quad (1)$$

Where  $C_0$  and  $C_e$  (mg/cm<sup>3</sup>) are the liquid phase initial and equilibrium concentrations of As (V) ion respectively.  $V$  is the volume of the solution (cm<sup>3</sup>) and  $W$  is the mass of sorbent (g) used.[277] The sorption equilibrium data of As (V) onto Fe-GN were analysed by fitting the data to Langmuir and Freundlich isotherm models summarised in Eqs. (2) and (3) respectively.[278]

$$q_e = \frac{b q_m C_e}{1 + b C_e} \quad (2)$$

Where  $q_e$  (mg/g) and  $C_e$  (mg/dm<sup>3</sup>) are the equilibrium concentrations of As (V) in the adsorbed and liquid phases, and  $q_m$  (mg/g) and  $b$  (L/ mg) are the Langmuir constants and  $q_m$  is the maximum monolayer capacity.

$$q_e = K_f C_e^{1/n} \quad (3)$$

where  $K_f$  (mg/g) and  $n$  (L/mg) are the Freundlich constants, which are related to the sorption capacity and intensity of adsorption, respectively. For predicting the favourability of an adsorption system, the Langmuir equation can also be expressed in terms of a dimensionless separation factor ( $R_L$ ) by using the Langmuir constant  $b$  and the initial concentration of As (V)  $C_0$  (see Eq. (4)).

$$R_L = \frac{1}{1 + C_0 b} \quad (4)$$

When,  $R_L > 1$ ,  $R_L = 1$ ,  $0 < R_L < 1$  and  $R_L = 0$ , indicates unfavourable, linear, favourable and irreversible, adsorption isotherms, respectively. [123,124]

### 7.2.8 Characterisation and analysis

Nitrogen adsorption–desorption isotherms were collected using a Micromeritics ASAP 2420 surface area and porosity analyser after sample degassing for 6 h at 200 °C. The Brunauer–Emmett–Teller (BET) surface areas were calculated using experimental points at a relative pressure ( $P/P_0$ ) of 0.05–0.25. The total pore volume was calculated from the  $N_2$  amount adsorbed at the  $P/P_0$  of 0.99, and the average pore size distribution of the materials was calculated using the Barret–Joyner–Halenda (BJH) model from a 28-point BET surface area plot. Desorption isotherms were used to calculate the pore diameters.

Elemental analysis was carried out using an Exeter Analytical CE440 elemental function to provide the functional group (carbon and nitrogen) and hydrogen content of the studied materials. Attenuated total reflectance Fourier transform infrared spectroscopy (ATR-FTIR) data were obtained using an ABB MB3000 combined with the Horizon MB™ FTIR software, which facilitated acquisition, processing and analysis of samples. A small amount of sample, approximately 1 mg was placed on the diamond sample holder and spectra were acquired at a resolution of  $4 \text{ cm}^{-1}$  with 32 scans. The deconvolution of silica peaks was performed using Grams programme. The transmission  $^{57}\text{Fe}$  Mössbauer spectra were collected using a Mössbauer spectrometer in a constant acceleration mode with a  $^{57}\text{Co}(\text{Rh})$  source. The isomer shift values were related to metallic  $\alpha\text{-Fe}$  at room temperature (RT). The measurements were performed at RT and 5 K in a zero external magnetic field and at 5 K in an external magnetic field of 5 T, applied parallel to the direction of the gamma-rays propagation. Low temperature and in-field measurements were obtained using a cryomagnetic system by Oxford Instruments.

X-ray photoelectron spectroscopy data were obtained using a Thermo Electron Corporation ESCA Lab 250 instrument with a chamber pressure maintained below  $1 \times 10^{-9}$  mbar during acquisition. A monochromated Al  $K_\alpha$  X-ray source (15 kV 150 W) irradiated the samples, with a spot diameter of approximately 0.5 mm. The spectrometer was operated in Large Area XL magnetic lens mode using pass energies of 150 and 20 eV for survey and detailed scans, respectively. The spectra were obtained with an

electron takeoff angle of  $90^\circ$ . Charge compensation was applied using a low energy flood gun. High-resolution spectra were fitted using Advantage (Thermo VG software package) peak fitting algorithms.

## 7.3 Results and discussion

### 7.3.1 Materials characterisation

#### ***7.3.1.1 Iron loading efficiency and nitrogen adsorption isotherms analysis:***

An initial investigations using iron loading from 0-50% indicated a gradual increase in the surface area from  $\sim 20 \text{ m}^2 \text{ g}^{-1}$  to  $\sim 240 \text{ m}^2 \text{ g}^{-1}$  with increasing iron loading, and typically samples with higher iron content exhibited higher pore volumes.[280] It is likely that since a mild room temperature aqueous synthesis method was used here, the solution chemistry of iron and its interactions with silicate may influence the properties of the final product. These possibilities are further explored in later sections. Nevertheless, it was clear that for attaining high porosities in this material, a high iron content was required, mutually beneficial qualities for pollutant removal and as a result, in the report, we decided to focus on 50% iron loaded samples in order to allow systematic investigations.

Five silica samples were assessed for removal of As (V) from solution: three contained Fe at a 50 % loading (as made Fe-GN, Fe-GN and R-Fe-GN) and two without iron (as made GN and GN). The samples prepared without Fe both demonstrated Type II isotherms, with the GN samples also illustrating a H4 hysteresis that was attributed to the presence of a small amount of mesopores (Fig 7-10 C&D). The results obtained from the BET analysis of the nitrogen adsorption experiments for the samples are summarised in Table 7-2. The as made GN had the lowest surface area at  $12 \text{ m}^2 \text{ g}^{-1}$  (and no pore volume or pore size, presumably due to template inclusion), which increased significantly as expected to  $347 \text{ m}^2 \text{ g}^{-1}$  after the removal of the bioinspired additive to produce a material with a pore size and pore volume of  $3.5 \text{ nm}$  and  $0.23 \text{ cm}^3 \text{ g}^{-1}$ . When iron was incorporated into the synthesis mixture the silica framework of GN appeared to greatly alter. The type IV  $\text{N}_2$  sorption isotherms given in (Fig 7-10 A&B) suggest that all GN containing Fe were mesoporous. Even without the removal of the template, as made Fe-

GN had a surface area of  $\sim 244 \text{ m}^2/\text{g}$  and an average pore size of  $\sim 18 \text{ nm}$ ; the latter being an interesting and remarkable feature that can provide accessibility to bulky analytes. This phenomenon is likely to provide a significant advantage to GN family of materials over conventional materials such as Fe-mesosilica which require the removal of the organic template in order to attain any useful surface area. This characteristic of as made Fe-GN could be attributed to the influence of the  $\text{Fe}^{3+}$  ions on silica condensation reactions, producing a significantly different microstructure compared to the as made GN.

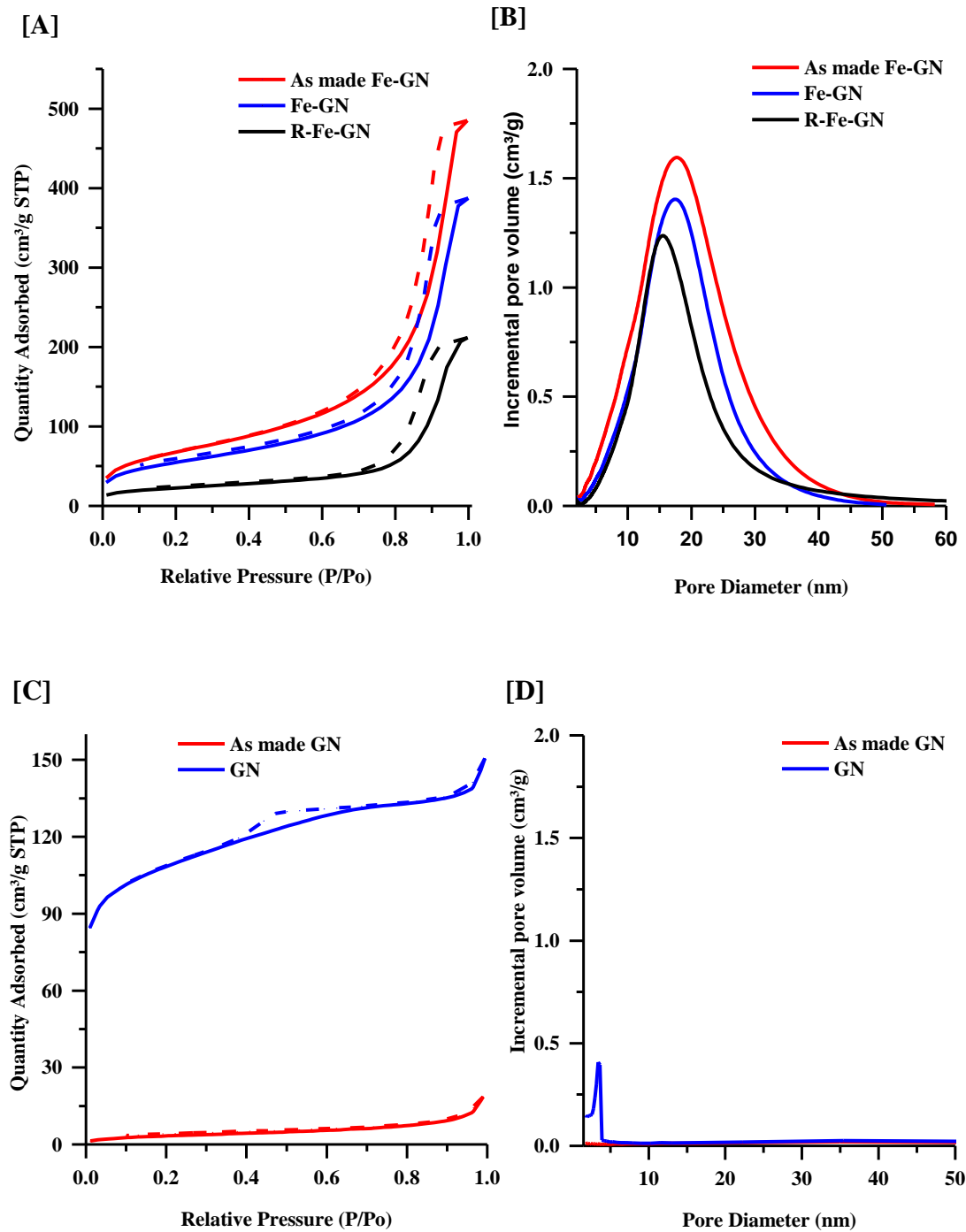
**Table 7-2: Porosity data for GNs and Fe-GNs.**

Sample	Surface area ( $\text{m}^2 \text{ g}^{-1}$ ) <sup>a</sup>	Pore size (nm) <sup>b</sup>	Pore volume ( $\text{cm}^3 \text{ g}^{-1}$ ) <sup>c</sup>
as made GN	12	Nil	Nil
GN	347	3.5	0.2
as made Fe-GN	244	18.6	0.8
Fe-GN	203	18.6	0.6
R-Fe-GN	129	18	0.5

<sup>a</sup> Calculated by the BET model from sorption data in a relative pressure range from 0.05 to 0.25.

<sup>b</sup> Calculated by the BJH model from the desorption branches of isotherms.

<sup>c</sup> Calculated from  $\text{N}_2$  amount adsorbed at a relative pressure  $P/P_0$  of 0.99.



**Figure 7.1: Nitrogen adsorption (–) desorption (···) isotherms (A,C) and pore size distribution (B,D) for GN with (a,b) and without (c,d) iron.**



### 7.3.1.2 Elemental (CHN) analysis

Further quantification of the chemical composition of the samples was performed using Elemental (CHN) analysis (**Table 7-3**). The presence of nitrogen and carbon in the air dried samples confirmed that these samples retained PEHA (samples as made GN and as made Fe-GN). Interestingly, when the samples with and without iron were compared, the amine loading reduced from 4.49 for as made GN to 2.66 mmolg<sup>-1</sup> for as made Fe-GN (reduction in both N and C content; **Table 7-3**). This implied that the presence of iron in the synthesis solution has an effect on amine loading. This can be explained from ionic interactions: both amine and iron being cationic they compete with each other for anionic silica sites. Calcination appeared to completely remove PEHA; the carbon content reduced to undetectable levels (GN vs. Fe-GN). Furthermore, the reduction by sodium borohydride seem to have increased the hydrogen content, perhaps through hydration of the samples, although the exact reason for this increase was not known.

**Table 7-3: Elemental analysis data recorded for the GN samples**

Sample	% C	% H	% N	L <sub>0</sub> (mmol/g) <sup>a</sup>
as made GN	9.4	3.1	6.3	4.5
GN	0	1.1	0	
as made Fe-GN	5.3	2.9	3.7	2.7
Fe-GN	0	0.2	0	
R-Fe-GN	0	1.1	0	

<sup>a</sup> degree of residual PEHA (L<sub>0</sub> millimoles of nitrogen per gram of silica)

### 7.3.1.3 X-ray Photoelectron Spectroscopy (XPS)

In order to further investigate the composition of inorganic components and the oxidation state of iron, XPS analyses were performed. XPS analysis provided the evidence of silicon and iron in the samples (Table 7-4 and Fig 7-3 a). The Si 2p peak was consistent with the silicon oxide bond. Upon chemical reduction of samples using sodium borohydride, residual sodium and boron were detected for R-Fe-GN but not for as made-Fe-GN. Iron content in as made-Fe-GN was 3 at% with Fe:Si atomic ratio of 0.11. 50 wt% Fe in silica samples corresponds to ~9 at% with an atomic ratio of Fe:Si calculated to be ~ 0.5. This difference between the iron content expected and measured by XPS could be attributed to the fact that XPS is a surface specific technique with sub-micron penetration depth. Since iron is loaded in situ, it is more likely that it will be present in the bulk of the sample and not only on the surface. Reduction in total iron and silicon content upon reduction was coupled with increased oxygen and hydrogen (Table 7-4 and Table 7-3) content, consistent with the possibility of hydration upon reduction. Further analysis of the Fe2p1 peak for the R-Fe-GN (Fig 7-3 b) indicated that most of the Fe species are likely to be either in the Fe<sup>+2</sup> or Fe<sup>+3</sup> oxidation state, while the lack of a strong satellite peak suggests it is more likely Fe<sup>+3</sup>. A weak shoulder at binding energy of 707 eV indicates the presence of very little amount of Fe<sup>0</sup> metal, if any. This result is surprising because it was expected that upon chemical reduction, most of the iron will be converted to zero valent metal. These results were further validated by using Mössbauer spectroscopy.

**Table 7-4: Elemental quantification obtained from XPS analysis.**

Element	BE (eV)	Atomic %	
		<i>As made-Fe-GN</i>	<i>R-Fe-GN</i>
O	530	19	37
Na	1070	0	5.8*
Fe	710	3	1.2
B	191	0	8.9*
Si	101	26	9.2

\**From reducing agent – sodium borohydride.*

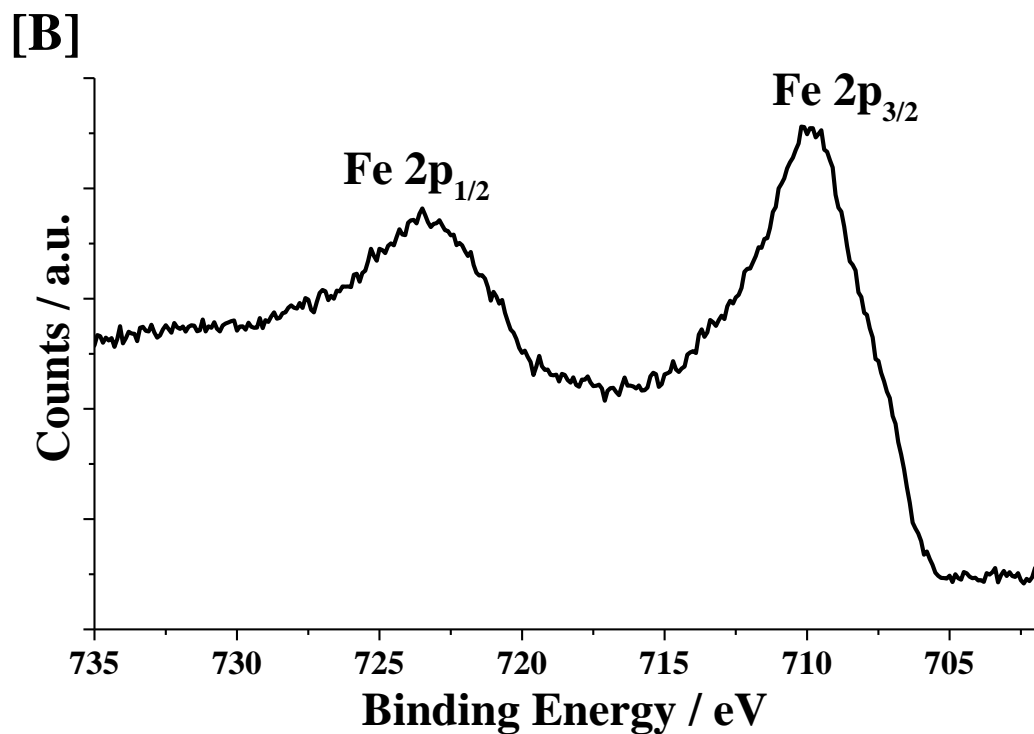
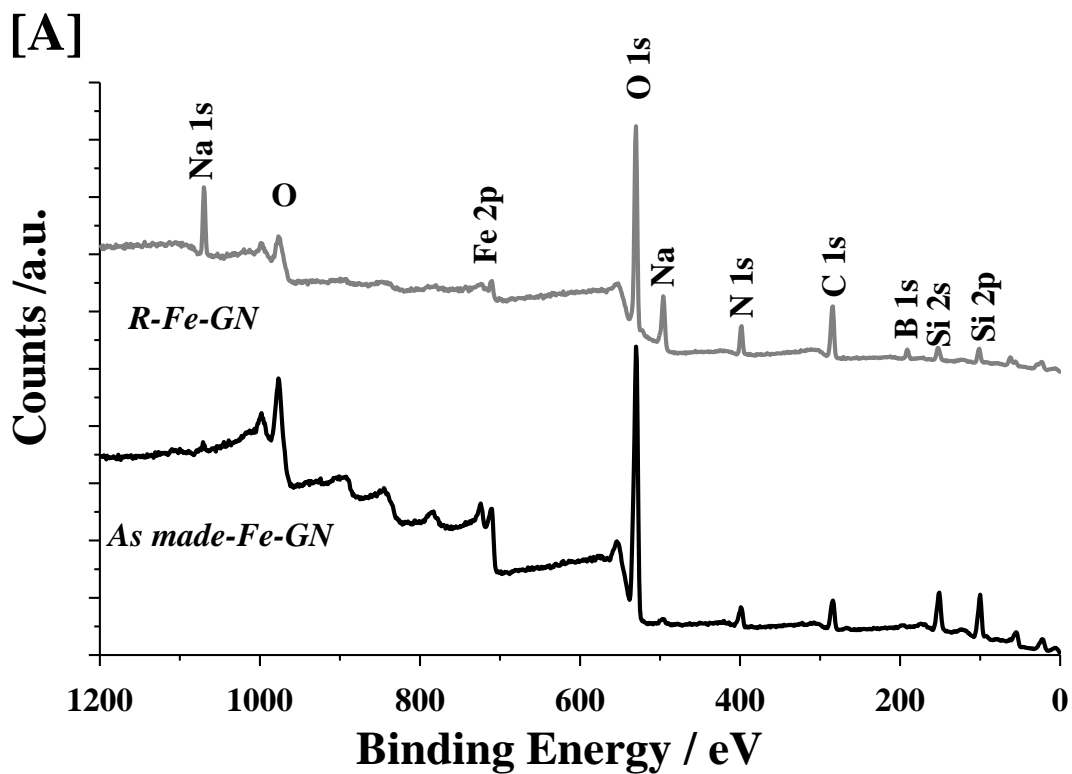


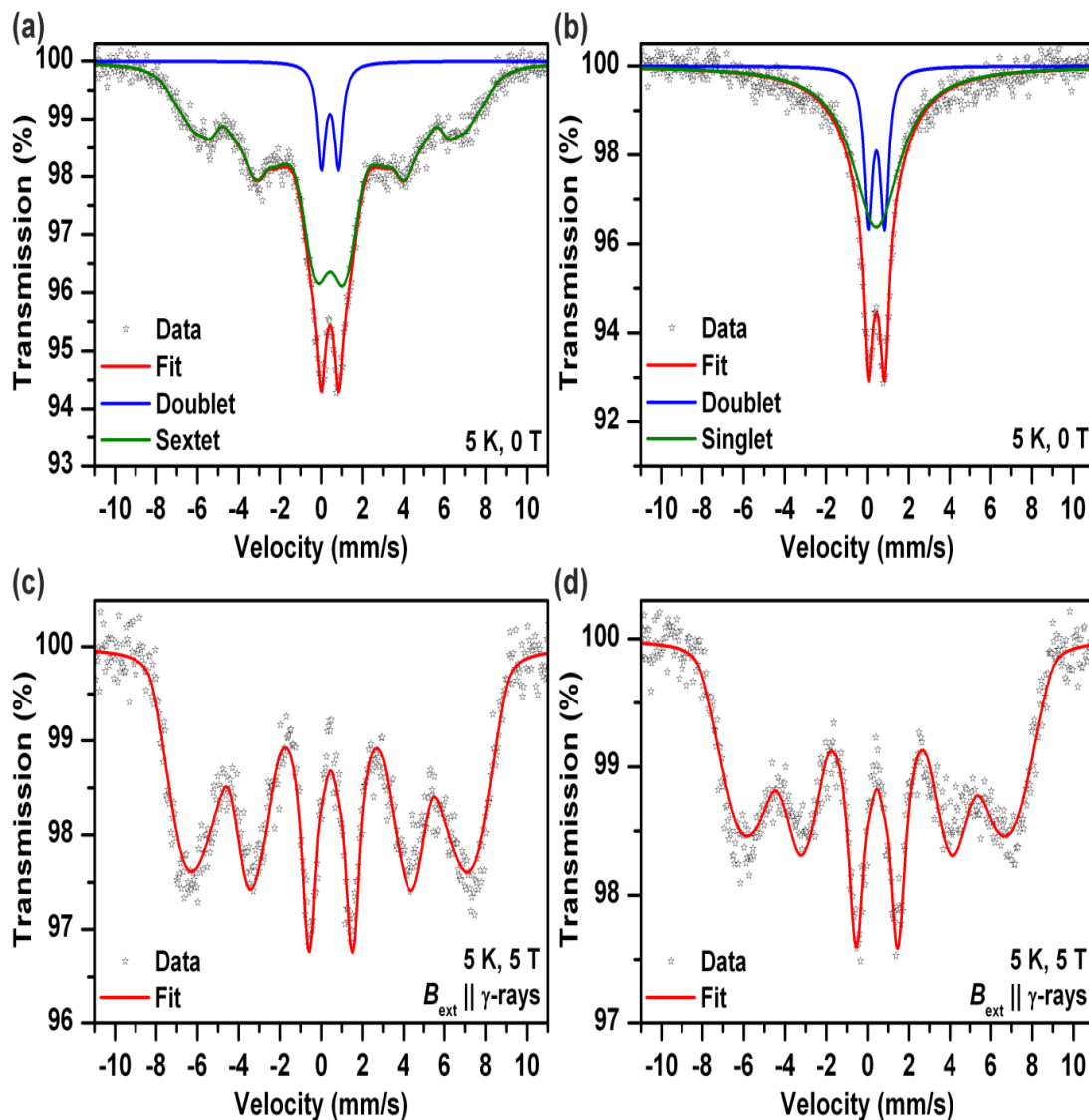
Fig 7-3: (a) Representative XPS survey scans for two iron containing samples. (b) High resolution Fe2p1 spectrum for R-Fe-GN sample.

### 7.3.1.4 Mössbauer Spectroscopy

Mössbauer spectroscopy provided additional information on the chemical nature of the iron in the samples. Room temperature Mössbauer spectra of the both samples (before and after the sodium borohydride treatment) could be fitted by one doublet component with isomer shift of  $\sim 0.35$  mm/s indicating a presence of octahedral trivalent iron atoms in the structure of ferric oxide or (oxy)hydroxide. No zero valent and/or divalent iron were detected in the spectra, even for samples reduced using sodium borohydride for extended periods. More detail information was obtained from low temperature ( $T = 5$  K) and in-field ( $B = 5$  T) spectra (Fig 7-4). The zero-field spectrum of the sample before the sodium borohydride treatment (Fig 7-4 a) showed two components including a minor doublet (isomer shift of 0.42 mm/s, quadrupole splitting of 0.81 mm/s) and a major sextet (isomer shift of 0.44 mm/s, quadrupole shift of -0.03 mm/s) with a broad and uniform distribution of hyperfine magnetic field ranging from 0 to 50 T. Such a spectrum reflects unusually low magnetic ordering temperature of the ferric oxide or (oxy)hydroxide phase and thus a presence of very small nanoparticles ( $< 10$  nm).

The 5 K zero-field spectrum of the sodium borohydride treated sample (Fig 7-4 b) shows even higher content of the doublet so the magnetic ordering temperature was even lower and the nanoparticles were smaller in comparison with the “non-treated” sample. It is known that small nanoparticles of iron oxide (approximately below 15 nm) can show superparamagnetic behavior under so called blocking temperature, which is usually much more lower than conventional Curie or Néel temperature of a magnetic ordering. Blocking temperature is strongly dependent on particle size (decreases with a decrease in the particle size) and also on the characteristic time of experimental technique. Mössbauer spectroscopy with very low characteristic time ( $\sim 10^{-8}$  s) presents the most suitable method for an observation of this superparamagnetic phenomenon. Thus the doublets in the low temperature spectra (Fig 7-4 a and b) corresponded to superparamagnetic (smaller) particles and the sextets result from bigger particles, which were in a magnetically blocked (ordered) state. The superparamagnetic regime was also confirmed by in-field Mössbauer spectra (Fig 7-4 c and d), where the sextets with effective magnetic field exceeding 30 T were observed. In contrast, with a paramagnetic phase, the effective magnetic field has to be equal to the external magnetic field (5 T in

our case). The quadrupole shifts of the both sextets (Fig 7-4 c and d) were close to zero indicating amorphous  $\text{Fe}_2\text{O}_3$  or  $\text{Fe}(\text{OH})_3$ . The Mössbauer spectroscopy data confirmed that nanoparticles of ferric oxide or hydroxide were incorporated, and were probably uniformly distributed, within the silica matrix. The long-term sodium borohydride treatment did not result in a reduction of the ferric oxide phase at all. It did however result in a particle size decrease.



**Fig 7-4: Zero-field and low temperature (5 K) Mössbauer spectrum of the sample before (a) and after (b) sodium borohydride treatment. In-field (5 T) and low temperature (5 K) Mössbauer spectrum of the sample before (c) and after (d) sodium borohydride treatment.**

### **7.3.1.5 Attenuated Total Reflectance Fourier Transform Infrared spectroscopy (ATR-FTIR)**

Further characterisation of the as made GN and as made Fe-GN samples was performed using ATR-FTIR (Fig 7-5 a). The results supported the formation of silica; as was evident from the siloxane (Si-O-Si) peaks at  $\sim 1100\text{ cm}^{-1}$  and  $800\text{ cm}^{-1}$ . The presence of PEHA was also detected from amine peaks located in the region of  $1500\text{-}1700\text{ cm}^{-1}$ . Although the shape of the siloxane peak at  $\sim 1100\text{ cm}^{-1}$  was as expected for the sample without iron (as made GN), the shape of this peak was found to significantly change for the sample containing iron (as made Fe-GN). This suggested that the inclusion of iron affected the materials produced at a molecular level and further supported the observed differences in porosities discussed above between samples with and without iron. In order to further probe the effect of iron on silica, peak deconvolution protocol was applied to the  $\sim 1100\text{ cm}^{-1}$  peak of both samples. In the sample without iron (as made GN), the usual silica peaks were identified ( Fig 7-5 b), which included asymmetric Si-O-Si stretching modes at  $\sim 1150\text{ cm}^{-1}$  and  $\sim 1060\text{ cm}^{-1}$  (transverse and longitudinal optic modes, TO and LO, respectively), symmetric Si-O-Si stretching modes at  $\sim 800\text{ cm}^{-1}$  and silanol (Si-OH) bonds at  $\sim 950\text{ cm}^{-1}$ . Analysis of the as made Fe-GN sample peak indeed highlighted drastic differences (Fig 7-6 a), in particular, the presence of additional peaks at  $\sim 954\text{ cm}^{-1}$  and  $\sim 870\text{ cm}^{-1}$ . In the literature, these peaks have been commonly found in sol-gel materials and were attributed to Fe-O-Si / Fe-O-OH.[281,282] Furthermore, as the iron content was increased from 0 % to 50 %, the area under the Fe-O-Si peak was found to increase (Fig 7-6 b), thus further strengthening the formation of iron oxide-silica composite material.

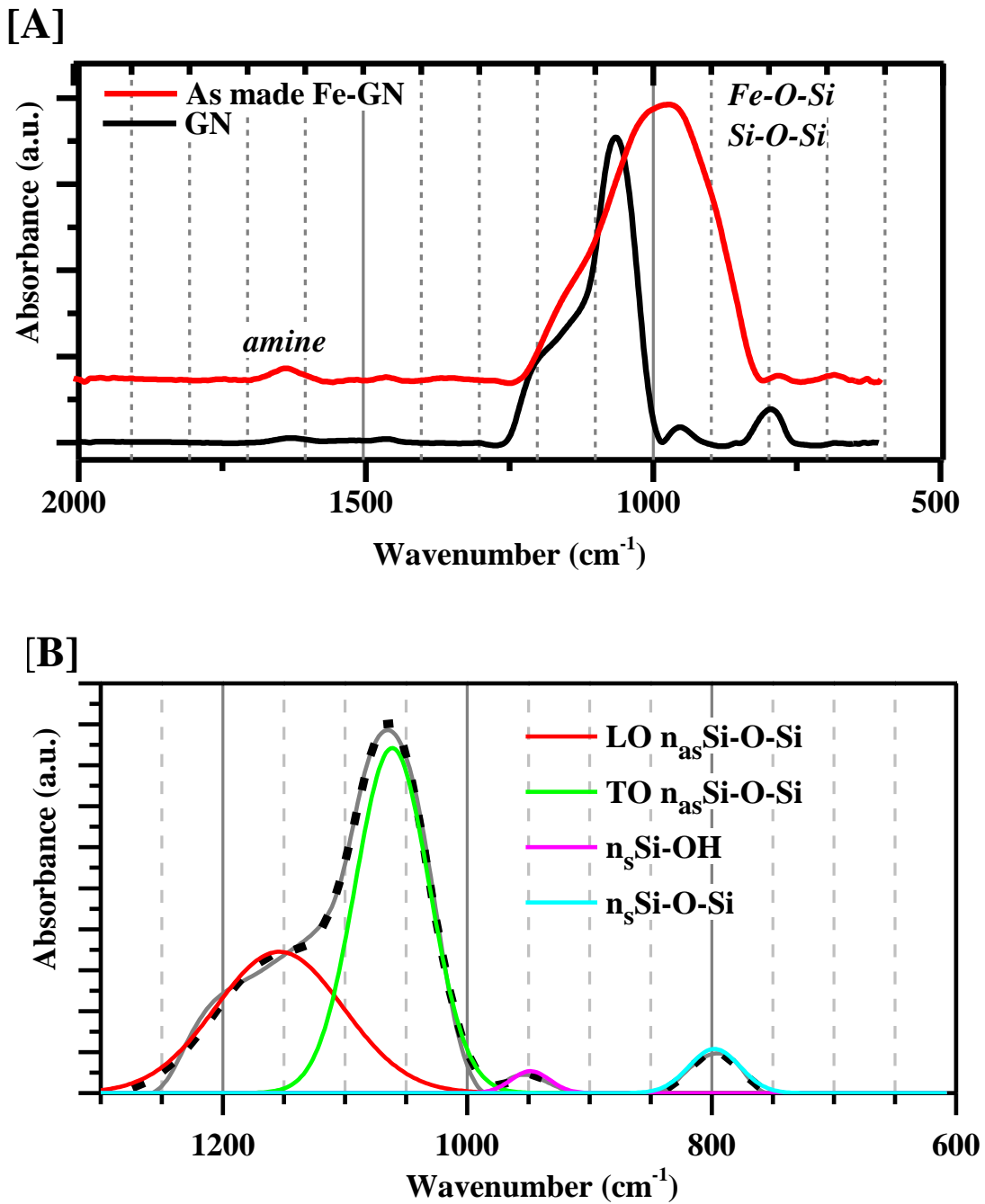


Fig 7-5: (A) ATR-FTIR spectra for samples with and without iron. (B) The deconvolution of  $\sim 1100\text{cm}^{-1}$  region for sample without iron.

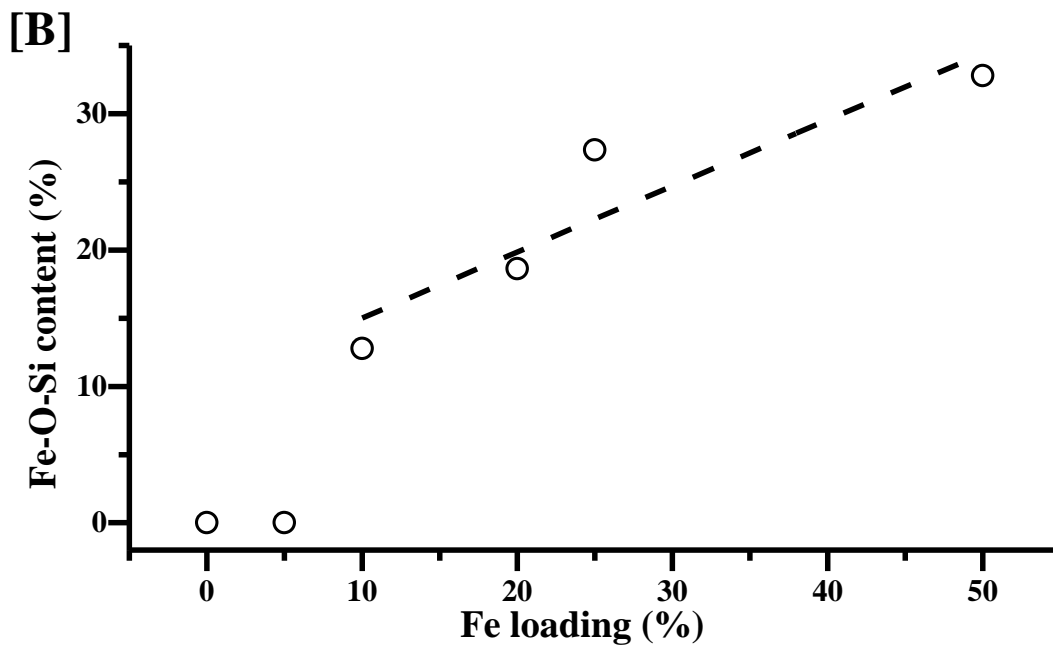
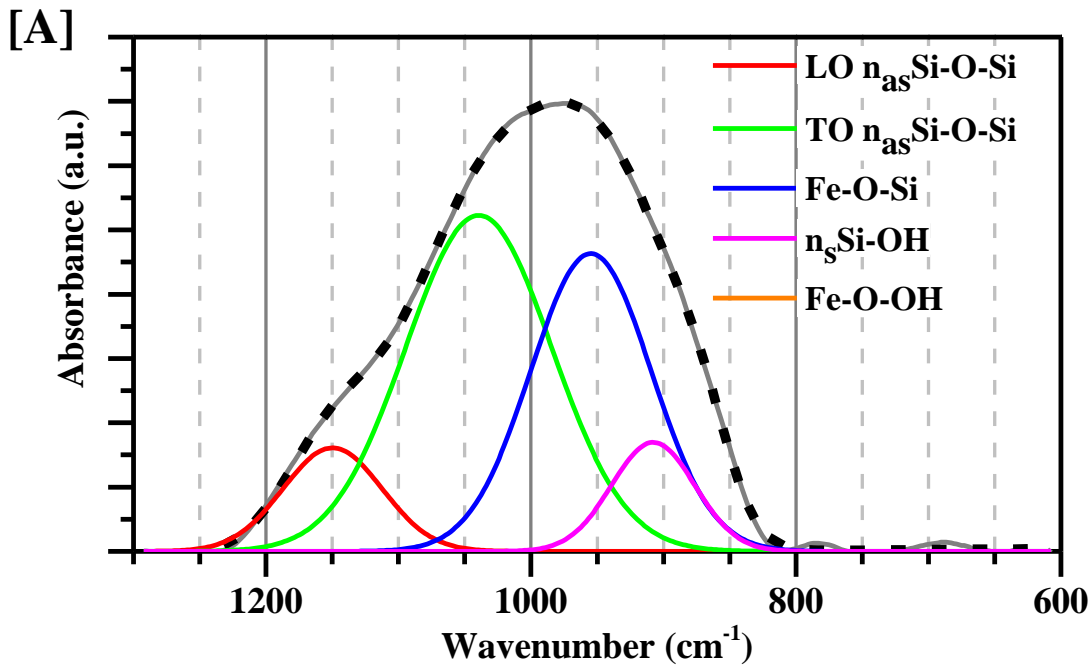


Fig 7-6: (A) The deconvolution of  $\sim 1100cm^{-1}$  region for sample with iron. (B) Iron content, measured from the area under the Fe-O-Si peak, as a function of iron loading.

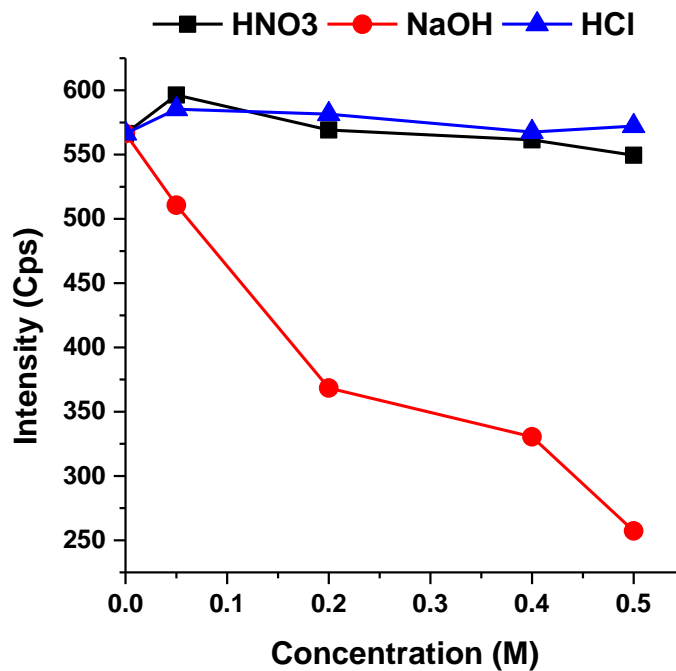


In summary, the materials characterisation suggested that the presence of iron profoundly affected the chemical nature of the GN samples, in addition to the physical properties, as observed from the porosity measurements. The surface area was found to depend on iron loading, calcination and chemical reduction. Further, chemical reduction increased the hydration of samples. It was clear that iron was not in a zero valent form, but rather in an Fe<sup>II</sup> or, more likely, Fe<sup>III</sup> oxidation state, presented as well-dispersed, 10 nm particles of iron oxide, hydroxide and/or oxyhydroxide, in addition to Si-O-Fe.

### **7.3.2. CASE STUDY: The adsorption of arsenic using different silica platforms.**

#### ***7.3.2.1 Effect of solvents on the signal intensity of ICP-OES.***

In order to eliminate variations in the arsenic signal intensities in the ICP, caused by the use of different matrices, solutions containing 0.5 µgcm<sup>-1</sup> of As were prepared in NaOH, HNO<sub>3</sub>, or HCl at concentrations ranging from 0.05 to 0.2 M. The results shown in Fig 7-7 indicated that almost no affect was observed on the As signal intensity when HNO<sub>3</sub> and HCl were used. Whereas, a significant decrease in the net As ion signal was observed on increasing NaOH concentration. Such a suppression of the arsenic signal intensity could be attributed to one or more of the following reasons (i) an easily ionised element (EIE) effect (elements with low ionisation potentials, such as alkaline elements), (ii) a reduction in the aerosol transport efficiency caused by a change in the aerosol density, (iii) an increase in the viscosity which results in a decrease in the uptake rate. [283,284]



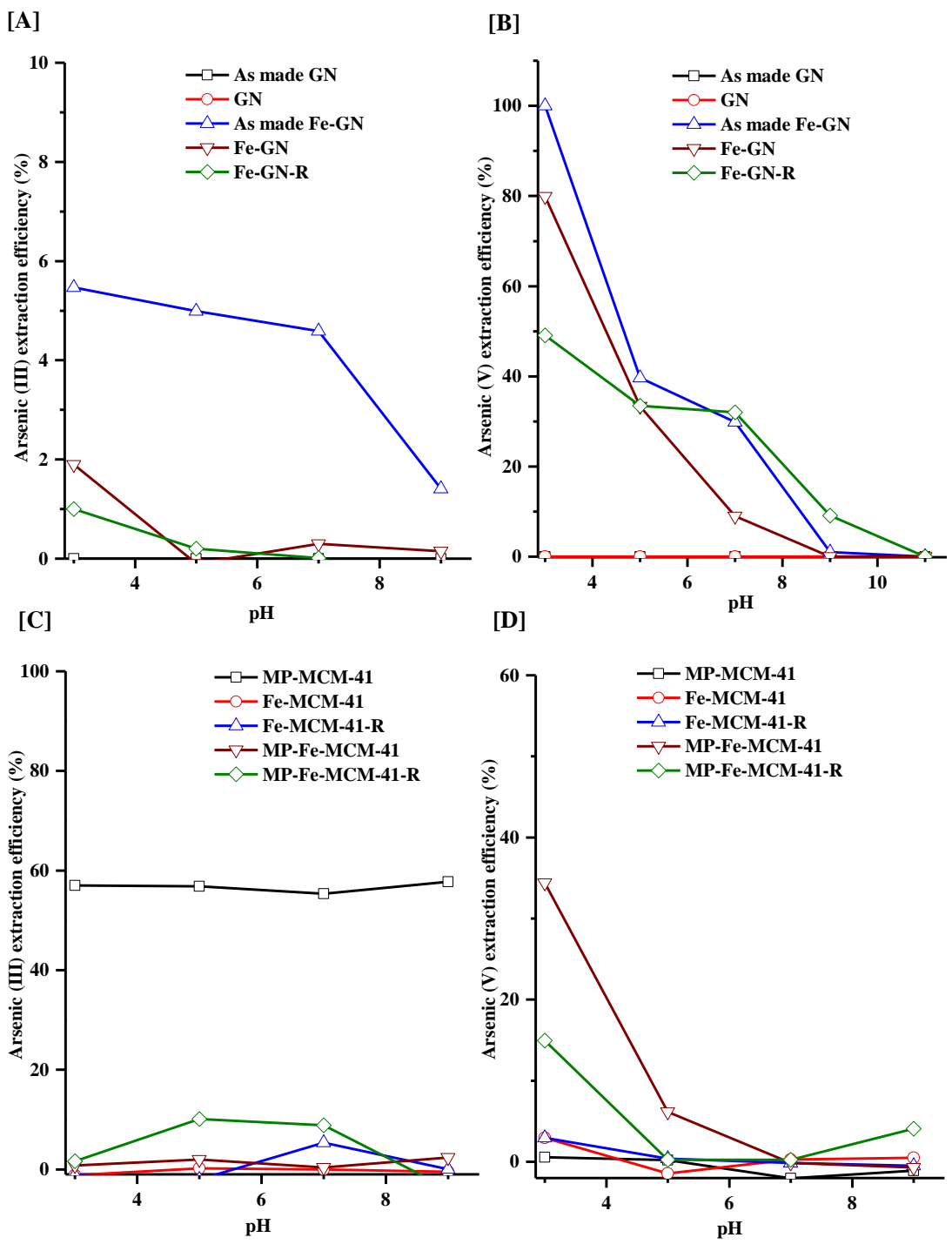
**Fig 7-7: Effect of NaOH, HNO<sub>3</sub>, or HCl concentration on net As ion signal (0.5  $\mu\text{gcm}^{-1}$  as As).**

On the basis of results presented above, matrix matching between the samples and the calibration standards would be essential in order to obtain an accurate quantitation of As. Furthermore, sodium hydroxide (0.1 M) used for the recovery of arsenic ions would be diluted with water more than 20 times before ICP analysis to minimise the signal intensity reduction.

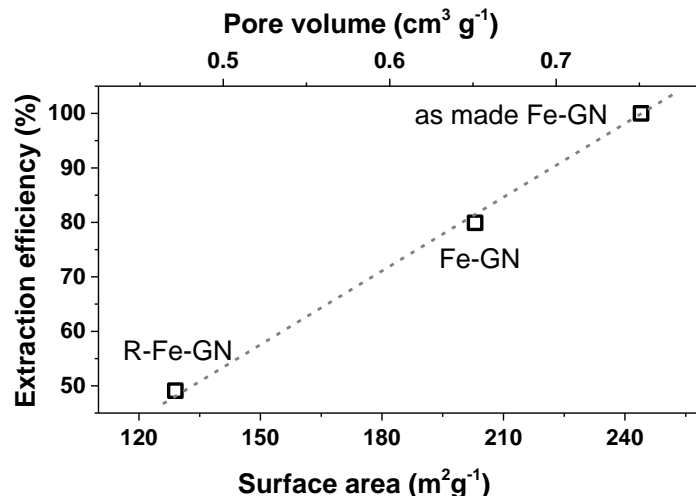
### **7.3.2.2 Effect of pH**

The 10 different samples of GN or MCM-41 based adsorbents were each added to 25  $\text{cm}^3$  aqueous solutions containing 20  $\mu\text{g cm}^{-1}$  of As (III) or As (V) ions. The solution pH was altered (to 3, 5, 7, 9, or 11), to test the materials' extraction efficiencies over a wide pH range see Fig 7-8. Only MP-MCM-41 was able to remove As (III) over the full pH range studied. This could be attributed to the high affinity of As (III) species for the sulphur-containing functional group. [217,218] As (V) was shown to have a high affinity towards iron containing sorbents, for example, it was found that neither as made GN nor GN on their own removed any As (V) from solution regardless of solution pH (Fig 7-8 B). In

contrast, all Fe-containing GN samples (as made-Fe-GN, Fe-GN, or Fe-GN-R) successfully removed As (V) ions from solution. This clearly suggested that the presence of iron was a dominated factor in As (V) removal. Highest extraction efficiencies were observed at a solution pH of 3 when the dominant species of As (V) ions is  $\text{H}_2\text{AsO}_4^-$ . [285] At pH 3, best extraction results (100 %) were demonstrated for as made-Fe-GN, indicating the possibility of co-operative effects from PEHA and iron towards the adsorption of this bulky inorganic anion. The surface amines, detected by FTIR and XPS, will be protonated at pH 3, further facilitating interactions between the negatively charged arsenic ions with the GN surface. It was interesting to note that Fe-GN-R exhibited the lowest arsenic extraction efficiency. Materials characterisation revealed that Fe-GN-R had a lower surface area compared to the un-reduced Fe-GN sample (Table 7-2). Furthermore, XPS analyses suggested that upon reduction, some iron was lost, thus reducing the total iron content of the Fe-GN-R sample. These two observations – reduced surface area and reduced iron content – perhaps help to explain why Fe-GN-R had the lowest arsenic extraction efficiency. This was further supported when the surface area and pore volume for all 3 iron containing samples were compared against extraction efficiencies (Fig 7-9). It was clear that both iron content and high surface area were crucial for As(V) removal – the former was known to actively interact with arsenic while the latter maximises the mass transport.



**Fig 7-8: Effect of pH on the extraction of As (III) and As (V) ions from water using variety of GNs (A and B) and MCM-41 (C and D) based materials.**

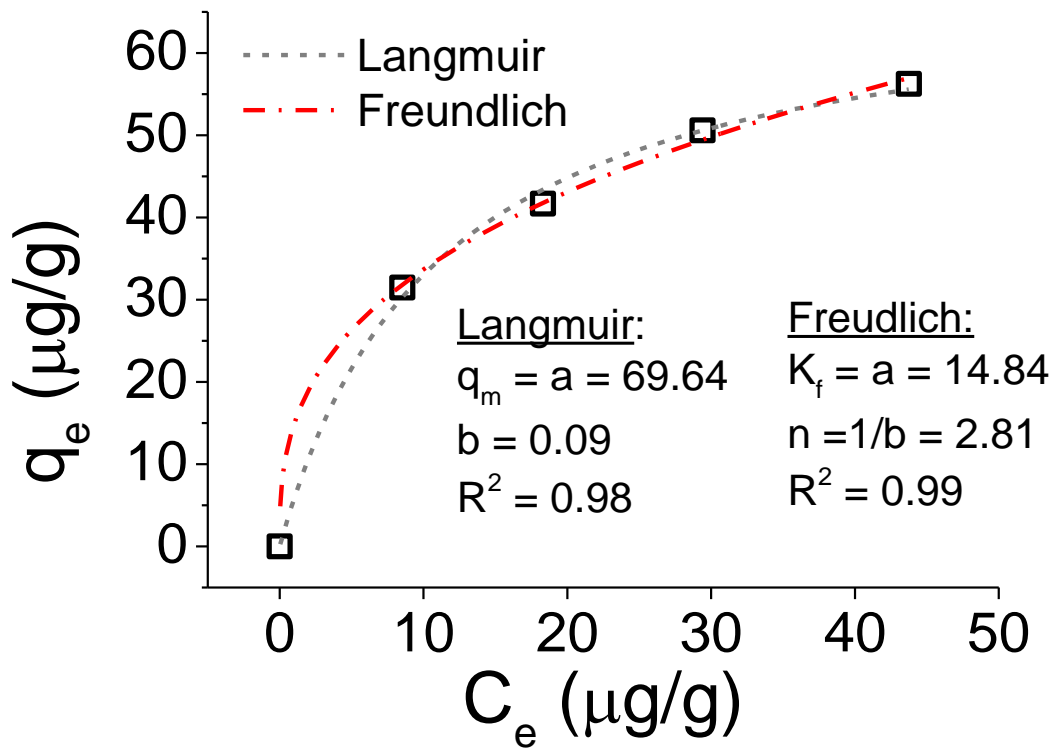


**Fig 7-9: Extraction efficiency as a function of surface area and pore volume of iron containing samples.**

### **7.3.2.3 Adsorption isotherms for As(V) on as made-Fe-GN**

Focusing on the most promising adsorption platform for As (V) removal at pH 3, the adsorption capacity value was determined and compared with other iron-encapsulated materials quoted in the literature. The results are plotted in Fig 7-10 as the amount of As (V) adsorbed at equilibrium ( $q_e$ ) as a function of initial concentration ( $C_e$ ). Langmuir and Freundlich isotherm models correspond to homogeneous and heterogeneous adsorbent surfaces, respectively.[277] The Langmuir isotherm was originally derived for the adsorption of gas molecules onto smooth and ideal solid surface, while for aqueous systems, the Freundlich isotherm is most adequate and hence was preferred.[286,287] However, most literature reports utilise the Langmuir model to calculate the adsorption capacity values, therefore the Langmuir isotherm adsorption capacity was reported here in order to this data with other materials reported in the literature. The experimental adsorption data of As (V) on as made Fe-GN had a good fit with both the Langmuir and Freundlich models (Fig 7-10) , which indicated that more than one type of interaction between the arsenic ions and the surface of Fe-GN had occurred.[288] It was generally believed that arsenic could link to iron through the oxygen atoms of the arsenate. [289] However, since the extraction here was performed under acidic conditions resulting in

protonation of the amine groups on PEHA, as a consequence electrostatic interactions between the protonated amine group and the negatively charged bulky arsenate ions may have occurred. [290] Using experimental data, the distribution of As (V) measured between the liquid phase and the solid adsorbent at equilibrium gave maximum adsorption capacity values of 69.64 and 14.84 mg g<sup>-1</sup>, calculated according to Langmuir and Freundlich isotherms, respectively (see Table 7-5 ). The calculated R<sub>L</sub> value was in the range of 0 and 1, suggesting favourable adsorption properties for arsenic species onto as made Fe-GN.



**Fig 7-10: Adsorption isotherms for As (V) on as made Fe-GN fitted using Freundlich and Langmuir isotherms.**

**Table 7-5: Isotherm parameters for arsenic sorption on Fe-GNs**

Method	Langmuir		Freundlich		
	$q_m$ (mg/g)	$b$ (L/mg)	$R_L$	$K_f$ (mg/g)	$n$ (L/mg)
As made Fe-GNs	69.64	0.09	0.2	14.84	2.81

A comparative evaluation of Fe-GNs and other iron containing low cost adsorbents for arsenic removal is listed in Table 7-6. It was observed that the adsorption capacity of as made-Fe-GN was higher than most other sorption materials reported in the literature. For example, Payne *et.al* [291] found that the maximum adsorption capacity (MAC) of the iron oxide nanoparticles immobilized on activated carbon was  $35.34 \text{ mg g}^{-1}$ . Gu *et.al* [292] measured the adsorption capacity of  $2.96 \text{ mg g}^{-1}$  was achieved. Despite the extensive use of activated carbon (AC) in the water and wastewater treatments, AC is perhaps not ideal as it is difficult to separate powdered AC from aquatic system when it becomes exhausted.[293] Furthermore, the regeneration of AC by chemical or thermal procedures are expensive and can result in sorbent loss.[294] To the best of the authors' knowledge the highest iron loading reported in the literature for GAC was 33.6 % [295], and as higher iron oxide loading provides better adsorption capacities, the material produced here with an iron loading of 50 % was higher than any other loading reported in the literature.

**Table 7-6: A list of maximum adsorption capacities calculated according to Langmuir isotherms for As (V) using modified Iron adsorbents.**

Sorbent	Capacity (mg/g)	Equilibration time (h)	Capacity (mg/ g/ h)	Ref.
Activated Carbon, Fe modified	35.34	48	0.74	[291]
Clinoptilolite, Fe modified	30.21	48	0.63	[291]
GAC-Fe (0.05 M)	2.96	24	0.12	[292]
Fe10SBA-15	12.68	24	0.53	[296]
cellulose loaded with iron oxyhydroxide	15.6	24	0.65	[297]
Synthetic siderite	31	3	10.33	[298]
Zr(IV)-loaded chelating resin (Zr-LDA)	88.73	24	3.70	[299]
Akaganeite $\beta$ -FeO(OH) nanocrystals	141.3	24	5.89	[300]
Poly ethylene mercaptoacetimide	105.75	20	5.29	[301]
magnetite–maghemite nanoparticles	6	3	2.00	[302]
as made-Fe-GN	69.64	2	34.82	this work

#### **7.3.2.4 Assessment of Fe-GN performance in real samples**

To examine the performance of as made Fe-GN for As (V) extraction in the presence of other cations, 25 mg of as made Fe-GN was added to 100 cm<sup>3</sup> samples of distilled water, tap water or river water each spiked with As (V) to a solution concentration of 1  $\mu\text{g cm}^{-3}$ . The results given for stirred batch experiments, in Table 7-7, indicate that extraction efficiencies of almost 100 % were achieved for the removal of As (V) from all samples. These exciting results implied that the coordination bonds between as made Fe-GN and the As(V) anions were not appreciably hindered by the presence of other coordinating ions at high concentration. Significantly, upon washing the As (V) loaded as made Fe-GN samples with 0.1 M sodium hydroxide 96+ % As (V) was recovered. This suggested a strong potential of these new materials in water treatment applications where regeneration



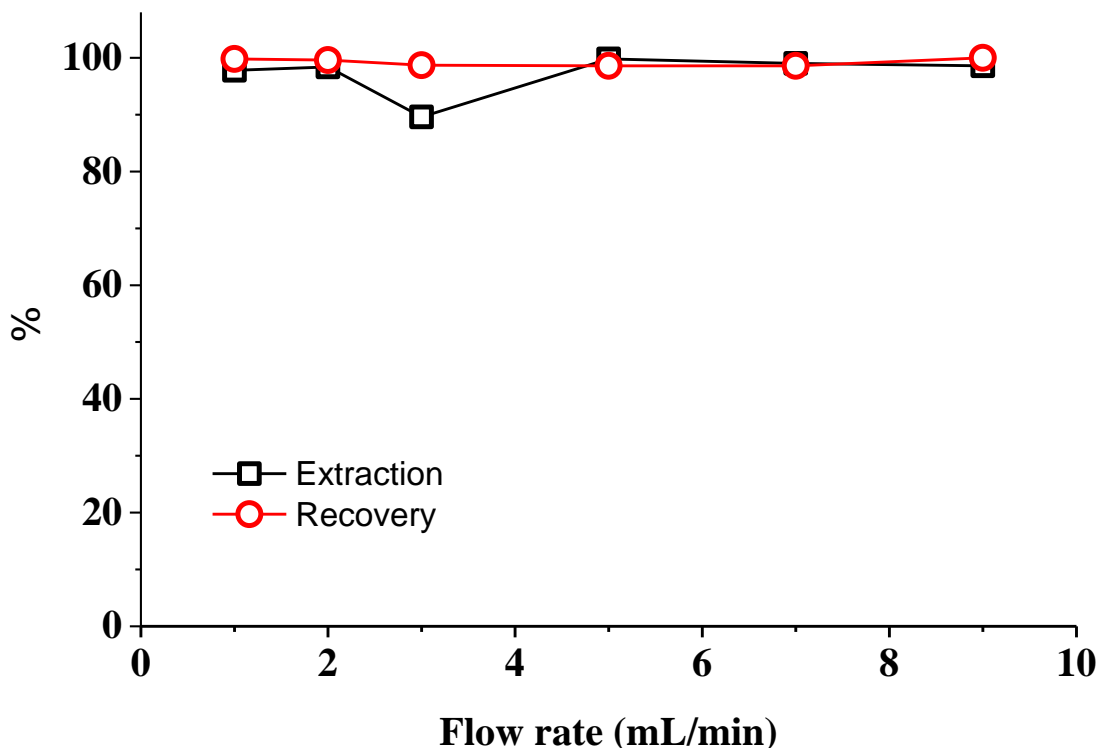
and reusability of sorbents, in addition to good adsorption capacities, is crucial to their economic success.

**Table 7-7: Concentration ( $\mu\text{g cm}^{-3}$ ) of As (V) in filtered solutions, as measured by ICP-OES.**

Sample	Prior to sorbent addition	After sorbent addition	As(V) recovered	Recovery %
Distilled Water	1.045	<0.005	1.042	99
River water	1.075	<0.005	1.052	98
Tap Water	1.041	<0.005	1.000	96

### ***7.3.2.5 Examination of sorbent performance in packed-bed under continuous flow systems***

Although the batch extraction results provide the fundamental information related to sorbent behaviour and metal sorption performance, a continuous mode of operation would be preferred in large scale water treatment applications with perceived advantages including high yields, simple operation, easy regeneration of packed bed, and ease of scale up from a laboratory to industrial or environmental application. Hence, the extraction of As (V) was also studied in continuous flow at a maximum flow rate of  $9 \text{ cm}^3 \text{ min}^{-1}$  (the flow limits of the system used). The results shown in Fig 7-11 indicate that almost 100% extraction efficiencies and 100% recovery efficiencies were achieved over the flow rate range studied. More importantly this system involved reuse and clean-up of the same sample cartridge which (as shown in Fig 7-11) has been used 6 times without any detrimental effects on either extraction or As (V) recovery values.



**Fig 7-11: The extraction of arsenic ions under different flow rate.**

## 7.4 Conclusion

In conclusion, we report the successful use of a new family of iron supported on green silicas for water remediation. The preparation of Fe-GN materials had the advantages of using neutral pH, room temperature conditions, rapid synthesis, and a substantial reduction in secondary pollution by the elimination of the need for organic solvents from the preparation method. These new iron encapsulated materials possessed unprecedented pore sizes for mesoporous materials with surface areas between 200-300 m<sup>2</sup> g<sup>-1</sup>. The addition of iron during synthesis was found to modify the silica framework produced. The incorporation of iron into the surface of GN resulted in a material with a porous system without the need for further thermal treatment to remove the organic template. This gives the material further advantages over the already present silica materials reported in the literature.

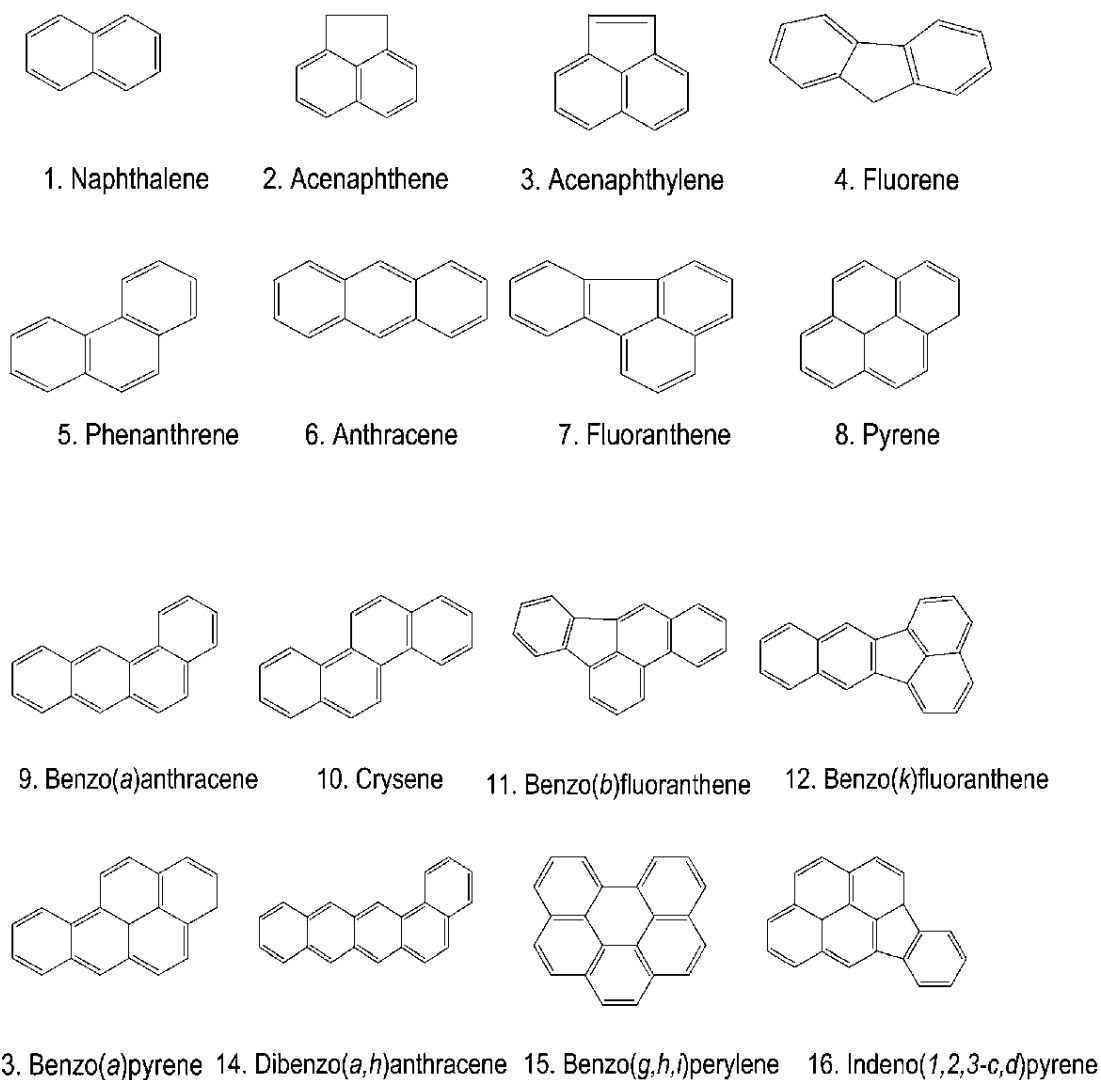
GN loaded with iron were found to be extremely efficient for the adsorption of As (V) from water (distilled, tap or river water). A maximum adsorption capacity of 34.82 mg of As (V)/g-h was obtained, which is higher than the maximum capacity of any materials reported to date for As (V) removal. Reduction in the performance was not observed even when removing As (V) from water that contained other metal ions (e.g.  $Mg^{2+}$  and  $Ca^{2+}$ ) at significantly higher concentrations. What is perhaps key to deployment of this material in industrial applications is the successive use of GNs to remove pollutants from water in a continuous mode for at least 6 repeated applications (with the potential to go much further). Sorbent regeneration was possible readily, allowing ~100% recovery of As (V) and reuse of the sorbent for subsequent extraction at ~100% extraction efficiency. Further research is directed into the optimisation of the catalyst system by systematically varying the parameters of the green chemistry. Together with the low cost, facile preparation method, and potential to scale up the synthesis it is suggested here that as made Fe-GN will prove to be an extremely attractive alternative adsorbent to help abate the global As (V) toxicity problem. These advantages represent a significant progress since the expensive, complex and lengthy synthesis of mesosilica materials such as MCM-41 or SBA-15, have prevented their widespread incorporation into industrial and/or environmental remediation technologies.

**Chapter 8 : Case study: Comparison of Polycyclic aromatic hydrocarbon removal from water for silica and carbon supports**

## 8.1 Introduction:

Polycyclic aromatic hydrocarbons (PAHs) are chemical compounds that consist of two or more fused aromatic rings in a linear or clustered arrangement and no elements other than carbon and hydrogen.[303-305] Other elements such as nitrogen, sulfur, and oxygen atoms may be readily substituted in the benzene ring leading to the formation of heterocyclic aromatic compounds. The formation of PAHs compounds can be through the incomplete combustion and pyrolysis of organic matter. Both natural and anthropogenic sources including vehicular emissions, residential wood burning, forest fires, volcanic eruptions, petroleum catalytic cracking and industrial combustion of fossil fuels contribute to the release of poly aromatic hydrocarbons into the environment.[306-308] In any fuel combustion, the formation and emission mechanisms of PAHs can be classified into two processes: pyrolysis and pyrosynthesis. Upon heating, the organic compounds are partially cracked leading to the formation of smaller and unstable fragments, this process is known as pyrolysis. These fragments are highly reactive free radicals with a very short average lifetime. By recombination reactions, these fragments will tend to form more stable PAHs and this process known as pyrosynthesis.[309-311] Thus, PAHs are formed through pyrolysis of acetylene, butadiene, methane and other compounds.[312-314]

Several hundred different combinations of PAHs exist, but the US Environmental Protection Agency has listed 16 PAHs as priority pollutants. The structures of these compounds are shown in Fig 8-1. PAHs are highly soluble in certain organic solvents and have low water solubility values ranging from 0.3  $\mu\text{g/L}$  to 30.2  $\text{mg/L}$ .[313,315,316] Compounds with low molecular weight such as acenaphthene, acenaphthylene or naphthalene, have the highest water solubility with values of 3.8, 16.1 or 30  $\text{mg/L}$ , respectively.[303,317]



**Fig 8-1: Chemical structure of EPA's 16 priority pollutant (PAHs).[304,306]**

Adsorption is a simple and efficient method for the removal of organic compounds in drinking water treatment. Among the various adsorbents commonly used, activated carbons (ACs), zeolites,  $\text{TiO}_2$ ,  $\text{Al}_2\text{O}_3$ ,  $\text{ZnO}$  or  $\text{SiO}_2$ , ACs are the most widely used. ACs possess several advantages which include a broad-spectrum of compound removal capability, chemical inertness and thermal stability. However, the application of ACs in water treatment also suffers from several limitations such as slow adsorption kinetics and a difficulty in sorbent regeneration. To overcome the above problems, activated carbon

fibers (ACFs) were developed as the second generation of carbonaceous adsorbents. The pores in ACFs are directly opening on the surface of carbon matrix, which shortens the diffusion distance of pollutants to adsorption sites. As a result, ACFs usually possess higher adsorption kinetics than ACs. Carbon nanotube, with their one-dimensional structure, are likened to miniaturised ACFs. All adsorption sites locate on the inner and outer layer surface of CNTs. With the hollow and layered structures and tunable surface chemistry, theoretically, CNTs may be a promising third generation of carbonaceous adsorbents. A wide spectrum of organic compounds or metal ions has been studied as the target pollutants on CNTs with various physical structures and surface chemistry. Gotovac *et. al* [307,309] observed remarkable differences between the adsorption capacities of tetracene and phenanthrene on the tube surface of CNTs because of the nanoscale curvature effect. The morphology difference of CNTs may also result in a difference in their aggregation tendency, which may further impact their adsorption ability. However, high rates of organic contaminants adsorbed onto CNTs may lead to the potential alteration of their fate and bioavailability in the environment and hence make greater environmental exposure risks of CNTs materials.[310,312] Other nanomaterials such as TiO<sub>2</sub>, Al<sub>2</sub>O<sub>3</sub>, ZnO and SiO<sub>2</sub> possess very low sorption potential for organic compounds due to their hydrophilic characteristics. However, surface modification of these materials with an organic functional group is possible and could increase the hydrophobicity.

Araujo *et.al* [313] prepared three different types of mesoporous silica MCM-41 (a pure silica and two aluminum doped silica with Si/Al molar ratios of 10 and 30) for adsorption of polycyclic aromatic hydrocarbons (PAHs) from an organic solution. The equilibrium data was found to fit with the Langmuir isotherm and the results showed an increase in the maximum adsorption capacity ( $q_m$ ) in the following order: MCM-41 < Al-MCM-41 (30) < Al-MCM-41 (10). These results indicated that the adsorption capacity of PAHs was strongly dependent on the concentration of surface acid sites (increasing aluminum content will lead to increase in the acid sites). Zhao *et. al* [304,315] synthesized mesoporous silica materials using two types of surfactant; cetylpyridinium bromide (CPB) and cetyltrimethylammonium bromide (CTAB). The ability of materials prepared using both templates was assessed for the removal of environmental pollutants e.g. mono-

, di-, tri-chloroacetic acid, toluene, naphthalene and methyl orange. The as made materials had excellent extraction efficiencies toward naphthalene, toluene, chloroacetic acids and methyl orange compared to the materials prepared without surfactants, which had no affinity for ionic or non-ionic analytes. Xie *et.al.* [303,307] studied the influence of chain length (from one carbon to 22 carbons) of surfactants on the adsorption of naphthalene. The results indicated that the amount of surfactant loaded increased with increasing chain length resulted in an increase in the amount of adsorbed organics.

Fe<sub>3</sub>O<sub>4</sub> nanoparticles have also been used to remove PAHs from water. However, due to the highly hydrophilic property of Fe<sub>3</sub>O<sub>4</sub>, a layer of hydrophobic coat, or a layer such as phenyl, C18 groups [306,310], polymers [309,313], or carbon [312,315], must be immobilized on the surface of Fe<sub>3</sub>O<sub>4</sub> nanomaterials. Lee *et.al* [305,318] reported a facile surface modification method in which self-polymerization of dopamine (Dopamine, commonly known as a neurotransmitter, and is a small molecule mimic of the adhesive proteins of muscles) at slightly weak alkaline pH to form thin, surface-adherent polydopamine (PDA) films onto a wide range of inorganic and organic materials. Polydopamine modification method has several significant advantages including multifunctional groups (catechol and amino groups), biocompatibility, dispersibility in water, and providing stacking interaction to targets. [308,319]

Zhou *et.al.* [311,320] developed a simple method for imprinting protein based on self-polymerization of dopamine in the presence of template protein on the surface of Fe<sub>3</sub>O<sub>4</sub> nanoparticles. These studies indicated that dopamine had the potential to directly apply for the modified Fe<sub>3</sub>O<sub>4</sub> nanoparticle surfaces leading to the formation of nanomaterial that was used as an adsorbent. Wang *et.al.* [314,319] reported the synthesis of a Core/shell structured Fe<sub>3</sub>O<sub>4</sub>/PDA nanoparticles as a solid-phase extraction (SPE) adsorbent for the removal of polycyclic aromatic hydrocarbons (PAHs) molecules. The results indicated that the extraction efficiency was not influenced by salt concentrations up to 300 mM or pH values over the range 4–11.

Despite the high adsorption affinity of CNTs toward organics and the extensive use in the water and wastewater treatments, the potential threat of CNTs to the environment and human health should be taken into account before large scale applications. Therefore, the



objectives of this work were to develop a method that is cost-effective, easy to synthesised and environmentally friendly. Thus, an attempt was performed to examine the potential of using GNs and Fe-GNs in the removal of organics pollutants such as naphthalene from aqueous solutions. Furthermore, a conventional activated carbon materials as well as synthesised MCM-41 was also tested for the sake of comparison.

## **8.2 Experimental**

### **8.2.1 materials and reagents**

Norit CA1, Darco (GAC) ,Norit CNR-150 samples were obtained from Sigma Aldrich. Naphthalene, ethanol, methanol, and acetonitrile were also purchased from Sigma Aldrich.

### **8.2.1 Synthesis of adsorbents**

MCM-41 was synthesised as described in section 3.1.1. The carbon based nanomaterials Norit CA1, Darco (GAC) or Norit CNR-150 were obtained from Sigma Aldrich and it was used as it is without any further modification. GNs and Fe-GNs were synthesised as described in sections 3.1.3 and 8.2.2, respectively.

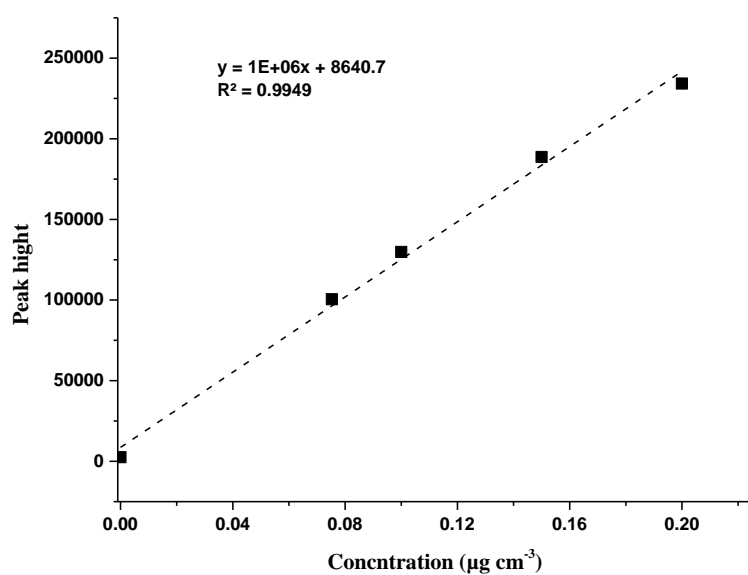
### **8.2.2 Adsorption of naphthalene using carbon and silica based materials**

A 30 cm<sup>3</sup> solution containing 150 µg of naphthalene was placed in a 30 cm<sup>3</sup> glass bottle and approximately 100 mg of each sorbent was added. The bottles were then closed with PTFE screw caps and the mixture stirred for 2 h. A reference sample was prepared in the same way as the samples but without a sorbent. Each mixture was then filtered using a glass syringe and 0.2µm PTFE syringe filter and analysed using the system discussed in Section 10.2.3.

### **8.2.3 Determination of naphthalene's concentration using high performance liquid chromatography with fluorescence detectors (HPLC/FLD)**

The quantification of naphthalene was performed using a spectrasystem HPLC , which contained a reverse phase Waters Ltd. C18 column (150 mm x 4.6 mm, 3.5 µm, 100 Å), a high performance solvent delivery pump (spectra system p4000 Gradient Pump) and a fluorescence detection system (spectra system FL2000). The sample injection loop was 20 µl. The mobile phase, (used in isocratic mode) contained 50/50 vol. % mixture of

deionized water and acetonitrile ( $\text{CH}_3\text{CN}$ , HPLC grade) at flow rate of  $1 \text{ cm}^3 \text{ min}^{-1}$ . The fluorescence detection system used was operated with excitation/emission ( $\lambda_{\text{ex}}/\lambda_{\text{em}}$ ) of 224/330 nm. The calibration of HPLC-FL for the quantification of naphthalene, 50 ppm of stock solution of naphthalene was prepared by dissolving the desired amount of naphthalene in methanol and diluted to working solutions of concentrations of 0, 75, 100, 150 and 200 ppb. An example of the calibration curve obtained is shown in Fig 8-2. The method detection limit was  $0.001 \mu\text{g cm}^{-3}$ .



**Fig 8-2: Calibration graph of HPLC-FL for the detection of naphthalene in solution.**

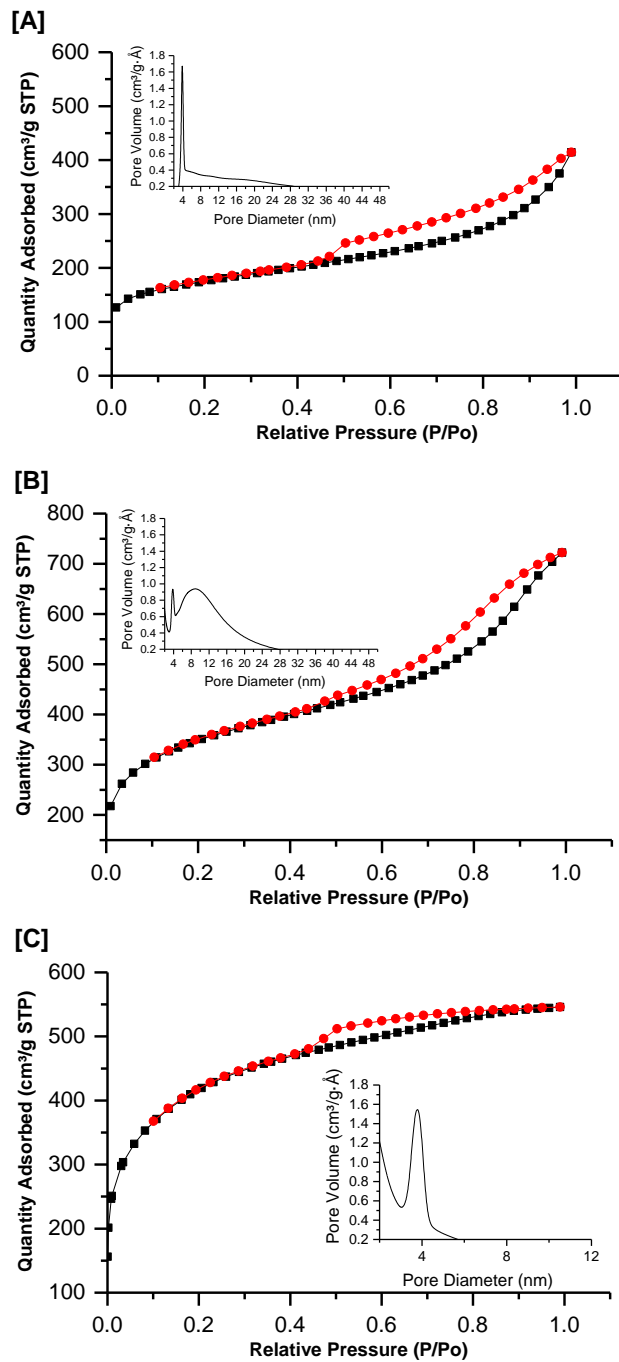
## 8.3 Results and discussion

### 8.3.1 Materials characterization

Experimental information on the nitrogen adsorption analyses (BET) of MCM-41 and GNs materials were described in sections 4.3.1 or 8.3.1.1. The nitrogen adsorption and desorption isotherms, and the porous data, for activated carbon nanoparticles are given in Fig 8-3 and Table 8-1. The Darco and Norit Ca1 type materials exhibited type IV isotherm confirming their mesoporous nature and the calculated surface area was 577.7 or 1165.7  $\text{m}^2\text{g}^{-1}$ ,. Norit-CNR 115 had different results as the isotherms exhibited a type I isotherm indicating it was a microporous material and a H4 hysteresis was observed and attributed to the presence of mesopores in addition the microspores, the calculated surface area was 1403  $\text{m}^2\text{g}^{-1}$ . [316,321]

**Table 8-1: Porosity data for ACs.**

Sample	$S_{\text{BET}}$ ( $\text{m}^2/\text{g}$ )	Average pore diameter (nm)	Micropore volume ( $\text{cm}^3/\text{g}$ )	Total pore volume ( $\text{cm}^3/\text{g}$ )
Darco	577	4	0.1	0.6
Norit Ca1	1165	(4-10)	0.2	1.1
Norit-CNR 115	1403	4	0.2	0.8



**Fig 8-3: Nitrogen adsorption isotherms and pore size distribution of a) Darco (GAC), b) Norit CA 1 (GAC), and c) Norit CNR-150 (PAC)**

### **8.3.2 Extraction efficiency of naphthalene using carbon and silica based materials**

Eight different materials were examined for the extraction of naphthalene from aqueous solution and the results are shown in Fig 8-4. The first 5 materials were prepared as described in sections 3.1.3, 8.2.2 and 3.1.1. It was found that neither as made GN or GN removed any naphthalene from solution. Whereas, an extraction efficiency of 20% was achieved when the materials were loaded with iron and this could be attributed to the present of organic PEHA along with the high pore size distribution which had a surface area of  $\sim 244 \text{ m}^2/\text{g}$  and an average pore size of  $\sim 18 \text{ nm}$ . Extraction efficiencies of 45 or 90 % were achieved using MCM-41 or as made MCM-41, respectively. This result was in agreement with the work that was conducted by Zhao *et.al* [315,317]. As expected the activated carbon nanoparticles exhibited the best performance toward naphthalene in this study. Among the three type of ACs, Norit CNR-115 was the most efficient material with 100 % extraction efficiency. This could be attributed to its high surface area compared to Darco or Norit CA 1. However, further work is required to study the chemical and physical properties of the AC materials.

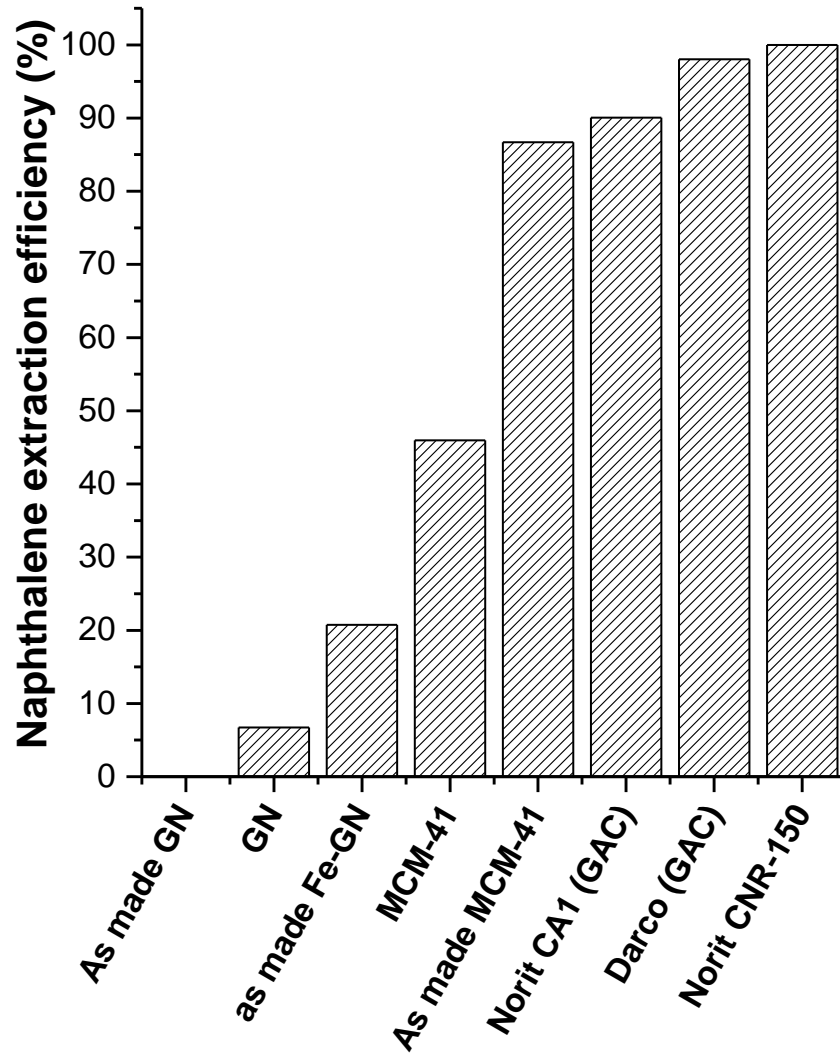


Fig 8-4: Extraction efficiency of naphthalene using different sorbent platforms

## 8.4 Conclusion

The obtained results of the mesoporous adsorbents allow us to correlate their chemical and physical properties to the adsorption affinity, thus helping us to selectively choose the right adsorbent according to the targeted analyte.

Activated carbon nanoparticles show excellent performance toward the naphthalene with different extraction efficiency. In order to justify such differences, further work is required to study the physical and chemical properties of the ACs materials.

The iron loaded GN has shown a slight affinity toward the adsorption of naphthalene and this could be enhanced by modifying the surface of Fe-GN material with a polydopamine (PDA).

## **Chapter 9 : Conclusions and future work**



## 9.1 The removal of potentially toxic elements from aqueous solutions using MWD-MCM-41

MCM-41 silica material was successfully synthesized using room temperature hydrolysis and condensation conditions together with microwave and nitric acid/hydrogen peroxide digestion of the organic template. The incorporation of a microwave digestion step into the synthesis of MCM-41 allowed the preparation of materials over faster time periods whilst the highly ordered framework was retained. The data collected using the Nanosight system indicated that most of the particles were in the range of 200 to 500 nm. Furthermore, the results obtained from BET and TEM analysis show that the material has an average pore diameter of 6.74 nm and pore thickness of 2.08 nm. The surface of the material was modified with amino propyl functional group (AP-MCM-41) in order to create a suitable environment to attract chromium species and to study the possibility of the speciation and separation of chromium (VI) and chromium (III) from aqueous solutions. The material appeared to remove Cr (VI) effectively and selectively from the contaminated water solution. Removal involved monolayer interaction with the chelate on the silica surface and the functionalisation, and loading, could be tracked using FTIR spectroscopy. The adsorption capacity was extremely high when AP-MCM-41 produced using a MWD method was used (compared to a production method which used calcination) or even compared to SBA-15. Almost exclusive removal of Cr (VI) was achieved at pH 3 and moreover, the sorbent could be used to extract a wide range of other metal ions from water if its pH was modified above 7. No reduction in performance was observed even when removing Cr (VI) from water which contained other metal ions (e.g.  $\text{Ca}^{2+}$  and  $\text{Mg}^{2+}$ ) at significantly higher concentration. Examination of the effect of pore size distribution on adsorption provided evidence that the material's extremely high adsorption capacity was due to the larger pores and surface activation. With the Cr (VI) concentration range studied here, within 10 min more than 99 % of Cr (VI) was removed from solution. The microwave digestion method provides a material with (i) higher degree of functionalisation due to the production of more silanol groups on the surface of the material and (ii) larger pores compared to the materials reported in the literature.

The regeneration of mercapto propyl MWD-MCM-41 loaded with Hg (II) ions was also investigated with batch and dynamic methods using thiourea that was acidified using different acidic solutions (i.e. HNO<sub>3</sub>, H<sub>2</sub>SO<sub>4</sub>, and HCl); with HCl being the most efficient with recovery efficiency of almost 90 %. The dynamic method regeneration experiments were conducted using HCl / thiourea. The results indicated that a high elution efficiencies, of almost 100 % could be achieved; the high elution efficiency was attributed to the fact that the loaded sorbent was in contact continuously with acidified thiourea. Furthermore, the results indicated that it was possible to pre-concentrate Hg (II) from a large sample volume using this dynamic recovery method.

The use of high volume of hydrogen peroxide and nitric acid has resulted in the damage of the microwave vessels. Therefore, an attempt was made to optimize the operation conditions in order to see the effect of the time and the acids volume on the mesoporous silica materials. The results indicated that both time and acids volume added have significant effects on the textural properties of the resultant material. When the volume of H<sub>2</sub>O<sub>2</sub> is altered from 0.5 to 2 cm<sup>3</sup>, and different digestion times were used, the effect obtained on the average pore size was more significant with times of 5, 10 or 15 min producing materials with average pore sizes of 7, 12 and 14 nm, respectively. A new material was also prepared using resol as swelling agent that was incorporated into the framework of MCM-41 materials. The material exhibited a higher surface area of 711 m<sup>2</sup> g<sup>-1</sup>, a significantly larger pore volume (1.17 cm<sup>3</sup> g<sup>-1</sup>) and a larger average pore size (12 nm) compared to the previous studied material. However, the materials production method needs to be altered to extend vessel lifetime. Therefore, further work is required to assess the ability of using longer digestion times with lower volumes for both MCM-41 and Resol-MCM-41 materials.

## **9.2 Synthesis of iron supported on bioinspired green silica for the removal of arsenic ions from aqueous solution**

A new porous silica materials encapsulated with iron was successfully synthesised using bio-inspired route drawing the inspiration from bio-silicification process. The preparation of Fe-GN materials had the advantages of using neutral pH, room temperature conditions, rapid synthesis, and a substantial reduction in secondary pollution by the elimination of the need for organic solvents from the preparation method. These new iron encapsulated materials possessed unprecedented pore sizes for mesoporous materials with surface areas between 200-300 m<sup>2</sup> g<sup>-1</sup>. The addition of iron during synthesis was found to modify the silica framework produced. The incorporation of iron into the surface of GN resulted in a material with a porous system without the need for further thermal treatment to remove the organic template. This gives the material further advantages over the already present silica materials reported in the literature.

GN loaded with iron were found to be extremely efficient for the adsorption of As (V) from water (distilled, tap or river water). A maximum adsorption capacity of 34.82 mg of As (V)/g-h was obtained, which is higher than the maximum capacity of any materials reported to date for As (V) removal. Reduction in the performance was not observed even when removing As (V) from water that contained other metal ions (e.g. Mg<sup>2+</sup> and Ca<sup>2+</sup>) at significantly higher concentrations. What is perhaps key to deployment of this material in industrial applications is the successive use of GNs to remove pollutants from water in a continuous mode for at least 6 repeated applications (with the potential to go much further). Sorbent regeneration was possible readily, allowing ~100% recovery of As (V) and reuse of the sorbent for subsequent extraction at ~100% extraction efficiency. Further research is directed into the optimisation of the catalyst system by systematically varying the parameters of the green chemistry. Finally the GN loaded iron material was evaluated for the removal of naphthalene and has shown a slight affinity toward the adsorption of naphthalene.

### **9.3 Challenges of using nanomaterials for *in situ* groundwater remediation:**

Growing need to address environmental contamination has led to the development of many remediation technologies to treat soil, wastewater and groundwater contaminated by various pollutants, using *in situ* and *ex situ* methods. Sites that are subject to such contamination may require a combination of procedures to obtain the optimum remediation results for the prevailing conditions. Physical, chemical and biological technologies could be utilised in accordance with one another to minimise the risk of contamination to a safe level. Therefore, for a successful treatment, suitable selection, design, and adjustment of the operated remediation technology should be carried out based on the nature of the contaminated site and the type of contaminants as well as the performance of the system. One of the method used for groundwater remediation is known as pump and treat technologies. This method involves the withdrawal of the contaminated water from wells and trenches and treats it by above-ground (*ex situ*) processes such as carbon adsorption, air stripping, chemical precipitation or biological reactors. However, most of these methods resulted in highly contaminated waste which then has to be disposed off, hence require a high operation time which is undesirable due to the large operation and maintenance costs associated with it. A common type of *in situ* remediation method used for removing contaminants known as the permeable reactive barrier (PRB). PRBs are subsurface emplacement of reactive materials that extract or immobilize contaminants as the groundwater moves through the barrier, typically under natural gradient. The material chosen for the barrier is based on the target contaminants. One disadvantage of PRBs is that they can only remove contaminants that pass through them; they do not address dense non aqueous-phase liquids or contaminated groundwater that is beyond the barrier.

Nanotechnology has emerged as effective technologies for *in situ* treatment of groundwater contaminant source zones. Rapid advances in nanotechnology have led to the development of novel nanoparticles with unique and tunable physical and chemical properties. Their properties can be adjusted to produce a material that is highly reactive with common organic and inorganic pollutants, and to minimise the possibility of

forming unwanted toxic by-products. Many highly reactive nanoparticles such as iron nanoparticles have been developed specifically to remediate contamination by organic and inorganic contaminants. In principle, their small size (less than 500 nm) also provides the possibility to deliver these materials to subsurface contaminants (*in situ*), and provides access to contamination trapped in the smallest pores in an aquifer matrix. Highly mobile nanoparticles are required that can move in the subsurface to where contaminants are located, which increases the potential for off-site migration hence, the potential for any undesired ecotoxicity or human health risks. The high reactivity, and the ability of the nanoparticles to migrate directly to the contaminant source, indicates that nanoparticles can increase the degradation rate of contaminants in the source zone, and reduce the time and cost required for the remediation.

For the nanomaterial to be effective will have to meet the following requirements:

- The *in situ* remediation using reactive nanoparticles must take into account the products formed, as some of the reaction products may potentially be more toxic or mobile than the starting compounds and as a result increasing the risks posed by the site.
- The evaluation of the potential risks associated with the use of the studied nanomaterial before their widespread release and this requires a fundamental understanding of their long-term fate and lifetime.
- The used nanomaterials must consider the cost of those materials, as the costs of the material are likely to be significant portion of the remediation's total cost.
- Less particle aggregation, which can be achieved by surface functionalisation.
- The ability to target specific contaminants (selectivity) or to concentrate the nanoparticles in the contaminated source zone will be required to make *in situ* groundwater remediation cost effective.
- The geochemistry of each site (e.g. ionic composition, ionic strength, and pH) will dramatically affect the selectivity and mobility of produced nanomaterials in the subsurface and must be considered in their design and application.

## 9.4 Future work

The work on polycyclic hydrocarbon compounds (PAHs) will be continued and surface of the GN loaded iron material will be modified with a polydopamine (PDA) and re-evaluated for the adsorption of polycyclic hydrocarbon compounds (PAHs). Moreover, the present of amino molecule on the pores of as made Fe-GN along with the large pore size distribution will benefit targeting other potentially toxic elements such as chromium and mercury species which approved to have high affinity toward the amino group.

Several studied reported the successes on the incorporation of metals such as titanium and aluminium into the silica surface to control their surface properties and to impart catalytic functions on the pores surface. Therefore, GN material could be a great host surface for these metals in order to produce suitable surface properties for different applications such as adsorption and catalysis.

## Reference

1. Ishizaki K, Komarneni S, Nanko M: *Porous Materials: Process technology and applications*. Chapman & Hall; 1998.
2. KLABUNDE KJ, RICHARDS RM: **Nanoscale materials in chemistry**. *Recherche* 2009, **67**:02.
3. Zhao DY, Feng JL, Huo QS, Melosh N, Fredrickson GH, Chmelka BF, Stucky GD: **Triblock copolymer syntheses of mesoporous silica with periodic 50 to 300 angstrom pores**. *Science* 1998, **279**:548–552.
4. Zhao DY, Feng JL, Huo QS, Melosh N, Fredrickson GH, Chmelka BF, Stucky GD: **Triblock copolymer syntheses of mesoporous silica with periodic 50 to 300 angstrom pores**. *Science* 1998, **279**:548–552.
5. Li Q, Brown SE, Broadbelt LJ, Zheng JG, Wu NQ: **Synthesis and characterization of MCM-41-supported Ba<sub>2</sub>SiO<sub>4</sub> base catalyst**. *Microporous and Mesoporous Materials* 2003, **59**:105–111.
6. Beck JS, Vartuli JC, Roth WJ, Leonowicz ME, Kresge CT, Schmitt KD, Chu CTW, Olson DH, Sheppard EW: **A new family of mesoporous molecular sieves prepared with liquid crystal templates**. *J. Am. Chem. Soc.* 1992, **114**:10834–10843.
7. Sing KW, Davis BH: **Handbook of Porous Solids**. 2002, **1**:3–15–18.
8. MacBain JW: *The sorption of gases and vapours by solids*. Routledge; 1932.
9. Barrer RM, Brook DW: **Molecular diffusion in chabazite, mordenite and levynite**. *Transactions of the Faraday Society* 1953, **49**.
10. Breck DW, Eversole WG, Milton RM: **New synthetic crystalline zeolites**. *J. Am. Chem. Soc.* 1956, **78**:2338–2339.
11. Breck DW, Eversole WG, Milton RM, Reed TB, Thomas TL: **Crystalline Zeolites. I. The Properties of a New Synthetic Zeolite, Type A**. *J. Am. Chem. Soc.* 1956, **78**:5963–5972.
12. Lok BM, Messina CA, Patton RL, Gajek RT, Cannan TR, Flanigen EM: **Silicoaluminophosphate molecular sieves: another new class of microporous crystalline inorganic solids**. *J. Am. Chem. Soc.* 1984, **106**:6092–6093.
13. Wilson Stephen T, Lok BM, Messina CA, Cannan TR, Flanigen EM: **Aluminophosphate molecular sieves: a new class of microporous crystalline inorganic solids**. *J. Am. Chem. Soc.* 1982, **104**:1146–1147.

14. Zhao XS, GQ Max Lu A, Millar GJ: **Advances in mesoporous molecular sieve MCM-41**. *Ind. Eng. Chem. Res.* 1996, **35**:2075–2090.
15. Young SK: **Sol-Gel Science for Ceramic Materials**. *sigmaaldrich.com* 2006.
16. Baldini F: *Optical chemical sensors*. Springer Verlag; 2006.
17. Sakka S: *Handbook of sol-gel science and technology: processing, characterization and applications*. Springer; 2005.
18. Wen JY, Wilkes GL: **Organic/inorganic hybrid network materials by the sol-gel approach**. *Chem. Mater.* 1996, **8**:1667–1681.
19. ALOthman Z: **A Review: Fundamental Aspects of Silicate Mesoporous Materials**. *Materials* 2012, **5**:2874–2902.
20. RAJPUT NVAS: **MESOPOROUS MATERIAL, MCM41: A NEW DRUG CARRIER**. *Asian J Pharm Clin Res* 2011, **4**:44–53.
21. Yanagisawa T, Shimizu T, Kuroda K, Kato C: **The preparation of alkyltrimethylammonium-kanemite complexes and their conversion to microporous materials**. *Bull. Chem. Soc. Jpn.* 1990, **63**:988–992.
22. Kresge CT, Leonowicz ME, Roth WJ, Vartuli JC, Beck JS: **Ordered mesoporous molecular-sieves synthesized by a liquid-crystal template mechanism**. *Nature* 1992, **359**:710–712.
23. Bruce DW, Walton R, O'Hare D: *Porous materials*. Wiley; 2011.
24. Sharifi M, Marschall R, Wilhelm M, Wallacher D, Wark M: **Detection of Homogeneous Distribution of Functional Groups in Mesoporous Silica by Small Angle Neutron Scattering and in Situ Adsorption of Nitrogen or Water**. *Langmuir* 2011.
25. Rathousky J, Zukal A, Franke O, Schulz-Ekloff G: **Adsorption on MCM-41 mesoporous molecular sieves. Part 1.-Nitrogen isotherms and parameters of the porous structure**. *Faraday Trans.* 1994, **90**.
26. Branton PJ, Hall PG, Treguer M, Sing KSW: **Adsorption of carbon dioxide, sulfur dioxide and water vapour by MCM-41, a model mesoporous adsorbent**. *Faraday Trans.* 1995, **91**.
27. Thomas JM: **The chemistry of crystalline sponges**. *Nature* 1994, **368**:289–290.
28. Belmabkhout Y, Serna-Guerrero R, Sayari A: **Adsorption of CO<sub>2</sub>-containing gas mixtures over amine-bearing pore-expanded MCM-41 silica: application for CO<sub>2</sub> separation**. *Adsorption* 2011.



29. Xia M, Chen C, Long MC, Cai WM, Zhou BX: **Magnetically separable mesoporous silica nanocomposite and its application in Fenton catalysis.** *Microporous and Mesoporous Materials* 2011, **145**:217–223.
30. Corma A, Martinez A, Martinez-Soria V: **Hydrocracking of vacuum gasoil on the novel mesoporous MCM-41 aluminosilicate catalyst.** *Journal Name: Journal of Catalysis; Journal Volume: 153; Journal Issue: 1; Other Information,* 1995.
31. Vartuli JC, Schmitt KD, Kresge CT, Roth WJ, Leonowicz ME, McCullen SB, Hellring SD, Beck JS, Schlenker JL: **Effect of surfactant/silica molar ratios on the formation of mesoporous molecular sieves: inorganic mimicry of surfactant liquid-crystal phases and mechanistic implications.** *Chem. Mater.* 1994, **6**:2317–2326.
32. Monnier A, Schüth F, Huo Q, Kumar D, Margolese D, Maxwell RS, Stucky GD, Krishnamurty M, Petroff P, Firouzi A, et al.: **Cooperative formation of inorganic-organic interfaces in the synthesis of silicate mesostructures.** *Science* 1993, **261**:1299–1303.
33. Occelli ML, Biz S: **Surfactant effects on the physical properties of mesoporous silica and silicates.** *Journal of Molecular Catalysis A: Chemical* 2000, **151**:225–231.
34. Osei-Prempeh G, Lehmler H-J, Rankin SE, Knutson BL: **Direct synthesis and accessibility of amine-functionalized mesoporous silica templated using fluorinated surfactants.** *Ind. Eng. Chem. Res.* 2011, **50**:5510–5522.
35. AlOthman ZA, Apblett AW: **Synthesis and characterization of a hexagonal mesoporous silica with enhanced thermal and hydrothermal stabilities.** *Applied Surface Science* 2010, **256**:3573–3580.
36. Athens GL, Shayib RM, Chmelka BF: **Functionalization of mesostructured inorganic, Åiorganic and porous inorganic materials.** *Current Opinion in Colloid & Interface Science* 2009, **14**:281–292.
37. Brühwiler D: **Postsynthetic functionalization of mesoporous silica.** *Nanoscale* 2010, **2**:887.
38. Blin JL, Du N, Stébé MJ: **Solubilization of alcohols in a non-ionic flourinated surfactant-based system: Effects on the characteristics of mesoporous silica.** *Journal of Colloid and Interface Science* 2012, **373**:34–45.
39. Anderson MT, Martin JE, Odinek JG, Newcomer PP: **Effect of methanol concentration on CTAB micellization and on the formation of surfactant-templated silica (sts) .** *Chem. Mater.* 1998, **10**:1490–1500.
40. Lebedev OI, Van Tendeloo G, Collart O, Cool P, Vansant EF: **Structure and**

- microstructure of nanoscale mesoporous silica spheres. *Solid State Sciences* 2004, **6**:489–498.**
41. Myers D: *Surfactant Science and Technology*. Wiley-VCH; 2005.
  42. Myers D, Wiley J: *Surfactant science and technology*. Wiley Online Library; 1988.
  43. Peter F: **Micelle structure: a surfactant-block model.** *Chemical physics letters* 1981, **77**:460–466.
  44. Lindlar B, Kogelbauer A, J Kooyman P, Prins R: **Synthesis of large pore silica with a narrow pore size distribution.** *Microporous and Mesoporous Materials* 2001, **44-45**:89–94.
  45. Boissiere C, Martines MAU, Tokumoto M, Larbot A, Prouzet E: **Mechanisms of Pore Size Control in MSU-X Mesoporous Silica.** *Chem. Mater.* 2002, **15**:509–515.
  46. Blin JL, Su BL: **Tailoring pore size of ordered mesoporous silicas using one or two organic auxiliaries as expanders.** *Langmuir* 2002, **18**:5303–5308.
  47. Boissière C, Larbot A, Bourgaux C, Prouzet E, Bunton CA: **A Study of the Assembly Mechanism of the Mesoporous MSU-X Silica Two-Step Synthesis.** *Chem. Mater.* 2001, **13**:3580–3586.
  48. Wan Y, Zhao D: **On the controllable soft-templating approach to mesoporous silicates.** *Chem. Rev.* 2007, **107**:2821–2860.
  49. Zhao D, Sun J, Li Q, Stucky GD: **Morphological control of highly ordered mesoporous silica SBA-15.** *Chem. Mater.* 2000, **12**:275–279.
  50. Kumar P, Mal N, Oumi Y, Yamana K, Sano T: **Mesoporous materials prepared using coal fly ash as the silicon and aluminium source.** *J. Mater. Chem.* 2001, **11**:3285–3290.
  51. Chang HL, Chun CM, Aksay IA, Shih WH: **Conversion of fly ash into mesoporous aluminosilicate.** *Ind. Eng. Chem. Res.* 1999, **38**:973–977.
  52. Bagshaw SA, Testa F: **Wairakei geothermal silica, a low cost reagent for the synthesis of mesostructured M41S aluminosilicate molecular sieves.** *Microporous and Mesoporous Materials* 2000, **39**:67–75.
  53. Chareonpanich M, Nanta-ngern A, Limtrakul J: **Short-period synthesis of ordered mesoporous silica SBA-15 using ultrasonic technique.** *Materials Letters* 2007, **61**:5153–5156.
  54. Tungkananurak K, Kerdsiri S, Jadsadapattarakul D, Burns DT: **Semi-micro**

- preparation and characterization of mesoporous silica microspheres from rice husk sodium silicate using a non-ionic surfactant as a template: application in normal phase HPLC columns.** *Microchim Acta* 2007, **159**:217–222.
55. Tanev PT, Pinnavaia TJ: **Mesoporous silica molecular sieves prepared by ionic and neutral surfactant templating: a comparison of physical properties.** *Chem. Mater.* 1996, **8**:2068–2079.
56. Bagshaw SA, Bruce IJ: **Rapid calcination of high quality mesostructured MCM-41, MSU-X, and SBA-15 silicate materials: A step towards continuous processing?** *Microporous and Mesoporous Materials* 2008, **109**:199–209.
57. Keene MTJ, Gougeon RDM, Denoyel R, Harris RK, Rouquerol J, Llewellyn PL: **Calcination of the MCM-41 mesophase: mechanism of surfactant thermal degradation and evolution of the porosity.** *J. Mater. Chem.* 1999, **9**:2843–2849.
58. Be rube F, Kaliaguine S: **Calcination and thermal degradation mechanisms of triblock copolymer template in SBA-15 materials.** *Microporous and Mesoporous Materials* 2008, **115**:469–479.
59. Kleitz F, Schmidt W, Schüth F: **Calcination behavior of different surfactant-templated mesostructured silica materials.** *Microporous and Mesoporous Materials* 2003, **65**:1–29.
60. Ryoo R, Kim JM: **Structural order in MCM-41 controlled by shifting silicate polymerization equilibrium.** *J. Chem. Soc., Chem. Commun.* 1995.
61. Yang CM, Zibrowius B, Schmidt W, Schüth F: **Stepwise removal of the copolymer template from mesopores and micropores in SBA-15.** *Chem. Mater.* 2004, **16**:2918–2925.
62. Kawi S, Lai MW: **Supercritical fluid extraction of surfactant from Si-MCM-41.** *Aiche Journal* 2002, **48**:1572–1580.
63. Huang L, Kawi S, Poh C, Hidajat K, Ng SC: **Extraction of cationic surfactant templates from mesoporous materials by CH<sub>3</sub>OH-modified CO<sub>2</sub> supercritical fluid.** *Talanta* 2005, **66**:943–951.
64. Tian B, Liu X, Yu C, Gao F, Luo Q, Xie S, Tu B, Zhao D: **Microwave assisted template removal of siliceous porous materials.** *Chem. Commun.* 2002.
65. Idris SA, Davidson CM, McManamon C, Morris MA, Anderson P, Gibson LT: **Large pore diameter MCM-41 and its application for lead removal from aqueous media.** *Journal of Hazardous Materials* 2011, **185**:898–904.

66. Wan Y, Zhang D, Hao N, Zhao D: **Organic groups functionalised mesoporous silicates.** *International Journal of Nanotechnology* 2007, **4**:66–99.
67. Burkett SL, Sims SD, Mann S: **Synthesis of hybrid inorganic/organic mesoporous silica by co-condensation of siloxane and organosiloxane precursors.** *Chem. Commun.* 1996.
68. Lim MH, Blanford CF, Stein A: **Synthesis of ordered microporous silicates with organosulfur surface groups and their applications as solid acid catalysts.** *Chem. Mater.* 1998, **10**:467-470.
69. Walcarius A, Mercier L: **Mesoporous organosilica adsorbents: nanoengineered materials for removal of organic and inorganic pollutants.** *J. Mater. Chem.* 2010, **20**:4478.
70. Sayari A, Hamoudi S: **Periodic Mesoporous Silica-Based Organic, Inorganic Nanocomposite Materials.** *Chem. Mater.* 2001, **13**:3151–3168.
71. Macquarrie DJ: **Direct preparation of organically modified MCM-type materials. Preparation and characterisation of aminopropyl-MCM and 2-cyanoethyl-MCM.** *Chem. Commun.* 1996.
72. Liu J, Shin Y, Nie Z, Chang JH, Wang LQ, Fryxell GE, Samuels WD, Exarhos GJ: **Molecular assembly in ordered mesoporosity: A new class of highly functional nanoscale materials.** *The Journal of Physical Chemistry A* 2000, **104**:8328–8339.
73. Lim MH, Stein A: **Comparative Studies of Grafting and Direct Syntheses of Inorganic, Organic Hybrid Mesoporous Materials.** *Chem. Mater.* 1999, **11**:3285–3295.
74. Lindén M, Schacht S, Schuth F, Steel A, Unger KK: **Recent Advances in Nano- and Macroscale Control of Hexagonal, Mesoporous Materials.** *J Porous Mater* 1998, **5**:177–193.
75. Chen CY, Li HX, Davis ME: **Studies on mesoporous materials:: I. Synthesis and characterization of MCM-41.** *Microporous Materials* 1993, **2**:17–26.
76. Huo Q, Margolese DI, Ciesla U, Demuth DG, Feng P, Gier TE, Sieger P, Firouzi A, Chmelka BF: **Organization of organic molecules with inorganic molecular species into nanocomposite biphasic arrays .** *Chem. Mater.* 1994, **6**:1176–1191.
77. Huo Q, Margolese DI, Ciesla U, Feng P, Gier TE, Sieger P, Leon R, Petroff PM, Schuth F, Stucky GD: **Generalized synthesis of periodic surfactant/inorganic composite materials.** *Nature* 1994, **368**:317–321.
78. Tanev PT, Pinnavaia TJ: **A neutral templating route to mesoporous molecular sieves.** *Science* 1995, **267**:865–867.

79. Bagshaw SA, Prouzet E, Pinnavaia TJ: **Templating of mesoporous molecular sieves by nonionic polyethylene oxide surfactants.** *Science* 1995, **269**:1242–1244.
80. Roth WJ, Vartuli JC: **Synthesis of mesoporous molecular sieves.** *Studies in Surface Science and Catalysis* 2005, **157**:91–110.
81. Morishige K, Tateishi M: **Accurate relations between pore size and the pressure of capillary condensation and the evaporation of nitrogen in cylindrical pores.** *Langmuir* 2006, **22**:4165–4169.
82. Nordstrom DK: **Worldwide Occurrences of Arsenic in Ground Water.** *Science* 2002, **296**:2143–2145.
83. Smith AH, Lingas EO, Rahman M: **Contamination of drinking-water by arsenic in Bangladesh: a public health emergency.** *Bull. World Health Organ.* 2000, **78**:1093–1103.
84. Meharg AA, Rahman M: **Arsenic contamination of Bangladesh paddy field soils: Implications for rice contribution to arsenic consumption.** *Environ. Sci. Technol.* 2003, **37**:229–234.
85. Gurian PL, Small MJ, Lockwood JR, Schervish MJ: **Addressing uncertainty and conflicting cost estimates in revising the arsenic MCL.** *Environ. Sci. Technol.* 2001, **35**:4414–4420.
86. U.S. Environmental Protection Agency (Ed): *National Primary Drinking Water Regulations; Arsenic and Clarifications to Compliance and New Source Contaminants Monitoring.* (accessed Oct 11, 2014).
87. Lyshevski SE, Contescu CI, Putyera K: *Dekker Encyclopedia of Nanoscience and Nanotechnology, Second Edition - Six Volume Set.* CRC Press; 2008.
88. Price PM, Clark JH, Macquarrie DJ: **Modified silicas for clean technology.** *J. Chem. Soc.-Dalton Trans.* 2000.
89. Parida K, Mishra KG, Dash SK: **Adsorption of copper(ii) on NH<sub>2</sub>-MCM-41 and its application for epoxidation of styrene.** *Ind. Eng. Chem. Res.* 2012, **51**:2235–2246.
90. Heidari A, Younesi H, Mehraban Z: **Removal of Ni(II), Cd(II), and Pb(II) from a ternary aqueous solution by amino functionalized mesoporous and nano mesoporous silica.** *Chemical Engineering Journal* 2009, **153**:70–79.
91. Idris SA, Harvey SR, Gibson LT: **Selective extraction of mercury(II) from water samples using mercapto functionalised-MCM-41 and regeneration of the sorbent using microwave digestion.** *Journal of Hazardous Materials* 2011, **193**:171–176.

92. Lam KF, Yeung KL, McKay G: **A Rational Approach in the Design of Selective Mesoporous Adsorbents.** *Langmuir* 2006, **22**:9632–9641.
93. Akl MAA, Kenawy IMM, Lasheen RR: **Organically modified silica gel and flame atomic absorption spectrometry: employment for separation and preconcentration of nine trace heavy metals for their determination in natural aqueous systems.** *Microchemical Journal* 2004, **78**:143–156.
94. Ribeiro Carrott MML, Est v o Candeias AJ, Carrott PJM, Unger KK: **Evaluation of the Stability of Pure Silica MCM-41 toward Water Vapor.** *Langmuir* 1999, **15**:8895–8901.
95. Trong On D, Zaidi SMJ, Kaliaguine S: **Stability of mesoporous aluminosilicate MCM-41 under vapor treatment, acidic and basic conditions.** *Microporous and Mesoporous Materials* 1998, **22**:211–224.
96. Ryoo R, Jun S: **Improvement of hydrothermal stability of MCM-41 using salt effects during the crystallization process.** *Journal of Physical Chemistry B* 1997, **101**:317–320.
97. Kisler JM, Gee ML, Stevens GW, O'Connor AJ: **Comparative Study of Silylation Methods to Improve the Stability of Silicate MCM-41 in Aqueous Solutions.** *Chem. Mater.* 2003, **15**:619–624.
98. Gusev VY, Feng X, Bu Z, Haller GL, O'Brien JA: **Mechanical Stability of Pure Silica Mesoporous MCM-41 by Nitrogen Adsorption and Small-Angle X-ray Diffraction Measurements.** *The Journal of Physical Chemistry* 1996, **100**:1985–1988.
99. Hartmann M, Vinu A: **Comparison of the mechanical stability of cubic and hexagonal meso- porous molecular sieves with different pore sizes.** In *Studies in Surface Science and Catalysis*. Edited by Sang-Eon Park RRW-SACWL, Jong-San C. Elsevier; 2003:285–288.
100. Rouquerol J, Rouquerol F, Llewellyn P, Maurin G, Sing KS: **Adsorption by powders and porous solids: principles, methodology and applications.** 2014.
101. SING K, EVERETT DH, HAUL R, MOSCOU L, PIEROTTI RA, Rouquerol J, SIEMIENIEWSKA T: **Reporting physisorption data for gas solid systems with special reference to the determination of surface-area and porosity (Recommendations 1984).** *Pure Appl. Chem.* 1985, **57**:603–619.
102. Wang W: **The pore structure of phosphoaluminate cement.** *OJCM* 2012, **02**:104–112.
103. Griffiths P, De Haseth JA: **Fourier transform infrared spectrometry, A JOHN WILEY & SONS, INC, 2007, 171.**

104. Derrick MR, Stulik D, Landry JM: **infrared\_spectroscopy**. 2009.
105. James W Robinson: **Undergraduate instrumental analysis**. 2005.
106. Harris DC: *Quantitative Chemical Analysis*. W H Freeman & Company; 2007.
107. Rouessac F, Rouessac A: **Chemical analysis: Modern instrumentation methods and techniques**. 2007.
108. Kollander B: **Inductively coupled plasma atomic emission spectrometry: exploring the limits of different sample preparation strategies**. 2011.
109. Boss CB, Fredeen KJ: *Concepts, Instrumentation and Techniques in Inductively Coupled Plasma Optical Emission Spectrometry*. 2004.
110. Hou X, Jones BT: **Inductively coupled plasma/optical emission spectrometry**. *Encyclopedia of Analytical Chemistry* 2000.
111. Girard JE, Girard J: *Principles of Environmental Chemistry*. Jones & Bartlett Publishers; 2014.
112. MANNING TJ, Grow WR: **Inductively coupled plasma-atomic emission spectrometry**. *The chemical educator* 1997, **2**:1–19.
113. University of california: **Plasma diagnostics**. *tempest.das.ucdavis.edu* , (accessed Oct 16, 2014).
114. Marcus RK, Broekaert JAC: *Glow Discharge Plasmas in Analytical Spectroscopy*. John Wiley & Sons; 2003.
115. McFee C: **An introduction to CCD operation** . *mssl.ucl.ac.uk* , (accessed Oct 14, 2014)
116. Heftmann E: *Chromatography*. Elsevier; 2004.
117. Tissue BM: *Basics of Analytical Chemistry and Chemical Equilibria*. John Wiley & Sons; 2013.
118. Christian GD, Dasgupta PS, Schug K: *Analytical Chemistry, 7th Edition*. Wiley Global Education; 2013.
119. Skoog DA, West DM, Holler JF, Crouch SR: **Fundamentals of analytical chemistry**. *Cole, Belmont* 2004.
120. Ewlad-Ahmed AM, Morris MA, Patwardhan SV, Gibson LT: **Removal of formaldehyde from air using functionalized silica supports**. *Environ. Sci. Technol.* 2012, **46**:13354–13360.
121. ankersmid.co.ro

[http://www.ankersmid.co.ro/AutoFiles/doc/3253\\_NanoSight\\_LM20\\_Specificatio\\_n\\_Sheetv2.0.pdf](http://www.ankersmid.co.ro/AutoFiles/doc/3253_NanoSight_LM20_Specificatio_n_Sheetv2.0.pdf) (accessed Oct 9, 2014).

122. Bayramoglu G, Altintas B, Arica MY: **Synthesis and characterization of magnetic beads containing aminated fibrous surfaces for removal of Reactive Green 19 dye: kinetics and thermodynamic parameters.** *J. Chem. Technol. Biotechnol.* 2012, **87**:705–713.
123. Guo TY, Xia YQ, Hao GJ, Song MD, Zhang BH: **Adsorptive separation of hemoglobin by molecularly imprinted chitosan beads.** *Biomaterials* 2004, **25**:5905–5912.
124. Pan J, Zou X, Wang X, Guan W, Yan Y, Han J: **Selective recognition of 2,4-dichlorophenol from aqueous solution by uniformly sized molecularly imprinted microspheres with  $\beta$ -cyclodextrin/attapulgitite composites as support.** *Chemical Engineering Journal* 2010, **162**:910–918.
125. Febrianto J, Kosasih AN, Sunarso J, Ju Y-H, Indraswati N, Ismadji S: **Equilibrium and kinetic studies in adsorption of heavy metals using biosorbent: A summary of recent studies.** *Journal of Hazardous Materials* 2009, **162**:616–645.
126. Jachula J, Hubicki Z: **Removal of Cr(VI) and As(V) ions from aqueous solutions by polyacrylate and polystyrene anion exchange resins.** *Appl Water Sci* 2013, **3**:653–664.
127. MATOUG IOM: *Analysis of Suspended Solids in River Water to Assess Their Role in Metal Transport.* University of Glasgow; 2011.
128. Davis ME: **Ordered porous materials for emerging applications.** *Nature* 2002, **417**:813–821.
129. Barton TJ, Bull LM, Klemperer WG, Loy DA, McEnaney B, Misono M, Monson PA, Pez G, Scherer GW, Vartuli JC, et al.: **Tailored Porous Materials.** *Chem. Mater.* 1999, **11**:2633–2656.
130. Selvam P, Bhatia SK, Sonwane CG: **Recent advances in processing and characterization of periodic mesoporous MCM-41 silicate molecular sieves.** *Ind. Eng. Chem. Res.* 2001, **40**:3237–3261.
131. Zhang Y, Wu D, Sun YH, Peng SY: **Synthesis of more stable MCM-41 under high-pressurized conditions.** *Materials Letters* 2002, **55**:17–19.
132. Lin W, Cai Q, Pang W, Yue Y, Zou B: **New mineralization agents for the synthesis of MCM-41.** *Microporous and Mesoporous Materials* 1999, **33**:187–196.
133. Brühwiler D, Frei H: **Structure of Ni(II) and Ru(III) ammine complexes**



- grafted onto mesoporous silicate sieve. *J. Phys. Chem. B* 2003, **107**:8547–8556.**
134. Ritter H, Nieminen M, Karppinen M, Brühwiler D: **A comparative study of the functionalization of mesoporous silica MCM-41 by deposition of 3-aminopropyltrimethoxysilane from toluene and from the vapor phase.** *Microporous and Mesoporous Materials* 2009, **121**:79–83.
135. Hitz S, Prins R: **Influence of template extraction on structure, activity, and stability of MCM-41 catalysts.** *Journal of Catalysis* 1997, **168**:194–206.
136. Shen SC, Kawi S: **MCM-41 with improved hydrothermal stability: formation and prevention of Al content dependent structural defects.** *Langmuir* 2002, **18**:4720–4728.
137. Xiao L, Li J, Jin H, Xu R: **Removal of organic templates from mesoporous SBA-15 at room temperature using UV/dilute H<sub>2</sub>O<sub>2</sub>.** *Microporous and Mesoporous Materials* 2006, **96**:413–418.
138. Yang LM, Wang YJ, Luo GS, Dai YY: **Simultaneous removal of copolymer template from SBA-15 in the crystallization process.** *Microporous and Mesoporous Materials* 2005, **81**:107–114.
139. Kawi S: **Supercritical fluid extraction of surfactant template from MCM-41.** *Chem. Commun.* 1998.
140. Van Grieken R, Calleja G, Stucky GD, Melero JA, García RA, Iglesias J: **Supercritical fluid extraction of a nonionic surfactant template from SBA-15 materials and consequences on the porous structure.** *Langmuir* 2003, **19**:3966–3973.
141. Gu D, Zhang F, Shi Y, Zhang F, Wu Z, Deng Y, Zhang L, Tu B, Zhao D: **A “teardown” method to create large mesotunnels on the pore walls of ordered mesoporous silica.** *Journal of Colloid and Interface Science* 2008, **328**:338–343.
142. SANSALONE J, BUCHBERGER S: **Characterization of solid and metal element distributions in urban highway stormwater.** *Water Science and Technology* 1997, **36**:155–160.
143. Pashley RM, Karaman ME: **Applied colloid and surface chemistry.** 2004.
144. Evangelista SM, DeOliveira E, Castro GR, Zara LF, Prado AGS: **Hexagonal mesoporous silica modified with 2-mercaptothiazoline for removing mercury from water solution.** *Surface Science* 2007, **601**:2194–2202.
145. Liu R, Shi Y, Wan Y, Meng Y, Zhang F, Gu D, Chen Z, Tu B, Zhao D: **Triconstituent co-assembly to ordered mesostructured polymer–silica and carbon–silica nanocomposites and large-pore mesoporous carbons with high**

- surface areas. *J. Am. Chem. Soc.* 2006, **128**:11652–11662.
146. Kotas J, Stasicka Z: **Chromium occurrence in the environment and methods of its speciation.** *Environmental Pollution* 2000, **107**:263–283.
147. Gupta VK, Rastogi A, Nayak A: **Adsorption studies on the removal of hexavalent chromium from aqueous solution using a low cost fertilizer industry waste material.** *Journal of Colloid and Interface Science* 2010, **342**:135–141.
148. Katz SA, Salem H: **The toxicology of chromium with respect to its chemical speciation: A review.** *Journal of Applied Toxicology* 1993, **13**:217–224.
149. Hawley EL, Deeb RA, Kavanaugh MC, Jacobs JA: **Treatment technologies for chromium (VI).** *Chromium (VI) handbook* 2004.
150. Eastmond DA, MacGregor JT, Slesinski RS: **Trivalent Chromium: Assessing the Genotoxic Risk of an Essential Trace Element and Widely Used Human and Animal Nutritional Supplement.** *Critical Reviews in Toxicology* 2008, **38**:173–190.
151. Beneitez P, Ayllon S: **Extraction studies on the system between bis(2-ethylhexyl) phosphoric acid and chromium(iii) in several aqueous solutions.** *Solvent Extraction and Ion Exchange* 1987, **5**:597–609.
152. Hansen MB, Johansen JD, Menné T: **Chromium allergy: significance of both Cr(III) and Cr(VI).** *Contact Derm.* 2003, **49**:206–212.
153. Petruzzelli D, Passino R, Tiravanti G: **Ion exchange process for chromium removal and recovery from tannery wastes.** *Ind. Eng. Chem. Res.* 1995, **34**:2612–2617.
154. IARC Working Group on the Evaluation of Carcinogenic Risks to Humans: **Arsenic, metals, fibres, and dusts.** *IARC Monogr Eval Carcinog Risks Hum* 2012, **100**:11–465.
155. Zhao D, SenGupta AK, Stewart L: **Selective removal of cr(vi) oxyanions with a new anion exchanger.** *Ind. Eng. Chem. Res.* 1998, **37**:4383–4387.
156. Zaporozhets O, Petruniack N, Sukhan V: **Determination of Ag(I), Hg(II) and Pb(II) by using silica gel loaded with dithizone and zinc dithizonate.** *Talanta* 1999, **50**:865–873.
157. Javadian H, Ghaemy M, Taghavi M: **Adsorption kinetics, isotherm, and thermodynamics of Hg<sup>2+</sup> to polyaniline/hexagonal mesoporous silica nanocomposite in water/wastewater.** *J Mater Sci* 2013, **49**:232–242.
158. Hakami O, Zhang Y, Banks CJ: **Thiol-functionalised mesoporous silica-coated**

- magnetite nanoparticles for high efficiency removal and recovery of Hg from water.** *Water Research* 2012, **46**:3913–3922.
159. Zhang L, Goh S, Hu X, Crawford R, Yu A: **Removal of aqueous toxic Hg(II) by functionalized mesoporous silica materials.** *J. Chem. Technol. Biotechnol.* 2012, **87**:1473–1479.
160. Wang Q, Chang X, Li D, Hu Z, Li R, He Q: **Adsorption of chromium(III), mercury(II) and lead(II) ions onto 4-aminoantipyrine immobilized bentonite.** *Journal of Hazardous Materials* 2011, **186**:1076–1081.
161. Benhamou A, Baudu M, Derriche Z, Basly JP: **Aqueous heavy metals removal on amine-functionalized Si-MCM-41 and Si-MCM-48.** *Journal of Hazardous Materials* 2009, **171**:1001–1008.
162. Liu Y, Guo L, Zhu L, Sun X, Chen J: **Chemical Engineering Journal.** *Chemical Engineering Journal* 2010, **158**:108–114.
163. Taha AA, Qiao J, Li F, Zhang B: **Preparation and application of amino functionalized mesoporous nanofiber membrane via electrospinning for adsorption of Cr.** *J Environ Sci (China)* 2012, **24**:610–616.
164. Mureseanu M, Reiss A, Stefanescu I, David E, Parvulescu V, Renard G, Hulea V: **Chemosphere.** *Chemosphere* 2008, **73**:1499–1504.
165. Li J, Miao X, Hao Y, Zhao J, Sun X, Wang L: **Synthesis, amino-functionalization of mesoporous silica and its adsorption of Cr(VI).** *Journal of Colloid and Interface Science* 2008, **318**:309–314.
166. Kurniawan TA, Chan GYS, Lo W-H, Babel S: **Physico-chemical treatment techniques for wastewater laden with heavy metals.** *Chemical Engineering Journal* 2006, **118**:83–98.
167. Greenberg AE, Eaton AD, Clesceri LS: *Standard Methods for the Examination of Water and Wastewater.* American Public Health Association; 1999.
168. Vaiopoulou E, Gikas P: **Effects of chromium on activated sludge and on the performance of wastewater treatment plants: A review.** *Water Research* 2012, **46**:549–570.
169. Long X, Miró M, Hansen EH: **Universal approach for selective trace metal determinations via sequential injection–bead injection–lab-on-valve using renewable hydrophobic bead surfaces as reagent carriers.** *Anal. Chem.* 2005, **77**:6032–6040.
170. Ho YS, McKay G: **Application of kinetic models to the sorption of copper (II) on to peat.** *Adsorption Science & Technology* 2002, **20**:797–815.

171. Ho Y-S: **Second-order kinetic model for the sorption of cadmium onto tree fern: A comparison of linear and non-linear methods.** *Water Research* 2006, **40**:119–125.
172. Weber WJ, Morris JC: **Kinetics of adsorption on carbon from solution.** *J. Sanit. Eng. Div. Am. Soc. Civ. Eng* 1963, **89**:31–60.
173. Gupta Sen S, Bhattacharyya KG: **Kinetics of adsorption of metal ions on inorganic materials: A review.** *Advances in Colloid and Interface Science* 2011, **162**:39–58.
174. Pérez-Quintanilla D, Hierro ID, Fajardo M, Sierra I: **2-Mercaptothiazoline modified mesoporous silica for mercury removal from aqueous media.** *Journal of Hazardous Materials* 2006, **134**:245–256.
175. Gurgel LVA, de Melo JCP, de Lena JC, Gil LF: **Bioresource Technology.** *Bioresource Technology* 2009, **100**:3214–3220.
176. Coates J: **Interpretation of infrared spectra, a practical approach.** *Encyclopedia of Analytical Chemistry* 2000.
177. Budiasih KS, Anwar C, Santosa SJ, Ismail H: **Synthesis and Characterization of Chromium (III) Complexes with L-Glutamic Acid, Glycine and L-Cysteine.** *World Academy of Science, Engineering and Technology, International Science Index* 78 2013, **7**:1924–1928.
178. Kapakoglou NI, Giokas DL, Tsogas GZ, Vlessidis AG: **Coacervation of surface-functionalized polymerized vesicles derived from ammonium bromide surfactants. application to the selective speciation of chromium in environmental samples.** *Anal. Chem.* 2008, **80**:9787–9796.
179. Ghiaci, Kia, Abbaspur: **Adsorption of chromate by surfactant-modified zeolites and MCM-41 molecular sieve.** *Separation and Purification Technology* 2004, **40**:11–11.
180. Mohan D, Singh KP, Singh VK: **Removal of hexavalent chromium from aqueous solution using low-cost activated carbons derived from agricultural waste materials and activated carbon fabric cloth.** *Ind. Eng. Chem. Res.* 2005, **44**:1027–1042.
181. Yoshitake H, Yokoi T, Tatsumi T: **Adsorption of chromate and arsenate by amino-functionalized MCM-41 and SBA-1.** *Chem. Mater.* 2002, **14**:4603–4610.
182. Phuengprasop T, Sittiwong J, Unob F: **Removal of heavy metal ions by iron oxide coated sewage sludge.** *Journal of Hazardous Materials* 2011, **186**:502–507.

183. Memon J-U-R, Memon SQ, Bhangar MI, Khuhawar MY: **Use of modified sorbent for the separation and preconcentration of chromium species from industrial waste water.** *Journal of Hazardous Materials* 2009, **163**:511–516.
184. Ding P, Huang K-L, Li G-Y, Zeng W-W: **Mechanisms and kinetics of chelating reaction between novel chitosan derivatives and Zn(II).** *Journal of Hazardous Materials* 2007, **146**:58–64.
185. Gili P, Lorenzo-Luis PA: **Compounds of chromium(VI) as ligands.** *Coordination Chemistry Reviews* 1999, **193-5**:747–768.
186. Sundberg MR, Valo J, Uggla R, Melnik M: **Conformational diversity of dichromate dianion .** *Inorganica Chimica Acta* 2012, **383**:164–168.
187. HOLCOMBE GW, PHIPPS GL, FIANDT JT: **Toxicity of Selected Priority Pollutants to Various Aquatic Organisms.** *Ecotoxicol Environ Saf* 1983, **7**:400–409.
188. Bose-O'Reilly S, McCarty KM, Steckling N, Lettmeier B: **Mercury exposure and children's health.** *Current problems in pediatric and adolescent health care* 2010, **40**:186–215.
189. Dujardin MC, Caze C, Vroman I: **Ion-exchange resins bearing thiol groups to remove mercury.: Part 1: synthesis and use of polymers prepared from thioester supported resin.** *Reactive and Functional Polymers* 2000, **43**:123–132.
190. Chiarle S, Ratto M, Rovatti M: **Mercury removal from water by ion exchange resins adsorption.** *Water Research* 2000, **34**:2971–2978.
191. Monteagudo JM, Ortiz MJ: **Removal of inorganic mercury from mine waste water by ion exchange.** *J. Chem. Technol. Biotechnol.* 2000, **75**:767–772.
192. HOSSEINI M, HASHEMIMOGHADDAM H: **Sensitized extraction spectrophotometric determination of Hg(II) with dithizone after its flotation as ion-associate using iodide and ferriin.** *Talanta* 2005, **67**:555–559.
193. Vircavs M, Rone V, Pelne A, Vircava D: **Coprecipitation behaviour of 5, 8-polyquinolyl polydisulphide for trace element preconcentration from aqueous solution.** *Analytica Chimica Acta* 1994, **299**:291–298.
194. Minowa H, Ebihara M: **Separation of rare earth elements from scandium by extraction chromatography.** *Analytica Chimica Acta* 2003, **498**:25–37.
195. Cobo EO, Bessone JB: **Recovery of mercury using an electrochemical flow-by reactor. Part I Reaction rate expression for mercury deposition in the presence of a side reaction.** *Electrochimica Acta* 1997, **43**:713–721.

196. Hsi H-C, Tsai C-Y: **Chemical Engineering Journal**. *Chemical Engineering Journal* 2012, **191**:378–385.
197. Wajima T, Sugawara K: **Adsorption behaviors of mercury from aqueous solution using sulfur-impregnated adsorbent developed from coal**. *Fuel Processing Technology* 2011, **92**:1322–1327.
198. Yu M, Tian W, Sun D, Shen W, Wang G, Xu N: **Systematic studies on adsorption of 11 trace heavy metals on thiol cotton fiber**. *Analytica Chimica Acta* 2001, **428**:209–218.
199. Mohan D, Gupta VK, Srivastava SK, Chander S: **Kinetics of mercury adsorption from wastewater using activated carbon derived from fertilizer waste**. *Colloids and Surfaces A: Physicochemical and Engineering Aspects* 2000, **177**:169–181.
200. Walcarius A, Delacôte C: **Mercury(II) binding to thiol-functionalized mesoporous silicas: critical effect of pH and sorbent properties on capacity and selectivity**. *Analytica Chimica Acta* 2005, **547**:3–13.
201. KRISHNA M, RANJIT M, KARUNASAGAR D, ARUNACHALAM J: **A rapid ultrasound-assisted thiourea extraction method for the determination of inorganic and methyl mercury in biological and environmental samples by CVAAS**. *Talanta* 2005, **67**:70–80.
202. Puanngam M, Unob F: **Preparation and use of chemically modified MCM-41 and silica gel as selective adsorbents for Hg(II) ions**. *Journal of Hazardous Materials* 2008, **154**:578–587.
203. Mureseanu M, Reiss A, Cioatera N, Trandafir I, Hulea V: **Mesoporous silica functionalized with 1-furoyl thiourea urea for Hg(II) adsorption from aqueous media**. *Journal of Hazardous Materials* 2010, **182**:197–203.
204. Feng X: **Functionalized Monolayers on Ordered Mesoporous Supports**. *Science* 1997, **276**:923–926.
205. Brown J, Richer R, Mercier L: **One-step synthesis of high capacity mesoporous Hg<sup>2+</sup> adsorbents by non-ionic surfactant assembly**. *Microporous and Mesoporous Materials* 2000, **37**:41–48.
206. Liu J, Feng X, Fryxell GE, Wang LQ, Kim AY, Gong M: **Hybrid mesoporous materials with functionalized monolayers**. *Adv. Mater.* 1998, **10**:161–165.
207. Arencibia A, Aguado J, Arsuaga JM: **Regeneration of thiol-functionalized mesostructured silica adsorbents of mercury**. *Applied Surface Science* 2010, **256**:5453–5457.
208. Hall GEM, Pelchat P: **The design and application of sequential extractions for**

- mercury, Part 2. Resorption of mercury onto the sample during leaching.** *Geochemistry: Exploration, Environment, Analysis* 2005, **5**:115–121.
209. Mensah-Biney R, Reid KJ, Hepworth MT: **The loading capacity of selected cation exchange resins and activated carbons for gold-thiourea complex.** *Minerals engineering* 1995, **8**:125–146.
210. Bhattacharjee S, Chakravarty S, Maity S, Dureja V, Gupta KK: **Metal contents in the groundwater of Sahebgunj district, Jharkhand, India, with special reference to arsenic.** *Chemosphere* 2005, **58**:1203–1217.
211. Harvey CF: **Arsenic mobility and groundwater extraction in bangladesh.** *Science* 2002, **298**:1602–1606.
212. Ng JC, Wang JP, Zheng B, Zhai C, Maddalena R, Liu F, Moore MR: **Urinary porphyrins as biomarkers for arsenic exposure among susceptible populations in Guizhou province, China.** *Toxicology and Applied Pharmacology* 2005, **206**:176–184.
213. Ng JC, Wang J, Shraim A: **A global health problem caused by arsenic from natural sources.** *Chemosphere* 2003, **52**:1353–1359.
214. EPA: *EPA Technologies and Costs for Removal of Arsenic from Drinking Water.* 2000.
215. Jain CK, Singh RD: **Technological options for the removal of arsenic with special reference to South East Asia.** *Journal of Environmental Management* 2012, **107**:1–18.
216. Bissen M, Frimmel FH: **Arsenic—a review. Part I: Occurrence, toxicity, speciation, mobility.** *Acta hydrochimica et hydrobiologica* 2003, **31**:9–18.
217. Sharma VK, Sohn M: **Aquatic arsenic: Toxicity, speciation, transformations, and remediation.** *Environment International* 2009, **35**:743–759.
218. Aposhian HV, Aposhian MM: **Arsenic Toxicology: Five Questions †.** *Chem. Res. Toxicol.* 2006, **19**:1–15.
219. Pena ME, Korfiatis GP, Patel M, Lippincott L, Meng X: **Adsorption of As(V) and As(III) by nanocrystalline titanium dioxide.** *Water Research* 2005, **39**:2327–2337.
220. Guan X, Ma J, Dong H, Jiang L: **Removal of arsenic from water: Effect of calcium ions on As(III) removal in the KMnO<sub>4</sub>-Fe(II) process.** *Water Research* 2009, **43**:5119–5128.
221. Mohan D, Pittman CU Jr.: **Arsenic removal from water/wastewater using adsorbents—A critical review.** *Journal of Hazardous Materials* 2007, **142**:1–

53.

222. Pierce ML, Moore CB: **Adsorption of arsenite and arsenate on amorphous iron hydroxide.** *Water Research* 1982, **16**:1247–1253.
223. Kim MJ, Nriagu J: **Oxidation of arsenite in groundwater using ozone and oxygen.** *Sci. Total Environ.* 2000, **247**:71–79.
224. Hao J, Han M-J, Meng X: **Preparation and evaluation of thiol-functionalized activated alumina for arsenite removal from water.** *Journal of Hazardous Materials* 2009, **167**:1215–1221.
225. McKimmy E, Dulebohn J, Shah J, Pinnavaia TJ: **Trapping of arsenite by mercaptopropyl-functionalized mesostructured silica with a wormhole framework.** *Chem. Commun.* 2005.
226. Fan H-T, Fan X, Li J, Guo M, Zhang D, Yan F, Sun T: **Selective removal of arsenic(V) from aqueous solution using a surface-ion-imprinted amine-functionalized silica gel sorbent.** *Ind. Eng. Chem. Res.* 2012, **51**:5216–5223.
227. Chen D, Huang C, He M, Hu B: **Separation and preconcentration of inorganic arsenic species in natural water samples with 3-(2-aminoethylamino) propyltrimethoxysilane modified ordered mesoporous silica micro-column and their determination by inductively coupled plasma optical emission spectrometry.** *Journal of Hazardous Materials* 2009, **164**:1146–1151.
228. Zhong LS, Hu JS, Liang HP, Cao AM, Song WG, Wan LJ: **Self-assembled 3D flowerlike iron oxide nanostructures and their application in water treatment.** *Adv. Mater.* 2006, **18**:2426–2431.
229. Jeon C-S, Baek K, Park J-K, Oh Y-K, Lee S-D: **Adsorption characteristics of As(V) on iron-coated zeolite.** *Journal of Hazardous Materials* 2009, **163**:804–808.
230. Zhu H, Jia Y, Wu X, Wang H: **Removal of arsenic from water by supported nano zero-valent iron on activated carbon.** *Journal of Hazardous Materials* 2009, **172**:1591–1596.
231. Pantani C, Spreti N, Maggitti MC, Germani R: **Acute toxicity of some synthetic cationic and zwitterionic surfactants to freshwater amphipod *Echinogammarus tibaldii*.** *Bull Environ Contam Toxicol* 1995, **55**:179–186.
232. Isomaa B, Reuter J, Djupsund BM: **The subacute and chronic toxicity of cetyltrimethylammonium bromide (CTAB), a cationic surfactant, in the rat.** *Arch. Toxicol.* 1976, **35**:91–96.
233. Brutchey RL, Morse DE: **Silicatein and the translation of its molecular mechanism of biosilicification into low temperature nanomaterial synthesis.**



- Chem. Rev.* 2008, **108**:4915–4934.
234. Hildebrand M: **Diatoms, biomineralization processes, and genomics.** *Chem. Rev.* 2008, **108**:4855–4874.
235. Belton DJ, Patwardhan SV, Annenkov VV, Danilovtseva EN, Perry CC: **From biosilicification to tailored materials: Optimizing hydrophobic domains and resistance to protonation of polyamines.** *Proc. Natl. Acad. Sci. U.S.A.* 2008, **105**:5963–5968.
236. Patwardhan SV, Clarson SJ, Perry CC: **On the role(s) of additives in bioinspired silicification.** *Chem. Commun.* 2005, **9**:1113–1121.
237. Forsyth C, Patwardhan SV: **Controlling performance of lipase immobilised on bioinspired silica.** *J. Mater. Chem. B* 2013, **1**:1164.
238. Patwardhan SV: **Biomimetic and bioinspired silica: recent developments and applications.** *Chem. Commun.* 2011, **47**:7567–7582.
239. Dickinson M, Scott TB: **The application of zero-valent iron nanoparticles for the remediation of a uranium-contaminated waste effluent.** *Journal of Hazardous Materials* 2010, **178**:171–179.
240. Barnes RJ, Riba O, Gardner MN, Scott TB, Jackman SA, Thompson IP: **Optimization of nano-scale nickel/iron particles for the reduction of high concentration chlorinated aliphatic hydrocarbon solutions.** *Chemosphere* 2010, **79**:448–454.
241. Wang CB, Zhang WX: **Synthesizing nanoscale iron particles for rapid and complete dechlorination of TCE and PCBs.** *Environ. Sci. Technol.* 1997, **31**:2154–2156.
242. Choe S, Lee SH, Chang YY, Hwang KY, Khim J: **Rapid reductive destruction of hazardous organic compounds by nanoscale Fe-0.** *Chemosphere* 2001, **42**:367–372.
243. Klausen J, Trober SP, Haderlein SB, Schwarzenbach RP: **Reduction of substituted nitrobenzenes by Fe(II) in aqueous mineral suspensions.** *Environ. Sci. Technol.* 1995, **29**:2396–2404.
244. Zhang WX: **Nanoscale iron particles for environmental remediation: An overview.** *J Nanopart Res* 2003, **5**:323–332.
245. Tang SCN, Lo IMC: **Magnetic nanoparticles: Essential factors for sustainable environmental applications.** *Water Research* 2013, **47**:2613–2632.
246. Zeng L: **A method for preparing silica-containing iron (III) oxide adsorbents for arsenic removal.** *Water Research* 2003, **37**:4351–4358.

247. Hoch LB, Mack EJ, Hydutsky BW, Hershman JM, Skluzacek IM, Mallouk TE: **Carbothermal synthesis of carbon-supported nanoscale zero-valent iron particles for the remediation of hexavalent chromium.** *Environ. Sci. Technol.* 2008, **42**:2600–2605.
248. Li S, Wu P, Li H, Zhu N, LI P, Wu J, Wang X, Dang Z: **Synthesis and characterization of organo-montmorillonite supported iron nanoparticles.** *Applied Clay Science* 2010, **50**:330–336.
249. Uezuem C, Shahwan T, Eroglu AE, Hallam KR, Scott TB, Lieberwirth I: **Synthesis and characterization of kaolinite-supported zero-valent iron nanoparticles and their application for the removal of aqueous Cu(2+) and Co(2+) ions.** *Applied Clay Science* 2009, **43**:172–181.
250. Ponder SM, Darab JG, Mallouk TE: **Remediation of Cr(VI) and Pb(II) aqueous solutions using supported, nanoscale zero-valent iron.** *Environ. Sci. Technol.* 2000, **34**:2564–2569.
251. Shi L-N, Lin Y-M, Zhang X, Chen Z-L: **Synthesis, characterization and kinetics of bentonite supported nZVI for the removal of Cr(VI) from aqueous solution.** *Chemical Engineering Journal* 2011, **171**:612–617.
252. Fernández-Pacheco R, Arruebo M, Marquina C, Ibarra R, Arbiol J, Santamaría J: **Highly magnetic silica-coated iron nanoparticles prepared by the arc-discharge method.** *Nanotechnology* 2006, **17**:1188–1192.
253. Cannas C, Concas G, Gatteschi D, Falqui A, Musinu A, Piccaluga G, Sangregorio C, Spano G: **Superparamagnetic behaviour of  $\gamma$ -Fe<sub>2</sub>O<sub>3</sub> nanoparticles dispersed in a silica matrix.** *Phys. Chem. Chem. Phys.* 2001, **3**:832–838.
254. Yang H-H, Zhang S-Q, Chen X-L, Zhuang Z-X, Xu J-G, Wang X-R: **Magnetite-Containing Spherical Silica Nanoparticles for Biocatalysis and Bioseparations.** *Anal. Chem.* 2004, **76**:1316–1321.
255. Santra S, Tapeç R, Theodoropoulou N, Dobson J, Hebard A, Tan W: **Synthesis and characterization of silica-coated iron oxide nanoparticles in microemulsion: the effect of nonionic surfactants.** *Langmuir* 2001, **17**:2900–2906.
256. Casula MF, Corrias A, Paschina G: **Iron oxide–silica aerogel and xerogel nanocomposite materials.** *Journal of Non-Crystalline Solids* 2001, **293**:25–31.
257. Barrado E, Rodríguez JA, Prieto F, Medina J: **Characterization of iron oxides embedded in silica gel obtained by two different methods.** *Journal of Non-Crystalline Solids* 2005, **351**:906–914.
258. Janzen C, Knipping J, Rellinghaus B, Roth P: **Formation of silica-embedded**

- iron-oxide nanoparticles in low-pressure flames.** *J Nanopart Res* 2003, **5**:589–596.
259. Del Monte F, Morales MP, Levy D, Fernandez A, Ocana M, Roig A, Molins E, O'Grady K, Serna CJ: **Formation of  $\gamma$ -Fe<sub>2</sub>O<sub>3</sub> isolated nanoparticles in a silica matrix.** *Langmuir* 1997, **13**:3627–3634.
260. Ennas G, Musinu A, Piccaluga G, Zedda D, Gatteschi D, Sangregorio C, Stanger JL, Concas G, Spano G: **Characterization of iron oxide nanoparticles in an Fe<sub>2</sub>O<sub>3</sub>-SiO<sub>2</sub> composite prepared by a sol-gel method.** *Chem. Mater.* 1998, **10**:495–502.
261. Cannas C, Gatteschi D, Musinu A, Piccaluga G, Sangregorio C: **Structural and magnetic properties of Fe<sub>2</sub>O<sub>3</sub> nanoparticles dispersed over a silica matrix.** *J. Phys. Chem. B* 1998, **102**:7721–7726.
262. Tronc, Chaneac, Jolivet: **Structural and Magnetic Characterization of  $\epsilon$ -Fe<sub>2</sub>O<sub>3</sub>.** *Journal of Solid State Chemistry* 1998, **139**:12–12.
263. Fabrizioli P, Bürgi T, Baiker A: **Environmental catalysis on iron oxide–silica aerogels: selective oxidation of NH<sub>3</sub> and reduction of NO by NH<sub>3</sub>.** *Journal of Catalysis* 2002, **206**:143–154.
264. Sartoratto PPC, Caiado KL, Pedroza RC, da Silva SW, Morais PC: **The thermal stability of maghemite-silica nanocomposites: An investigation using X-ray diffraction and Raman spectroscopy.** *Journal of Alloys and Compounds* 2007, **434-435**:650–654.
265. Mornet S, Grasset F, Portier J, Duguet E: **Maghemite@ silica nanoparticles for biological applications.** *Eur Cell Mater* 2002, **3**:110–113.
266. Zhang L, Papaefthymiou GC, Ziolo RF, Ying JY: **Novel  $\gamma$ -Fe<sub>2</sub>O<sub>3</sub>/SiO<sub>2</sub> magnetic nanocomposites via sol-gel matrix-mediated synthesis.** *Nanostructured Materials* 1997, **9**:185–188.
267. Su C, Puls RW: **Arsenate and arsenite removal by zerovalent iron: kinetics, redox transformation, and implications for in situ groundwater remediation.** *Environ. Sci. Technol.* 2001, **35**:1487–1492.
268. Biterna M, Arditoglou A, Tsikouras E, Voutsas D: **Arsenate removal by zero valent iron: Batch and column tests.** *Journal of Hazardous Materials* 2007, **149**:548–552.
269. Cantrell KJ, Kaplan DI, Wietsma TW: **Zero-valent iron for the in situ remediation of selected metals in groundwater.** *Journal of Hazardous Materials* 1995, **42**:201–212.
270. Fiedor JN, Bostick WD, Jarabek RJ, Farrell J: **Understanding the mechanism**

- of uranium removal from groundwater by zero-valent iron using X-ray photoelectron spectroscopy. *Environ. Sci. Technol.* 1998, **32**:1466–1473.**
271. Puls RW, Paul CJ, Powell RM: **The application of in situ permeable reactive (zero-valent iron) barrier technology for the remediation of chromate-contaminated groundwater: a field test.** *Appl Geochem* 1999, **14**:989–1000.
272. Dickerson MB, Sandhage KH, Naik RR: **Protein- and peptide-directed syntheses of inorganic materials.** *Chem. Rev.* 2008, **108**:4935–4978.
273. Knecht MR, Wright DW: **Dendrimer-mediated formation of multicomponent nanospheres.** *Chem. Mater.* 2004, **16**:4890–4895.
274. Naik RR, Tomczak MM, Luckarift HR, Spain JC, Stone MO: **Entrapment of enzymes and nanoparticles using biomimetically synthesized silica.** *Chem. Commun.* 2004, doi:10.1039/B404586f.
275. Patwardhan SV, Perry CC: **Synthesis of enzyme and quantum dot in silica by combining continuous flow and bioinspired routes.** *SILICON* 2010, **2**:33–39.
276. Mokhonoana MP, Coville NJ: **Highly loaded Fe-MCM-41 materials: synthesis and reducibility studies.** *Materials* 2009, **2**:2337–2359.
277. Purna Chandra Rao G, Satyaveni S, Ramesh A, Sessaiah K, Murthy KSN, Choudary NV: **Sorption of cadmium and zinc from aqueous solutions by zeolite 4A, zeolite 13X and bentonite.** *Journal of Environmental Management* 2006, **81**:265–272.
278. Zolfaghari G, Esmaili-Sari A, Anbia M, Younesi H, Amirmahmoodi S, Ghafari-Nazari A: **Taguchi optimization approach for Pb(II) and Hg(II) removal from aqueous solutions using modified mesoporous carbon.** *Journal of Hazardous Materials* 2011, **192**:1046–1055.
279. Drummond C, McCann R, Patwardhan SV: **A feasibility study of the biologically inspired green manufacturing of precipitated silica.** *Chemical Engineering Journal* 2014, **244**:483–492.
280. Goh SL: **Zero valence iron (ZVI) supported by bio-inspired silica for environmental remediation.** 2011.
281. Fu Y, Yu SL, Yu YZ, Qiu, L. P., Hui B: **Reaction mode between Si and Fe and evaluation of optimal species in poly-silicic-ferric coagulant.** *J Environ Sci (China)* 2007, **19**:678–688.
282. Siskova K, Tucek J, Machala L, Otyepkova E, Filip J, Safarova K, Pechousek J, Zboril R: **Air-stable nZVI formation mediated by glutamic acid: solid-state storable material exhibiting 2D chain morphology and high reactivity in aqueous environment.** *J Nanopart Res* 2012, **14**.

283. Yu C, Cai Q, Guo ZX, Yang Z, Khoo SB: **Inductively coupled plasma mass spectrometry study of the retention behavior of arsenic species on various solid phase extraction cartridges and its application in arsenic speciation.** *Spectrochim Acta Part B At Spectrosc* 2003, **58**:1335–1349.
284. Hou X, Jones B: **Inductively coupled plasma/optical emission spectrometry.** *Encyclopedia of Analytical Chemistry* 2000.
285. Cullen WR, Reimer KJ: **Arsenic speciation in the environment.** *Chem. Rev.* 1989, **89**:713–764.
286. Sohn S, Kim D: **Modification of langmuir isotherm in solution systems—definition and utilization of concentration dependent factor.** *Chemosphere* 2005, **58**:115–123.
287. Do Duong D: *Adsorption Analysis*. Imperial College Pr; 1998.
288. Zhang S, Li X-Y, Chen JP: **Preparation and evaluation of a magnetite-doped activated carbon fiber for enhanced arsenic removal.** *Carbon* 2010, **48**:60–67.
289. Roddick-Lanzilotta AJ, McQuillan AJ, Craw D: **Infrared spectroscopic characterisation of arsenate (V) ion adsorption from mine waters, Macraes mine, New Zealand.** *Appl Geochem* 2002, **17**:445–454.
290. Da Sacco L, Masotti A: **Chitin and chitosan as multipurpose natural polymers for groundwater arsenic removal and As<sub>2</sub>O<sub>3</sub> delivery in tumor therapy.** *Marine Drugs* 2010, **8**:1518–1525.
291. Payne K, Abdel-Fattah T: **Adsorption of arsenate and arsenite by iron-treated activated carbon and zeolites: effects of PH, temperature, and ionic strength.** *J. of Env. Sc. & Hlth., Part A* 2005, **40**:723–749.
292. Gu Z, Fang J, Deng B: **Preparation and evaluation of GAC-based iron-containing adsorbents for arsenic removal.** *Environ. Sci. Technol.* 2005, **39**:3833–3843.
293. Shareef KM: **Sorbents for contaminants uptake from aqueous solutions. Part I: Heavy metals.** *World Journal of Agricultural Sciences* 2009, **5**:819–831.
294. Jiuhui Q: **Research progress of novel adsorption processes in water purification: A review.** *J Environ Sci (China)* 2008, **20**:1–13.
295. Chen W, Parette R, Zou J, Cannon FS, Dempsey BA: **Arsenic removal by iron-modified activated carbon.** *Water Research* 2007, **41**:1851–1858.
296. Jang M, Shin EW, Park JK: **Removal of arsenic using mesoporous silicate media impregnated metal oxides nano-particles.** *Proceedings of the Water Environment Federation* 2002, **2002**:40–54.

297. Guo X, Chen F: **Removal of arsenic by bead cellulose loaded with iron oxyhydroxide from groundwater.** *Environ. Sci. Technol.* 2005, **39**:6808–6818.
298. Guo H, Li Y, Zhao K: **Arsenate removal from aqueous solution using synthetic siderite.** *Journal of Hazardous Materials* 2010, **176**:174–180.
299. Balaji T, Yokoyama T, Matsunaga H: **Adsorption and removal of As(V) and As(III) using Zr-loaded lysine diacetic acid chelating resin.** *Chemosphere* 2005, **59**:1169–1174.
300. Solozhenkin PM, Deliyanni EA, Bakoyannakis VN, Zouboulis AI, Matis KA: **Removal of As (V) ions from solution by akaganeite  $\beta$ -FeO (OH) nanocrystals.** *Journal of Mining Science* 2003, **39**:287–296.
301. Styles PM, Chanda M, Rempel GL: **Sorption of arsenic anions onto poly (ethylene mercaptoacetimide).** *Reactive and Functional Polymers* 2003, **31**:89–102.
302. Chowdhury SR, Yanful EK, Pratt AR: **Arsenic removal from aqueous solutions by mixed magnetite–maghemite nanoparticles.** *Environ Earth Sci* 2010, **64**:411–423.
303. Xie Q, Xie J, Wang Z, Wu D, Zhang Z, Kong H: **Adsorption of organic pollutants by surfactant modified zeolite as controlled by surfactant chain length.** *Microporous and Mesoporous Materials* 2013, **179**:144–150.
304. Bruzzoniti MC, Fungi M, Sarzanini C: **Determination of EPA's priority pollutant polycyclic aromatic hydrocarbons in drinking waters by solid phase extraction-HPLC.** *Anal. Methods* 2010, **2**:739.
305. Henner P, Schiavon M, Morel J-L, Lichtfouse E: **Polycyclic aromatic hydrocarbon (PAH) occurrence and remediation methods.** *Analisis* 1997, **25**.
306. Zhang X-L, Niu H-Y, Li W-H, Shi Y-L, Cai Y-Q: **A core–shell magnetic mesoporous silica sorbent for organic targets with high extraction performance and anti-interference ability.** *Chem. Commun.* 2011, **47**:4454.
307. Gotovac S, Honda H, Hattori Y, Takahashi K, Kanoh H, Kaneko K: **Effect of nanoscale curvature of single-walled carbon nanotubes on adsorption of polycyclic aromatic hydrocarbons.** *Nano Lett.* 2007, **7**:583–587.
308. Mumtaz M, George J: **Toxicological profile for polycyclic aromatic hydrocarbons (PAHs).** *U.S. Department of Health and Human Services, Agency for Toxic Substances and Disease Registry* 1995.
309. Ding J, Gao Q, Luo D, Shi Z-G, Feng Y-Q: **N-Octadecylphosphonic acid grafted mesoporous magnetic nanoparticle: Preparation, characterization, and application in magnetic solid-phase extraction.** *J Chromatogr A* 2010,

- 1217:7351–7358.
310. Yang K, Zhu L, Xing B: **Adsorption of polycyclic aromatic hydrocarbons by carbon nanomaterials.** *Environ. Sci. Technol.* 2006, **40**:1855–1861.
  311. Mastral AM, Callén MS: **A review on polycyclic aromatic hydrocarbon (PAH) emissions from energy generation.** *Environ. Sci. Technol.* 2000, **34**:3051–3057.
  312. Zhang S, Niu H, Hu Z, Cai Y, Shi Y: **Preparation of carbon coated Fe<sub>3</sub>O<sub>4</sub> nanoparticles and their application for solid-phase extraction of polycyclic aromatic hydrocarbons from environmental water samples.** *J Chromatogr A* 2010, **1217**:4757–4764.
  313. Araújo RS, Azevedo DCS, Cavalcante CL Jr., Jiménez-López A, Rodríguez-Castellón E: **Adsorption of polycyclic aromatic hydrocarbons (PAHs) from isooctane solutions by mesoporous molecular sieves: Influence of the surface acidity.** *Microporous and Mesoporous Materials* 2008, **108**:213–222.
  314. Liu G, Niu Z, Van Niekerk D, Xue J, Zheng L: **Polycyclic aromatic hydrocarbons (PAHs) from coal combustion: emissions, analysis, and toxicology.** *Rev Environ Contam Toxicol* 2008, **192**:1–28.
  315. Zhao YX, Ding MY, Chen DP: **Adsorption properties of mesoporous silicas for organic pollutants in water.** *Analytica Chimica Acta* 2005, **542**:193–198.
  316. Williamson KS, Petty JD, Huckins JN, Lebo JA, Kaiser EM: **HPLC-PFD determination of priority pollutant PAHs in water, sediment, and semipermeable membrane devices.** *Chemosphere* 2002, **49**:703–715.
  317. Bojes HK, Pope PG: **Characterization of EPA's 16 priority pollutant polycyclic aromatic hydrocarbons (PAHs) in tank bottom solids and associated contaminated soils at oil exploration and production sites in Texas.** *Regulatory Toxicology and Pharmacology* 2007, **47**:288–295.
  318. Lee H, Dellatore SM, Miller WM, Messersmith PB: **Mussel-inspired surface chemistry for multifunctional coatings.** *Science* 2007, **318**:426–430.
  319. Wang Y, Wang S, Niu H, Ma Y, Zeng T, Cai Y, Meng Z: **Preparation of polydopamine coated Fe<sub>3</sub>O<sub>4</sub> nanoparticles and their application for enrichment of polycyclic aromatic hydrocarbons from environmental water samples.** *J Chromatogr A* 2013, **1283**:20–26.
  320. Zhou W-H, Lu C-H, Guo X-C, Chen F-R, Yang H-H, Wang X-R: **Mussel-inspired molecularly imprinted polymer coating superparamagnetic nanoparticles for protein recognition.** *J. Mater. Chem.* 2010, **20**:880.
  321. Einicke WD, Uhlig H, Enke D, Gläser R, Reichenbach C, Ebbinghaus SG:

**Synthesis of hierarchical micro/mesoporous Y-zeolites by pseudomorphic transformation.** *Colloids and Surfaces A: Physicochemical and Engineering Aspects* 2013, **437**:108–112.

## **Publications from this work**

- [1] S.A. Idris, K. Alotaibi, T.A. Peshkur, P. Anderson, Preconcentration and selective extraction of chromium species in water samples using amino modified mesoporous silica, *Journal of Colloid and Interface Science*. (2012) 1–9.
- [2] S.A. Idris, K.M. Alotaibi, T.A. Peshkur, P. Anderson, M. Morris, L.T. Gibson, Adsorption kinetic study: Effect of adsorbent pore size distribution on the rate of Cr (VI) uptake, *Microporous and Mesoporous Materials*. 165 (2013) 99–105.
- [3] K.M. Alotaibi, L. Shiels, L. Lacaze, T.A. Peshkur, P. Anderson, L. Machala, K. Critchley, S.V. Patwardhan, L.T. Gibson, Iron Supported On Bioinspired Green Silica for Water Remediation, Submitted.